

NAVAL POSTGRADUATE SCHOOL

Monterey, California



THESIS

**PREDICTION OF SURFACE SHIP RESPONSE TO
SEVERE UNDERWATER EXPLOSIONS USING A
VIRTUAL UNDERWATER SHOCK ENVIRONMENT**

by

Nathan A. Schneider

June 2003

Thesis Advisor:

Young S. Shin

Approved for public release; distribution is unlimited.

THIS PAGE INTENTIONALLY LEFT BLANK

REPORT DOCUMENTATION PAGE			<i>Form Approved OMB No. 0704-0188</i>	
Public reporting burden for this collection of information is estimated to average 1 hour per response, including the time for reviewing instruction, searching existing data sources, gathering and maintaining the data needed, and completing and reviewing the collection of information. Send comments regarding this burden estimate or any other aspect of this collection of information, including suggestions for reducing this burden, to Washington headquarters Services, Directorate for Information Operations and Reports, 1215 Jefferson Davis Highway, Suite 1204, Arlington, VA 22202-4302, and to the Office of Management and Budget, Paperwork Reduction Project (0704-0188) Washington DC 20503.				
1. AGENCY USE ONLY (Leave blank)		2. REPORT DATE June 2003	3. REPORT TYPE AND DATES COVERED Master's Thesis	
4. TITLE AND SUBTITLE: Prediction of Surface Ship Response to Severe Underwater Explosions Using a Virtual Underwater Shock Environment			5. FUNDING NUMBERS	
6. AUTHOR(S) Nathan A. Schneider				
7. PERFORMING ORGANIZATION NAME(S) AND ADDRESS(ES) Naval Postgraduate School Monterey, CA 93943-5000			8. PERFORMING ORGANIZATION REPORT NUMBER	
9. SPONSORING /MONITORING AGENCY NAME(S) AND ADDRESS(ES) N/A			10. SPONSORING/MONITORING AGENCY REPORT NUMBER	
11. SUPPLEMENTARY NOTES The views expressed in this thesis are those of the author and do not reflect the official policy or position of the Department of Defense or the U.S. Government.				
12a. DISTRIBUTION / AVAILABILITY STATEMENT Approved for public release; distribution is unlimited.			12b. DISTRIBUTION CODE	
13. ABSTRACT (maximum 200 words) During World War II many surface combatants were damaged or severely crippled by close-proximity underwater explosions from ordnance that had actually missed their target. Since this time all new classes of combatants have been required to conduct shock trial tests on the lead ship of the class in order to test the survivability of mission essential equipment in a severe shock environment. While these tests are extremely important in determining the vulnerabilities of a surface ship, they require an extensive amount of preparation, manhours, and money. Furthermore, these tests present an obvious danger to the crew on board, the ship itself, and any marine life in the vicinity. Creating a virtual shock environment by use of a computer to model the ship structure and the surrounding fluid presents a valuable design tool and an attractive alternative to these tests. This thesis examines the accuracy of shock simulation using the shock trials conducted on USS WINSTON S. CHURCHILL (DDG 81) in 2001. Specifically, all three explosions that DDG 81 was subjected to are simulated and the resulting predictions compared with the actual shock trial data. The effects of fluid volume size, mesh density, mesh quality, and shot location are investigated.				
14. SUBJECT TERMS Underwater Explosion, Modeling and Simulation, Shock and Vibration, Ship Shock, Virtual Environment, UNDEX, Shock Measurement			15. NUMBER OF PAGES 184	
			16. PRICE CODE	
17. SECURITY CLASSIFICATION OF REPORT Unclassified	18. SECURITY CLASSIFICATION OF THIS PAGE Unclassified	19. SECURITY CLASSIFICATION OF ABSTRACT Unclassified	20. LIMITATION OF ABSTRACT UL	

THIS PAGE INTENTIONALLY LEFT BLANK

Approved for public release; distribution is unlimited.

**PREDICTION OF SURFACE SHIP RESPONSE
TO SEVERE UNDERWATER EXPLOSIONS USING
A VIRTUAL UNDERWATER SHOCK ENVIRONMENT**

Nathan A. Schneider
Lieutenant, United States Navy
B.S., United States Naval Academy, 1996

Submitted in partial fulfillment of the
requirements for the degree of

MECHANICAL ENGINEER

and

MASTER OF SCIENCE IN MECHANICAL ENGINEERING

from the

**NAVAL POSTGRADUATE SCHOOL
June 2003**

Author: Nathan A. Schneider

Approved by: Young S. Shin
Thesis Advisor

Young W. Kwon
Chairman, Department of Mechanical Engineering

THIS PAGE INTENTIONALLY LEFT BLANK

ABSTRACT

During World War II many surface combatants were severely crippled by close-proximity underwater explosions from ordnance that had actually missed their target. Since this time, in order to test the survivability of mission essential equipment in a severe shock environment, all new classes of combatants have been required to have shock trial tests conducted on the lead ship of the class. While these tests are extremely important in determining the vulnerabilities of a surface ship, they require an extensive amount of preparation, manhours, and money. Furthermore, these tests present an obvious danger to the crew onboard, the ship itself, and any marine life in the vicinity.

Creating a virtual shock environment by use of a computer to model the ship structure and the surrounding fluid presents a valuable design tool and an attractive alternative to these tests. This thesis examines the accuracy of shock simulation using the shock trials conducted on USS WINSTON S. CHURCHILL (DDG 81) in 2001. Specifically, all three explosions DDG 81 was subjected to are simulated and the resulting predictions compared with actual shock trial data. The effects of the fluid volume size, mesh density, mesh quality, and shot location are investigated.

THIS PAGE INTENTIONALLY LEFT BLANK

TABLE OF CONTENTS

I.	INTRODUCTION.....	1
A.	BACKGROUND	1
B.	SCOPE OF RESEARCH	3
II.	UNDERWATER SHOCK PHENOMENA	5
A.	INCIDENT PRESSURE WAVE	5
B.	EXPLOSIVE GAS BUBBLE	7
C.	CAVITATION.....	9
1.	Bulk Cavitation	10
2.	Local Cavitation	13
D.	STRUCTURAL RESPONSE TO UNDERWATER SHOCK	15
1.	Analytical Kick-Off Velocity Approximation	15
2.	Computational Structural Response Approximation.....	16
III.	UNDERWATER SHOCK MODELING AND SIMULATION	19
A.	STRUCTURAL MODEL.....	19
1.	USS WINSTON S. CHURCHILL (DDG 81)	19
2.	Ship System Damping.....	22
B.	SIMULATION CODE.....	25
1.	Model Generation and Pre-Processing	25
2.	Simulation Processing.....	27
a.	<i>FLUMAS</i>	28
b.	<i>AUGMAT</i>	28
c.	<i>TIMINT</i>	28
3.	Simulation Post Processing and Data Extraction	28
4.	Data Processing and Comparison.....	29
IV.	FLUID MESH MODELING.....	31
A.	FLUID MESH CONSTRUCTION.....	31
1.	Inner Liner	31
a.	<i>USA Code Stability Criteria</i>	32
b.	<i>Orthogonality</i>	33
c.	<i>Waterline</i>	33
2.	Inner Mesh.....	34
a.	<i>Thomas-Middlecoff Relaxation</i>	34
b.	<i>Equipotential Relaxation</i>	35
3.	Transitional Mesh	36
4.	Outer Mesh	37
B.	FLUID MODEL DEPTH	38
C.	FLUID MODEL PROCESSING	39
V.	DATA COLLECTION AND ANALYSIS	41
A.	VELOCITY RESPONSE “DRIFT”	41

B.	HIGH FREQUENCY “NOISE”	46
VI.	SIMULATION RESULTS AND ANALYSIS	49
A.	ANALYSIS AND COMPARISON	49
1.	Sensor/Node Location	49
2.	Error Measurement	50
B.	SEVERE SHOCK (SHOT 3)	53
1.	Fluid Mesh Depth.....	56
2.	Fluid Mesh Quality	59
3.	Fluid Mesh Density	64
a.	Error Comparison	66
b.	Velocity Plots.....	70
C.	SHOT 1	74
1.	Fluid Mesh Depth.....	74
2.	Mesh Quality	75
3.	Mesh Density	76
a.	Error Comparison	77
b.	Velocity Plots.....	81
D.	SHOT 2	85
1.	Error Comparison	86
2.	Velocity Plots	90
E.	QUALITATIVE COMPARISON	94
F.	EXTENDED DEPTH FLUID MODEL	96
VII.	CONCLUSIONS AND RECOMMENDATIONS.....	103
APPENDIX A.	DDG 81 VERTICAL VELOCITY RESPONSE PLOTS	107
A.	SHOT 1	107
B.	SHOT 2	112
C.	SHOT 3	118
APPENDIX B:	FLUID MODELING IN TRUEGRID	125
A.	STRUCTURAL MODEL.....	125
B.	INNER LINER.....	127
C.	INNER MESH.....	134
D.	TRANSITIONAL MESH.....	141
E.	OUTER MESH.....	144
F.	DAA BOUNDARY	146
APPENDIX C:	TRUEGRID MODELING COMMANDS.....	149
APPENDIX D:	USA/LS-DYNA INPUT DECKS	157
A.	LS-DYNA KEYWORD FILE	157
B.	USA INPUT FILES.....	159
1.	<u>FLUMAS</u>	159
2.	<u>AUGMAT</u>	159
3.	<u>TIMINT</u>	160
	LIST OF REFERENCES.....	161

INITIAL DISTRIBUTION LIST	163
--	------------

THIS PAGE INTENTIONALLY LEFT BLANK

LIST OF FIGURES

Figure 1.	Shock Wave Profiles From a 300 lb. TNT Charge [from Ref 9.].....	6
Figure 2.	Oscillatory Bubble Pulse of and Migration Path of Explosive Gas Bubble [from Ref. 9]	9
Figure 3.	2-Dimensional Long Range Underwater Shock Wave Propagation Pattern [from Ref. 9]	10
Figure 4.	Shock Wave Pressure Profile Showing Cut Off Upon Rarefaction Wave Arrival [from Ref. 9].....	11
Figure 5.	Example of Cavitation Region From a Large Charge of HBX-1 Explosive (not to scale).....	13
Figure 6.	Taylor Air Blacked Plate Subjected to a Plane Wave [from Ref. 11]	14
Figure 7.	USS WINSTON S. CHURCHILL (DDG 81) FINITE ELEMENT MODEL [from Ref. 14].	19
Figure 8.	Equipment Modeled as Rigid Bodies in DDG 81 FEM [from Ref. 14]	21
Figure 9.	Vertical Modal Damping Ratio for Single Area Group of DDG 53 [from Ref. 19]	23
Figure 10.	Damping Ratio Curve Plot for Using Recommended Rayleigh Damping Coefficients for DDG 53 [from Ref. 19]	25
Figure 11.	Model Generation and Simulation Flow Chart.....	26
Figure 12.	Fluid Model Two Layer Inner Liner	34
Figure 13.	Fluid Model Inner Mesh	35
Figure 14.	Fluid Model Transitional Mesh	37
Figure 15.	Fluid Model Outer Mesh.....	38
Figure 16.	Complete Coupled Fluid-Structure Model (Shot 1)	39
Figure 17.	Raw Velocity Data Showing Drift.....	42
Figure 18.	Velocity Data After Drift Compensation Has Been Applied.....	42
Figure 19.	Comparison of High Pass Filtering vs. Drift Compensation	43
Figure 20.	Two-Pole High-Pass Bessel Filter With 3Hz Cut-off Frequency.....	44
Figure 21.	Fourier Spectra Plot Showing Structural Low Frequency Response (Vertical Velocity Input).....	45
Figure 22.	Butterworth vs. Bessel High Pass Filter	45
Figure 23.	Velocity Response After Filtering 0.5Hz High-Pass Butterworth Filter (Third-Order)	46
Figure 24.	Effect of Low-Pass Filtering Data	47
Figure 25.	Shot 3 Geometry. Most Severe Shot, Charge Off Port Midships	54
Figure 26.	1 st Generation Fluid and Structural Model [from Ref. 21]	57
Figure 27.	2 nd Generation Fluid and Structural Model.....	58
Figure 28.	Sonar Dome Region Showing Improvement in Mesh Uniformity of 3 rd Generation Fluid Model.....	60
Figure 29.	Keel Region Showing Improvement in Mesh Uniformity of 3 rd Generation Fluid Model.....	60

Figure 30.	Comparison of 2 nd and 3 rd Generation Fluid Model Errors in Relation to Longitudinal Position on the Structural Model.....	62
Figure 31.	Sonar Dome Region Velocity Plot Comparison	63
Figure 32.	Midship Region Velocity Plot Comparison.....	63
Figure 33.	Stern Region Velocity Plot Comparison.....	64
Figure 34.	Natural Frequency Error of FEM Pin-Pin Beam as a Function of Number of Elements Used.	65
Figure 35.	Russell's Error Factors for Coarse Mesh Fluid Model Comparison.....	66
Figure 36.	Russell's Error Factors for Medium Mesh Fluid Model Comparison	66
Figure 37.	Russell's Error Factors for Dense Mesh Fluid Model Comparison.....	67
Figure 38.	Russell's Comprehensive Error Trend as a Function of Longitudinal Position	69
Figure 39.	Keel Sensor V2000V.	70
Figure 40.	Keel Sensor V2016V	71
Figure 41.	Keel Sensor V2020V	72
Figure 42.	Bulkhead Sensor V2124V.....	73
Figure 43.	Mast Sensor A2240V	73
Figure 44.	Shot 1 Geometry. Most Extreme Aspect	74
Figure 45.	Russell's Error Factors for Coarse Mesh Fluid Model Comparison.....	77
Figure 46.	Russell's Error Factors for Medium Mesh Fluid Model Comparison	77
Figure 47.	Russell's Error Factors for Dense Mesh Fluid Model Comparison.....	78
Figure 48.	Shot 1 Russell's Comprehensive Error Trends.....	80
Figure 49.	Keel Sensor V2000V.	82
Figure 50.	Bulkhead Sensor V2124V.....	82
Figure 51.	Keel Sensor V2016V	83
Figure 52.	Keel Sensor V2020V.	84
Figure 53.	Mast Sensor A2240V.....	84
Figure 54.	Shot 2 Geometry. Charge Off Starboard Midships.....	85
Figure 55.	Russell's Error Factors for Coarse Mesh Fluid Model Comparison.....	86
Figure 56.	Russell's Error Factors for Medium Mesh Fluid Model Comparison	87
Figure 57.	Russell's Error Factors for Dense Mesh Fluid Model Comparison.....	87
Figure 58.	Russell's Comprehensive Error Trend as a Function of Longitudinal Position	90
Figure 59.	Keel Sensor V2000V	91
Figure 60.	Bulkhead Sensor V2124V.....	92
Figure 61.	Keel Sensor V2016V	92
Figure 62.	Keel Sensor V2020V	93
Figure 63.	Mast Sensor A2237V	94
Figure 64.	Average Russell's Comprehensive Error Factor Vertical Trend	95
Figure 65.	Bulkhead Sensor A2104V.....	100
Figure 66.	Keel Sensor V2034V	101
Figure 67.	Keel Sensor V2002V: (RM=0.0772, RP=0.1755, RC=0.1699)	107
Figure 68.	Keel Sensor V2007V: (RM=-0.1178, RP=0.1760, RC=0.1877)	108
Figure 69.	Bulkhead Sensor A2109V: (RM=-0.0679, RP=0.0848, RC=0.0962)	108
Figure 70.	Bulkhead Sensor V2013V: (RM=-0.1366, RP=0.1819, RC=0.2016)	109

Figure 71.	Bulkhead Sensor A2104V: (RM=-0.2235, RP=0.1184, RC=0.2241)	109
Figure 72.	Bulkhead Sensor A2116V: (RM=-0.0679, RP=0.0848, RC=0.0962)	110
Figure 73.	Bulkhead Sensor A2237V (RM=-0.0906, RP=0.1203, RC=0.1334)	110
Figure 74.	Keel Sensor V2034V: (RM=0.0296, RP=0.2233, RC=0.1996)	111
Figure 75.	Keel Sensor V2019V: (RM=-0.1463, RP=0.2447, RC=0.2526)	111
Figure 76.	Keel Sensor A2413V: (RM=0.0171, RP=0.3649, RC=0.3238)	112
Figure 77.	Keel Sensor V2002V: (RM=0.0579, RP=0.2001, RC=0.1846)	113
Figure 78.	Keel Sensor V2007V: (RM=-0.0245, RP=0.2092, RC=0.1866)	113
Figure 79.	Bulkhead Sensor A2109V: (RM=0.1170, RP=0.1647, RC=0.1790)	114
Figure 80.	Bulkhead Sensor V2013V: (RM=-0.1049, RP=0.1420, RC=0.1565)	114
Figure 81.	Bulkhead Sensor A2104V: (RM=-0.0388, RP=0.0953, RC=0.0912)	115
Figure 82.	Bulkhead Sensor A2116V: (RM=0.0070, RP=0.1003, RC=0.0891)	115
Figure 83.	Mast Sensor A2240V: (RM=-0.0626, RP=0.1335, RC=0.1307)	116
Figure 84.	Keel Sensor V2034V: (RM=-0.1442, RP=0.1874, RC=0.2095)	116
Figure 85.	Keel Sensor V2019V: (RM=-0.1327, RP=0.2391, RC=0.2423)	117
Figure 86.	Keel Sensor A2413: (RM=-0.1245, RP=0.2219, RC=0.2255)	117
Figure 87.	Keel Sensor V2002V: (RM=0.0762, RP=0.2303, RC=0.2150)	118
Figure 88.	Keel Sensor V2007V: (RM=-0.1198, RP=0.2883, RC=0.2766)	119
Figure 89.	Bulkhead Sensor A2109V: (RM=0.1353, RP=0.1846, RC=0.2028)	119
Figure 90.	Bulkhead Sensor V2013V: (RM=-0.0342, RP=0.1970, RC=0.1772)	120
Figure 91.	Bulkhead Sensor A2104V: (RM=0.0207, RP=0.1760, RC=0.1571)	120
Figure 92.	Bulkhead Sensor: (RM=0.0353, RP=0.1789, RC=0.1616)	121
Figure 93.	Mast Sensor A2237: (RM=0.0613, RP=0.1877, RC=0.1750)	121
Figure 94.	Keel Sensor V2034V: (RM=-0.0966, RP=0.1537, RC=0.1608)	122
Figure 95.	Keel Sensor V2019V: (RM=-0.1212, RP=0.1830, RC=0.1945)	122
Figure 96.	Bulkhead Sensor A2413V: (RM=-0.1315, RP=0.2150, RC=0.2233)	123
Figure 97.	Example of Curves Used for Construction of Inner Fluid Mesh Layer	127
Figure 98.	Face Sets Used to Generate Inner Fluid Mesh Layer [from Ref. 21].	128
Figure 99.	Inner Mesh: Lower Port and Starboard Hull, Sonar Dome, and Seams.	129
Figure 100.	Transition to Test Waterline: Aft Section of Upper Inner Liner	131
Figure 101.	Transition to Test Waterline: Forward Section of Upper Inner Fluid Mesh ..	132
Figure 102.	Completed Inner Mesh Layer of Inner Liner	132
Figure 103.	Completed Outer Mesh Layer of Inner Liner.	134
Figure 104.	Fluid Model Projection Illustration Showing “Shadow Regions” Created by the Contours of the Ship Model	135
Figure 105.	Curves and Surfaces Used to Form Outer Boundary of Inner Mesh	137
Figure 106.	Completed Inner Mesh	141
Figure 107.	Curves and Surfaces Used to Form Outer Boundary of Transitional Mesh ..	142
Figure 108.	Completed Transitional Fluid Mesh	143
Figure 109.	Completed Outer Mesh	146
Figure 110.	Coupled Fluid-Structural Model	147

THIS PAGE INTENTIONALLY LEFT BLANK

LIST OF TABLES

Table 1.	DDG 81 Finite Element Model Specifications [from Ref. 14]	21
Table 2.	Weighted Mean of α (DDG 53) [from Ref. 19]	24
Table 3.	Weighted Mean of β (DDG 53) [from Ref. 19]	24
Table 4.	DDG 81 Wetted Surface Shell Element Properties	32
Table 5.	Statistical Study of Low-Pass Filtered vs. Unfiltered Simulation Data	48
Table 6.	Vertical Velocity Response Sensor Location (N/A = no data available)	50
Table 7.	Russell's Comprehensive Error Factor Acceptance Criteria	53
Table 8.	Russell's Error Factor Using High Pass Filtered Data (420 msec) [from Ref. 21]	55
Table 9.	Russell's Error Factor Using Drift Compensated Data (500 msec)	56
Table 10.	Summary of Prediction Error Measures Using Dense 2 nd Generation Model	59
Table 11.	Summary of Simulation Error Measures using Dense 3 rd Generation Model	61
Table 12.	Shot 3 Fluid Model Properties	65
Table 13.	Shot 3: Russell's Error Factor	68
Table 14.	Shot 1 Russell Error Factors With Varying Fluid Model Depth	75
Table 15.	Shot 1 Fluid Model Mesh Properties	76
Table 16.	Shot 1: Russell's Error Factor	79
Table 17.	Shot 2 Fluid Model Properties	86
Table 18.	Shot 2: Russell's Error Factor	89
Table 19.	Accelerometer vs. Velocity Meter Correlation Comparison	96
Table 20.	2X Cavitation Fluid Mesh Russell's Error Comparison (120 msec) [from Ref. 21]	97
Table 21.	2X Cavitation Depth Fluid Mesh Russell's Error Comparison (120 msec)	98
Table 22.	Russell's Error Comparison: Cavitation Depth Model vs. 2X Cavitation Depth Model (500 msec)	99

THIS PAGE INTENTIONALLY LEFT BLANK

ACKNOWLEDGEMENTS

I would like to sincerely thank Dr. Young S. Shin for his guidance and support throughout the course of this study and my time here at the Naval Postgraduate School. Without his expertise and direction, this study would not have been possible.

I am also thankful for the many others who have helped to make this study a success. I would especially like to thank:

Dr. Robert Rainsberger for his continuous support, free lunches, and invaluable technical expertise regarding TrueGrid and Dr. John DeRuntz for his patient support and expert technical advice regarding underwater shock and USA.

Dr. Ilbae Ham for his support of many technical aspects of this study. Tom Christian for his technical assistance and tireless maintenance of all things computer related. Lieutenant David Hart and Lieutenant Jake Didoszak for their input and help along the way.

CAPT David Lewis and CDR Jeff Riedel for their funding and support of the ship shock program here at the Naval Postgraduate School.

Finally, I am most greatly indebted to my most loving and beautiful wife Nicole. Her support and understanding throughout the course of this study has been invaluable. The companionship and confidence she has given me has directly contributed to making my time here successful.

THIS PAGE INTENTIONALLY LEFT BLANK

I. INTRODUCTION

A. BACKGROUND

In World War II, the U.S. Navy experienced the highly destructive effects of near proximity underwater explosions (UNDEX) from mines and torpedoes. Many combatants with the latest in combat technology for the time were rendered helpless due to inadequate shock proofing of the ship systems. Since this time, extensive work has gone into the research and study of the effects of UNDEX. A major goal in the design of modern combatant ships has been to eliminate or at least reduce damage caused by UNDEX.

Guidelines and specifications have been developed for the shock testing and hardening of shipboard equipment and systems. NAVSEA 0908-LP-000-3010A [Ref.1] and MIL-S-901D [Ref. 2] set forth much of this guidance. As directed by OPNAVINST 9072.2 [Ref. 3], the complete ship system is tested by performing what are called underwater shock trials. These shock trials attempt to test the ship under “near combat conditions” by igniting a large charge of HBX-1 underwater at varying standoff distances from the ship. The effect of the shocks to ship systems is observed and the response of the ship is monitored and recorded for each shot. The lead ship of each class, or a ship substantially deviating from other ships of the same class, is required to undergo these trials in order to correct any deficiencies on that ship as well as the follow on ships of the class.

These shock trials, while beneficial in determining the wartime survivability of surface ships, require years of planning and preparation and are extremely expensive. In the Aegis Destroyer program alone, tens of millions of dollars were spent for the shock trials conducted on USS JOHN PAUL JONES (DDG 53) in 1994 and again for the shock trials conducted on USS WINSTON S. CHURCHILL (DDG 81) in 2001. In addition, these tests present an obvious danger to the crew onboard, the ship itself, and any marine life in the vicinity of the test. Due to this inherent safety risk, shock trials do not test up

to the ship's design limits or even the true combat shock environment. This has raised the question as to whether or not the information gleaned from doing the tests is worth the high cost of conducting them [Ref. 4].

Advances in the capabilities of computers in the last few decades have allowed many events to be tested in a virtual world. This has allowed engineers not only to save millions of dollars, but it has also allowed for faster advancements in design. Creating a virtual UNDEX environment for ship system underwater shock testing presents an extremely useful design tool and an attractive alternative to future shock trials. This would save the Navy millions of dollars while at the same time not harm our sailors or the environment. To date however, virtual UNDEX testing of ship systems has not been considered sufficiently reliable and the U.S. Navy, though very interested in the simulations, has not considered it an acceptable alternative to actual shock trials.

To obtain accurate results from a simulation, the structural finite element model must be extremely detailed. Additionally, the surrounding acoustic medium must be coupled with the wetted surface of the structural model almost perfectly. The resulting coupled fluid and structural model necessary for an accurate simulation is enormous computationally. The UNDEX environment is very complex, made up of an initial "kick" from the incident shock wave followed by the effects of cavitation, bubble pulse, and structural whipping [Ref. 4]. While the computational time step must be very small, on the order of microseconds, the entire UNDEX ship response lasts on the order of seconds. Because of this, current computer simulations cannot realistically predict the complete response from start to finish.

Current technology is capable of creating a simulation to predict the initial "early time" peak response of a surface ship subjected to an underwater shock [Ref. 4]. By capturing the peak response, simulations can provide very useful insight into ship system design. Because they are virtual in nature, shock simulations can be conducted at or beyond design limits, providing more useful design information than that which is gained by conducting real world shock trials. By validating the predictions made using UNDEX simulation, virtual testing can be used to improve and accelerate combatant ship system

design. Through this validation and further advancements in computer processing technology, virtual shock trials may one day reduce or eliminate the requirement for live fire testing of entire ship systems.

B. SCOPE OF RESEARCH

This paper investigates the feasibility of creating a virtual UNDEX environment to model the response of a surface ship exposed to an underwater shock. This is accomplished using the shock trial data from the shock trial conducted on USS WINSTON S. CHURCHILL (DDG 81) in June of 2001. DDG 81 was subjected to three different underwater explosions during these trials, each explosion having a different geometry. Comparisons between the simulated response predictions and the actual measured response are made for all three shots. The effects of charge location in relation to the ship, size of the fluid mesh, fluid mesh density, and the quality of the fluid mesh are investigated. By creating an easily modified fluid mesh model, a wide range of shot and ship loading conditions can be simulated. This creates unlimited potential for future UNDEX simulation research. The modifiability of the fluid models investigated in this paper and the modeling techniques that permit this easy modification are discussed.

These underwater shock simulations were conducted using the most accurate and state of the art finite element ship model to date. The fluid volume models were generated using the TrueGrid finite element mesh generator program [Ref. 5]. The simulation processing was conducted using the LS-DYNA/USA (Underwater Shock Analysis) coupled computer code [Ref. 6,7].

THIS PAGE INTENTIONALLY LEFT BLANK

II. UNDERWATER SHOCK PHENOMENA

Underwater shock is complex consisting of numerous phenomena. Many of these phenomena can have devastating effects on a submerged structure and cannot be ignored. To create and analyze a virtual underwater shock environment, it is first necessary to have a thorough understanding of these phenomena.

A. INCIDENT PRESSURE WAVE

An underwater shock first begins with the presence of an explosive such as HBX-1, TNT, or RDX detonated underwater. While explosive fuels generally do not contain high amounts of energy in relation to other fuels, their explosive power is due to their rapid combustion. Upon detonation, combustion of the explosive fuel occurs within nanoseconds. During combustion, products inside of the charge undergo a chemical reaction, transforming from a solid or liquid to a gaseous product. Due to the speed of the combustion process, the gases produced are confined to the volume of the explosive. This results in these gases becoming very highly compressed. The pressure of these gases may reach hundreds of thousands of atmospheres [Ref.8]. This high-pressure gas then propagates through the explosive, exceeding the speed of sound by three to five times and creating a shock wave. This shock wave in turn ignites more of the combustion products as it propagates. In very short time, this shock wave is released into the surrounding fluid under extreme pressure.

Although water is normally incompressible, the high-pressure, high-energy shock wave actually causes the water surrounding the charge to compress. This compression creates a high-pressure shock wave in the water which propagates outward from the charge. Initially traveling much faster than the speed of sound, as this pressure wave expands outward, it rapidly slows to the speed of sound [Ref.9]. While such factors as temperature, pressure, and salinity affect the actual speed of sound, for purposes of simulation 5057 ft/s is used.

The pressure wave generated by this detonation process is very large, on the order of 2×10^{-6} lb/in² for TNT at the charge. Figure 1 shows the initial shock wave pressure

discontinuity and the exponential decay of this discontinuity as it radiates outward. The pressure profile is proportional to the inverse of the standoff distance, the distance from the charge to the submerged structure, decreasing in magnitude and broadening as it travels outward in a spherical wave pattern.

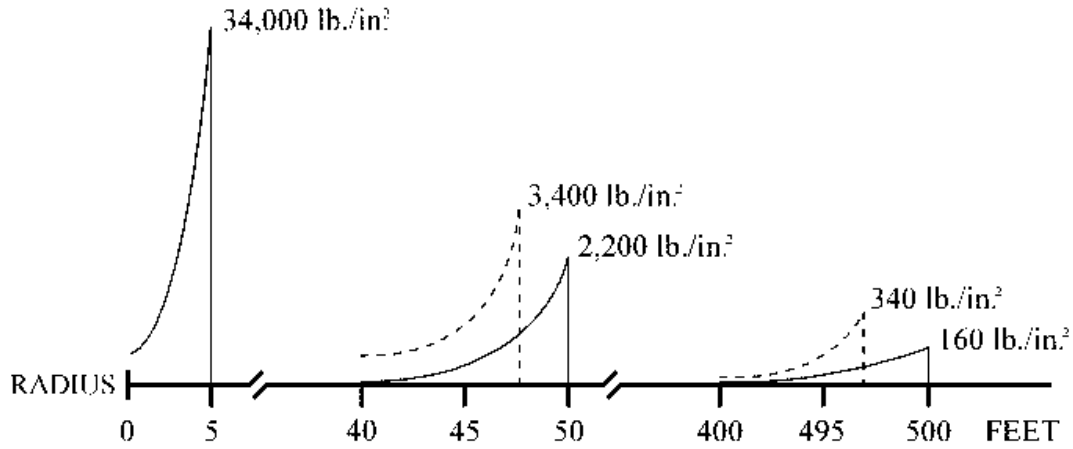


Figure 1. Shock Wave Profiles From a 300 lb. TNT Charge [from Ref 9.]

The pressure profile can be described using the following set of equations [Ref. 9]:

$$P(t) = P_{\max} e^{-\frac{t-t_1}{\theta}} \quad (\text{psi}) \quad (1)$$

$$P_{\max} = K_1 \left(\frac{W^{\frac{1}{3}}}{R} \right)^{A_1} \quad (\text{psi}) \quad (2)$$

$$\theta = K_2 W^{\frac{1}{3}} \left(\frac{W^{\frac{1}{3}}}{R} \right)^{A_2} \quad (\text{msec}) \quad (3)$$

$$T = K_5 \frac{W^{\frac{1}{3}}}{(D+33)^{\frac{5}{6}}} \quad (\text{sec}) \quad (4)$$

where:

$t-t_1$ = the time after arrival of the shock wave

P_{\max} = the peak magnitude of the pressure in the shock front

θ = the decay constant describing the exponential decay

R = distance from the explosive to the target in feet (radially)

W = weight of the explosives in pounds

K_1, K_2, K_5, A_1, A_2 = explosive specific constants

These equations are valid for distances 10 to 100 times the charge radii away from the detonation point and for a duration of up to one decay constant after the initial detonation occurs.

B. EXPLOSIVE GAS BUBBLE

The highly compressed gases that initially prompted the shock wave continue to expand outward forming a bubble of very hot gases. This bubble expands rapidly until the pressure inside the bubble falls below the surrounding hydrostatic pressure. Due to the momentum of the bubble expansion, this bubble actually expands beyond equilibrium. In fact, the point of equilibrium is reached when the bubble is less than half of the maximum radius it will grow to. Equation (5) is an empirical equation for calculating the maximum bubble radius [Ref. 9].

$$A_{\max} = K_6 \frac{W^{\frac{1}{3}}}{(D+33)^{\frac{1}{3}}} \quad (\text{ft}) \quad (5)$$

where

K_6 = explosive specific constant

D = depth of the explosive in feet

From this equation it is evident that the maximum bubble radius is proportional to the one-third power of charge weight and inversely proportional to the one-third power of the depth of the charge. Once the bubble reaches its maximum radius, there is a large positive pressure gradient between the bubble and the surrounding fluid. This causes the bubble to collapse upon itself until the volume of the bubble is small enough so as to increase the pressure inside the bubble sufficiently high enough to stop further collapse. At this point, a negative pressure gradient between the bubble and surrounding fluid exists. The bubble now attempts to achieve equilibrium expanding once again to a size smaller than the initial maximum radius, but still larger than the point of equilibrium. This results in the collapse and expansion process repeating itself again. This oscillatory action occurs until the energy inside the bubble exhausts itself due to viscous resistance from the fluid around it or the bubble vents itself on the surface of the water. Figure 2 shows this expansion and contraction of the bubble as well as its normal migration pattern towards the surface of the water.

The vertical migration velocity can be calculated using Equation (6) where the vertical velocity (U) is a function of the bubble radius.

$$U = \frac{2g}{a^3(t)} \int_0^T a^3(t) dt \quad (6)$$

where

g = gravitational acceleration (constant)

a = radius of gas bubble (time dependent)

While highly dependent upon the location of the charge and the size of the charge, the bubble pulse contributes primarily to the late time response of the ship. The bubble pulse oscillates at a frequency very close to the first bending mode of the ship [Ref. 9].

This could be even more destructive than the incident pressure wave should the bubble migrate into or near enough to the ship to excite this mode.

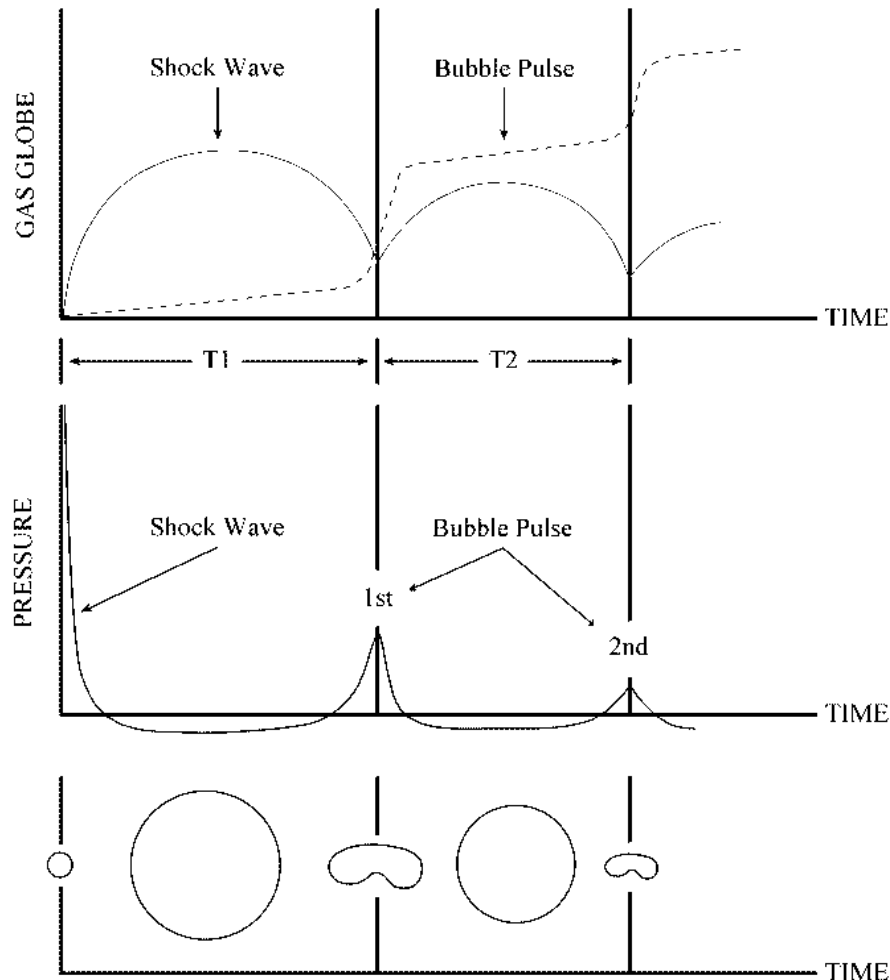


Figure 2. Oscillatory Bubble Pulse and Migration Path of Explosive Gas Bubble [from Ref. 9]

C. CAVITATION

Cavitation occurs in water when there is area of negative absolute pressure present. This negative pressure causes a tensile force in the water. Since water cannot withstand this force, separation, or cavitation, occurs. In an UNDEX event, two types of cavitation occur, “bulk” and “local” cavitation. As the name insinuates, “bulk” cavitation is a large region of low pressure while “local” cavitation is a small region of low pressure generally occurring at the fluid structure interface. Cavitation has a large impact on the

overall response of the ship structure to an UNDEX event and must be properly simulated for an accurate prediction.

1. Bulk Cavitation

When UNDEX occurs, a three-dimensional spherical pressure wave is formed propagating outward in all directions from the charge center. This propagation can be visualized more clearly using a two-dimensional model as shown in Figure 3.

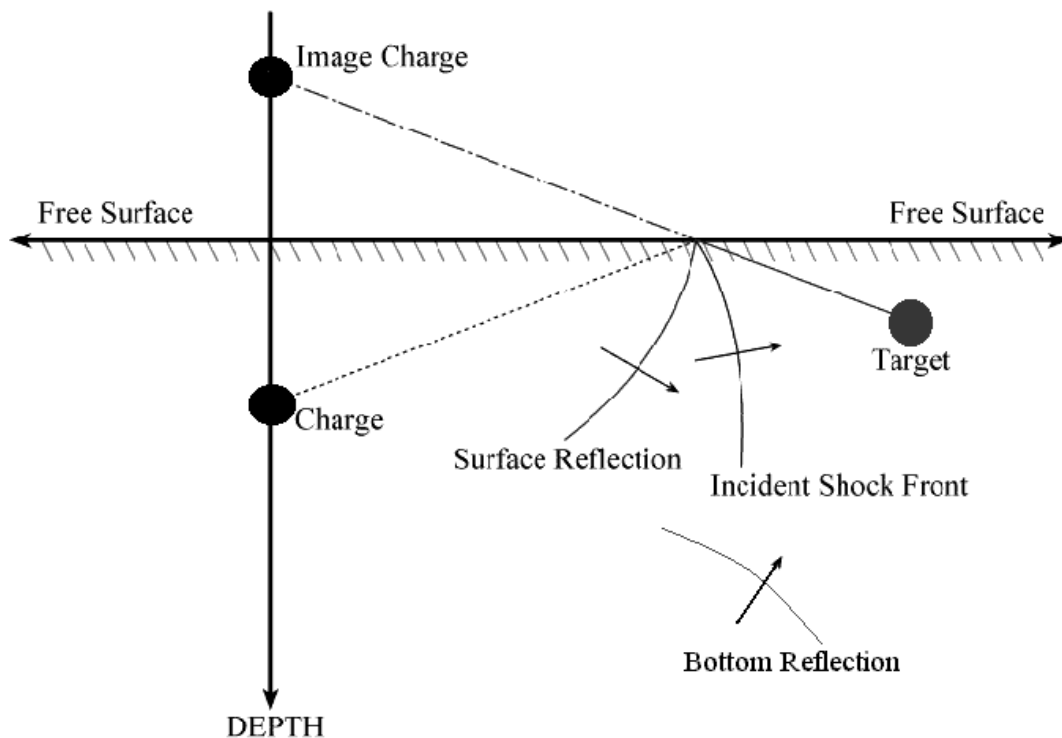


Figure 3. 2-Dimensional Long Range Underwater Shock Wave Propagation Pattern [from Ref. 9]

The incident pressure wave is the compressive wave traveling directly from the charge to the image. It reaches the image first and is the strongest wave. When the shock wave reaches the free surface, it is reflected as a rarefaction or tensile pressure wave. This phenomenon occurs due to the boundary condition at the free surface where the net pressure due to the incident and reflected wave must be equal to zero [Ref. 9]. As shown in Figure 4, the rarefaction wave arrives at the image after the incident pressure wave. The incident wave pressure has decayed and the arrival of the rarefaction wave causes a

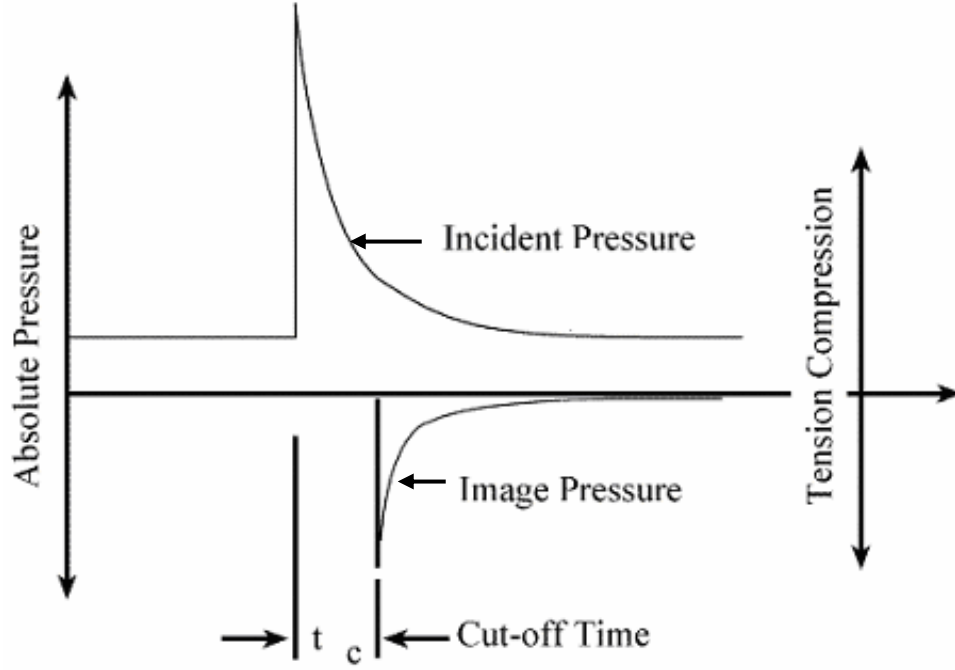


Figure 4. Shock Wave Pressure Profile Showing Cut Off Upon Rarefaction Wave Arrival [from Ref. 9]

sharp drop in pressure, called cut-off. Cavitation occurs at cut off when the absolute pressure in the water falls below the cavitation pressure, approximately negative three to four lb/in² [Ref. 10]. Since water cannot support the resulting tensile load, cavitation occurs. This forms the upper boundary of the cavitation region. This upper cavitation boundary can be found analytically using Equations (7) through (9).

$$F(x,y)=K_1 \left(\frac{W^{\frac{1}{3}}}{r_1} \right)^{A_1} e^{\frac{(r_2-r_1)}{C\theta}} + P_A + \gamma y - K_1 \left(\frac{W^{\frac{1}{3}}}{r_2} \right)^{A_1} = 0 \quad (7)$$

and

$$r_1 = \sqrt{(D-y)^2 + x^2} \quad \text{and} \quad r_2 = \sqrt{(D+y)^2 + x^2} \quad (8) \text{ and } (9)$$

where:

x = horizontal range from charge to target
 y = target depth
 r_1 = standoff distance from charge to target
 r_2 = standoff distance from image charge to target
 C = acoustic velocity
 D = charge depth
 θ = shock wave decay constant
 P_A = atmospheric pressure
 γ = weight density of water
 W = charge weight
 K_1, A_1 = shock wave parameters

To determine the lower cavitation boundary, it is necessary to equate the decay rates of both the absolute pressure, which includes the incident pressure wave, as well as the reflected wave. This calculation is solved using the same constants used in the upper cavitation boundary equations in Equation (10).

$$\begin{aligned}
 G(x,y) = & -\frac{P_i}{C\theta} \left\{ 1 + \left[\frac{r_2 - 2D \left(\frac{D+y}{r_2} \right)}{r_1} \right] \left[\frac{A_2 r_2}{r_1} - A_2 - 1 \right] \right\} - \\
 & \frac{A_1 P_i}{r_1^2} \left[r_2 - 2D \left(\frac{D+y}{r_2} \right) \right] + \gamma \left(\frac{D+y}{r_2} \right) + \frac{A_1}{r_2} (P_i + P_A + \gamma y) = 0
 \end{aligned} \tag{10}$$

In this equation, P_i is equal to the incident pressure at cut-off given by,

$$P_i = P_{\max} e^{-\left[\frac{(r_2 - r_1)}{C\theta} \right]} \tag{11}$$

where P_{\max} is calculated using Equation (2).

Using MatLab, these equations can be used to solve for the pressure distribution in a large volume of water. Figure 5 shows an example of the cavitation region for a large charge of HBX-1 found using MatLab. It should be noted that while the example is shown in only two dimensions, the actual cavitation region is three-dimensional, generally symmetric about an imaginary vertical axis passing through the charge.

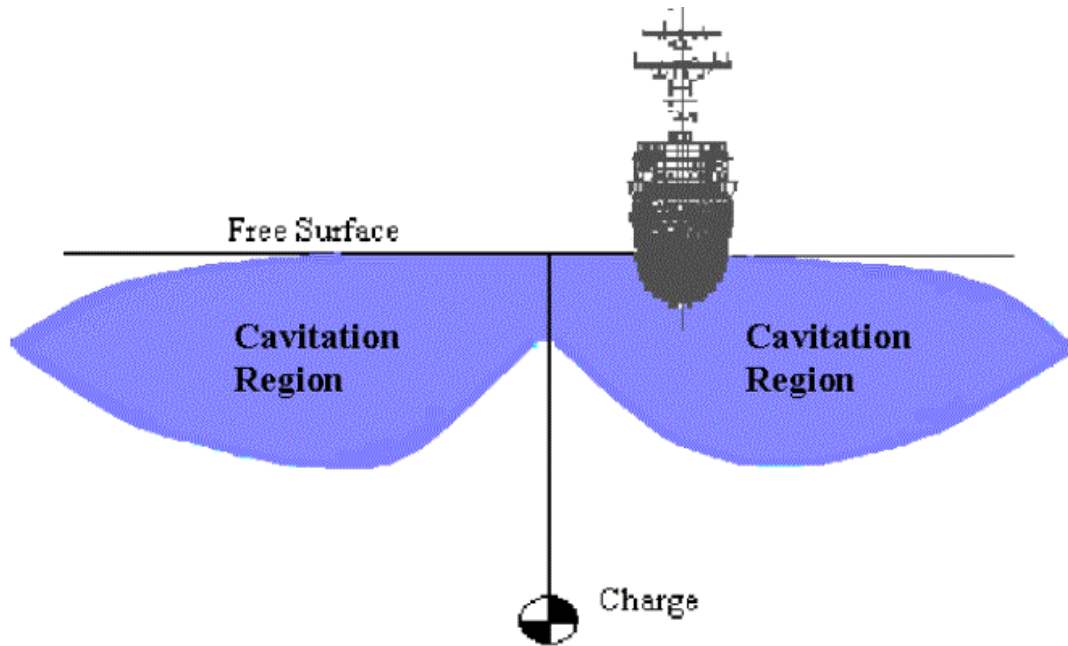


Figure 5. Example of Cavitation Region From a Large Charge of HBX-1 Explosive (not to scale).

An important characteristic of the cavitation region is that the size of the region is controlled primarily by the depth of the charge while the depth of the cavitation region is controlled primarily by the size of the charge.

2. Local Cavitation

Local cavitation occurs at the fluid structure interface due to the deflection and resulting vibrations of the hull from the initial impact of the shock wave. This can most easily be explained using Taylor Plate Theory [Ref. 11]. This theory uses a simple infinite air backed plate of mass per unit area as shown in Figure 6 to describe the reaction of the hull to an impinging shock wave.

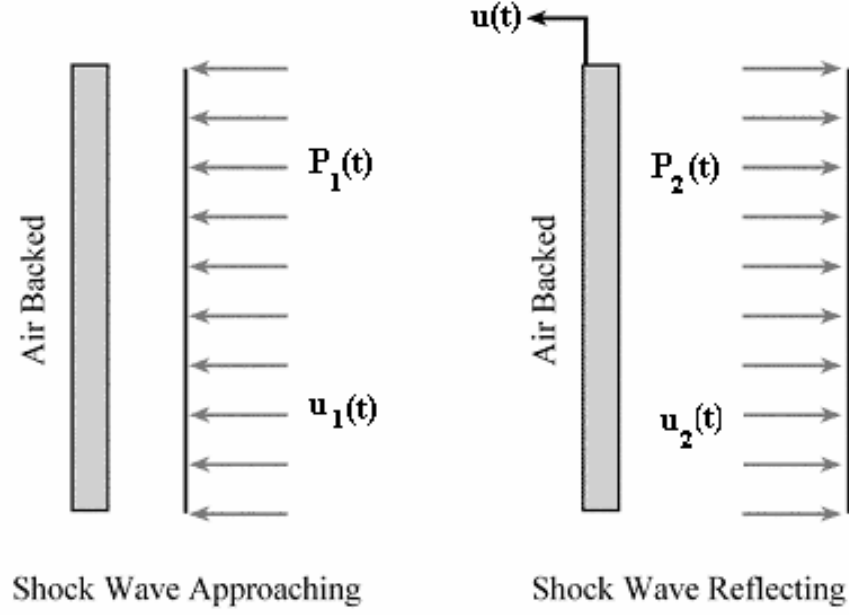


Figure 6. Taylor Air Backed Plate Subjected to a Plane Wave [from Ref. 11]

If $u(t)$ is the velocity of the plate, it can be shown using Newton's second law of motion that

$$m \frac{du(t)}{dt} = P_1(t) + P_2(t) \quad (12)$$

where $P_1(t)$ and $u_1(t)$ are the incident shock wave and fluid particle velocity behind the wave respectively while $P_2(t)$ and $u_2(t)$ are the reflected shock wave and fluid particle velocity respectively. The plate velocity can be found using the following relation:

$$u(t) = u_1(t) - u_2(t) \quad (13)$$

Since pressure is equal to the product of the fluid density (ρ), acoustic velocity (C), and the fluid particle velocity Equations (1), (12), and (13) can be used to form the following relationship:

$$P_2(t) = P_{\max} e^{-\left(\frac{t-t_1}{\theta}\right)} - \rho C u(t) \quad (14)$$

Equation (12) can now be written as a first order differential equation using Equation (14).

$$m \left(\frac{du}{dt} \right) + \rho C u(t) = P_{\max} e^{-\left(\frac{t-t_1}{\theta} \right)} \quad (15)$$

Solving this equation for the plate velocity,

$$u(t) = \frac{2P_{\max}\theta}{m(1-\beta)} \left\{ e^{-\left[\frac{\beta(t-t_1)}{\theta} \right]} - e^{-\left[\frac{t-t_1}{\theta} \right]} \right\} \quad (16)$$

where $\beta = \frac{\rho C \theta}{m}$. The net pressure at the plate using Equation (16) in Equation (12) is then

$$P_1 + P_2 = \frac{2P_{\max}\theta}{(1-\beta)} \left\{ e^{-\left[\frac{t-t_1}{\theta} \right]} - \beta e^{-\left[\frac{\beta(t-t_1)}{\theta} \right]} \right\} \quad (17)$$

This relationship shows that as β becomes large (a lightweight plate) the net pressure at the plate becomes negative very early. As with bulk cavitation, this low pressure zone creates a tensile force in the fluid which results in local cavitation at the hull.

D. STRUCTURAL RESPONSE TO UNDERWATER SHOCK

1. Analytical Kick-Off Velocity Approximation

The primary component of fluid and structural motion during an underwater shock event is in the vertical direction. The simple equations used to describe the motion of water particles can be used to estimate the motion of the ship. Going back to the previous section, the water particle velocities inside the cavitation region are dependent upon the incident shock wave as well as the rarefaction wave, or image tensile pressure wave. Using geometry and the acoustic velocity, the cut-off time can be calculated for incremental depths along the submerged surface. These times are then used to determine the incident pressure and image pressure at cut-off using Equation (1). The net pressure

at cut-off is equal to the incident wave pressure plus the atmospheric and hydrostatic pressure at the incremental depth minus the image pressure. The vertical component of the water particle can then be described as

$$u = \frac{P_1}{\rho_o C_o} \sin \phi + \frac{P_1 + P_a + \rho x}{\rho_o C_o} \sin \phi_i \quad (18)$$

where P_1 is the incident pressure, ϕ is the angle from the charge to the incremental depth on the hull, and ϕ_i is the angle from the image charge to the incremental depth on the hull as depicted in Figure 3. The structural velocity can be found using conservation of momentum,

$$M_s V_s = \sum_i \rho \Delta x_i u_i \quad (19)$$

Since the mass of the ship and the displaced water are the same, this problem reduces to a simple averaging of the water particle velocities along the hull. While not an exact approximation, this method has been shown to be within 10-20% of measured values making it a reasonable first estimate [Ref. 9].

2. Computational Structural Response Approximation

A more accurate approximation can be achieved computationally using an approximation method called the Doubly Asymptotic Approximation (DAA). This approximation method begins first with the structural equation of motion

$$[M]\{\ddot{x}\} + [C]\{\dot{x}\} + [K]\{x\} = \{f\} \quad (20)$$

where $[M]$, $[C]$, and $[K]$ make up the symmetric linear structural mass, damping and stiffness matrices respectively and $\{f\}$ is the external forcing vector. For a submerged structure excited by an acoustic wave this external forcing vector is

$$\{f\} = -[G][A_f]\{(p_I + p_S)\} + \{f_D\} \quad (21)$$

where $\{p_I\}$ and $\{p_S\}$ are the nodal incident and scattered pressure vectors respectively for the wetted surface structure, $\{f_d\}$ is the dry structure applied force vector,

$[A_f]$ is the diagonal area matrix pertaining to the fluid elements, and $[G]$ is the transformation matrix that relates the structural and fluid nodal surface forces. While the incident pressure vector is known, the scattered pressure vector is unknown [Ref. 12].

The DAA is used to determine the fluid structure interaction. The DAA is so named as it approaches exactness in both the high-frequency (early time) and low frequency (late time) limits [Ref. 13]. This approximation uses two equations, the structural equation of motion and a fluid particle equation,

$$[M_f]\{\dot{p}_s\} + \rho c [A_f]\{p_s\} = \rho c [M_f]\{\dot{u}_s\} \quad (22)$$

where $\{u_s\}$ is the scattered-wave fluid particle velocity vector normal to the structural wetted surface, $[M_f]$ is the symmetric fluid mass matrix for the fluid mesh on the wet surface, and c is the acoustic velocity. The DAA is able to represent the entire fluid surrounding a submerged structure through variables associated only with the wetted surface.

The fluid particle velocities are related to the structural response through the compatibility relation

$$[G]^T \{\dot{x}\} = \{u_I\} + \{u_S\} \quad (23)$$

This equation contains the constraint that the normal fluid particle velocity must match the normal structural velocity on the wet surface of the structure [Ref. 13].

Equations (20) through (23) can now be combined to form two equations

$$[M_s]\{\ddot{x}\} + [C_s]\{\dot{x}\} + [K_s]\{x\} = -[G][A_f]\{(p_I + p_S)\} \quad (24)$$

$$[M_f]\{\dot{p}_S\} + \rho c [A_f]\{p_S\} = \rho c [M_f]([G]^T \{\ddot{x}\} - \{\dot{u}_I\}) \quad (25)$$

Equations (24) and (25) are solved using a staggered solution scheme in the Underwater Shock Analysis (USA) code in order to approximate the forces at the fluid structure interface [Ref. 7]. These forces can then be input into a finite element solver to determine the structural response throughout the ship structure.

THIS PAGE INTENTIONALLY LEFT BLANK

III. UNDERWATER SHOCK MODELING AND SIMULATION

A. STRUCTURAL MODEL

1. USS WINSTON S. CHURCHILL (DDG 81)

A finite element model (FEM) of USS WINSTON S. CHURCHILL (DDG 81) built by Gibbs & Cox, Inc [Ref. 14] was used for the investigations conducted in this thesis. This model, shown in Figure 7, is a modification of the USS JOHN PAUL JONES (DDG 53) model used in the UNDEX simulations conducted at the Naval Postgraduate School (NPS) from 1999 to 2000 [Ref. 15, 16.].

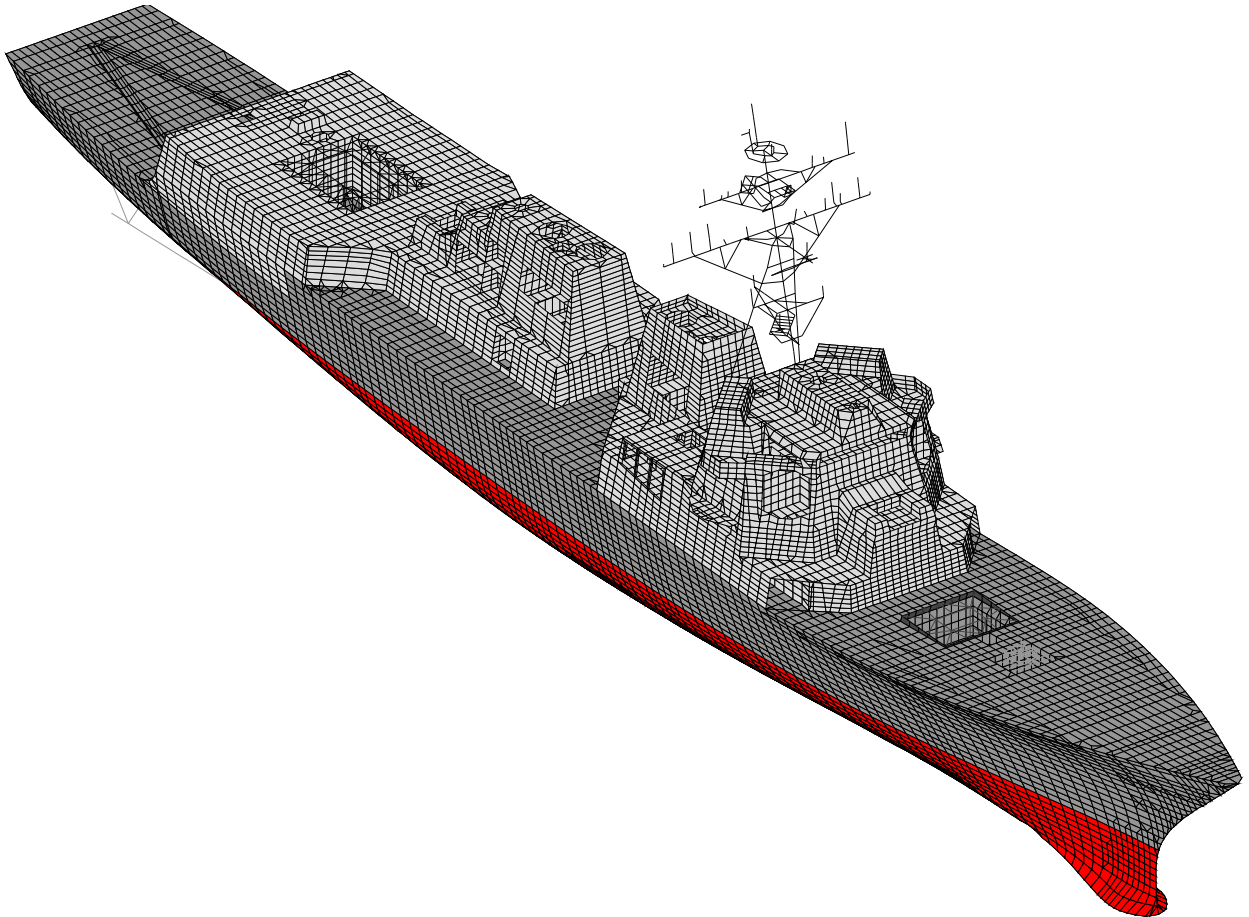


Figure 7. USS WINSTON S. CHURCHILL (DDG 81) FINITE ELEMENT MODEL [from Ref. 14].

DDG 81 is a Flight IIA Arleigh Burke Class destroyer having significant modifications from prior destroyers in the class. The major structural modifications include:

- the addition of dual helicopter hangars
- six additional vertical launch system (VLS) cells, three forward and three aft
- installation of a 5"/62 caliber gun
- a five foot extension of the transom
- addition of five blast hardened bulkheads

Delivered in MSC/NASTRAN input deck form, this model represents the largest and most complex finite element ship model to date [Ref. 17]. Though based on the DDG 53 model, this model was greatly improved. Structural beam elements were refined to reflect true areas, volumes, and densities and end constraints were modified to better reflect actual structural boundary conditions. The mass distribution was improved significantly. Following completion of the model, nodal masses were added throughout the model to reflect such masses such as weapons loadout, liquid loading, equipment, and even personnel loading. Rather than the normal smearing of this mass arbitrarily onto the entire model, masses were distributed onto nodes in the model that corresponded to the associated mass on the actual ship. Since the three underwater shocks were accomplished on separate days, three separate models were delivered, each with a unique mass distribution applicable to the actual ship condition when the shot was conducted. Table 1 is a summary of this finite element model.

Complex equipment such as the gas turbine engines, shafts, generators, reduction gear, VLS launchers, and the gun mount were modeled as rigid body elements. Since the internal response of this equipment is not measured, modeling these individual components in detail is unnecessary. Each of these element groups was attached to the nodal points on the ship structure at their foundations with their spring-mass representation applied to the supporting nodes. To separate the propulsion shafts from the reduction gear, a beam element was added as a link between the two groupings. The shaft mass was then represented by each of the shaft bearing assemblies. Figure 8 shows

the significant rigid body element groups. A total of 107 total rigid body element groups were in the final models used in the simulations. In addition to those shown, many of these groups were small groups of one, two, or three elements that make up antennas on the mast and the ship's Recovery, Assist, Securing, and Traversing (RAST) system located on the flight deck.

Table 1. DDG 81 Finite Element Model Specifications [from Ref. 14]

Nodes	40,514
Degrees of Freedom	243,084
Beam Elements	49,397
Shell Elements	48,662
Spring Elements	416
Rigid Body Element Groups	107
Lumped Masses	92,541

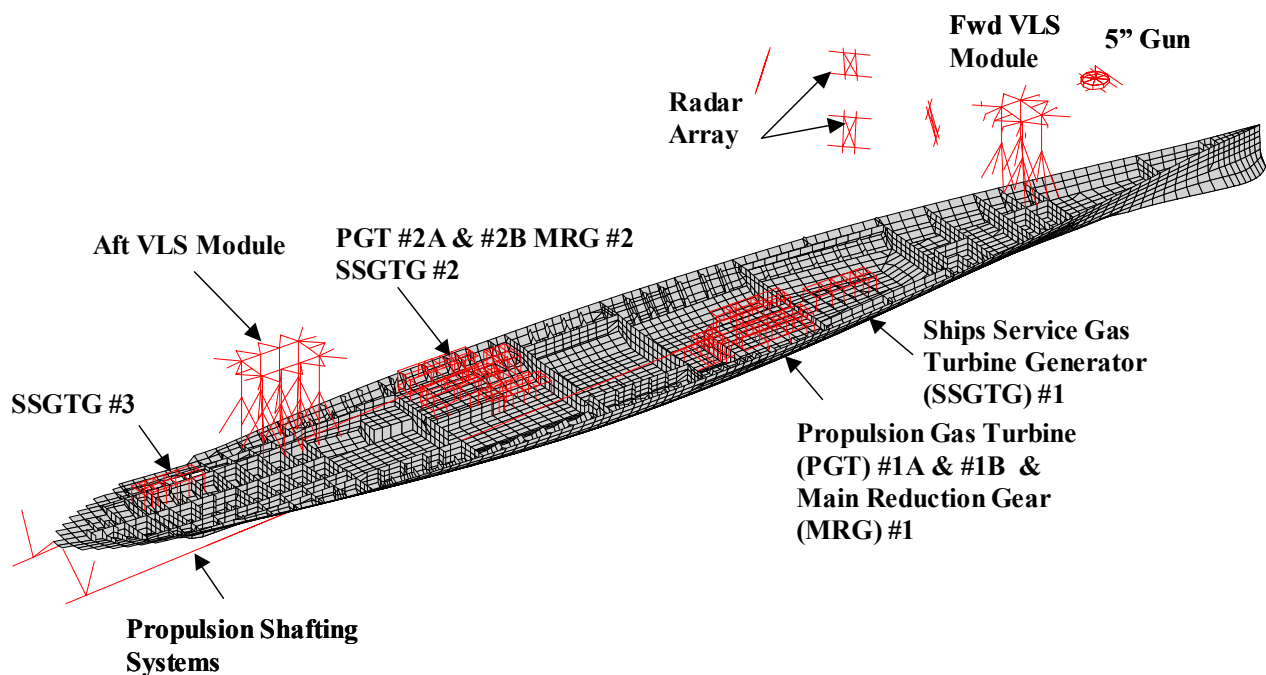


Figure 8. Equipment Modeled as Rigid Bodies in DDG 81 FEM [from Ref. 14]

2. Ship System Damping

Ninety percent of damping in a structure occurs due to frictional energy dissipation in bolted or riveted mechanical joints. The vast majority of joints on naval combatant ship structure systems are welded while all stiffeners are welded directly to the hull plates, decks, and bulkheads. These welded joints provide minimal energy dissipation [Ref. 18]. Regardless, many energy dissipation sources such as long cable trays, hangers, snubbers, and the surrounding fluid coupled with the hull are inherent to all ship systems. While ship system damping is measurable, it is difficult to quantify for modeling purposes. Extensive study was conducted at NPS in conjunction with the ship shock simulation of USS JOHN PAUL JONES (DDG 53) using 2000 msec of measured shock trial data [Ref. 19]. The results of this study were applied to the Rayleigh damping coefficients used for the DDG 81 model

Rayleigh damping is a general form of proportional damping representing the damping matrix, $[C]$, in the structural equation of motion.

$$[M]\{\ddot{x}\}+[C]\{\dot{x}\}+[K]x = \{F\} \quad (26)$$

The $[C]$ matrix is represented by

$$[C] = \alpha[M] + \beta[K] \quad (27)$$

where α and β are constants. This equation can be normalized using the mass normalization matrix $[\phi]$

$$[\phi]^T [C] [\phi] = [2\zeta_\gamma \omega_\gamma]_{\text{diag}} = \alpha[I] + \beta[\omega_\gamma^2]_{\text{diag}} \quad (28)$$

Determining these damping coefficients for a simple system having only two modes with two modal frequencies of interest is academic. Determining them for complex systems such as a ship structure with more than two modes of interest presents a much greater challenge. In this case, Equation (28) becomes over determined, having more equations than unknowns. These coefficients can be determined using measured data and a least squares curve fitting technique.

For comparison with measured ship response the modal damping ratio is calculated. This is determined for each mode by

$$\zeta_i = \alpha \frac{1}{2\omega_i} + \beta \frac{\omega_i}{2} \quad (29)$$

DDG 53 was divided into 67 area groups for the comparison study. Measured modal response was recorded over the entire frequency spectrum of interest, 0 to 250 Hz, for both athwartship and vertical response. A least squares curve fit was then applied and the corresponding α and β were recorded for each area. Figure 9 shows an example of this curve fitting for one area group. This particular plot includes the measured data outliers and “noise” that were subsequently discarded in performing the final curve fit.

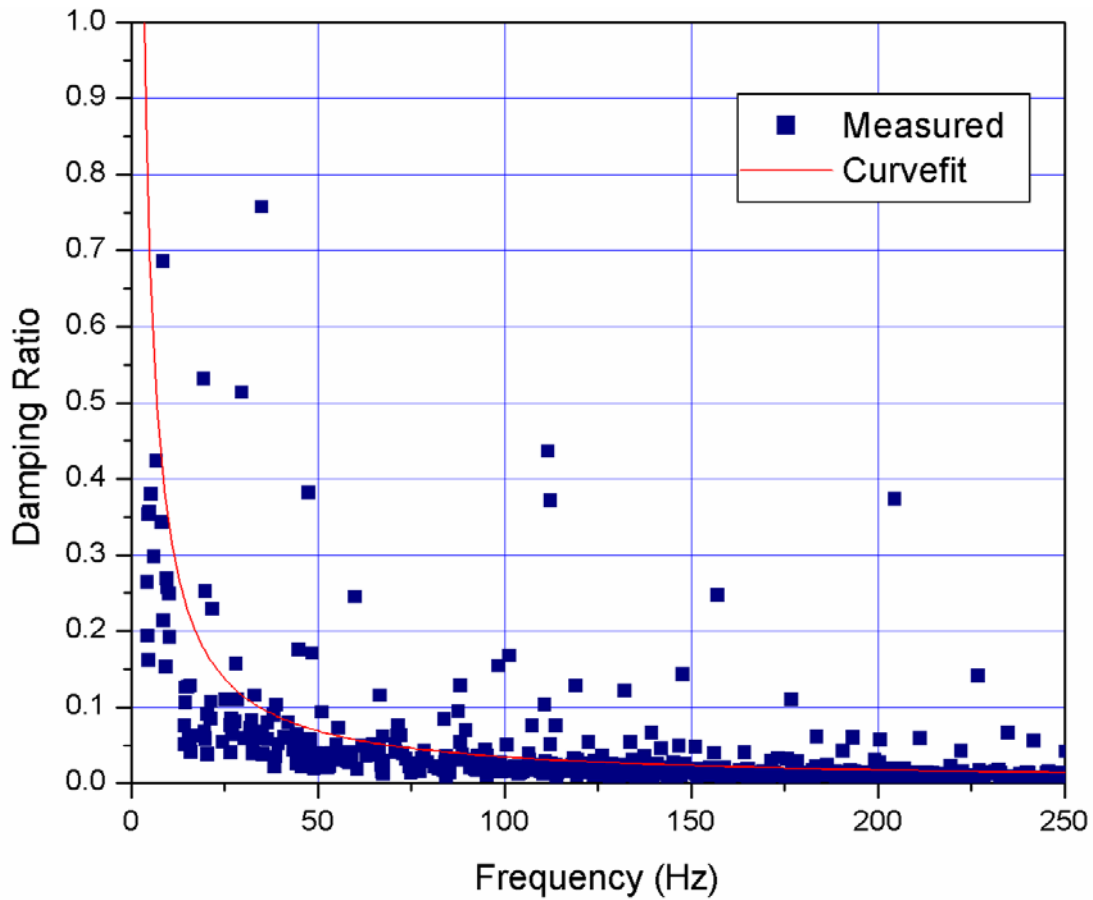


Figure 9. Vertical Modal Damping Ratio for Single Area Group of DDG 53 [from Ref. 19]

Each area group was given a weight based upon the number of modes used in determining the least squares curve fit for that area group. These values were summed and divided by the sum of the modes used to find both the weighted α_{mean} and the weighted β_{mean} . These values are shown in Tables 2 and 3. The recommended values for α and β for DDG 53 were determined to be 19.2 and 2.09e-6 respectively. These values were chosen due to the fact that the vertical response is much larger in magnitude than the athwartship response. The resulting damping ratio curve for both response directions is shown in Figure 10 [Ref. 19].

Table 2. Weighted Mean of α (DDG 53) [from Ref. 19]

Athwartship Direction	Vertical Direction
18.4	19.2

Table 3. Weighted Mean of β (DDG 53) [from Ref. 19]

Athwartship Direction	Vertical Direction
2.82E-6	2.09E-6

From a structural damping perspective, DDG 53 and DDG 81 are virtually identical. Due to this similarity these values were used for the DDG 81 model [Ref. 19]. Application of Rayleigh damping to the model is performed in the “GLOBAL_DAMPING” card of LS-DYNA [Ref. 6]. All structural shell and beam elements in the model were assigned the same proportional damping value.

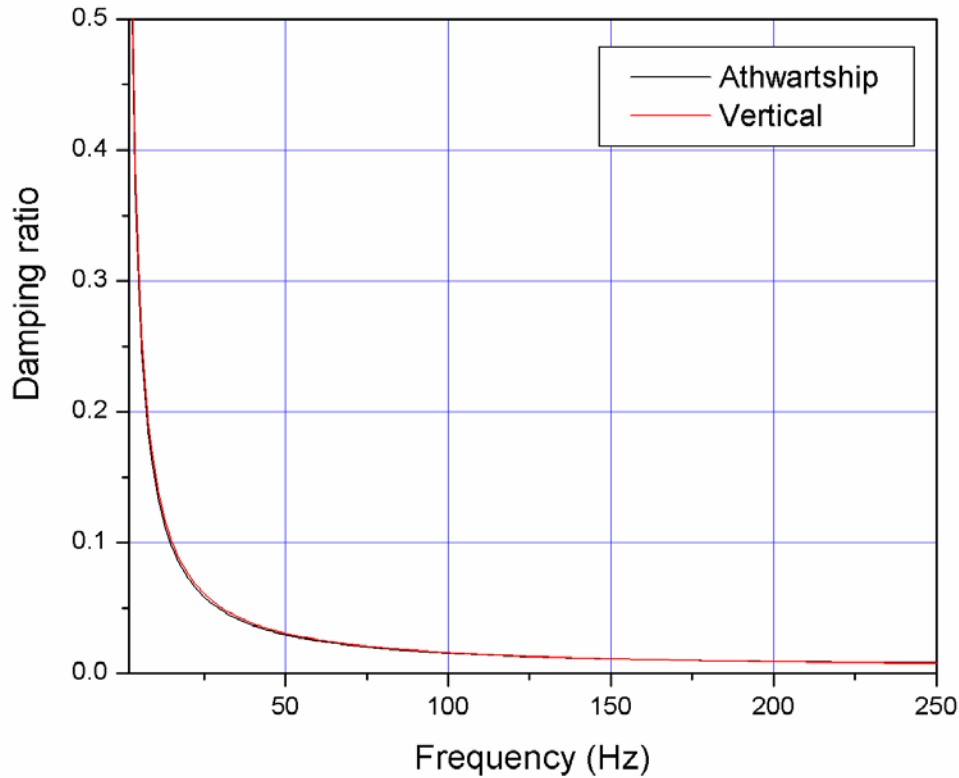


Figure 10. Damping Ratio Curve Plot for Using Recommended Rayleigh Damping Coefficients for DDG 53 [from Ref. 19]

B. SIMULATION CODE

Several analysis programs were used in the modeling and simulation of DDG 81. The model building, simulation, and data analysis procedure is outlined on the following page in Figure 11.

1. Model Generation and Pre-Processing

The USS WINSTON S. CHURCHILL structural finite element model was originally constructed by Gibbs & Cox, Inc using FEMAP. FEMAP is a Windows-based pre- and post-processor used for engineering finite element analysis. It is CAD neutral and solver neutral, making it a very useful modeling tool for a wide range of applications [Ref. 20]. The model was output from FEMAP in MSC/NASTRAN format and delivered in this form. MSC/NASTRAN/PATRAN was then initially used to identify elements and element properties and as a quality control check to verify all element and material properties were properly defined.

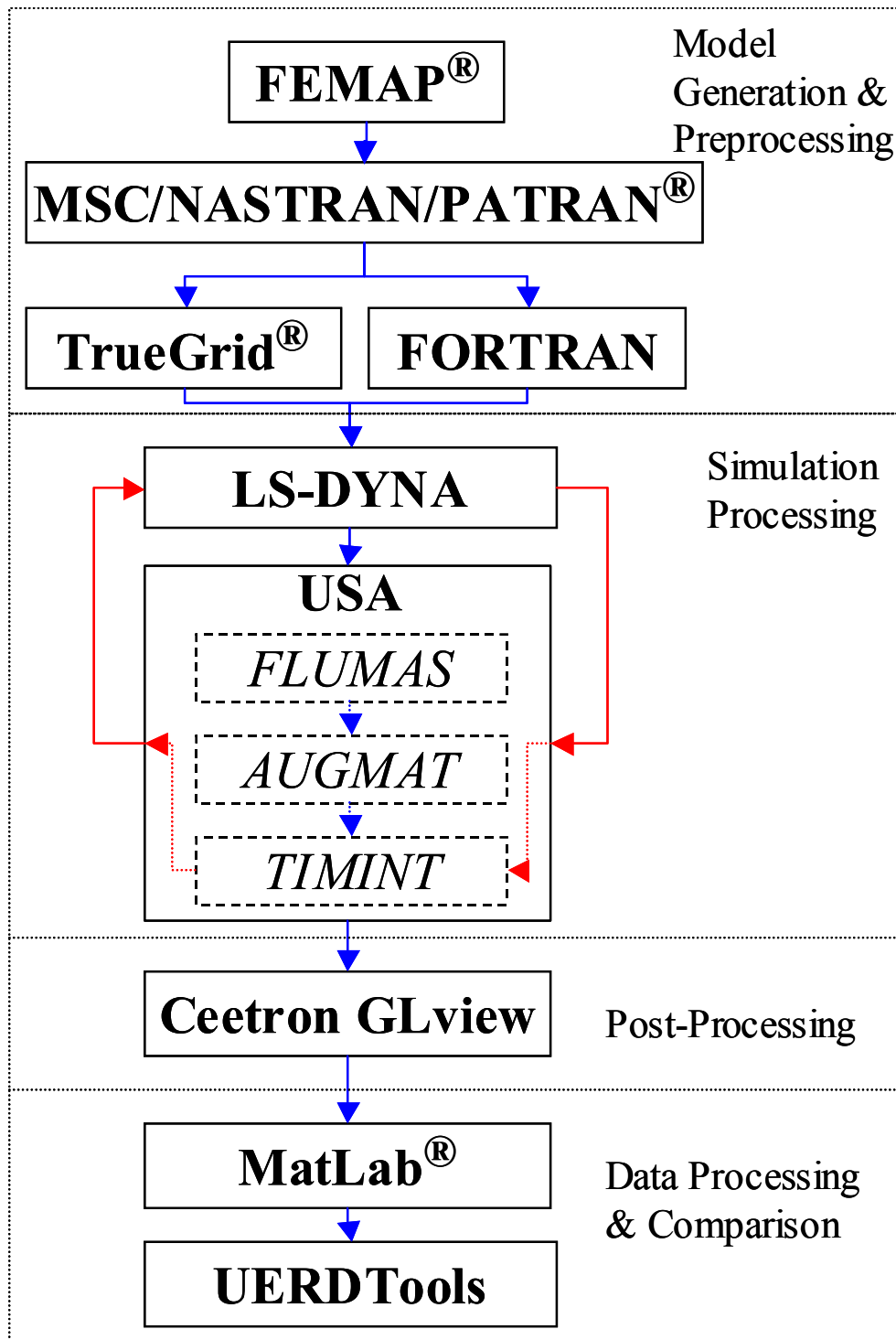


Figure 11. Model Generation and Simulation Flow Chart

The actual simulations were performed using LS-DYNA coupled with USA. This required that the model be translated from NASTRAN format to LS-DYNA keyword format. This was a complicated, but critical, step that was done manually and through a

conversion code written in FORTRAN. For construction of the surrounding fluid model, the structural model was imported directly into the TrueGrid mesh generator in NASTRAN format. More will be discussed on the construction of the fluid mesh using TrueGrid in Chapter IV.

2. Simulation Processing

LS-DYNA (Version 960) and USA were used to simulate the underwater shock and solve for the response of the structural model. LS-DYNA is a computational tool very popular in the automotive industry where it is commonly used to simulate such events as automobile crashes and airbag deployment. It is an explicit and implicit finite element program capable of analyzing the nonlinear dynamic response of three-dimensional inelastic structures [Ref. 6].

Working in concert with LS-DYNA, USA was used to calculate the transient response of the ship's wetted surface structure to the incident shock wave. As discussed in Chapter II, USA uses the Doubly Asymptotic Approximation (DAA) to solve the fluid structure interaction equations. This method allows the problem to be solved without requiring a large fluid volume mesh. This works very well for incident shock wave predictions, but does not consider cavitation, making it ideal for structures not affected by cavitation such as a deeply submerged submarine.

Cavitation has a major impact on the response of a surface ship subjected to an underwater shock, particularly in the late time response. A fluid volume finite element model (FEM) must surround the ship an adequate distance in order to capture the effects of bulk and local cavitation. Previous studies have shown that the minimum depth of this fluid mesh should be at least one half the cavitation depth for a reasonable approximation [Ref. 16, 21]. This fluid volume model should be extruded from the wetted surface structure, matching the structural element faces and node points as perfectly as possible [Ref. 22]. The DAA boundary is then placed on the outer surface of the fluid volume. This requires considerably more computational resources, but the improvement in the predicted response is substantial, making it a necessary requirement [Ref. 23]. The USA code consists of three components, FLUMAS; AUGMAT; and TIMINT.

a. FLUMAS

This component of USA constructs the fluid mass matrix for the wetted surface structure using the boundary element technique. It sets the fluid mesh properties, such as density, acoustic velocity, atmospheric pressure, and gravity. The set of transformation coefficients that relate to the structural and fluid degrees of freedom on the wetted surface structure are determined in this component. It also has the capability to solve the fluid boundary eigenvalue problem and automatically calculates the rigid body added mass coefficients [Ref. 7, 24].

b. AUGMAT

The purpose of this component is to use the data determined by the FLUMAS component to determine the compatibility relation matrix used in the staggered solution procedure described in Chapter II. This solution procedure is used to determine the transient response of a submerged structure [Ref. 24].

c. TIMINT

The TIMINT component of USA is where the majority of the simulation takes place. It conducts a step-by-step direct numerical time integration of the wetted surface structure exposed to the spherical shock wave. This component utilizes the DAA described in Chapter II where a staggered solution technique is used solving the structural and fluid response equations separately [Ref. 24]. Time histories of the structural and fluid response are output from this component. Also output from this component are the plot files necessary to perform the simulation animation. The vast majority of the computational resources used for the simulations were used by this component.

3. Simulation Post Processing and Data Extraction

After LS-DYNA and USA completed processing the model, the data stored in the output files were extracted using GLview. GLview is a very capable 3D visualization and animation post-processor [Ref. 25]. The simulations required tremendous quantities of data to be processed due to the extremely small calculation time step necessary. GLview is capable of handling these large quantities, producing a spectacular interactive animation of the virtual shock environment. In addition, it was used to download and

display the structural response time history graphically. It served as an interface between the raw simulation data output from USA and the data comparison tools used to compare the simulation predictions with measured test results. These raw files were loaded into GLview and then structural response parameters such as nodal velocities and accelerations were exported as ASCII files for further analysis.

4. Data Processing and Comparison

The nodal velocities and accelerations exported from GLview required filtering to remove undesirable frequencies. This was accomplished by importing the data files into a MATLAB code which processed the data through a low-pass Butterworth filter. This process and the reasons for doing it will be discussed in greater detail in Chapter V. The data was then imported into UERDTools for comparison with measured shock trial data. UERDTools was developed by the Underwater Explosions Research and Development (UERD) project office in Bethesda, Maryland for the purpose of analyzing shock trial data. It has numerous features specific to ship shock analysis such as unit scaling of data, filtering, interpolation, time shift, and error criteria calculations. More will be discussed about many of these features in Chapter V.

THIS PAGE INTENTIONALLY LEFT BLANK

IV. FLUID MESH MODELING

Fluid mesh modeling is the primary focus of this thesis. Several fluid models were constructed to model the three different shock environments. These models were all constructed using TrueGrid. TrueGrid is a powerful mesh generator that allows meshes of all types to be created interactively. While its full capabilities cannot be overstated, one key feature that makes it ideal for modeling the underwater shock environment is its ability to extrude the fluid mesh through the structural mesh. This results in a fluid mesh that aligns perfectly with the structural mesh from the fluid-structure interface out to the Doubly Asymptotic Approximation (DAA) boundary. While several models were used in the simulations, all of these models were variations of just three models. The construction of the third model, an improvement over the first two models, is highlighted in this chapter and described in greater detail in Appendix B. A list of many of the useful commands used to generate this model in TrueGrid is contained in Appendix C.

A. FLUID MESH CONSTRUCTION

The fluid mesh was constructed using essentially four subdivisions merged together; the inner liner, the inner mesh, the transitional mesh, and the outer mesh. By building the fluid mesh in this manner, several goals were accomplished:

- USA code stability criteria was met
- The fluid volume was meshed perfectly orthogonal to the structural mesh
- A quality mesh was maintained throughout the fluid volume from the fluid structure interface out to the boundary
- The fluid model was easily modified
- The proper waterline was achieved

1. Inner Liner

The inner liner of the fluid mesh serves as the fluid structure interface. It is the most critical part of the fluid mesh. The liner must mesh perfectly with the structural mesh, it must be as orthogonal to the hull as possible, and it must meet USA code

stability criteria. Regardless of the quality of the remainder of the fluid mesh, a poorly constructed inner liner will result in a poor approximation. This segment of the fluid mesh consists of 37 subparts and accounts for approximately 50% of the fluid mesh model code written.

a. USA Code Stability Criteria

The nodal spacing of this inner liner is critical to the stability of the USA code. The code requires that the nodal spacing of this inner layer cannot exceed a defined thickness, D, given by the following equation:

$$\frac{2D\rho}{\rho_s t_s} \leq 5 \quad (30)$$

where ρ is the density of water and ρ_s and t_s are the density and thickness respectively of the wetted surface shell elements.

The DDG 81 model wetted surface was constructed using a variety of quadrilateral and triangle shell elements. A listing of these elements and their associated thickness is shown in Table 4.

Table 4. DDG 81 Wetted Surface Shell Element Properties

Shell Part ID	Material ID	Thickness (in)
1062	2	0.375
1072	2	0.4375
1073	3	0.4380
1082	2	0.5
1102	2	0.625
1112	2	0.6875
1122	2	0.75
1123	3	0.75
1124	3	0.75
1163	3	1.0
1202	2	1.25

As shown in Table 4, the thinnest shell element used is Shell Part ID 1062 which is 0.375 inches thick. The material density of this shell element is $\rho_s=7.324\text{E-}4$

(lbf-s²/in⁴) while the density used for the water is $\rho=9.3601\text{E-}5$ (lbf-s²/in⁴). Applying the values in Equation (30) results in the maximum allowable thickness of the inner liner being 7.33 inches. To ensure that this was not exceeded, a thickness of seven inches was used for the entire inner liner.

b. Orthogonality

The majority of the inner liner was made orthogonal to the hull by using TrueGrid's "BLUDE" command along with the "NORMAL" command. The BLUDE command extrudes the fluid mesh through the structural mesh resulting in a fluid mesh which is merged perfectly with the structural mesh. While the BLUDE command does generally achieve normality, the NORMAL command was used to ensure that the fluid mesh was normal to the hull over its entirety and only seven inches in thickness.

The abrupt structural transitions such as the keel, bow, sonar dome, and stern areas did not allow for a single continuous fluid liner to be extruded from the hull. In these areas the liner was first extruded on all faces around the transition area. The gaps that were left between these meshes were filled in using wedge shaped elements. This ensured that orthogonality was maintained at these transitions while filling in the gap to allow for further construction of the fluid mesh.

c. Waterline

The proper waterline is essential for two reasons, to ensure proper global orientation of the fluid model and to accurately model the fluid structural interface. The DDG 81 structural model was constructed without mesh lines at the test waterline. To ensure that the fluid mesh was merged properly with and orthogonal to the structural mesh at the waterline, wedge shaped elements were constructed to transition from the structural mesh line to the actual waterline. Fluid-structure orthogonality was compromised in the aft section of the ship due to the extreme transition from the structural mesh line to the test waterline. To minimize this compromise, an additional layer was constructed to encapsulate the inner liner and continue the transition to the test waterline in this area. This second layer was eight inches in thickness, bringing the total thickness of the inner liner to fifteen inches nominally. Figure 12 shows the completed fluid mesh two layer inner liner.

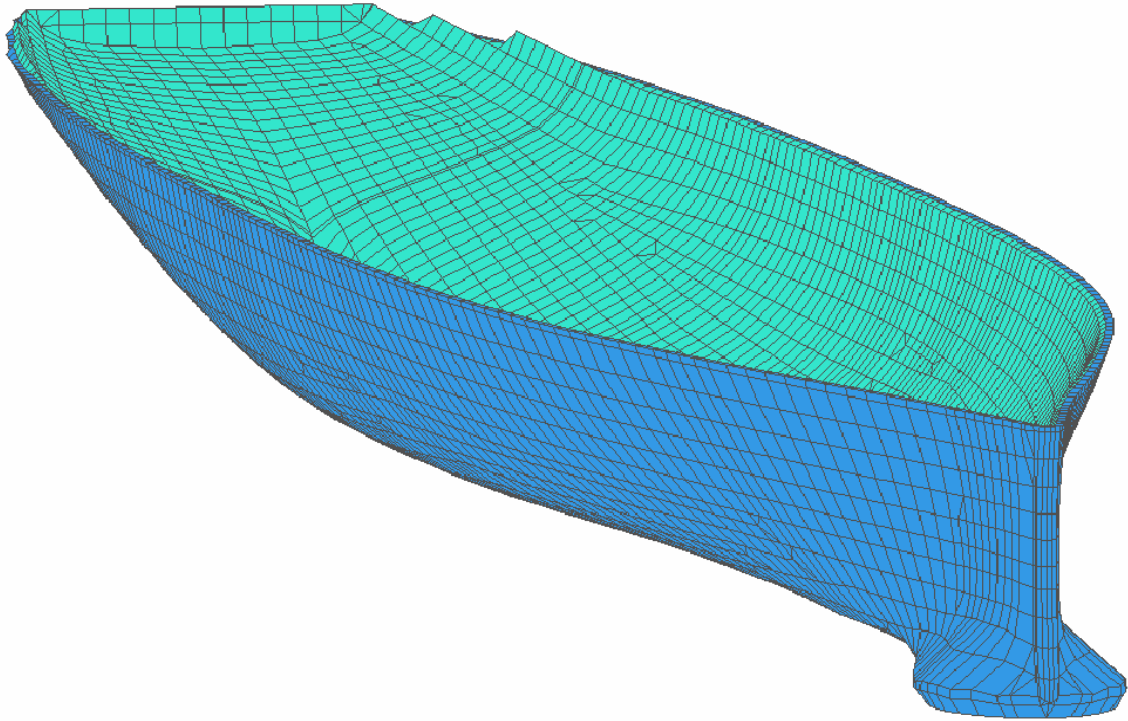


Figure 12. Fluid Model Two Layer Inner Liner

2. Inner Mesh

Many of the contours of the ship, particularly the sonar dome region and areas around the keel, form concave surfaces and have sharp transition areas. The purpose of this inner mesh is to provide a transition from these complex contours of the structural model to a surface convex in nature. The quality of the entire fluid mesh depends greatly upon the quality of this region. Complex control of the fluid mesh through the use of proper vertices placement, curve attachments, and surface projections is key to constructing this region of the mesh. Proper use of mesh interpolation methods is essential in this region to obtain a quality mesh. TrueGrid uses several interpolation techniques to ensure a quality, uniform mesh.

a. Thomas-Middlecoff Relaxation

Using linear iteration as described in Reference [26], Thomas-Middlecoff relaxation (TME) improves the mesh by solving a Poisson equation. This relaxation method excels in propagating the edge's nodal distribution into the interior of the mesh. In doing this, it attempts to maintain orthogonality throughout the mesh [Ref. 5].

b. Equipotential Relaxation

This method of mesh interpolation treats the mesh lines as solutions to the Laplace equation with the boundary conditions formed by the boundary nodes. This allows the interior volume of a mesh to be relaxed while maintaining the boundary nodal distributions. The primary purpose of using this interpolation method is to maintain a defined boundary while producing a uniform interior mesh [Ref. 5].

The inner mesh was constructed to allow for variation of mesh density, allowing the number of elements between the inner and outer boundaries to be changed using parameters. In its entirety, five separate subparts were constructed separately and merged together to form this region of the fluid model. The finished inner mesh extended outward a nominal distance of five feet from the inner liner. It is shown in Figure 13.

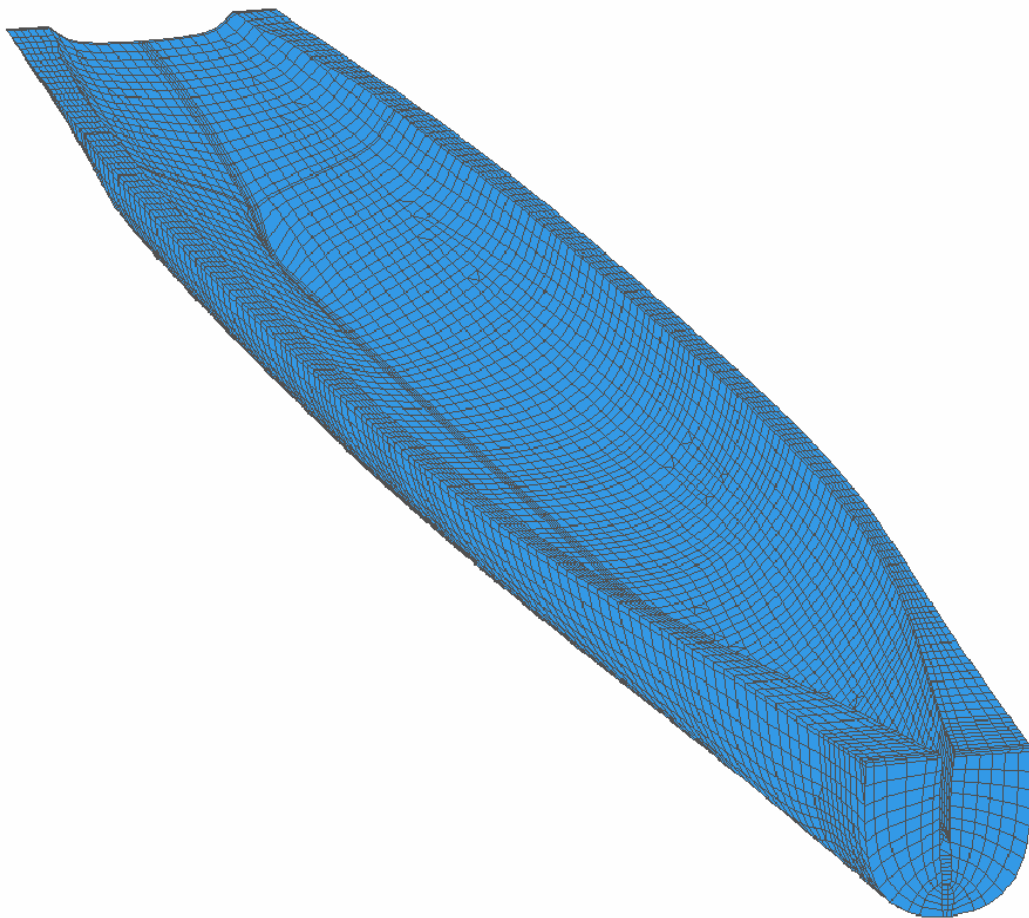


Figure 13. Fluid Model Inner Mesh

3. Transitional Mesh

The transitional mesh encapsulates the inner mesh and extends out to approximately ten feet from the hull. Conical shaped mesh regions were used to extend the bow and stern areas outward to merge perfectly with the contoured outer boundary of this mesh.

The fluid model has the ability to model the underwater shock environment for DDG 81 under varying loading conditions by allowing the waterline to be adjusted. The ability of the model to adjust to these different conditions occurs in this region of the mesh. This is accomplished by allowing the inner mesh to “float” along with the ship model inside this transitional mesh. The transitional mesh then transitions from the fixed 258 inch waterline of the inner mesh to the actual test waterline. The simulations investigated in this thesis all had a test waterline of 258 inches fore and aft which the inner liner and mesh was initially designed for. This feature was not necessary in these simulations, but was added to allow for future underwater shock simulation modeling of DDG 81.

In addition to allowing for variation in waterline, this region also allows for variation in mesh density. It consists of three parts constructed separately and merged together and with the previously constructed fluid model. The finished transitional mesh is shown in Figure 14.

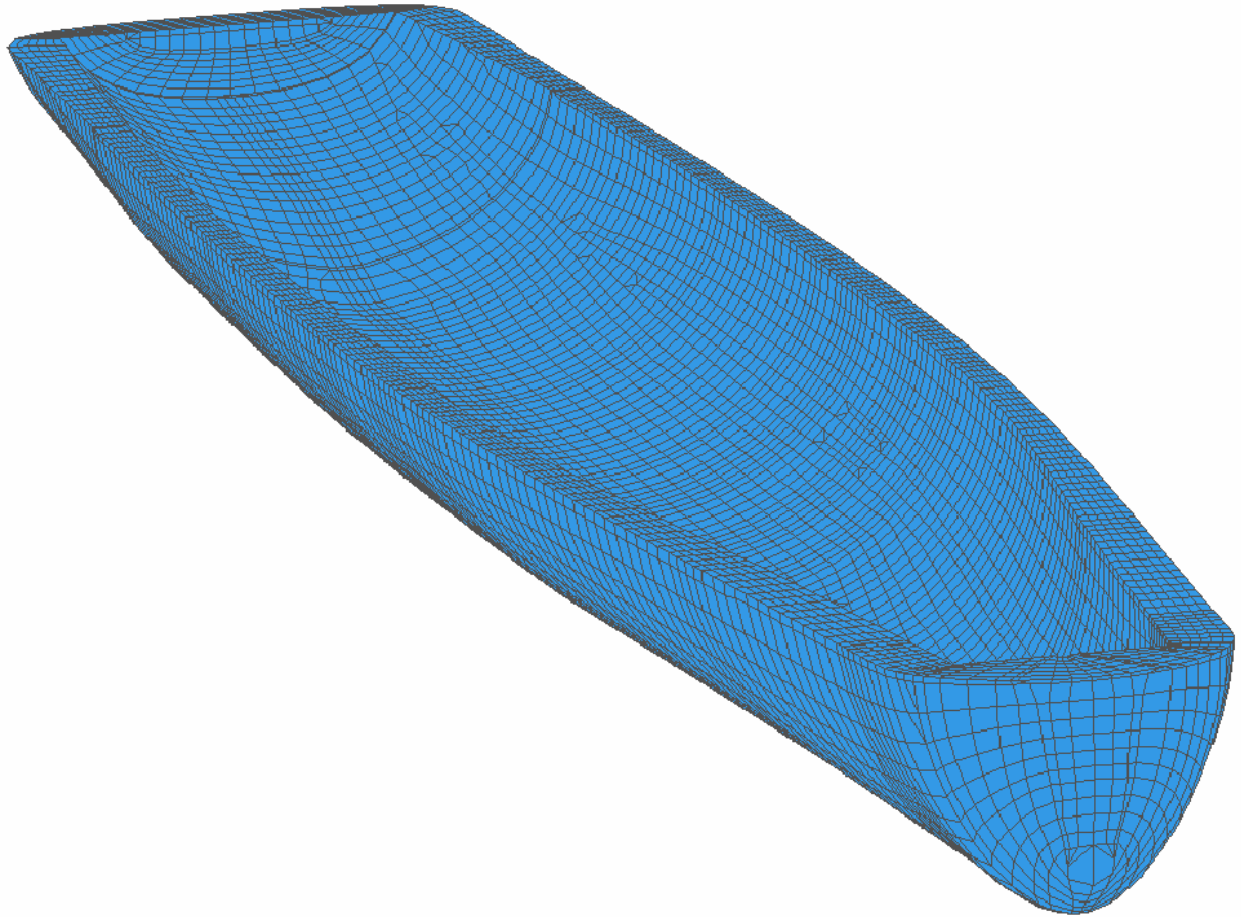


Figure 14. Fluid Model Transitional Mesh

4. Outer Mesh

The outer mesh extends the fluid volume out to the DAA boundary. The DAA boundary is formed on the outer surface of this mesh by selecting the outer faces of this mesh. Constructed to allow for the simulation of virtually any underwater shock environment, the depth, fluid mesh density, waterline, and contour of this outer mesh can be modified with just a few simple parameter inputs. Though comprising the majority of the fluid model, this region was constructed using only one part. The completed outer mesh is shown in Figure 15.

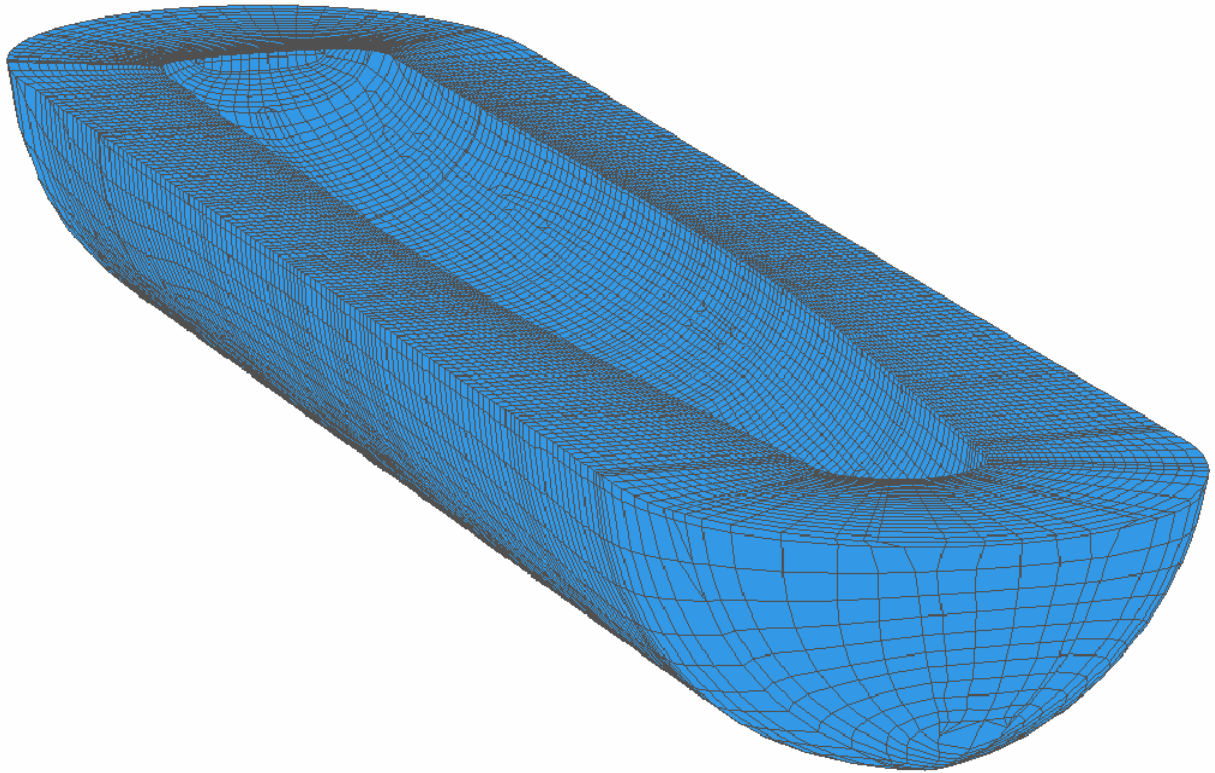


Figure 15. Fluid Model Outer Mesh

B. FLUID MODEL DEPTH

The effect of surrounding fluid on simulation predictions was the focus of the study conducted in Reference [21]. In this study, three fluid volumes of varying depths were modeled and compared using the most severe shock DDG 81 was subjected to. The conclusion of this study was that a fluid model depth equal to the cavitation depth was required for an accurate simulation. Based on this study, each underwater explosion investigated in this thesis was initially simulated using fluid models having depths equal to their respective cavitation depths. Figure 16 shows a complete fluid-structure model.

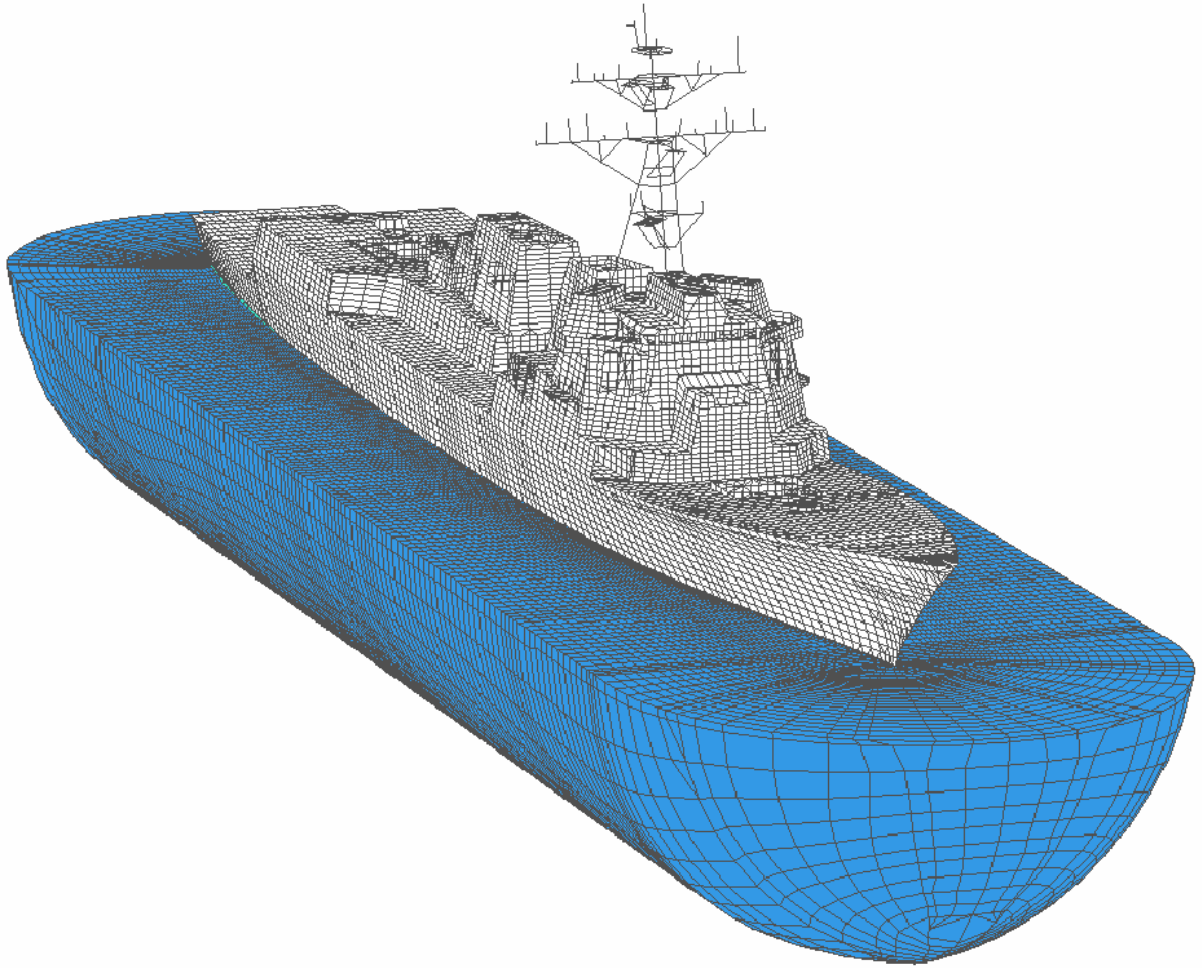


Figure 16. Complete Coupled Fluid-Structure Model (Shot 1)

C. FLUID MODEL PROCESSING

The completed fluid models were output from TrueGrid in LS-DYNA “Keyword” format. The fluid model output file consists of the nodal coordinate definitions, the fluid volume element nodal assignments, and the face set constituting the outer DAA boundary. Of particular importance here is that the fluid nodes corresponding to the same nodes on the ship cannot be redefined. Additionally, the DAA boundary face set must be defined with the normal pointing outward using a counter-clockwise nodal assignment [Ref. 7].

The fluid models were all assigned as material property Material Type 90 in LS-DYNA, an acoustic material. The LS-DYNA acoustic pressure element has a cavitation flag which can be turned on and off. When on, this flag prevents negative pressures from

occurring by cutting off any negative pressure at zero. This indicates the presence of cavitation [Ref. 6]. This flag was turned on for all simulations presented in this thesis.

The simulations began with an initial pressure field established and defined using a card in LS-DYNA specifically for explosive detonations. This pressure field is determined with the incident pressure wave already propagated out to one element away from the closest structural node to the charge. This fluid node, termed the reference node, was identified using a Microsoft Excel spreadsheet and defined in the LS-DYNA keyword file. In addition, the closest point on the DAA boundary, termed the standoff point, was identified using Excel and the coordinates defined in LS-DYNA. The coordinates of the charge, standoff point, and the reference node were defined in the TIMINT component of USA along with the slant distance, the radial distance from the charge to the standoff point on the boundary. Examples of the LS-DYNA keyword file and USA component files are included in Appendix D.

V. DATA COLLECTION AND ANALYSIS

Many variables exist in the underwater shock environment, one of those being the method in which the measured data is collected and analyzed. Prior to making any comparisons with simulation predictions, the data must be properly analyzed. The existence of low frequency “drift” and high frequency “noise” in shocktrial data present a formidable challenge to overcome.

A. VELOCITY RESPONSE “DRIFT”

The velocity meter and accelerometer were originally intended for measuring short duration transient motion signals over a limited frequency bandwidth. The accelerometer is ideal for frequency response measurement at frequencies far below its own resonant frequency while the velocity meter is more suitable for measuring the response to frequencies far above its own resonant frequency [Ref. 27]. For purposes of underwater shock simulation measurement it is desirable to extend the measurement time out to capture more of the response. This results in requiring the sensors to measure a considerably larger range of frequencies than they were intended for. Velocity and displacement time histories acquired by integrating acceleration time histories have a tendency to drift due to errors in the zero reference portion of the time history. This problem exists as well in velocity meter time history as velocity meters require seismic correction, which involves integration as well. As a result, the measured data displays a substantial amount of drift as shown in Figure 17.

A significant amount of study was conducted to determine how to eliminate this drift. UERDTools has a built-in function called “Drift Compensation” which uses an algorithm to eliminate this drift. Figure 18 shows the same velocity data after this drift compensation has been used. The advantages of using this technique are that the magnitude of the response is maintained and there is no shift in phase. The disadvantages are that it does not always eliminate the drift as shown in Figure 18. Further curve fitting where the analyzer uses his/her own judgment to determine where the data begins to drift is often required. This requires the user to determine a best-fit polynomial to the spurious

trend. This polynomial curve is subsequently subtracted from the data. This technique has proven to be effective in “cleaning” the data, but it invites a fair amount of subjective interpretation and potential for biased modification of the data. Ideally, a method involving less “hands-on” manipulation of the data would be preferable.

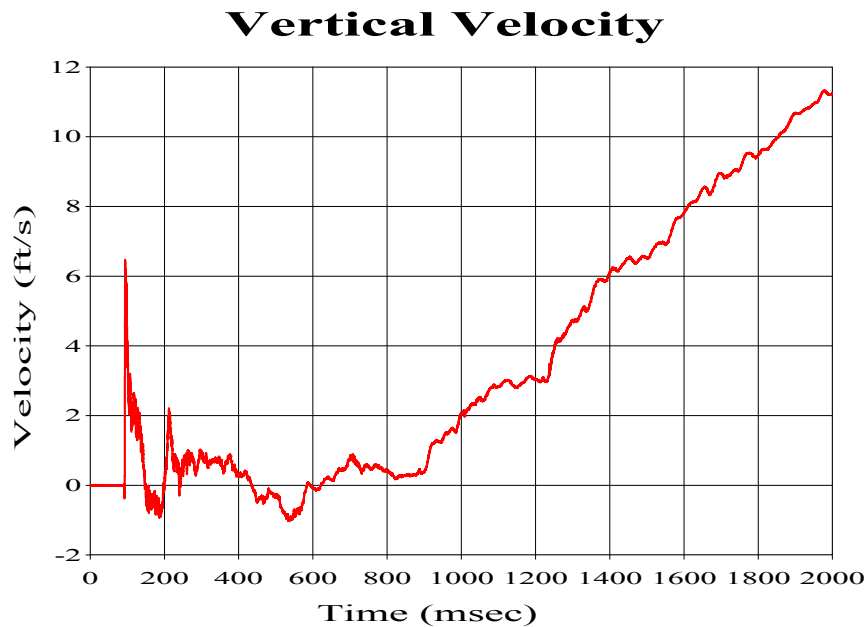


Figure 17. Raw Velocity Data Showing Drift

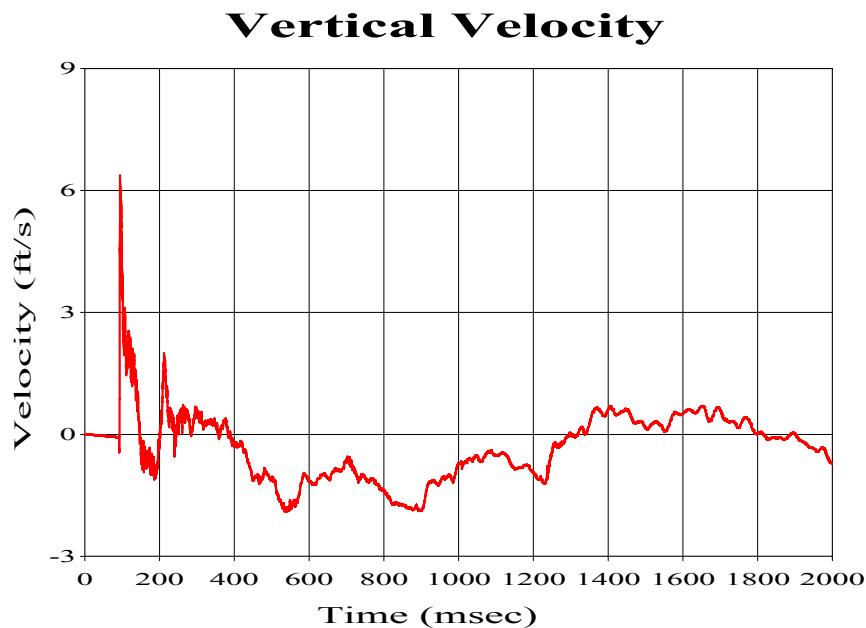


Figure 18. Velocity Data After Drift Compensation Has Been Applied

An alternate method of dealing with this drift is to process the data through a high-pass filter. While velocity meters record the global response, it is most desirable to determine only the local response at a particular location. To determine the local response it is therefore desirable to eliminate any rigid body modes from the sensor response. This can be measured by analyzing the late time displacement response of the structure where rigid body modes reveal themselves in the form of a non-zero steady state displacement. Doing this rigid body motion study for a number of sensors, it was initially determined that the measured data should be filtered using a Bessel two-pole high-pass filter set at a cut-off frequency of 3Hz. The same was done with the simulation data where a cut-off frequency of 1.8Hz was necessary. A two-pole Bessel filter was chosen as it is the only built-in high-pass filter in UERDTools. Figure 19 shows a comparison of filtered versus drift compensated velocity data. As shown in Figure 19, filtering results in a velocity plot with no significant drift apparent, while the drift compensated data still shows strong evidence of low frequency drift.

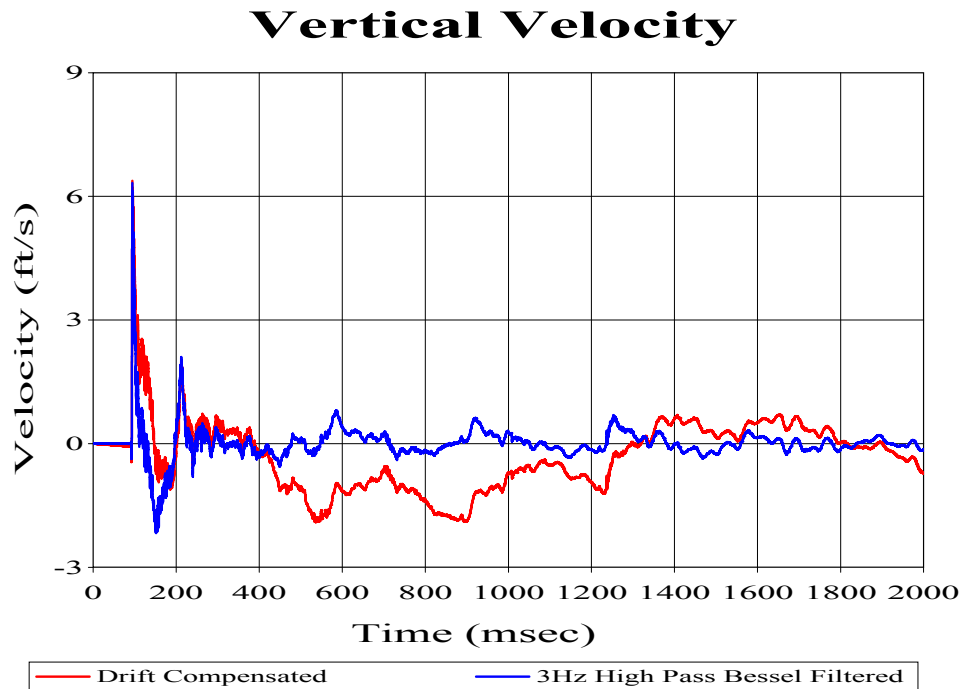


Figure 19. Comparison of High Pass Filtering vs. Drift Compensation

The disadvantage of using this high-pass filter is that desirable frequencies above 3Hz are filtered out due to the characteristic of the two-pole Bessel filter. Figure 20 shows a frequency response of a two-pole high-pass Bessel filter set at a cut-off frequency of 3Hz. As is shown in the Fourier spectra shown in Figure 21, a significant portion of the structural response occurs in the 5-10Hz frequency spectrum. Figure 20 shows that with the cut-off set at 3Hz the two-pole Bessel filter actually filters frequencies well above 10Hz. While not easily apparent in this comparison, this results in a significant loss of magnitude in the structural velocity response, particularly after 50 msec. Lowering the cut-off frequency to 0.5Hz results in less unwanted filtering, but as with drift compensation, evidence of rigid body motion still exist afterwards.

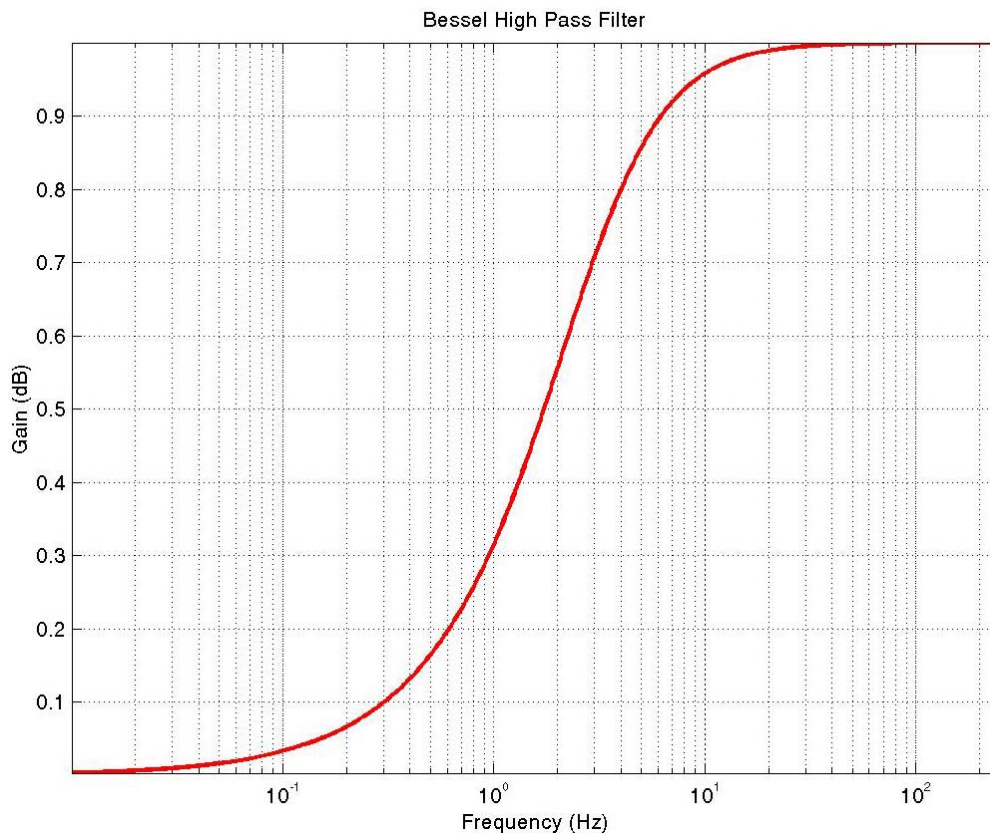


Figure 20. Two-Pole High-Pass Bessel Filter With 3Hz Cut-off Frequency.

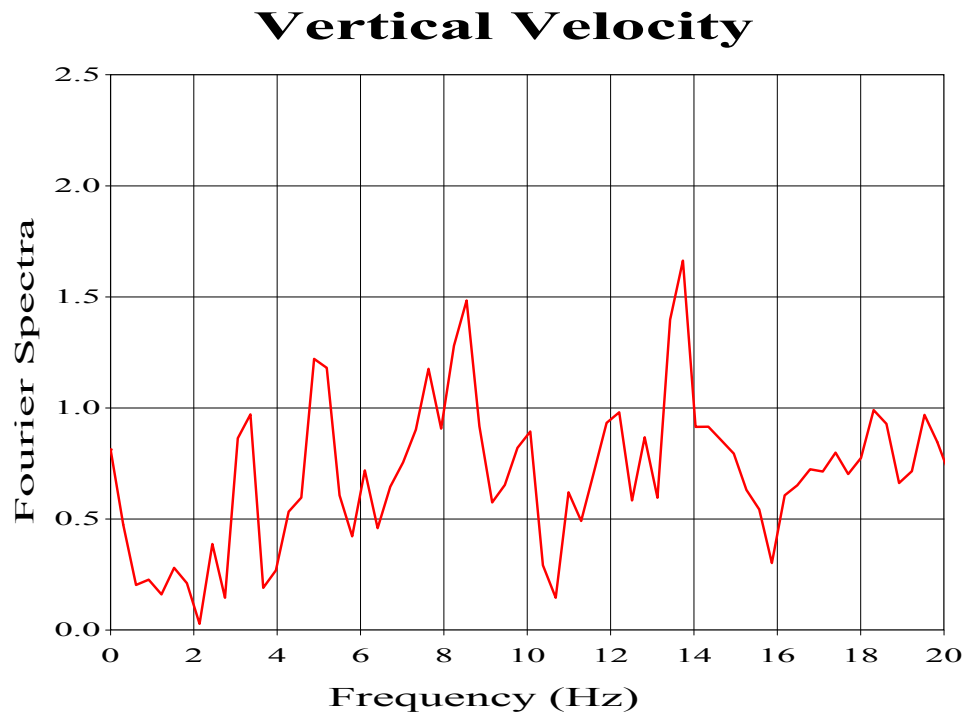


Figure 21. Fourier Spectra Plot Showing Structural Low Frequency Response (Vertical Velocity Input)

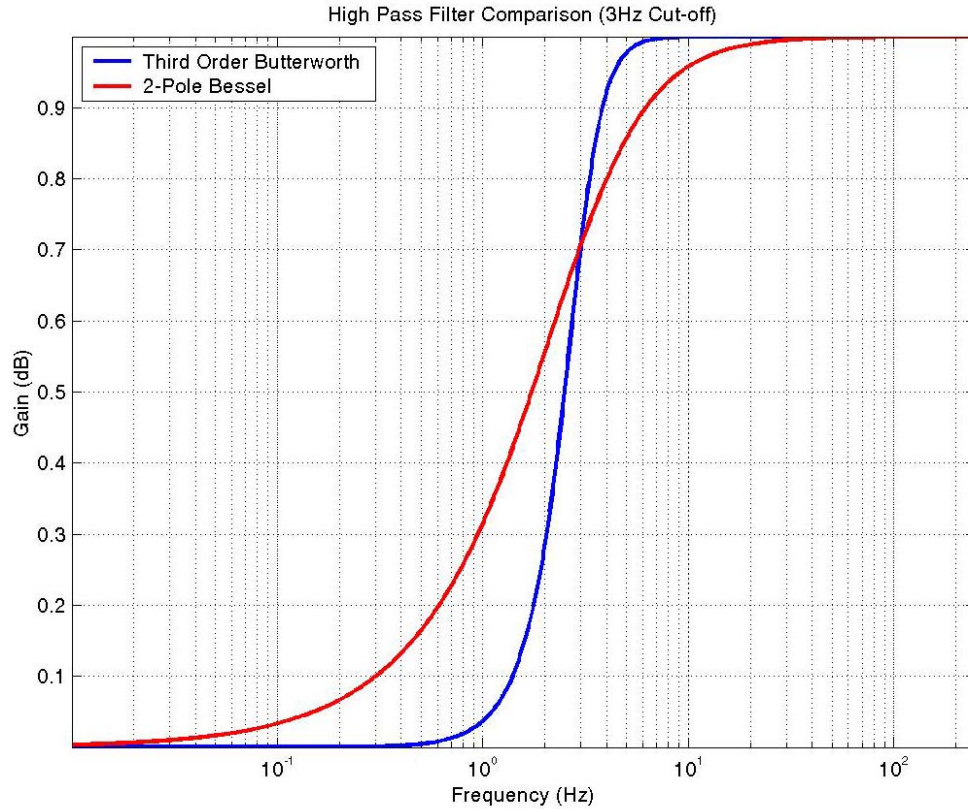


Figure 22. Butterworth vs. Bessel High Pass Filter

A third-order high-pass Butterworth filter has a preferable high-pass characteristic. As shown by Figure 22, a third-order Butterworth filter reduces the amount of desirable frequency response that is filtered, but still has a small effect on the low frequency response. Figure 23 shows the result after applying a 0.5Hz cut-off to the data using a Butterworth filter. As with the 0.5Hz cut-off Bessel filter, a small amount of low frequency drift is still apparent.

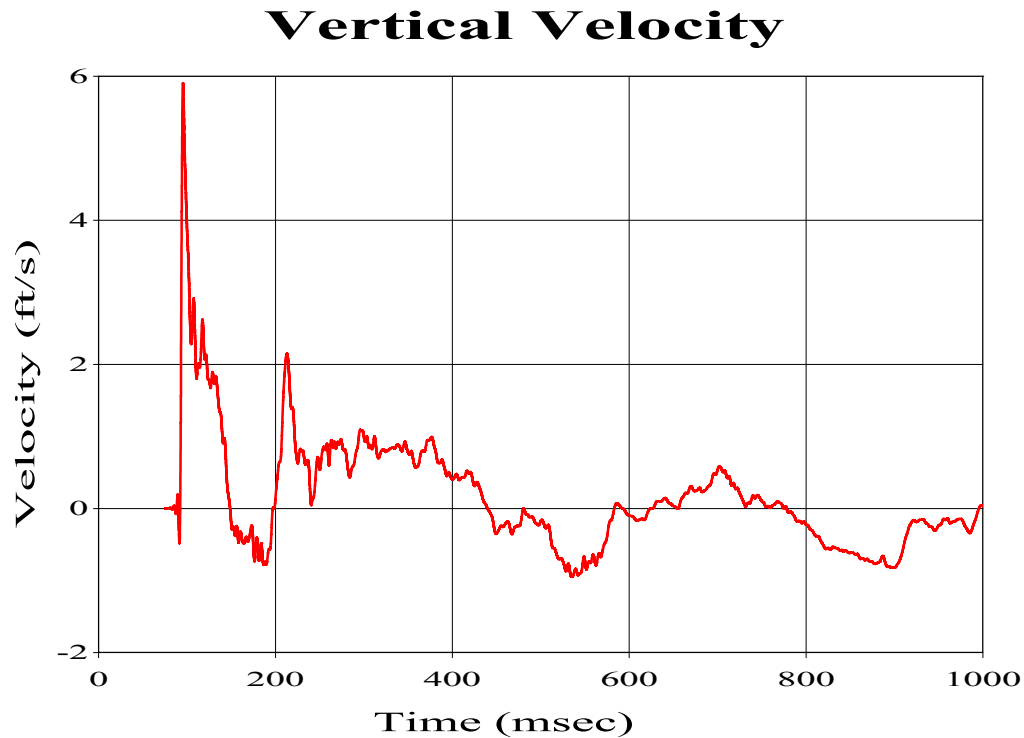


Figure 23. Velocity Response After Filtering 0.5Hz High-Pass Butterworth Filter (Third-Order)

Previous UNDEX research has utilized only drift compensated data and it is currently the recognized method of shock trial data analysis. Simulation comparisons made using filtered data versus using drift compensated/polynomial fitted data were comparable. While the comparisons made in this thesis use drift compensated data, high-pass filtering the data offers an easier alternative worthy of consideration in the future.

B. HIGH FREQUENCY “NOISE”

In addition to drift, raw shock trial data has a fair amount of high frequency “noise” which clutters the data. The high frequency response is not of concern in

UNDEX. These high frequencies are filtered out using a 250Hz cut-off low-pass filter. Figure 24 shows an example of the effects this filtering has on the data.

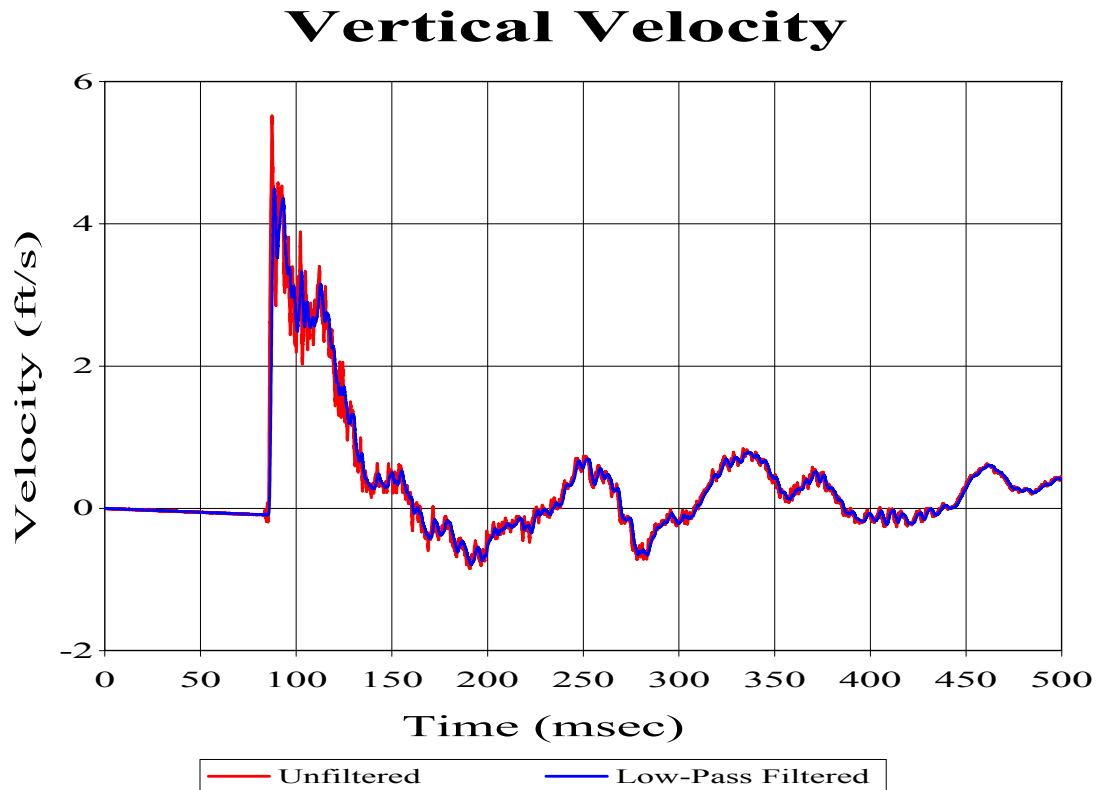


Figure 24. Effect of Low-Pass Filtering Data

While applying this low-pass filter to trial data has been widely accepted, some debate has risen over the validity of applying the same low-pass filter to simulation data. To answer this, a statistical study was conducted using 223 accelerometer measurements low-pass filtered at 250Hz. These were compared with 33 nodal acceleration predictions from a simulation of the same shot. The simulation data was compared before and after being low-pass filtered. The results of this study showed an unfiltered simulation prediction mean much higher than the measured values and an excessively large variation. The filtered simulation predictions not only displayed a more accurate mean, but had a more reasonable variation as well. As recommended by this study, all

simulation response predictions compared in this thesis were low-pass filtered using the same cut-off frequency as was used with the measured data. A summary of the results of this study is shown in Table 5.

Table 5. Statistical Study of Low-Pass Filtered vs. Unfiltered Simulation Data

	Shock Trial Data (Filtered)	Simulation Data (Unfiltered)	Simulation Data (Filtered)
Mean	26.225	82.985	34.297
Variance	520.229	5775.711	606.426
Standard Deviation	22.809	75.998	24.626

VI. SIMULATION RESULTS AND ANALYSIS

Three underwater explosions, shots, were conducted during the DDG 81 shock trials. The most severe of these shots was the third shot, “Shot 3”, while the least severe shot was the first shot, “Shot 1”. All three of these shots have been simulated using the structural model described in Chapter III coupled with several fluid models. The primary focus of this thesis is to investigate the effects of fluid mesh density, the number of elements between the outer DAA boundary and the fluid-structure interface, as well as the ability to accurately simulate different shot geometries. In addition to this, the effects of varying mesh quality and fluid volume depth are investigated.

A. ANALYSIS AND COMPARISON

1. Sensor/Node Location

Over 600 sensors were mounted onboard DDG 81 to measure the response during each shot conducted. These sensors consisted of accelerometers, velocity meters and strain gauges. For comparison purposes, corresponding nodes were built into the structural model representing several of these sensors. These nodes were defined in LS-DYNA allowing a transient response time history to be kept for each one. This time history was then downloaded into GLview and subsequently imported into UERDTools for comparison with the measured sensor response.

During an underwater shock event, the primary structural response is in the vertical direction. For this reason, only the vertical velocities were compared in this paper. In total 32 sensors were compared for Shot 3, 30 for Shot 2, and 28 for Shot 1. While the majority of these sensors were vertical velocity meters, several accelerometers were used as well. The accelerometer data was subsequently integrated for comparison with predicted velocity response. A list of all of the sensors used in the comparisons is shown in Table 6. Those sensors beginning with an “A” are accelerometers while those beginning with a “V” are velocity meters.

Table 6. Vertical Velocity Response Sensor Location (N/A = no data available)

Sensor	NODE	X(Node)	Y(Node)	Z(Node)	Compartment/Location	Compt#/Area	Shot 1	Shot 2	Shot 3
V2000V	120217	5328.0	0.0	82.0	PASSAGE	4-022-0-L	X	X	X
V2002V	142489	4656.0	27.0	82.0	SONAR COOLING EQ RM	4-042-0-L	X	X	X
A4701V	211371	4080.0	0.0	280.0	CREW LVG SPACE #2	3-097-2-L	N/A	N/A	X
A8516V	210993	4080.0	238.5	202.0	CREW LVG SPACE #2	3-097-2-L	X	X	X
V2107V	211904	4080.0	-312.0	390.0	PASSAGE	1-078-1-L	N/A	N/A	X
V2108V	212196	4080.0	312.0	390.0	PASSAGE	1-078-1-L	N/A	X	X
V2007V	210430	4080.0	0.0	82.0	AMR #1	4-126-0-E	X	X	X
V2009V	210808	4080.0	-174.0	177.0	AMR #1	4-126-0-E	X	X	X
V2008V	210894	4080.0	174.0	177.0	AMR #1	4-126-0-E	X	X	X
A2109V	414953	4059.1	0.0	722.8	RR #1	03-128-0-C	X	X	X
V2011V	221188	3504.0	216.0	177.0	AMR #1	4-126-0-E	X	X	X
V2010V	220589	3504.0	0.0	85.5	AMR #1	4-126-0-E	X	X	X
V2012V	221102	3504.0	-216.0	177.0	AMR #1	4-126-0-E	X	X	X
V2124V	222060	3504.0	-375.4	390.0	PASSAGE	1-158-1-L	X	X	X
V2125V	222436	3504.0	375.4	390.0	PASSAGE	1-158-8-L	N/A	X	X
V2013V	221601	3504.0	0.0	280.0	ENGINE RM #1	4-174-0-E	X	X	X
A2116V	414367	3504.0	0.0	702.0	RR #2	03-142-0-C	X	X	X
A2237V	416419	3504.0	135.0	848.0	PORT MAST LEG	MAST	X	X	X
A2240V	416269	3504.0	-135.0	848.0	STBD MAST LEG	MAST	X	X	X
A2104V	222240	3504.0	0.0	390.0	CIC ANNEX	1-126-0-C	X	X	X
V2014V	230461	2952.0	0.0	85.5	AMR #2	4-220-0-E	X	X	X
A3565V	231696	2952.0	-81.0	316.7	ACCESS TRUNK	3-220-0-T	X	X	X
V2016V	242399	2544.0	0.0	116.0	ENGINE RM #2	4-254-0-E	X	X	X
V2026V	312302	1992.0	0.0	55.0	ESCAPE TRUNK	4-296-1-T	X	X	X
A2310V	320746	1536.0	0.0	177.0	A/C MCHY & PUMP RM	5-300-01-E	X	X	X
V2034V	330759	1152.0	-135.0	193.3	FAN ROOM	3-362-0-E	X	X	X
V2032V	330764	1152.0	0.0	196.0	FAN ROOM	3-362-0-E	X	X	X
V2035V	330769	1152.0	135.0	193.3	FAN ROOM	3-362-0-E	X	X	X
V2019V	340167	672.0	0.0	196.5	GENERATOR RM	3-370-0-E	X	X	X
V2018V	340992	672.0	0.0	364.8	PASSAGE	2-410-0-L	X	X	X
A2413V	350220	288.0	0.0	273.4	RAST MACHINERY RM	2-442-0-E	X	X	X
V2020V	350052	288.0	0.0	211.0	STEERING GEAR RM	4-442-0-E	X	X	X

2. Error Measurement

Quantifying how well a calculated transient response compares to a measured response is very subjective. One way to eliminate any bias from the comparison is by using an impartial error measure such as Russell's error factor. Russell's error factor evaluates the magnitude and phase errors separately, combining the two to form a single comprehensive error factor [Ref. 28].

The relative magnitude error is found by first forming two variables,

$$A = \sum_{i=1}^N f_1(i)^2 \quad (31)$$

and

$$B = \sum_{i=1}^N f_2(i)^2 \quad (32)$$

where $f_1(i)$ and $f_2(i)$ are the measured and predicted response magnitudes respectively at a given time step, i . The two variables can then be used to find the relative magnitude error,

$$m = \frac{(A-B)}{\sqrt{AB}} \quad (33)$$

The phase error contributes significantly to the error between two transient responses. If $\hat{\phi}$ is allowed to be the normalized unit vector of a transient response, the phase correlation between the measured and predicted responses can be defined by,

$$p = \hat{\phi}_1 \cdot \hat{\phi}_2 \quad (34)$$

Since the unit vectors are normalized, the values of p can range from -1.0 to 1.0 where -1.0 indicates that the two responses are completely out of phase, while 1.0 indicates that they are completely in phase.

A measure of the phasing between two transient response vectors in terms of correlation can be found by defining a new term,

$$C = \sum_{i=1}^N f_1(i)f_2(i) \quad (35)$$

The phase correlation between the two responses can then be computed by

$$p = \frac{C}{\sqrt{AB}} \quad (36)$$

It is important to note that p represents the phasing correlation between the two responses, it is not a measure of phase error. To calculate phase error, the following equation is used:

$$RP = \frac{\cos^{-1}(p)}{\pi} \quad (37)$$

The phase error factor has an error range of 0.0 to 1.0 where 0.0 indicates both responses are completely in phase while 1.0 indicates they are completely out of phase.

Although the phase error factor has a maximum value of 1.0, the relative magnitude error factor is unbounded. Since the two are combined to form the comprehensive error, it is easy to see that the magnitude error could easily dominate the comprehensive error, presenting an undesirable bias. To apply a similar bound to the magnitude error factor the following magnitude error factor is defined:

$$RM = \text{sign}(m)\log_{10}(1+|m|) \quad (38)$$

This maintains the sign unbiased nature of m while effectively artificially bounding the magnitude error factor since a RM value of 1.0 represents an order of magnitude error between the two responses. The comprehensive error factor can now be determined using the following equation:

$$RC = \sqrt{\frac{\pi}{4}(RM^2 + RP^2)} \quad (39)$$

where the $\frac{\pi}{4}$ term is a scale factor found by calculating the area of a square with a width of length RM and height of length RP. A circle with a corresponding area has a radius equal to $\frac{\pi}{4}$ times the diagonal of the square [Ref. 28]. The comprehensive error factor is not bounded, but errors in excess of 1.0 indicate substantial error between data sets and virtually no correlation.

Russell's error factor allows an unbiased error value to be assigned to the correlation between the measured and predicted transient responses. The determination

as to what justifies an acceptable or unacceptable prediction is more subjective however. It has been suggested that the values outlined in Table 7 should be used for acceptance criteria of a 500 msec processed velocity data comparison [Ref. 29]. Processed data in this sense means both measured and predicted response data low pass filtered with a cut-off frequency of 250 Hz and measured data drift compensated to remove gauge drift. This acceptance criteria is not valid for shorter duration comparisons or data which has been processed using other techniques [Ref. 30].

Table 7. Russell’s Comprehensive Error Factor Acceptance Criteria

$RC \leq 0.15$	EXCELLENT
$0.15 < RC \leq 0.28$	ACCEPTABLE
$RC > 0.28$	POOR

It should be noted that this acceptance criteria is only an agreed upon means of determining an acceptable or unacceptable prediction. While these error factors present a useful tool for statistical comparison between models, there are no magical lines of distinction drawn at the levels of acceptance. This is to say that a comparison resulting in a comprehensive error factor of 0.148 placing it in the “Excellent” category is not significantly better than an “Acceptable” comparison resulting in a comprehensive error factor of 0.152. Similarly, though unacceptable, a comparison resulting in a 0.285 error factor is not significantly worse than one whose comprehensive error factor is 0.275, an “Acceptable” value. With this in mind, comparisons should be summarized using the actual error factor values, not the subjective ratings applied to those numbers.

B. SEVERE SHOCK (SHOT 3)

The most severe shock conducted on DDG 81 was Shot 3. A diagram showing the relative aspect of this shot to the ship is shown in Figure 25.

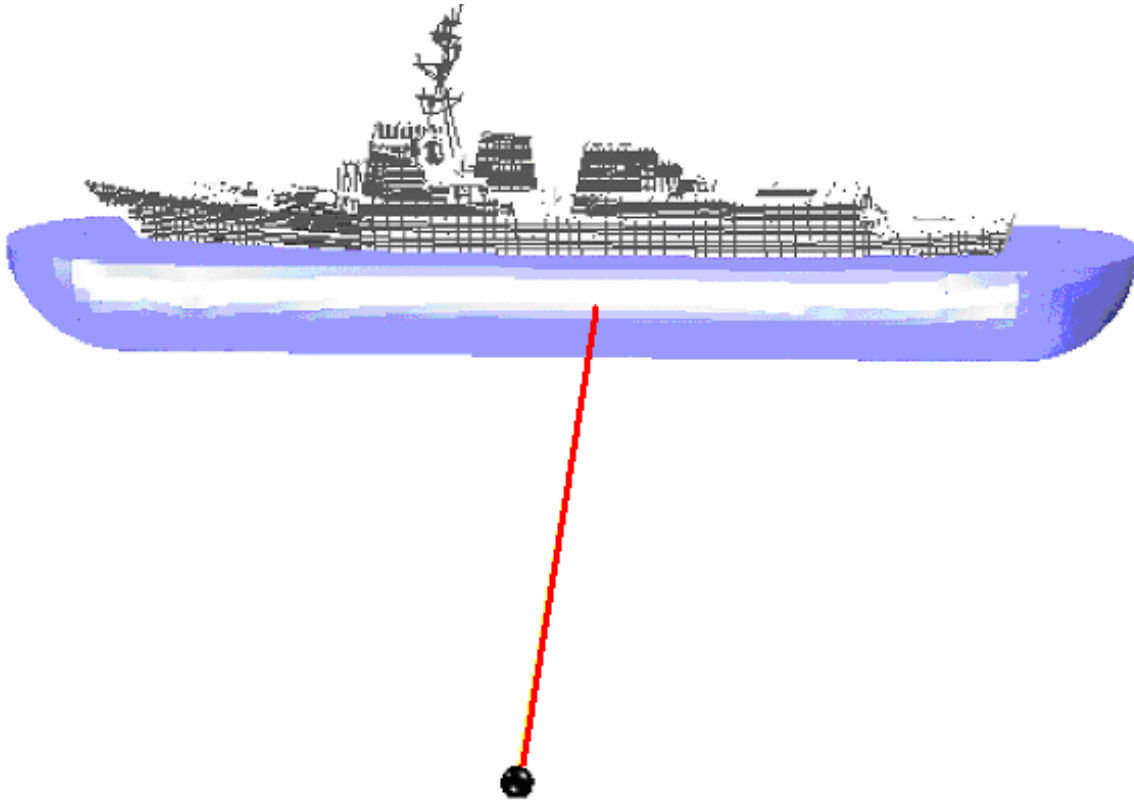


Figure 25. Shot 3 Geometry. Most Severe Shot, Charge Off Port Midships

This particular shot was the focus of the surrounding fluid effect study conducted in Reference [21]. In this study the Russell's error factors were determined after high-pass filtering the measured data using a cut-off frequency of 3 Hz and filtering the predicted response data using a high-pass filter cut-off frequency of 1.8 Hz [Ref. 21]. This filtering was performed using a two-pole Bessel filter. The resulting Russell's error factors found using this data processing technique for the "Full Cavitation Depth" model comparison are shown in Table 8.

Table 8. Russell's Error Factor Using High Pass Filtered Data (420 msec) [from Ref. 21]

Sensor	RM	RP	RC
V2013V	0.0263	0.1329	0.1200
V2012VI	0.0583	0.1424	0.1363
V2108V	0.0038	0.1543	0.1368
V2124V	0.0386	0.1562	0.1425
V2016V	0.0291	0.1592	0.1434
V2009VI	0.1113	0.1388	0.1577
V2034V	0.0173	0.1787	0.1591
V2026V	0.0542	0.1849	0.1707
V2014V	0.0372	0.1949	0.1759
V2011VI	0.0906	0.1972	0.1923
V2002V	0.1240	0.1873	0.1991
V2035V	0.0513	0.2243	0.2039
V2018VI	0.1039	0.2055	0.2041
V2008VI	0.1290	0.1937	0.2063
V2125V	0.0488	0.2334	0.2113
V2010V	0.0449	0.2456	0.2213
V2032V	0.1399	0.2083	0.2224
V2020V	0.1334	0.2165	0.2254
V2019V	0.1059	0.2331	0.2269
V2007V	0.1464	0.2122	0.2285
V2000V	0.2419	0.3164	0.3529

The same predicted response data were used to find the Russell's error factors summarized in Table 9 where no high pass filtering has been applied. The measured response data has instead been corrected using the drift compensation method described previously. As shown in the two comparisons, the filtered data yields artificially low Russell's comprehensive error factors, primarily due to the magnitude error factor. This is consistent with the discussion in the previous chapter where filtering results in a significant reduction in the response magnitude. This reduction tends to reduce the error between the two responses as indicated by the reduction in the magnitude error factor.

Table 9. Russell’s Error Factor Using Drift Compensated Data (500 msec)

Sensor	RM	RP	RC
V2013V	-0.1123	0.1859	0.1925
V2124V	-0.1543	0.1716	0.2045
V2012VI	-0.1435	0.1864	0.2085
V2034V	0.1857	0.1450	0.2088
V2016V	-0.1481	0.1948	0.2169
V2002V	0.0310	0.2466	0.2203
V2014V	-0.1086	0.2414	0.2346
V2018VI	0.1306	0.2304	0.2347
V2108V	-0.1372	0.2274	0.2354
V2026V	-0.1723	0.2219	0.2490
V2008VI	-0.1394	0.2476	0.2519
V2009VI	-0.1511	0.2543	0.2621
V2019V	0.1780	0.2420	0.2662
V2125V	-0.1982	0.2277	0.2675
V2035V	0.2364	0.2082	0.2791
V2032V	-0.2280	0.2200	0.2807
V2011VI	-0.2121	0.2436	0.2863
V2010V	-0.2358	0.2425	0.2997
V2007V	-0.2296	0.2676	0.3125
V2020V	0.2165	0.2843	0.3167
V2000V	0.2891	0.3109	0.3763

1. Fluid Mesh Depth

The “Full Cavitation Depth” simulation in Reference [21] used a fluid model with a depth of 840 inches as a rough approximation to the actual cavitation depth. Although the outer boundary of the fluid model is perfectly cylindrical, the cavitation depth changes along the length of the ship. Due to this, a perfectly cylindrical model can only approximate the cavitation depth and, in this case, was modeled having a sufficient depth to include the cavitation region throughout the length of the ship. This model, termed the 1st generation model, is shown in Figure 26.

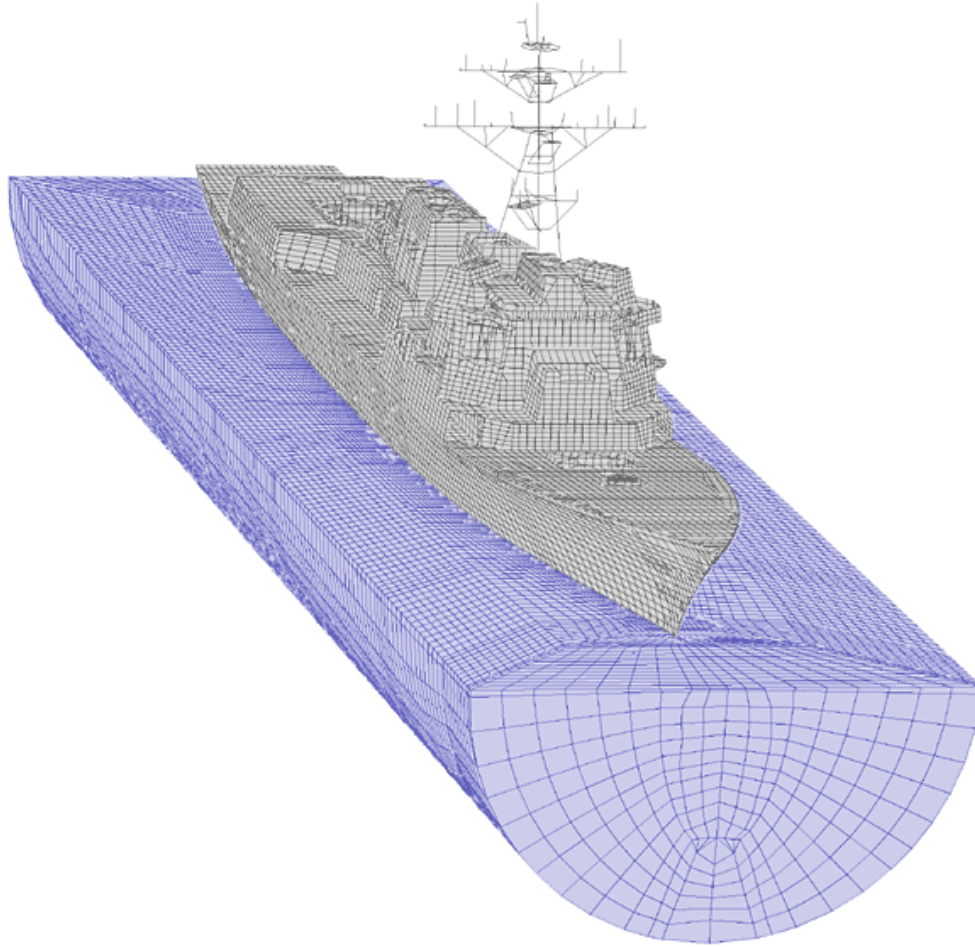


Figure 26. 1st Generation Fluid and Structural Model [from Ref. 21]

The cavitation depth model used in the study conducted in Reference [21] was constructed having a depth of 840 inches to account for the greatest cavitation depth, that depth at a point on the ship's keel furthest from the charge. The cavitation depth at the point on the keel closest to the charge was found to be only 738 inches for this shot. Simulations conducted using a similar model, but with a reduced depth, resulted in a decrease of over 0.01 in the average Russell's comprehensive error factor. This suggests that the simulation is particularly sensitive to small changes in the depth of the fluid modeled. This model was subsequently modified, retaining the initial inner liner and majority of the inner mesh while replacing the flat end caps with spherical end caps. This modification eliminated the need for multiple parts in the outer fluid mesh, facilitating more efficient modification of the outer fluid mesh, and improved the fluid model's applicability to a wider variety of underwater explosion geometries. No appreciable

change in the average Shot 3 error factors resulted from this modification. This 2nd generation model is shown in Figure 27.

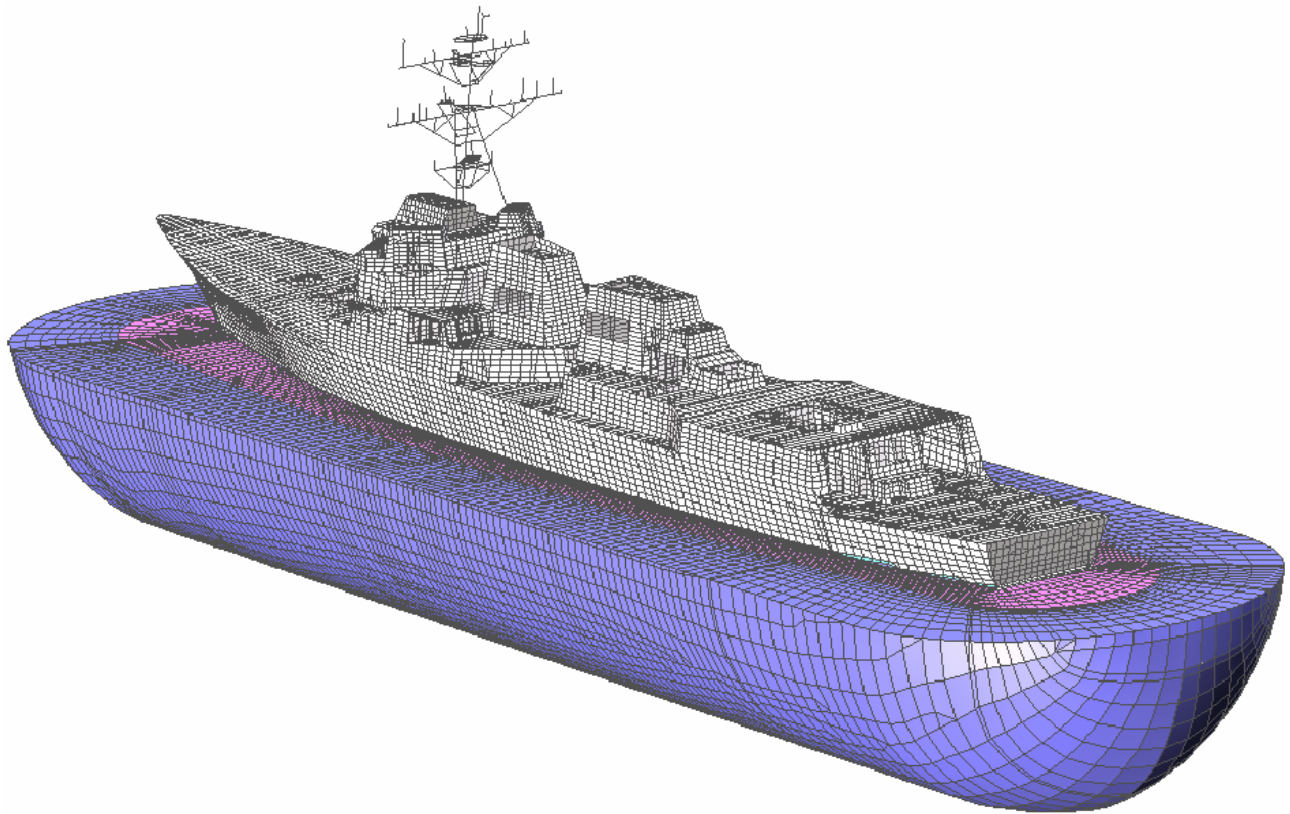


Figure 27. 2nd Generation Fluid and Structural Model

Table 10 summarizes the best correlation achieved using the model shown in Figure 27. This was done using a densely packed fluid mesh where the average hull normal spacing between elements was less than 12 inches. Compared with the original 1st generation model, the improvement in the average comprehensive error was over 0.02, a significant reduction.

Table 10. Summary of Prediction Error Measures Using Dense 2nd Generation Model

Sensor	NODE	Bulkhead Keel	Location (in)			Dense Fluid Mesh (2nd Generation Model)		
			x	y	z	RM	RP	RC
V2000V	120217	Keel	5328	0	82	-0.1968	0.2980	0.3165
V2002V	142489	Keel	4656	27	82	0.0612	0.2403	0.2197
V2007V	210430	Keel	4080	0	82	-0.1274	0.2875	0.2787
V2009VI	210808	Bulkhead	4080	-174	177	-0.0793	0.2145	0.2026
V2008VI	210894	Bulkhead	4080	174	177	-0.0124	0.2623	0.2327
A8516V	210993	Bulkhead	4080	239	202	0.1128	0.2551	0.2472
A4701V	211371	Bulkhead	4080	0	280	0.0080	0.2042	0.1811
V2107V	211904	Bulkhead	4080	-312	390	-0.0427	0.2205	0.199
V2108V	212196	Bulkhead	4080	312	390	-0.0344	0.2394	0.2143
V2010V	220589	Keel	3504	0	86	-0.1732	0.2630	0.2791
V2012VI	221102	Bulkhead	3504	-216	177	-0.0803	0.2054	0.1954
V2011VI	221188	Bulkhead	3504	216	177	-0.1594	0.2454	0.2593
V2013V	221601	Bulkhead	3504	0	280	-0.0366	0.2088	0.1878
V2124V	222060	Bulkhead	3504	-375	390	-0.1013	0.1833	0.1856
A2104V	222240	Bulkhead	3504	0	390	0.0109	0.1797	0.1596
V2125V	222436	Bulkhead	3504	375	390	-0.1453	0.2280	0.2396
V2014V	230461	Keel	2952	0	86	-0.0992	0.2565	0.2438
A3565V	231696	Bulkhead	2952	-81	317	0.0492	0.1847	0.1694
V2016V	242399	Keel	2544	0	116	-0.1050	0.2235	0.2189
V2026V	312302	Keel	1992	0	55	-0.1334	0.2228	0.2302
A2310V	320746	Bulkhead	1536	0	177	-0.0970	0.1496	0.1580
V2034V	330759	Keel	1152	-135	193	-0.0704	0.1439	0.1419
V2032V	330764	Keel	1152	0	196	-0.1305	0.2247	0.2303
V2035V	330769	Keel	1152	135	193	-0.1447	0.2189	0.2325
V2019V	340167	Keel	672	0	197	0.0053	0.2771	0.2456
V2018VI	340992	Bulkhead	672	0	365	0.0539	0.2710	0.2449
V2020V*	350052	Keel	288	0	211	-0.0801	0.2422	0.2261
A2413V	350220	Bulkhead	288	0	273	-0.0602	0.2351	0.2151
A2116V	414367	Bulkhead	3504	0	702	0.0175	0.1749	0.1557
A2109V	414953	Bulkhead	4059	0	723	0.1189	0.1801	0.1913
A2240V	416269	Bulkhead	3504	-135	848	-0.0034	0.1697	0.1504
A2237V	416419	Bulkhead	3504	135	848	0.0382	0.1855	0.1678
Sum(E(X))						-1.63710	7.09560	6.82010
Sum(E(X ²))						0.29793	1.62116	1.50719
Mean						-0.05116	0.22174	0.21313
Variation						0.00691	0.00154	0.00173

* 350 msec comparison due to long time sensor data inaccuracy

2. Fluid Mesh Quality

After several simulations were conducted and compared using the 2nd generation model, a 3rd generation model was developed in an attempt to improve the simulation predictions. Retaining only the inner liner from the first two models, this model focused on eliminating the “trouble spots” on the 1st and 2nd generation models where the fluid

mesh was extremely non-uniform, particularly the areas surrounding the sonar dome and skeg as shown in Figures 28 and 29. This fluid mesh also utilized the interpolation methods discussed in Chapter IV more heavily than the first two models. The end result is that this model had an improved mesh quality over the previous two models.

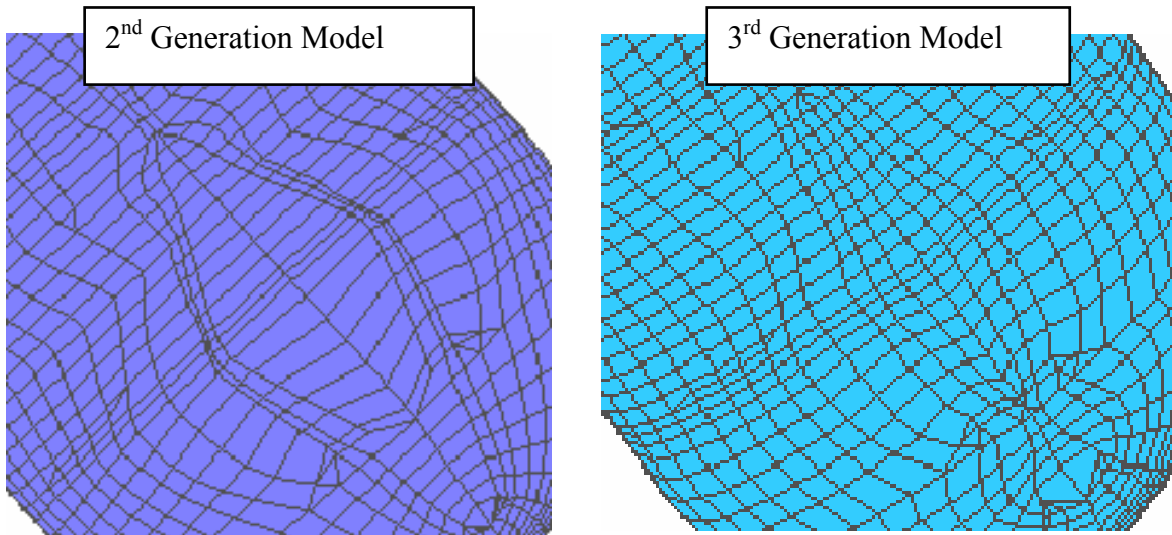


Figure 28. Sonar Dome Region Showing Improvement in Mesh Uniformity of 3rd Generation Fluid Model.

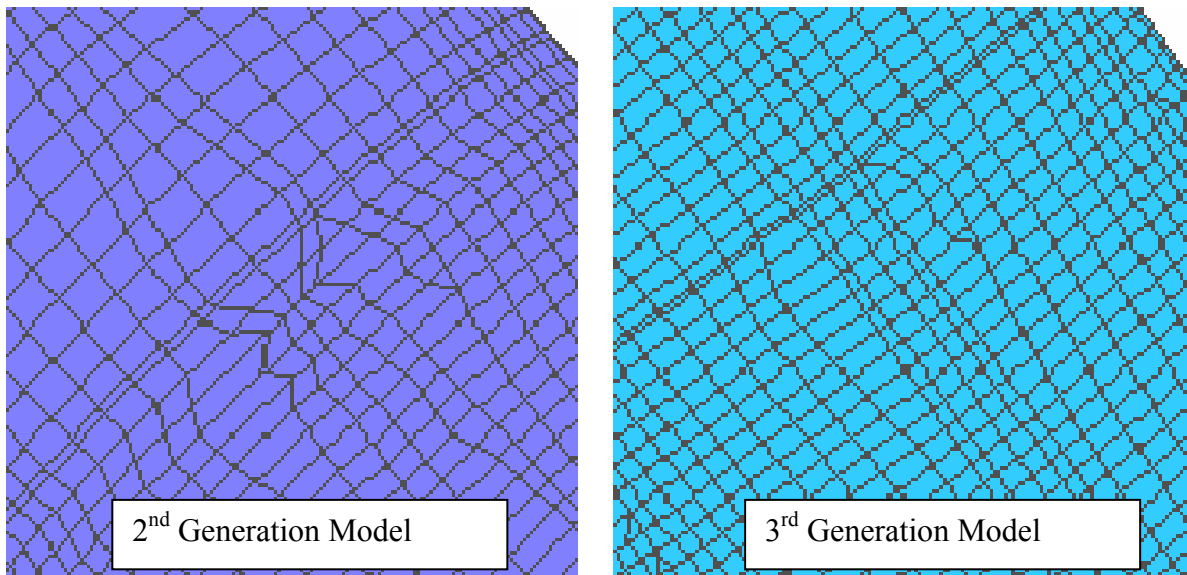


Figure 29. Keel Region Showing Improvement in Mesh Uniformity of 3rd Generation Fluid Model

The comparison of the 2nd generation model simulation was summarized in Table 10. Table 11 is a summary of the comparable 3rd generation model comparison. A graphical comparison of the comprehensive error trendlines is shown with respect to location on the ship in Figure 30.

Table 11. Summary of Simulation Error Measures using Dense 3rd Generation Model

Sensor	NODE	Bulkhead Keel	Location (in)			Dense Fluid Mesh (3rd Generation Model)		
			x	y	z	RM	RP	RC
V2000V	120217	Keel	5328	0	82	-0.1795	0.2842	0.2979
V2002V	142489	Keel	4656	27	82	0.0762	0.2303	0.2150
V2007V	210430	Keel	4080	0	82	-0.1198	0.2883	0.2766
V2009VI	210808	Bulkhead	4080	-174	177	-0.0690	0.2144	0.1996
V2008VI	210894	Bulkhead	4080	174	177	0.0014	0.2561	0.2270
A8516V	210993	Bulkhead	4080	239	202	0.1217	0.2547	0.2502
A4701V	211371	Bulkhead	4080	0	280	0.0282	0.2149	0.1921
V2107V	211904	Bulkhead	4080	-312	390	-0.0295	0.2420	0.2161
V2108V	212196	Bulkhead	4080	312	390	-0.0216	0.2348	0.2089
V2010V	220589	Keel	3504	0	86	0.1353	0.1846	0.2028
V2012VI	221102	Bulkhead	3504	-216	177	-0.1729	0.2549	0.2730
V2011VI	221188	Bulkhead	3504	216	177	-0.0777	0.1935	0.1848
V2013V	221601	Bulkhead	3504	0	280	-0.1468	0.2398	0.2468
V2124V	222060	Bulkhead	3504	-375	390	-0.0342	0.1970	0.1772
A2104V	222240	Bulkhead	3504	0	390	-0.0872	0.1882	0.1838
V2125V	222436	Bulkhead	3504	375	390	0.0207	0.1760	0.1571
V2014V	230461	Keel	2952	0	86	-0.1264	0.2264	0.2298
A3565V	231696	Bulkhead	2952	-81	317	0.0353	0.1789	0.1616
V2016V	242399	Keel	2544	0	116	0.0122	0.1747	0.1552
V2026V	312302	Keel	1992	0	55	0.0613	0.1877	0.1750
A2310V	320746	Bulkhead	1536	0	177	-0.0861	0.2501	0.2344
V2034V	330759	Keel	1152	-135	193	0.0646	0.2003	0.1865
V2032V	330764	Keel	1152	0	196	-0.0879	0.2085	0.2005
V2035V	330769	Keel	1152	135	193	-0.0910	0.2312	0.2202
V2019V	340167	Keel	672	0	197	-0.1037	0.1635	0.1716
V2018VI	340992	Bulkhead	672	0	365	-0.0966	0.1537	0.1608
V2020V*	350052	Keel	288	0	211	-0.1534	0.2103	0.2307
A2413V	350220	Bulkhead	288	0	273	-0.1598	0.2233	0.2434
A2116V	414367	Bulkhead	3504	0	702	-0.1344	0.2266	0.2335
A2109V	414953	Bulkhead	4059	0	723	-0.1212	0.1830	0.1945
A2240V	416269	Bulkhead	3504	-135	848	-0.1499	0.2178	0.2343
A2237V	416419	Bulkhead	3504	135	848	-0.1315	0.2150	0.2233
Sum(E(X))						-1.82320	6.90470	6.76420
Sum(E(X ²))						0.34947	1.52398	1.47020
Mean						-0.05698	0.21577	0.21138
Variation						0.00792	0.00110	0.00130

* 350 msec comparison due to long time sensor data inaccuracy

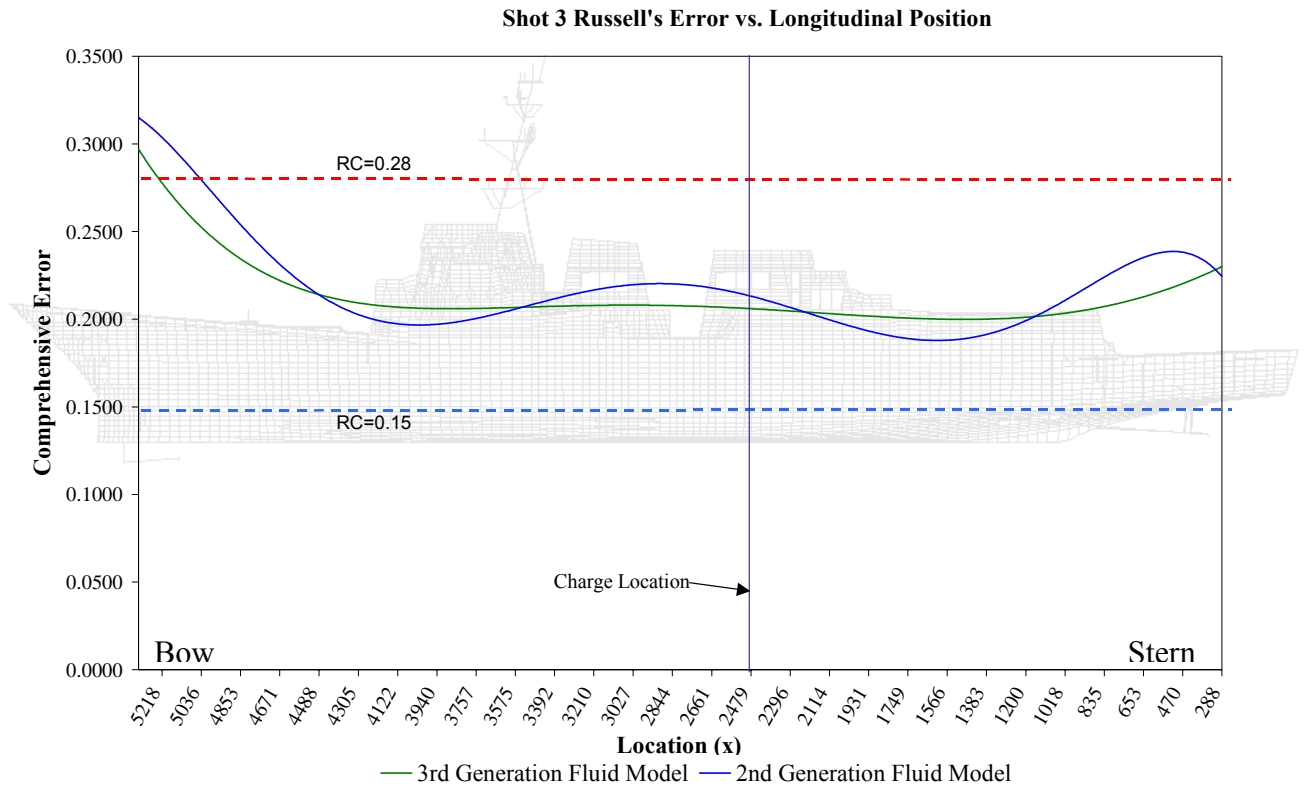


Figure 30. Comparison of 2nd and 3rd Generation Fluid Model Errors in Relation to Longitudinal Position on the Structural Model.

From Tables 10 and 11 and the comparison in Figure 30, the results from this quality comparison are inconclusive. The average comprehensive error difference is less than 0.002, a relatively insignificant amount. Notable improvement in the error factor is shown in the regions around the sonar dome and the stern area, all areas where significant improvements were made to the mesh. However, the 2nd generation model had smaller errors in other regions of the structure. These inconsistencies indicate that other variables, such as data processing, sensor error, and environmental factors, have more of an effect on simulation error factors than small variations in the quality of the fluid model mesh. Figures 31 through 33 show three of the areas with the largest variations in error factors. With the exception of the sonar dome region, where the 3rd generation model does a better job of capturing the initial peak magnitude, the primary difference lies in the late time response. This is to be expected, since improving the mesh quality should have an affect primarily on the ability to simulate cavitation which occurs after this initial peak response.

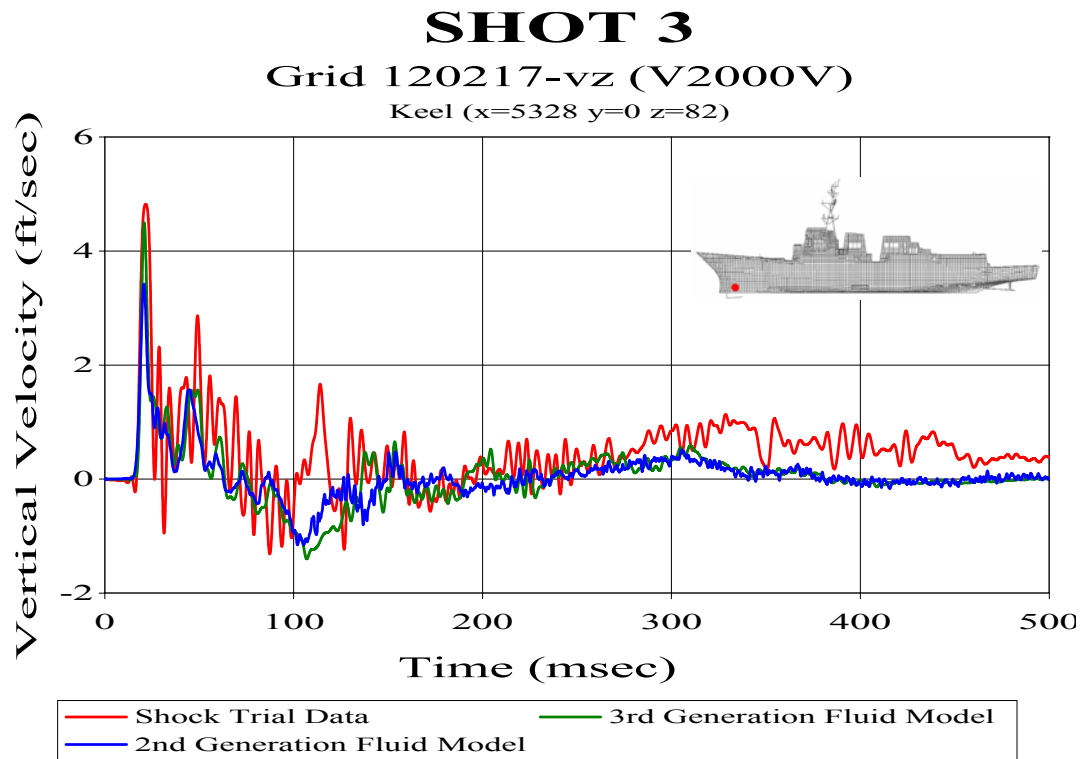


Figure 31. Sonar Dome Region Velocity Plot Comparison

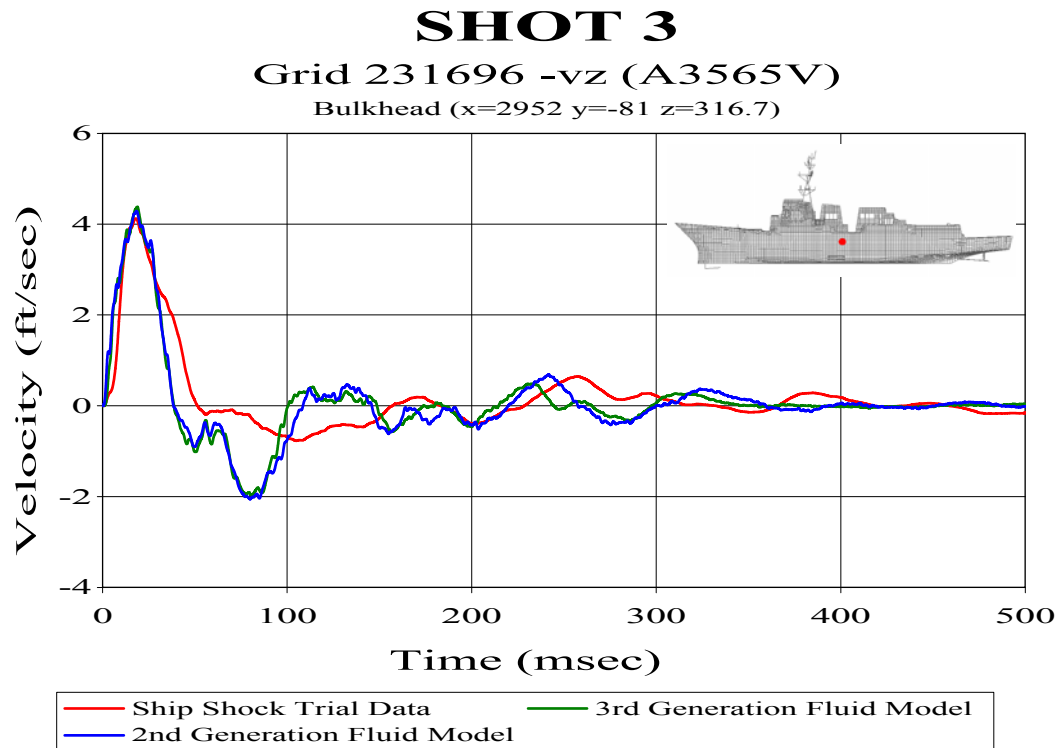


Figure 32. Midship Region Velocity Plot Comparison

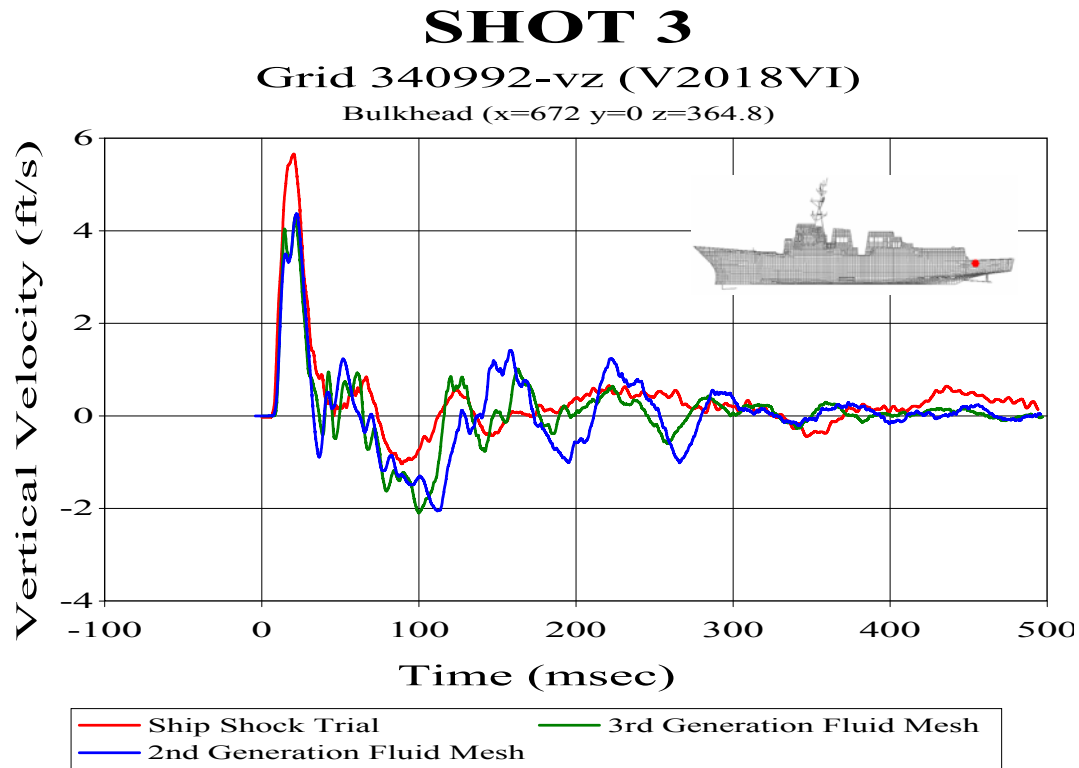


Figure 33. Stern Region Velocity Plot Comparison

3. Fluid Mesh Density

The accuracy of a finite element model (FEM) in predicting the dynamic response of a structure is improved by increasing the number elements used to model that structure. As illustrated in Figure 34, this improvement in accuracy due to increasing the number of elements is usually quite large with a relatively small number of elements and decreases to becoming insignificant with a relatively large number of elements. It would stand to reason then that the accuracy of the fluid mesh FEM would be improved by increasing the number of elements in the model. For purposes of this discussion, the number of elements is not the total number of elements in the model. If looking at a two-dimensional cross sectional cut of the fluid-structure model, the number of elements in the fluid would be the number of elements in each mesh line extending outward in a normal direction from the hull.

Three fluid mesh FEM's of varying densities were modeled for Shot 3. All of the models maintained the same thickness of the inner two layers. The inner mesh and transitional mesh were varied from each having five to seven elements in the normal

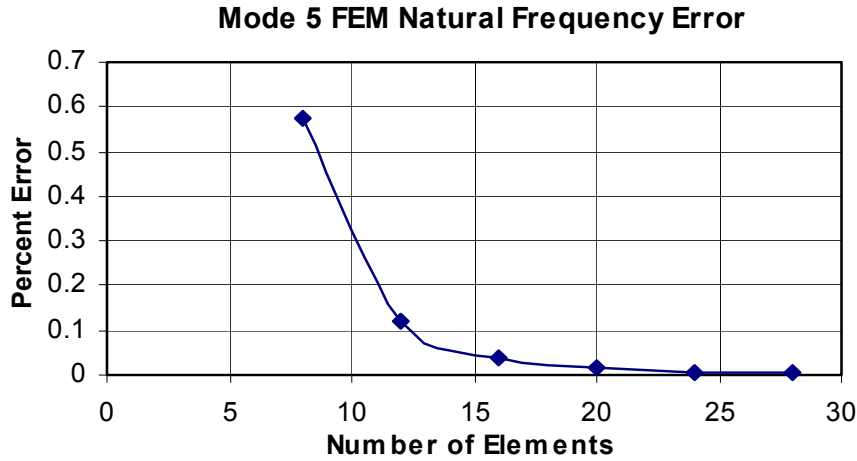


Figure 34. Natural Frequency Error of FEM Pin-Pin Beam as a Function of Number of Elements Used.

direction. The outer mesh was varied from having as few as 8 elements to as many as 23 elements in the normal direction. Table 12 lists a summary of the properties for each fluid model constructed for Shot 3.

Table 12. Shot 3 Fluid Model Properties

Property	Coarse Mesh	Medium Mesh	Dense Mesh
Inner Mesh Elements	5	6	7
Inner Mesh Element Spacing (Ave.)	11.4 in	10.0 in	9.3 in
Transition Mesh Elements	5	6	7
Transition Mesh Element Spacing (Ave.)	13.4 in	11.6 in	10.1 in
Outer Mesh Elements	8	14	23
Outer Mesh Element Spacing (Ave.)	36 in	20 in	12 in
Fluid Nodes	150,607	197,429	250,181
DAA Elements	5048	5090	5132
Simulation Run Time	32.5 hrs	34.1 hrs	37.3 hrs

To avoid a sharp transition in the spacing of the elements in the coarse and medium fluid meshes, the outer mesh element spacing was graduated from smallest on the inner boundary to largest on the outer boundary. This was not required for the dense

mesh. Table 12 lists the simulation run time. As shown, it took nearly five additional hours to run the dense model than the coarse model.

a. Error Comparison

The Russell's error factors are summarized in Figures 35 through 37.

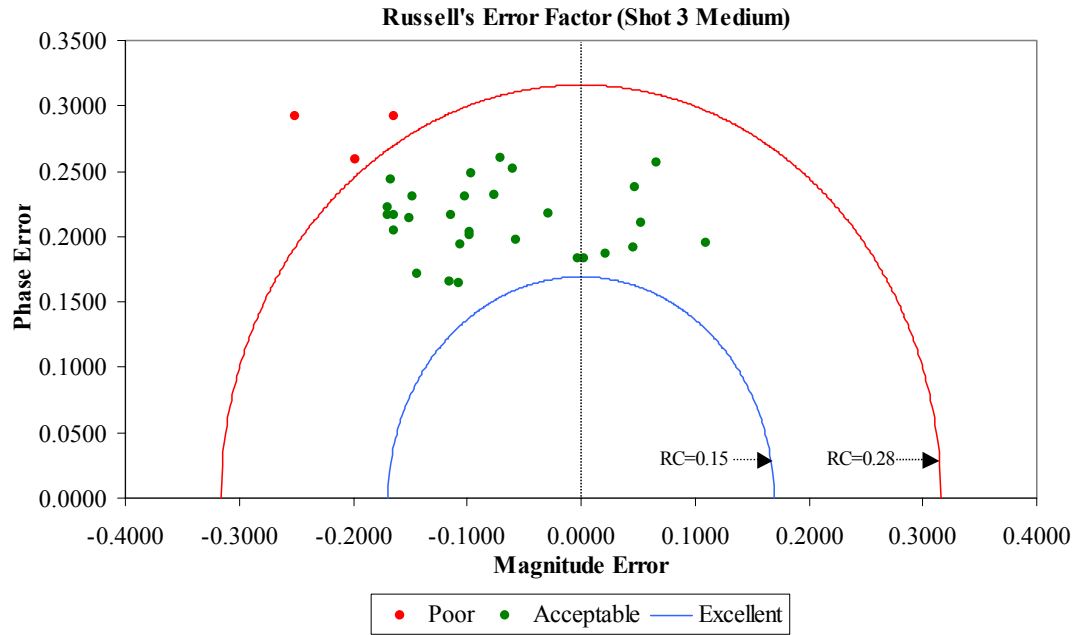


Figure 35. Russell's Error Factors for Coarse Mesh Fluid Model Comparison

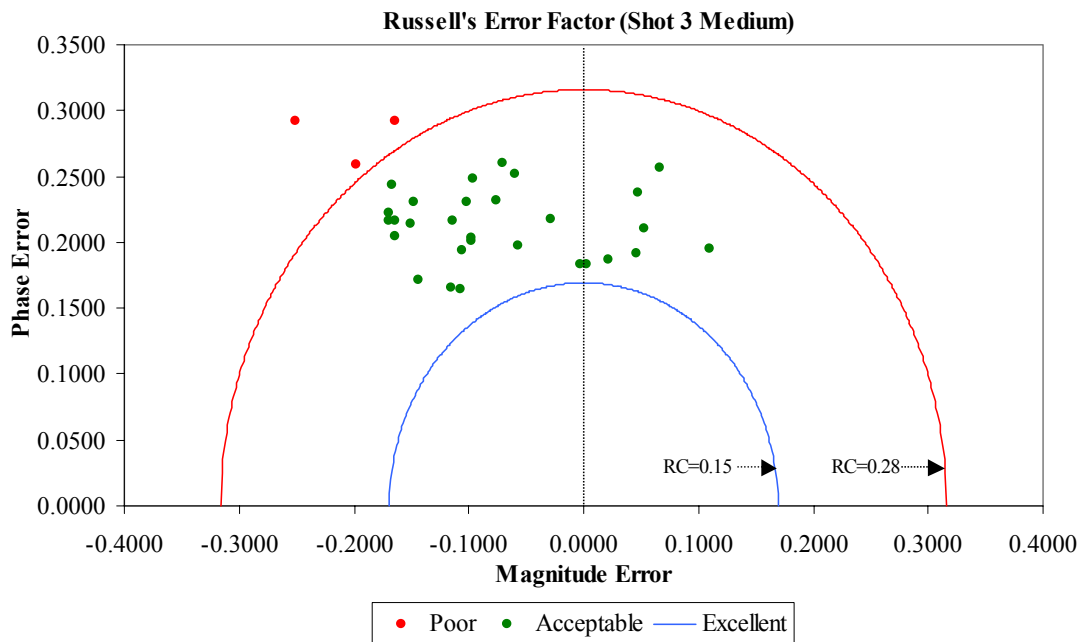


Figure 36. Russell's Error Factors for Medium Mesh Fluid Model Comparison

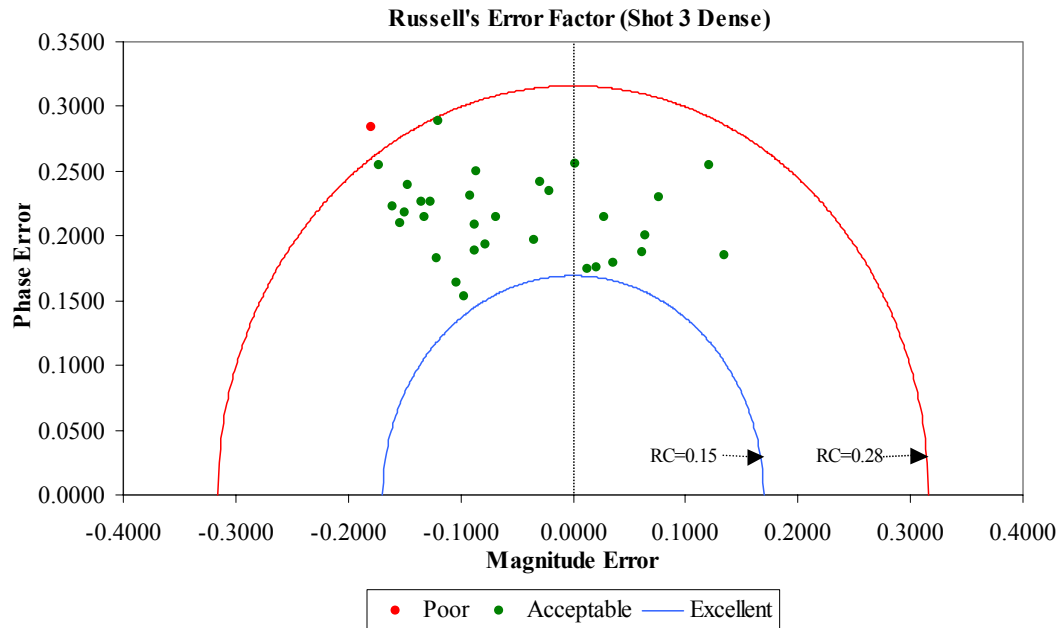


Figure 37. Russell's Error Factors for Dense Mesh Fluid Model Comparison

The most significant change occurs between the dense and the medium mesh fluid model comparisons. The large number of negative magnitude error factors is indicative of the predicted response magnitude being lower than the measured response magnitude. The trend when increasing the density of the fluid mesh is that the errors tend to move primarily to the right and slightly downward. This indicates that the predicted response magnitude is increasing as the density of the mesh is increased. At the same time, though not as pronounced, the phase error is decreasing as the mesh density is increased.

Table 13 lists all of the sensors compared and their corresponding Russell's error factors. The averages for each error factor are shown at the bottom of their respective columns along with the variation. These averages show that the dense mesh does in fact have lower overall magnitude, phase, and comprehensive error factor. In addition, the largest reduction in these error factors occurs between the medium and dense fluid mesh comparisons where the most significant improvement is in the magnitude error.

Table 13. Shot 3: Russell's Error Factor.

Sensor	NODE	Bulkhead Keel	Location (in)			Coarse Mesh			Medium Mesh			Dense Mesh		
			x	y	z	RM	RP	RC	RM	RP	RC	RM	RP	RC
V2000V	120217	Keel	5328	0	82	-0.2872	0.2836	0.3577	-0.2507	0.2925	0.3414	-0.1795	0.2842	0.2979
V2002V	142489	Keel	4656	27	82	0.0362	0.2411	0.2160	0.0468	0.2378	0.2148	0.0762	0.2303	0.2150
V2007V	210430	Keel	4080	0	82	-0.1806	0.2952	0.3067	-0.1647	0.2923	0.2973	-0.1198	0.2883	0.2766
V2009VI	210808	Bulkhead	4080	-174	177	-0.1273	0.2280	0.2315	-0.1145	0.2167	0.2172	-0.0690	0.2144	0.1996
V2008VI	210894	Bulkhead	4080	174	177	-0.0789	0.2530	0.2348	-0.0593	0.2520	0.2294	0.0014	0.2561	0.2270
A8516V	210993	Bulkhead	4080	239	202	0.0520	0.2609	0.2358	0.0667	0.2571	0.2354	0.1217	0.2547	0.2502
A4701V	211371	Bulkhead	4080	0	280	-0.0464	0.2229	0.2017	-0.0284	0.2181	0.1949	0.0282	0.2149	0.1921
V2107V	211904	Bulkhead	4080	-312	390	-0.0813	0.2794	0.2579	-0.0710	0.2596	0.2385	-0.0295	0.2420	0.2161
V2108V	212196	Bulkhead	4080	312	390	-0.0886	0.2329	0.2208	-0.0766	0.2320	0.2165	-0.0216	0.2420	0.2089
V2010V	220589	Keel	3504	0	86	-0.2085	0.2582	0.2941	-0.1973	0.2589	0.2885	-0.1729	0.2549	0.2730
V2012VI	221102	Bulkhead	3504	-216	177	-0.1123	0.2027	0.2054	-0.0983	0.2016	0.1987	-0.0777	0.1935	0.1848
V2011VI	221188	Bulkhead	3504	216	177	-0.1675	0.2473	0.2647	-0.1666	0.2435	0.2615	-0.1468	0.2398	0.2468
V2013V	221601	Bulkhead	3504	0	280	-0.0563	0.1975	0.1820	-0.0563	0.1975	0.1820	-0.0342	0.1970	0.1772
V2124V	222060	Bulkhead	3504	-375	390	-0.1146	0.1961	0.2013	-0.1059	0.1938	0.1957	-0.0872	0.1882	0.1838
A2104V	222240	Bulkhead	3504	0	390	-0.0020	0.1886	0.1672	0.0022	0.1834	0.1625	0.0207	0.1760	0.1571
V2125V	222436	Bulkhead	3504	375	390	-0.1480	0.2335	0.2450	-0.1473	0.2302	0.2422	-0.1264	0.2264	0.2298
V2014V	230461	Keel	2952	0	86	-0.0989	0.2522	0.2401	-0.0966	0.2484	0.2362	-0.0861	0.2501	0.2344
A3565V	231696	Bulkhead	2952	-81	317	0.0498	0.2130	0.1939	0.0525	0.2103	0.1921	0.0646	0.2003	0.1865
V2016V	242399	Keel	2544	0	116	-0.0935	0.2085	0.2025	-0.0982	0.2035	0.2003	-0.0879	0.2085	0.2005
V2026V	312302	Keel	1992	0	55	-0.1092	0.2318	0.2271	-0.1018	0.2306	0.2234	-0.0910	0.2312	0.2202
A2310V	320746	Bulkhead	1536	0	177	-0.1177	0.1789	0.1898	-0.1159	0.1653	0.1789	-0.1037	0.1635	0.1716
V2034V	330759	Keel	1152	-135	193	-0.1162	0.1713	0.1835	-0.1073	0.1648	0.1743	-0.0966	0.1537	0.1608
V2032V	330764	Keel	1152	0	196	-0.1666	0.2039	0.2333	-0.1634	0.2041	0.2317	-0.1534	0.2103	0.2307
V2035V	330769	Keel	1152	135	193	-0.1724	0.2242	0.2507	-0.1701	0.2226	0.2483	-0.1598	0.2233	0.2434
V2019V	340167	Keel	672	0	197	-0.1588	0.2319	0.2491	-0.1647	0.2166	0.2411	-0.1344	0.2266	0.2335
V2018VI	340992	Bulkhead	672	0	365	-0.1352	0.1858	0.2036	-0.1435	0.1711	0.1979	-0.1212	0.1830	0.1945
V2020V*	350052	Keel	288	0	211	-0.2000	0.2134	0.2592	-0.1697	0.2165	0.2438	-0.1499	0.2178	0.2343
A2413V	350220	Bulkhead	288	0	273	-0.1804	0.2132	0.2475	-0.1507	0.2144	0.2323	-0.1315	0.2150	0.2233
A2116V	414367	Bulkhead	3504	0	702	0.0195	0.1918	0.1709	0.0211	0.1865	0.1664	0.0353	0.1789	0.1616
A2109V	414953	Bulkhead	4059	0	723	0.1052	0.2052	0.2052	0.1093	0.1949	0.1981	0.1353	0.1846	0.2028
A2240V	416269	Bulkhead	3504	-135	848	-0.0059	0.1888	0.1674	-0.0024	0.1831	0.1623	0.0122	0.1747	0.1552
A2237V	416419	Bulkhead	3504	135	848	0.0464	0.1962	0.1787	0.0460	0.1920	0.1750	0.0613	0.1877	0.1750
Sum(E(X))						-2.94520	7.13100	7.22510	-2.67660	6.99170	7.01860	-1.82320	6.91190	6.76420
Sum(E(X^2))						0.52795	1.61991	1.68734	0.46380	1.56144	1.59066	0.34947	1.52742	1.47020
Mean						-0.09204	0.22284	0.22578	-0.08364	0.21849	0.21933	-0.05698	0.21600	0.21138
Variation						0.00829	0.00099	0.00181	0.00774	0.00109	0.00165	0.00792	0.00111	0.00130

*350msec comparison due to long time sensor data inaccuracy.

Of particular interest in Table 13 are the errors associated with the accelerometer data (indicated by a sensor number preceded by an “A”). As a whole, the errors associated with these sensors are significantly lower than the velocity meters. This gives evidence that perhaps a large portion of the error measurement is actually error in the measured data.

Figure 38 is a plot of the cumulative Russell’s error factor trend for each fluid model as a function of the longitudinal position. .

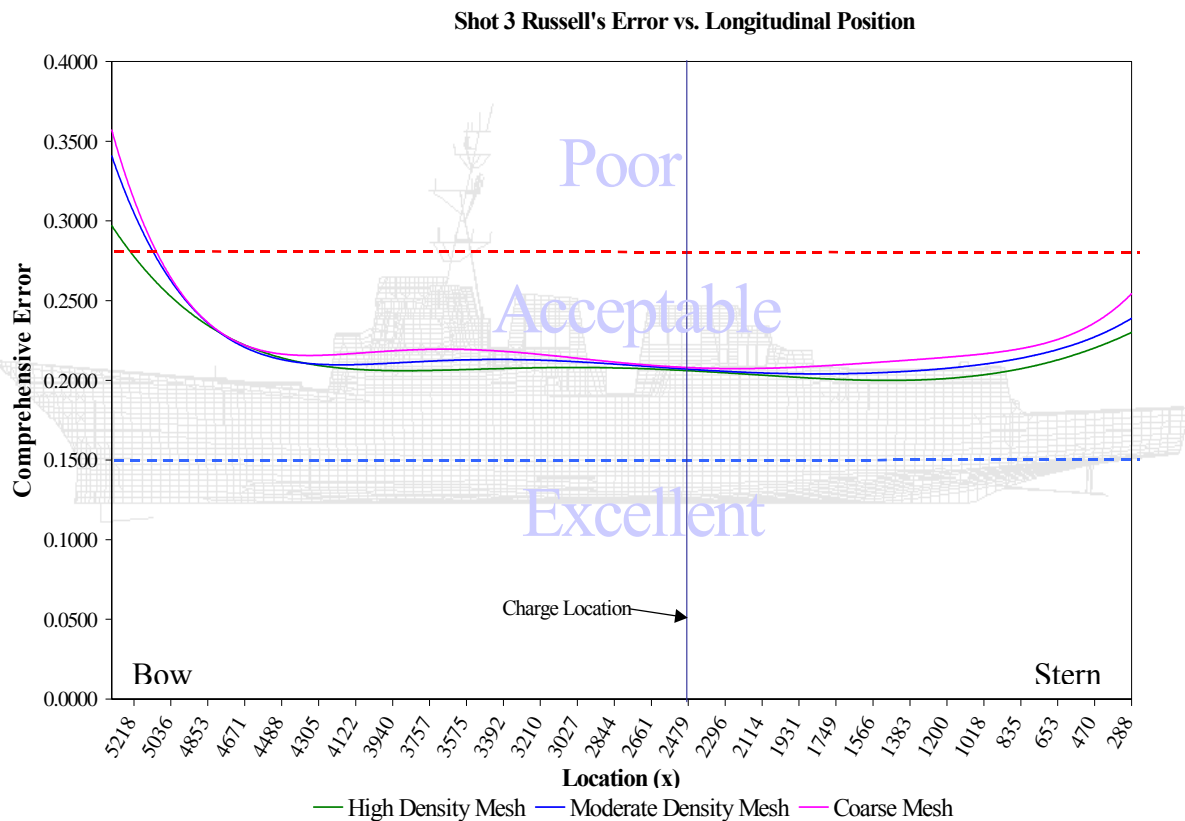


Figure 38. Russell’s Comprehensive Error Trend as a Function of Longitudinal Position

For Shot 3, the shock wave initially impacts the structure at midships. Since the shock wave initiates at a node one element away from this point of impact, it propagates through very little of the fluid model before reaching the structure. The remainder of the structure, particularly the stern and bow sections, are not impacted until the shock wave has propagated through more of the fluid and structural model. The

resulting error is reduced by increasing the normal direction mesh density, but not eliminated as shown in Figure 38. In terms of fluid mesh density comparison, it is apparent that the mesh density has the largest effect in these outer regions. Very little noticeable improvement is shown in the regions closest to the charge location.

b. Velocity Plots

It is useful to observe the velocity plots to help visualize how the predicted response varies as the fluid mesh density is increased. Figure 39 shows the predicted and measured 500 msec velocity response plots for sensor V2000V. This sensor is the forward most sensor, located above the sonar dome. This sensor resulted in the greatest comprehensive error in all three cases. From this plot it is evident that at least some of this error is due to the late time drift in the sensor. This drift was significant and could not be removed.

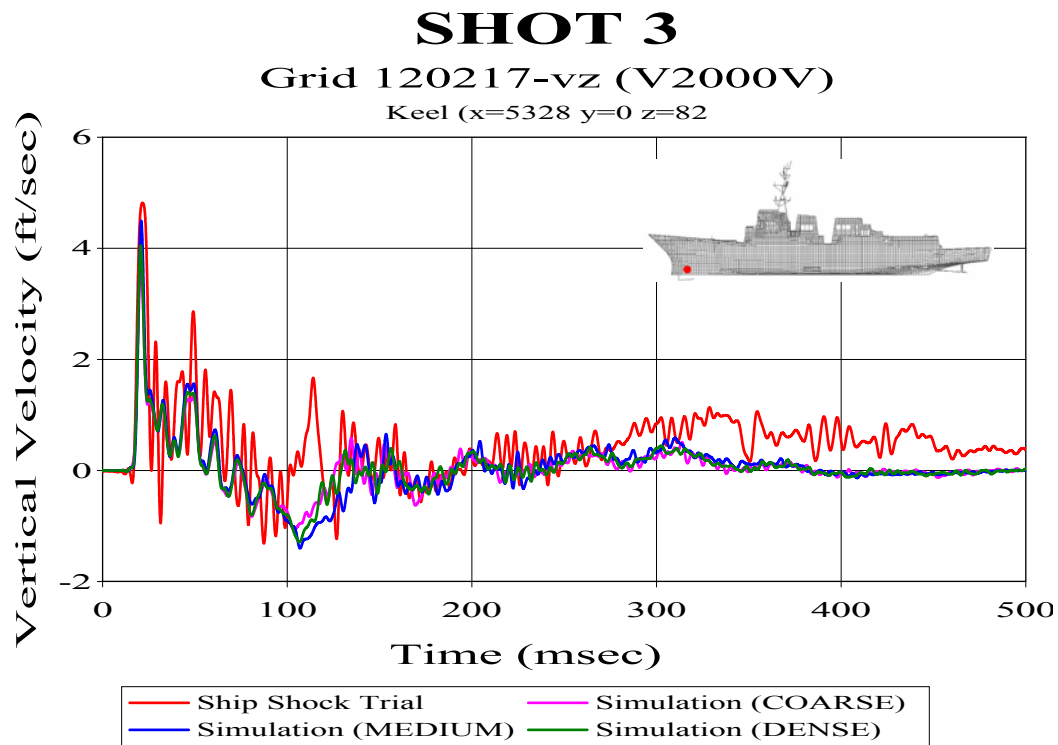


Figure 39. Keel Sensor V2000V.

Figure 40 shows the velocity response plots for keel sensor V2016V. This sensor is significant as it is the closest sensor to the charge. This plot shows much better agreement between the predicted and measured response, having a comprehensive error

factor of around 0.20 for all three fluid models. This plot also shows how the late time predicted response settles out similarly to the measured response. This is a measure of the quality of the structural damping coefficients which appear to be very accurate in this case.

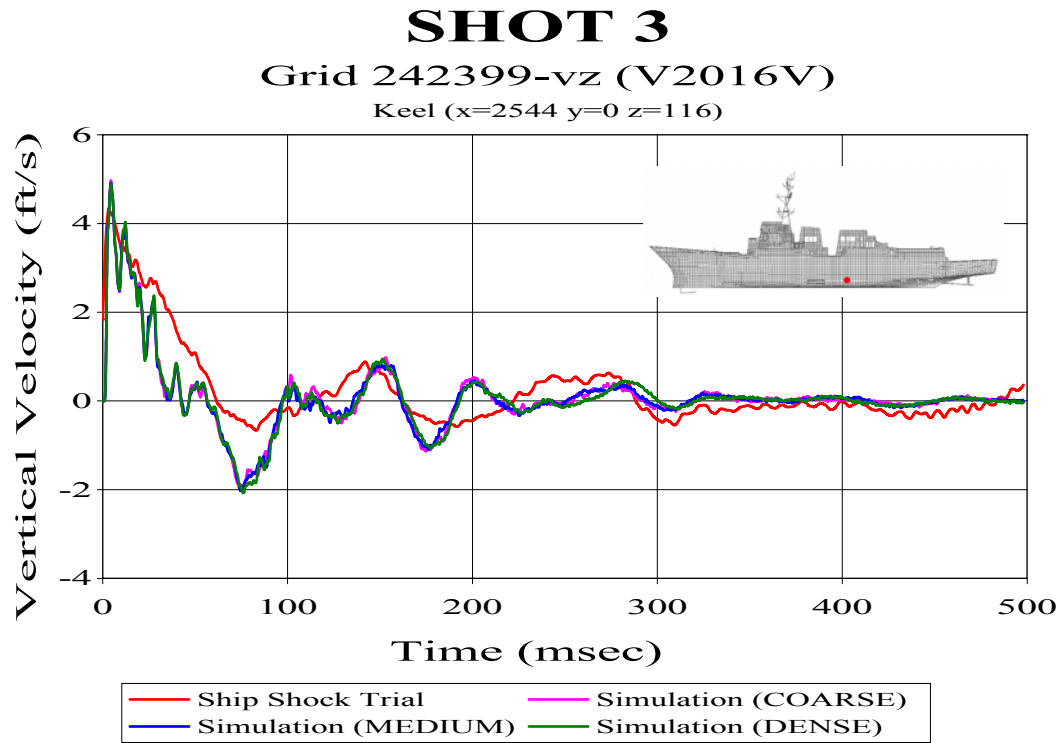


Figure 40. Keel Sensor V2016V

The third sensor shown is keel sensor V2020V shown in Figure 41. This sensor is one of the furthest aft sensors, located at frame 442. Due to excessive drift in the last portion of the sensor data only 350 msec of data was compared. Though better than sensor V2000V, this sensor shows how there are apparent transmission losses in the shock wave as it propagates outward through the fluid and structural model. Here the predicted late time response is in better agreement than the early time response. As in Figure 40, this is evidence of accurate structural damping.

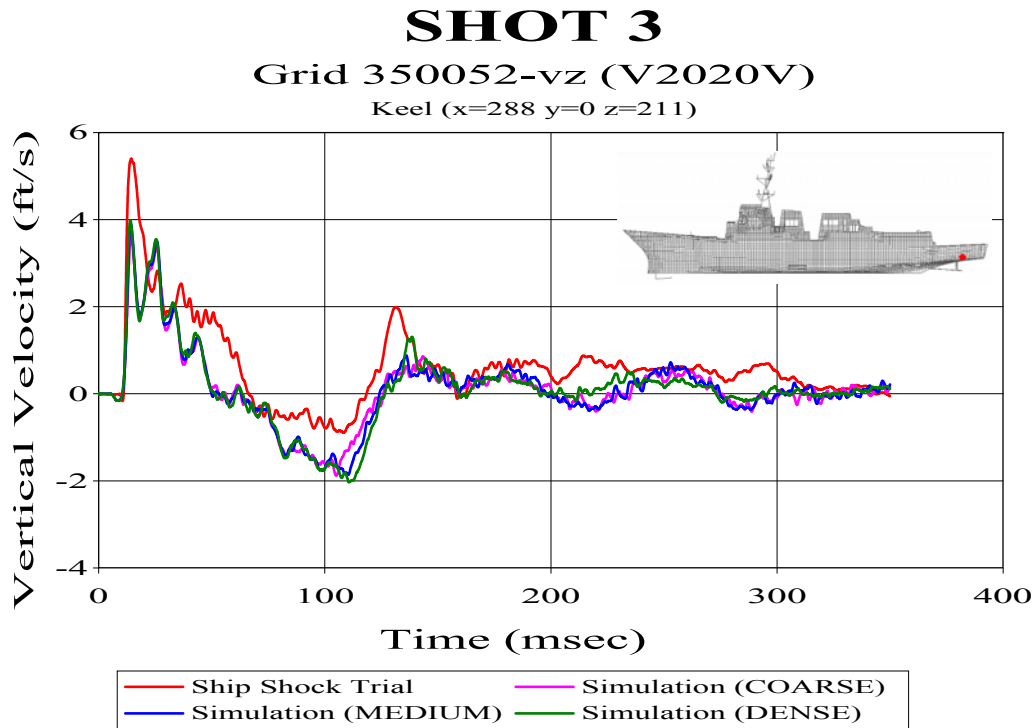


Figure 41. Keel Sensor V2020V

Figure 42 shows bulkhead sensor V2124V. This sensor is bulkhead mounted on the starboard side, just forward of midships. Located higher in the structure than the four sensors shown above, this plot shows how the structure dampens the shock wave as it passes through. The response is more linear and settles down more rapidly than the keel response. This plot shows good agreement, both in phase and magnitude, between the measured and predicted velocity responses. The cumulative Russell's error factor for this comparison was 0.1838 for the dense fluid mesh, 0.1957 for the medium density fluid mesh, and 0.2013 for the coarse fluid mesh.

The velocity plot shown in Figure 43 uses integrated acceleration data from sensor A2240V located on the starboard mast leg. This sensor had the best correlation between measured and predicted response of all sensors compared for this shot. The comprehensive error factor of the comparison using the dense mesh was 0.1552. Most of the comparisons utilizing data gathered using accelerometers showed results similar to this. Several additional Shot 3 velocity plots are included in Appendix A.

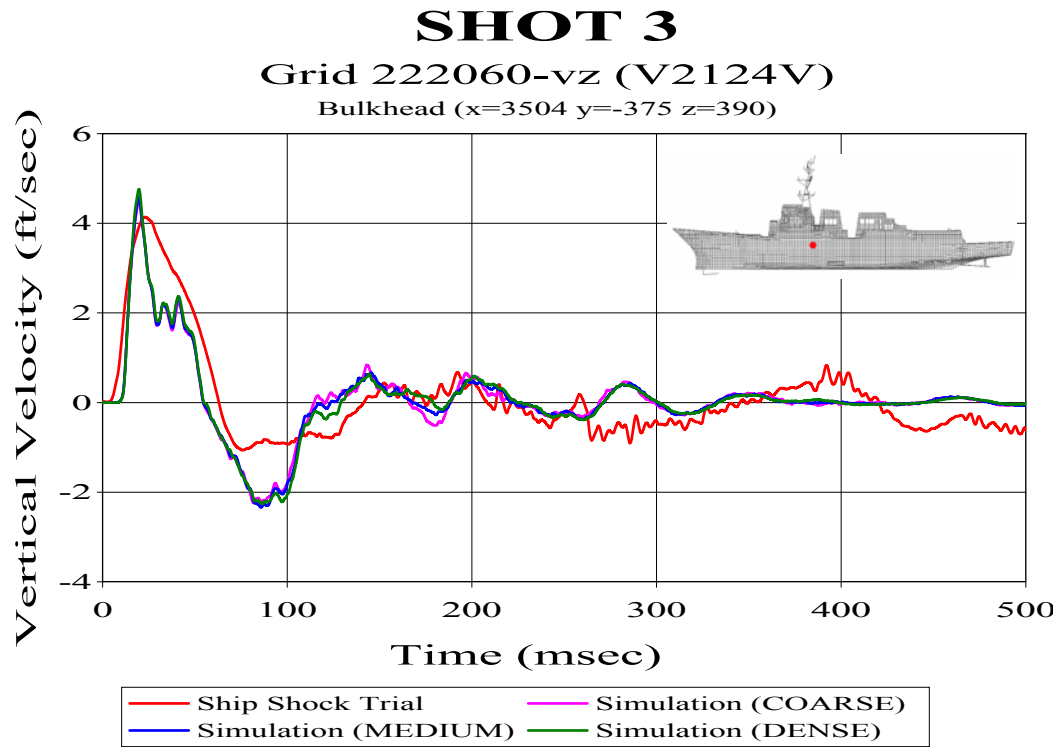


Figure 42. Bulkhead Sensor V2124V

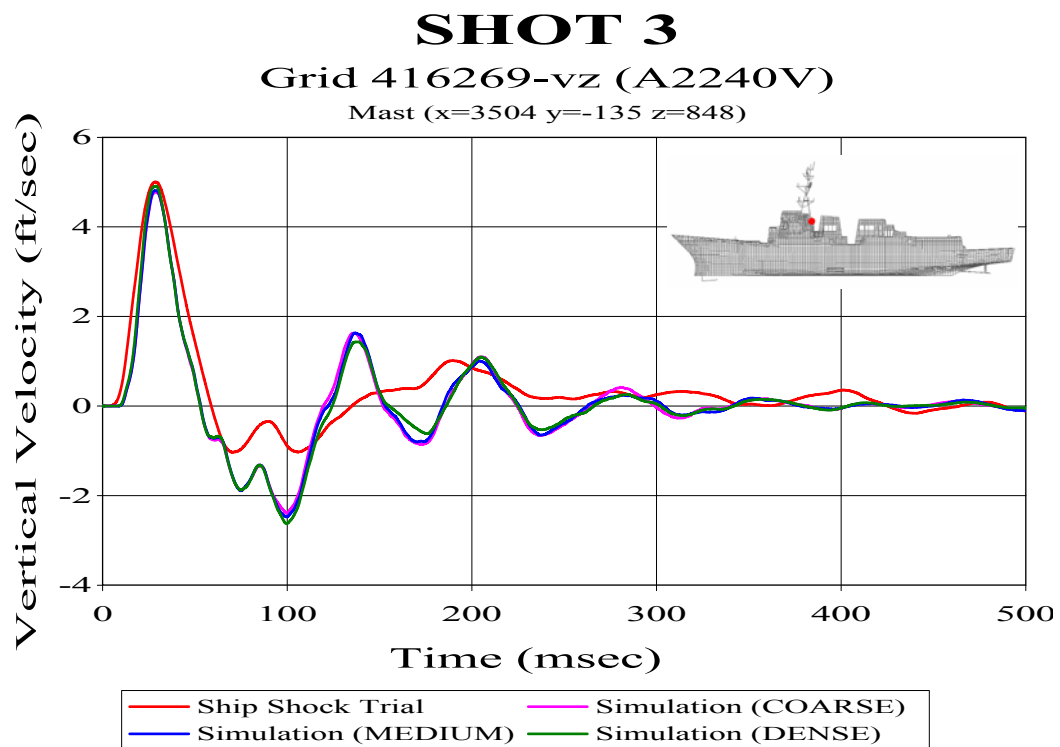


Figure 43. Mast Sensor A2240V

C. SHOT 1

The first shot, though the least severe, presented an interesting comparison due to its geometry. This shot was detonated outside of its intended box off the ships port bow, its longitudinal position actually forward of the ship. Figure 44 shows the relative aspect of this shot to the ship.

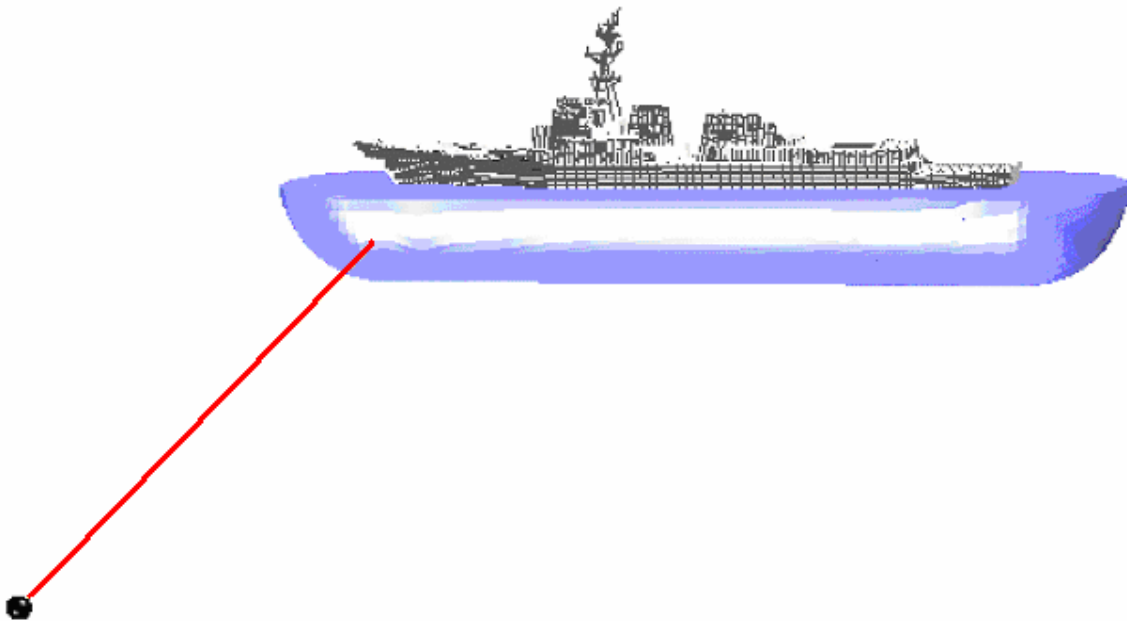


Figure 44. Shot 1 Geometry. Most Extreme Aspect

1. Fluid Mesh Depth

The first Shot 1 simulation was conducted and compared using the 1st generation fluid model shown in Figure 26. This model was constructed having a maximum depth of 70 feet. The actual cavitation depth for Shot 1 at the point closest to the charge location was found to be 75 feet.

The average Russell's comprehensive error factor was found to be 0.27179 using the 1st generation 70-foot depth fluid model. The 2nd generation Shot 1 fluid model was constructed with a maximum depth of 75 feet. A comparison of this model showed that the average Russell's comprehensive error factor was reduced to 0.21627. The majority

of this comprehensive improvement was due to the magnitude error which was reduced from 0.14389 down to -0.01656. The average phase error was reduced from 0.25849 down to 0.21886, a significant improvement as well. Further study showed that the majority of this improvement was due primarily due to the change in depth. The modification of the shape of the outer boundary from having flat ends to having spherical ends also contributed to this improvement. Table 14 lists the error factors for all of the sensors compared using both models.

Table 14. Shot 1 Russell Error Factors With Varying Fluid Model Depth

Sensor	NODE	Bulkhead Keel	Location (in)			Shot 1 - 840 inch			Shot 1- 900 inch		
			x	y	z	RM	RP	RC	RM	RP	RC
V2000V	120217	Keel	5328	0	82	0.1397	0.1803	0.2022	0.0453	0.1744	0.1597
V2002V	142489	Keel	4656	27	82	0.0719	0.4053	0.3648	-0.0975	0.2899	0.2711
A8516V	210993	Bulkhead	4080	239	202	0.2314	0.2414	0.2964	0.0062	0.2055	0.1822
V2008VI	210894	Bulkhead	4080	174	177	0.2479	0.3099	0.3517	0.0578	0.2692	0.2440
V2007V	210430	Keel	4080	0	82	0.2533	0.3368	0.3735	0.0715	0.3498	0.3164
V2009VI	210808	Bulkhead	4080	-174	177	0.2747	0.3533	0.3966	0.1959	0.3595	0.3628
A2109V	414953	Bulkhead	4059	0	723	0.0459	0.2083	0.1891	-0.0555	0.0958	0.0981
V2010V	220589	Keel	3504	0	86	0.0820	0.1993	0.1910	-0.1086	0.1513	0.1650
A2104V	222240	Bulkhead	3504	0	390	0.2504	0.2173	0.2938	0.1422	0.1718	0.1976
V2011VI	221188	Bulkhead	3504	216	177	0.1513	0.2528	0.2611	-0.1129	0.2062	0.2083
V2013V	221601	Bulkhead	3504	0	280	0.3048	0.3119	0.3865	0.1532	0.3042	0.3018
V2012VI	221102	Bulkhead	3504	-216	177	0.1903	0.3712	0.3696	-0.0186	0.2786	0.2475
V2124V	222060	Bulkhead	3504	-375	390	0.1894	0.3750	0.3723	0.0986	0.3887	0.3554
A2237V	416419	Bulkhead	3504	135	848	0.1794	0.1892	0.2310	0.0676	0.1256	0.1265
A2116V	414367	Bulkhead	3504	0	702	0.0598	0.1807	0.1687	-0.0462	0.0922	0.0914
A2240V	416269	Bulkhead	3504	-135	848	0.0176	0.2288	0.2034	-0.0801	0.1231	0.1302
V2014V	230461	Keel	2952	0	86	0.1698	0.1772	0.2175	0.0253	0.1730	0.1550
A3565V	231696	Bulkhead	2952	-81	317	-0.1198	0.2494	0.2452	-0.2076	0.1380	0.2209
V2016V	242399	Keel	2544	0	116	0.2568	0.3535	0.3872	0.1142	0.2836	0.2710
V2026V	312302	Keel	1992	0	55	0.0195	0.2213	0.1969	-0.1100	0.1846	0.1904
A2310V	320746	Bulkhead	1536	0	177	0.1251	0.2677	0.2619	-0.0808	0.2309	0.2168
V2035V	330769	Keel	1152	135	193	0.1703	0.1771	0.2177	0.0141	0.1634	0.1454
V2032V	330764	Keel	1152	0	196	0.1001	0.2548	0.2426	-0.0847	0.2287	0.2162
V2034V	330759	Keel	1152	-135	193	0.0704	0.2084	0.1950	-0.0418	0.2625	0.2356
V2019V	340167	Keel	672	0	197	0.0671	0.2264	0.2093	-0.1403	0.1901	0.2094
V2018VI	340992	Bulkhead	672	0	365	0.1931	0.2554	0.2837	0.0838	0.2426	0.2275
V2020V	350052	Keel	288	0	211	0.1866	0.2658	0.2878	-0.2590	0.2646	0.3282
A2413V	350220	Bulkhead	288	0	273	0.1000	0.2192	0.2136	-0.0959	0.1804	0.1811
Sum(E(X))						4.02880	7.23770	7.61010	-0.46380	6.12820	6.05550
Sum(E(X^2))						0.83054	1.99418	2.21855	0.34044	1.50779	1.45173
Mean						0.14389	0.25849	0.27179	-0.01656	0.21886	0.21627
Variation						0.00929	0.00457	0.00556	0.01232	0.00617	0.00526

2. Mesh Quality

Comparing Shot 1 predictions, the 3rd generation model showed minor improvement over the 1st and 2nd generation model overall, reducing the average

comprehensive Russell's error factor by approximately 0.005. Similar to what was found in the Shot 3 mesh quality comparison discussed previously, individual sensor comparisons showed mixed results. Despite having a slightly more significant improvement overall than Shot 3, this mesh quality comparison proved to be inconclusive due to these inconsistencies.

3. Mesh Density

Shot 1 was the furthest shot from the ship. As a result the fluid models were the largest cavitation depth models constructed, extending to a depth of 75 feet. For these models the number of normal fluid elements in the outer mesh ranged from 13 in the coarse mesh to 38 in the dense mesh. Table 15 summarizes the mesh properties of three of the fluid models constructed for the Shot 1.

Table 15. Shot 1 Fluid Model Mesh Properties

Property	Coarse Mesh	Medium Mesh	Dense Mesh
Inner Mesh Elements	5	6	7
Inner Mesh Element Spacing (Ave.)	11.4 in	10.0 in	9.3 in
Transition Mesh Elements	5	6	7
Transition Mesh Element Spacing (Ave.)	13.4 in	11.6 in	10.1 in
Outer Mesh Elements	14	24	38
Outer Mesh Element Spacing (Ave.)	36 in	20 in	12 in
Fluid Nodes	176,287	244,049	328,541
DAA Elements	5048	5090	5132
Simulation Run Time	34.75 hrs	40.48 hrs	47.33 hrs

The simulations of Shot 1 took considerably longer to run than Shot 3 due to the larger volume of the fluid mesh requiring more nodes. While all of the Shot 3 runs could be completed in a day and a half timeframe, the medium and dense mesh Shot 1 runs took nearly two days to process. While less than 5 hours separated the run times for all of the Shot 3 fluid meshes, there is over a 12 hour time difference between the coarse Shot 1 mesh and the dense Shot 1 mesh run times. This time difference is indicative of how quickly the model grows in size when extending the depth of the fluid model.

a. Error Comparison

A summary of the Russell's error factors found for each model comparison are shown in Figures 45 through 47.

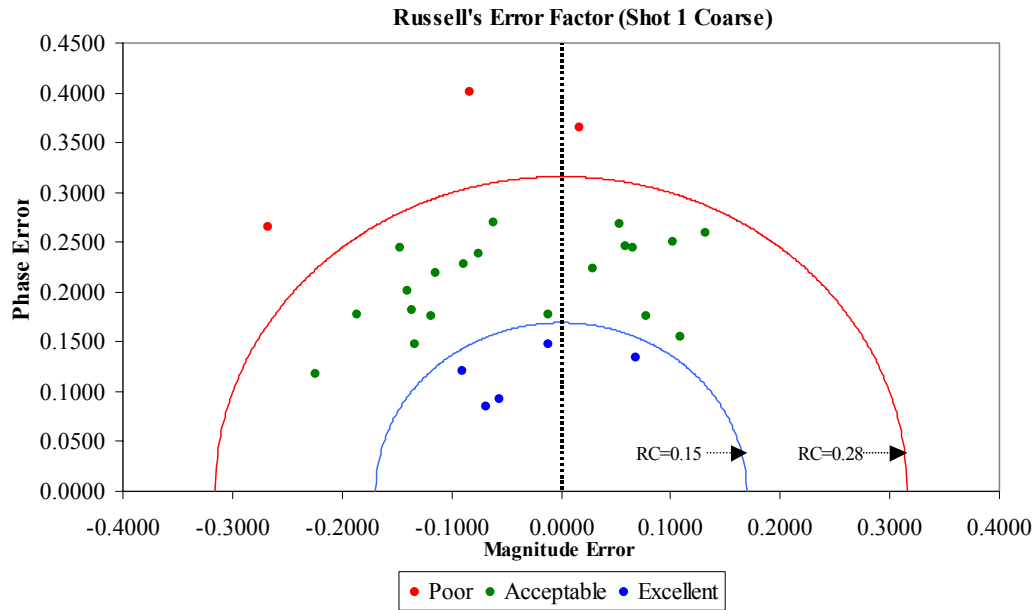


Figure 45. Russell's Error Factors for Coarse Mesh Fluid Model Comparison

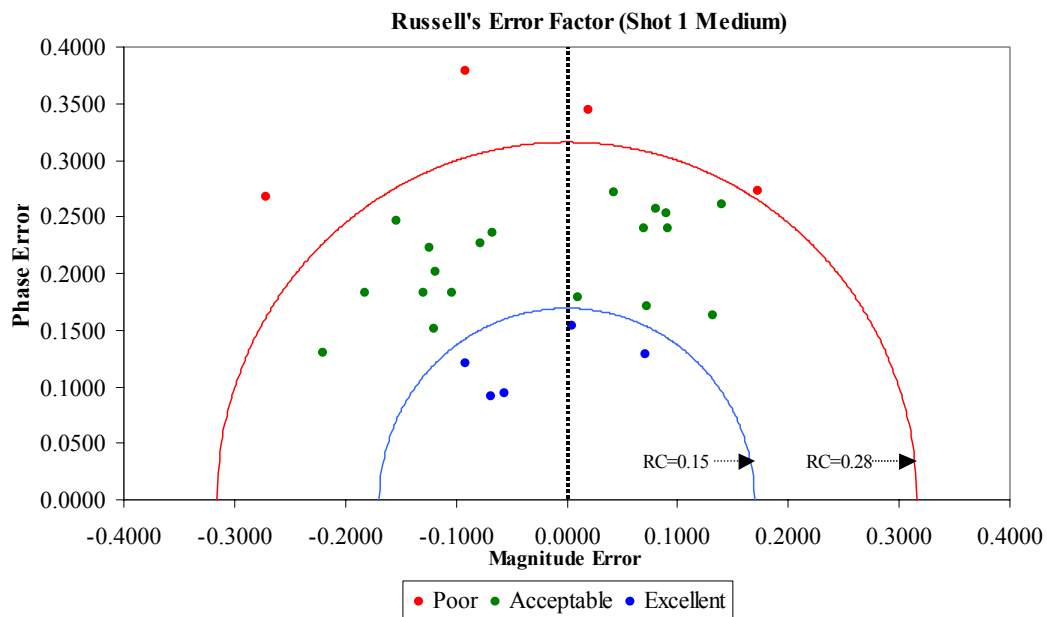


Figure 46. Russell's Error Factors for Medium Mesh Fluid Model Comparison

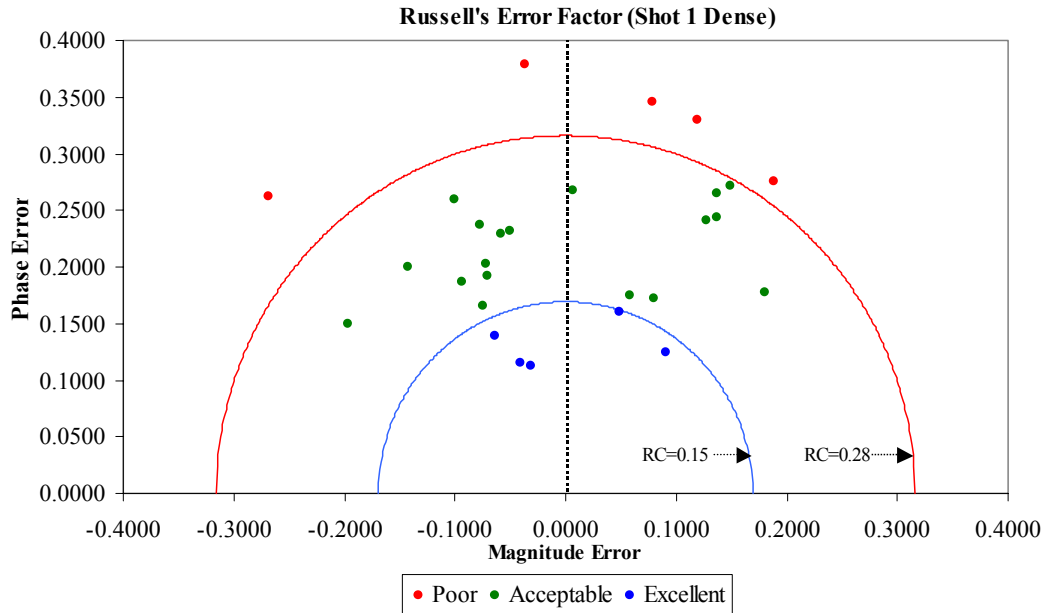


Figure 47. Russell's Error Factors for Dense Mesh Fluid Model Comparison

Unlike the Shot 3 comparison error plots, there are no apparent trends in the Shot 1 comparisons. The plots suggest that there is a large variation in both phase and magnitude error as the error factors are very scattered in all three plots. Interestingly, the coarse model had smaller errors than the other two models, opposite of what was observed in the Shot 3 case.

Table 16 lists all of the sensors compared and their corresponding Russell's error factors. The averages for each error factor are shown at the bottom of their respective columns along with the variation. These averages show that, the coarse mesh does in fact have lower average comprehensive and phase error factor at 0.21019 and 0.20767 respectively, while the dense mesh has the lowest average magnitude error factor at 0.00094. It should be noted that the average magnitude error factor can portray a better correlation than what really exists since negative magnitude error factors exist. The average magnitude error then indicates how much less or more the predicted response magnitudes were overall. The variation is a good indicator of how consistent the predictions were. In this case, the variation of the dense mesh comparison is largest for three error factors indicating that not only was the dense mesh the least accurate overall, but it was also the least consistent.

Table 16. Shot 1: Russell's Error Factor

Sensor	NODE	Bulkhead Keel	Location (in)			Dense Mesh			Medium Mesh			Coarse Mesh		
			x	y	z	RM	RP	RC	RM	RP	RC	RM	RP	RC
V2026V	312302	Keel	1992	0	55	0.1275	0.2417	0.2422	0.0811	0.2575	0.2392	0.0534	0.2684	0.2425
V2000V	120217	Keel	5328	0	82	-0.2684	0.2621	0.3325	-0.2713	0.2670	0.3374	-0.2670	0.2654	0.3336
V2002V	142489	Keel	4656	27	82	0.0797	0.1723	0.1682	0.0729	0.1711	0.1648	0.0772	0.1755	0.1699
V2007V	210430	Keel	4080	0	82	-0.0706	0.1914	0.1808	-0.1041	0.1833	0.1868	-0.1178	0.1760	0.1877
V2010V	220589	Keel	3504	0	86	0.0073	0.2670	0.2367	0.0420	0.2710	0.2431	-0.0620	0.2697	0.2452
V2014V	230461	Keel	2952	0	86	0.1370	0.2433	0.2474	0.0911	0.2395	0.2271	0.0653	0.2440	0.2238
V2016V	242399	Keel	2544	0	116	-0.0723	0.2032	0.1912	-0.1185	0.2009	0.2067	-0.1396	0.2013	0.2171
A2310V	320746	Bulkhead	1536	0	177	0.1492	0.2711	0.2742	0.0905	0.2525	0.2377	0.0584	0.2458	0.2239
V2008VI	210894	Bulkhead	4080	174	177	-0.0580	0.2289	0.2092	-0.0772	0.2264	0.2120	-0.0887	0.2284	0.2171
V2009VI	210808	Bulkhead	4080	-174	177	0.0482	0.1607	0.1486	0.0048	0.1541	0.1367	-0.0121	0.1480	0.1316
V2011VI	221188	Bulkhead	3504	216	177	-0.1420	0.1996	0.2171	-0.1822	0.1834	0.2291	-0.1863	0.1772	0.2279
V2012VI	221102	Bulkhead	3504	-216	177	0.0584	0.1745	0.1631	0.0095	0.1784	0.1583	-0.0116	0.1778	0.1579
V2034V	330759	Keel	1152	-135	193	0.1365	0.2649	0.2641	0.0699	0.2393	0.2209	0.0296	0.2233	0.1996
V2035V	330769	Keel	1152	135	193	0.1192	0.3301	0.3110	0.1720	0.2726	0.2856	0.1321	0.2592	0.2578
V2032V	330764	Keel	1152	0	196	0.1891	0.2754	0.2960	0.1407	0.2611	0.2628	0.1022	0.2501	0.2394
V2019V	340167	Keel	672	0	197	-0.1004	0.2598	0.2469	-0.1539	0.2463	0.2574	-0.1463	0.2447	0.2526
A8516V	210993	Bulkhead	4080	239	202	-0.0497	0.2324	0.2107	-0.0676	0.2363	0.2173	-0.0751	0.2389	0.2220
V2020V	350052	Keel	288	0	211	-0.0370	0.3792	0.3376	-0.0909	0.3782	0.3447	-0.0827	0.4013	0.3631
A2413V	350220	Bulkhead	288	0	273	0.0781	0.3461	0.3144	0.0200	0.3449	0.3062	0.0171	0.3649	0.3238
V2013V	221601	Bulkhead	3504	0	280	-0.0933	0.1866	0.1849	-0.1288	0.1827	0.1981	-0.1366	0.1819	0.2016
A3565V	231696	Bulkhead	2952	-81	317	0.1805	0.1773	0.2242	0.1324	0.1623	0.1856	0.1093	0.1557	0.1686
V2018VI	340992	Bulkhead	672	0	365	-0.0775	0.2370	0.2210	-0.1242	0.2230	0.2262	-0.1149	0.2197	0.2198
A2104V	222240	Bulkhead	3504	0	390	-0.1963	0.1496	0.2187	-0.2204	0.1297	0.2266	-0.2235	0.1184	0.2241
V2124V	222060	Bulkhead	3504	-375	390	-0.0741	0.1653	0.1605	-0.1200	0.1509	0.1708	-0.1330	0.1473	0.1759
A2116V	414367	Bulkhead	3504	0	702	-0.0402	0.1149	0.1079	-0.0679	0.0915	0.1010	-0.0679	0.0848	0.0962
A2109V	414953	Bulkhead	4059	0	723	0.0904	0.1239	0.1359	0.0709	0.1281	0.1298	0.0682	0.1342	0.1334
A2237V	416419	Bulkhead	3504	135	848	-0.0634	0.1386	0.1351	-0.0915	0.1205	0.1341	-0.0906	0.1203	0.1334
A2240V	416269	Bulkhead	3504	-135	848	-0.0316	0.1122	0.1033	-0.0567	0.0943	0.0975	-0.0556	0.0926	0.0957
Sum(E(X))						0.02630	6.10910	6.08340	-0.87740	5.84680	5.94350	-1.29850	5.81480	5.88520
Sum(E(X^2))						0.36994	1.45976	1.43693	0.39283	1.35133	1.36958	0.36280	1.35485	1.34893
Mean						0.00094	0.21818	0.21726	-0.03134	0.20881	0.21227	-0.04638	0.20767	0.21019
Variation						0.01370	0.00470	0.00427	0.01353	0.00483	0.00400	0.01121	0.00545	0.00415

Figure 48 shows the Russell's comprehensive error factor trend in relation to the longitudinal position on the ship for each fluid mesh. As is shown, all three meshes have poor correlation in the sonar dome region as was the case for Shot 3. For Shot 1 however, the sonar dome region was the closest region on the ship to the charge. This should have resulted in much better accuracy in the prediction. This anomaly may be due to other factors such as gauge error or the effects of the sonar dome which has been omitted from the structural model.

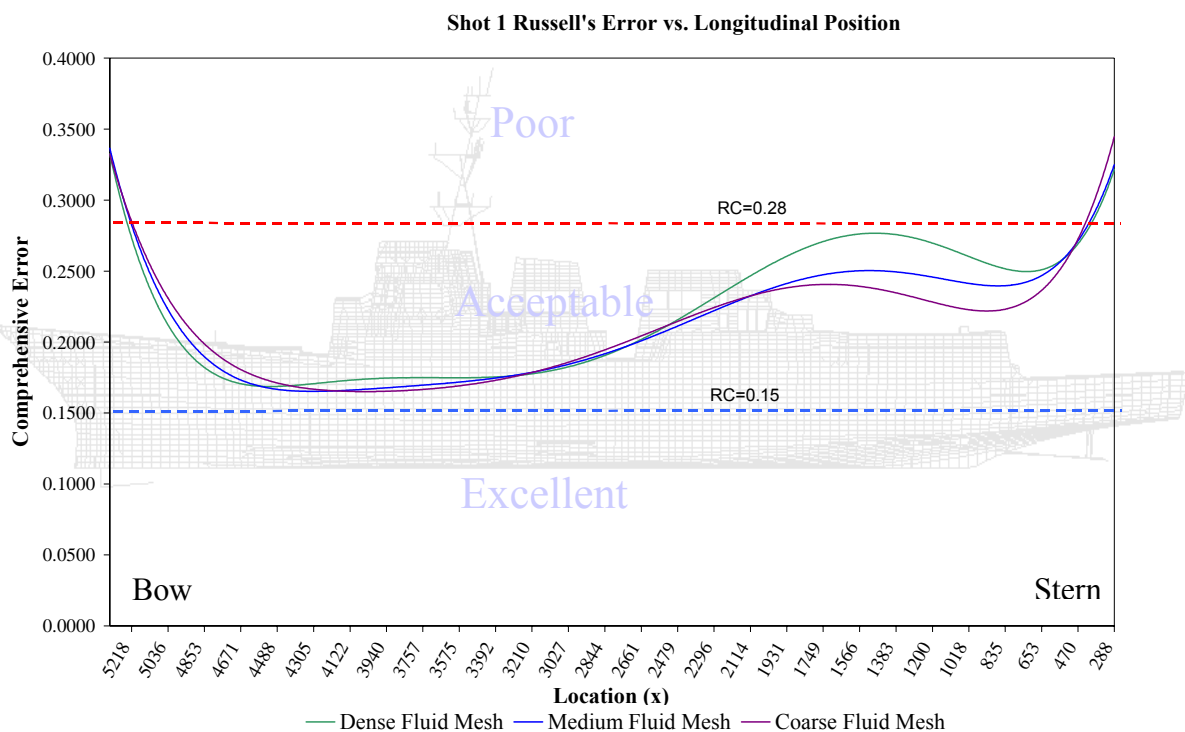


Figure 48. Shot 1 Russell's Comprehensive Error Trends

Very good correlation exists in the forward areas of the ship, particularly for those sensors located in the superstructure of the ship. The trends begin to diverge aft of midships where the coarse mesh correlation is significantly better than the medium and dense mesh. This is contradicted by the stern region correlation which is poor for all meshes, but poorest for the coarse mesh.

The interaction at the hull is a result of the pressure wave as well as the fluid particle velocities. While pressure always acts normal to the structure, the fluid particle velocities do not. In Shot 3, the fluid particle velocities acted primarily normal to the majority of the structure since the charge was located off the beam. In Shot 1, the charge was located very far forward off the bow. A large portion of the structure, primarily the aft portion of the ship, is subjected to fluid particle velocities which are nearly tangent to the hull. This coupled with the fact that the incident pressure wave decreases as the wave propagates aft tends to magnify any prediction error.

The increased error in the dense fluid mesh in the aft sections of the ship may also be due to this nearly tangential flow. In a shot off the beam, the element aspect ratios of concern are those which make up the DAA boundary and the wetted surface structure interface. When the shot is a bow or stern shot, the cross-sectional aspect ratios of the fluid element become important in calculating the wave propagation. While Shot 1 is not a direct end-on shot, as the wave propagates aft, the propagation becomes increasingly tangential to the hull. As the density of the mesh is increased, the aspect ratios become much smaller and the resulting approximation less accurate [Ref. 31].

b. Velocity Plots

To help visualize the Russell's error factor correlation discussed, five velocity plots are shown in Figures 49 through 53. Additional velocity plots can be found in Appendix A. The first plot is sensor V2000V, located in the sonar dome region. This plot shows little correlation between the predicted and measured response. The measured response is oscillating at a higher frequency and magnitude than the predicted response. This poor correlation is similar to that of Shot 3 indicative of the possible contributing factors mentioned earlier.

Figure 50 shows bulkhead sensor V2124V, located forward of midships and above the waterline. This shows exceptional correlation in all three cases. The peak response is captured very well as is the recovery region immediately following this peak. The predicted response settles out faster than the measured response, suggesting that the model may be over-damped in this case.

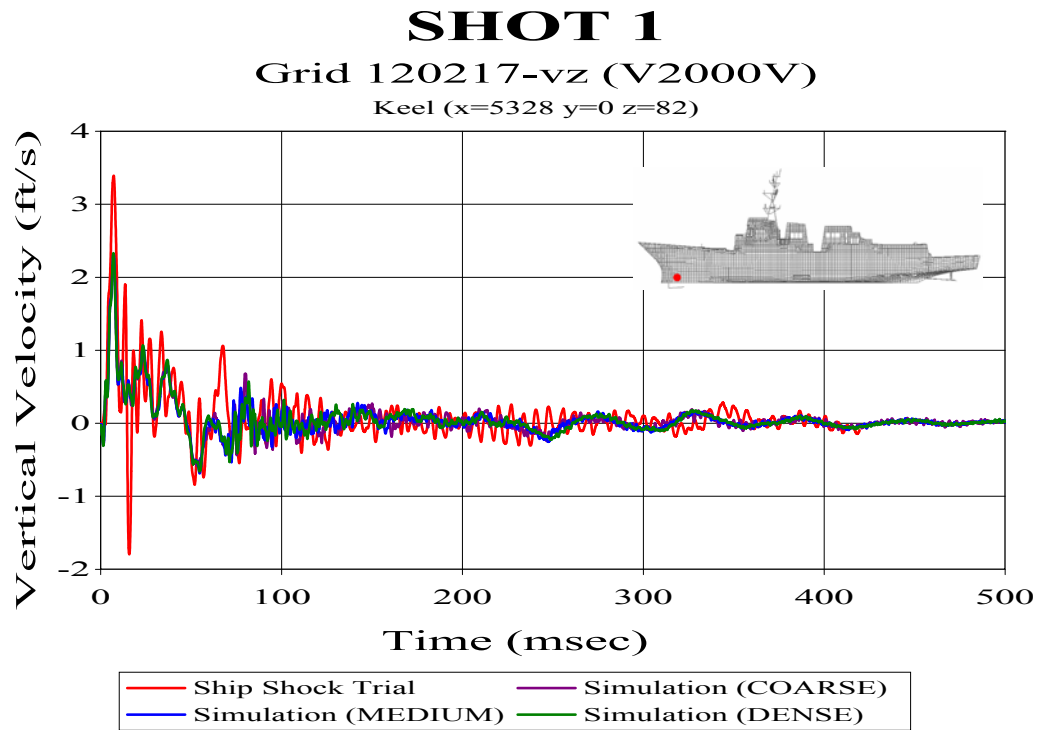


Figure 49. Keel Sensor V2000V.

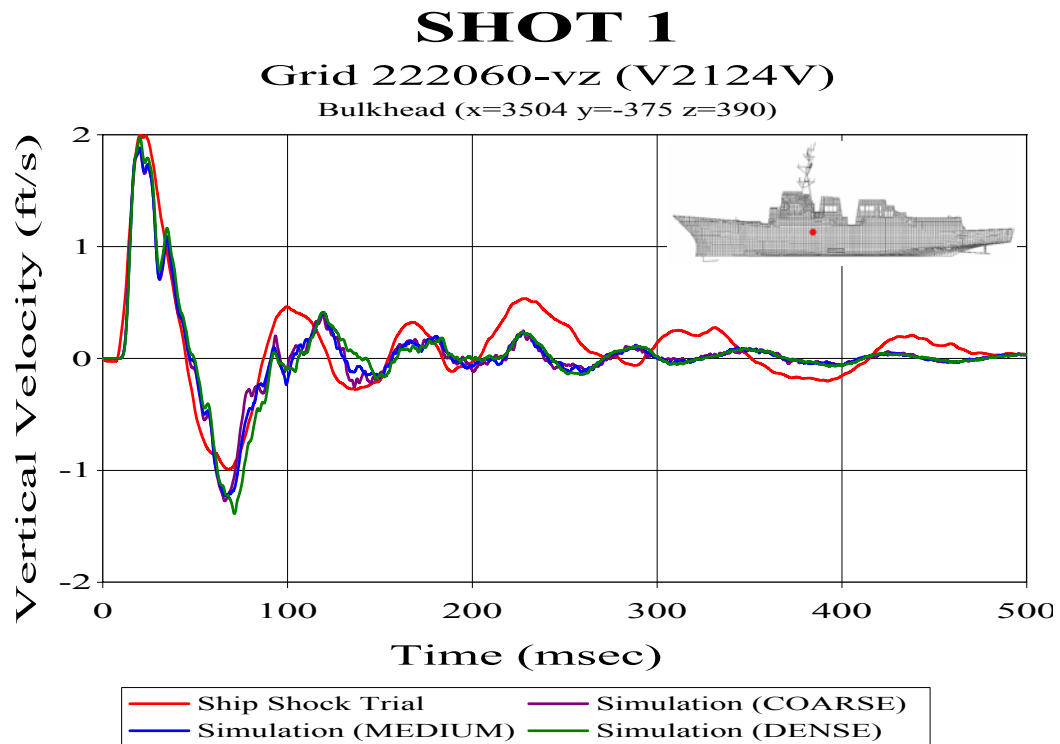


Figure 50. Bulkhead Sensor V2124V.

Figure 51 is keel sensor V2016V located just aft of midships. This shows good correlation in the early and late time response with a bit of a phase miscorrelation after the initial peak. This is most apparent in the dense mesh prediction. This region of the ship is where the predictions from each mesh began to diverge.

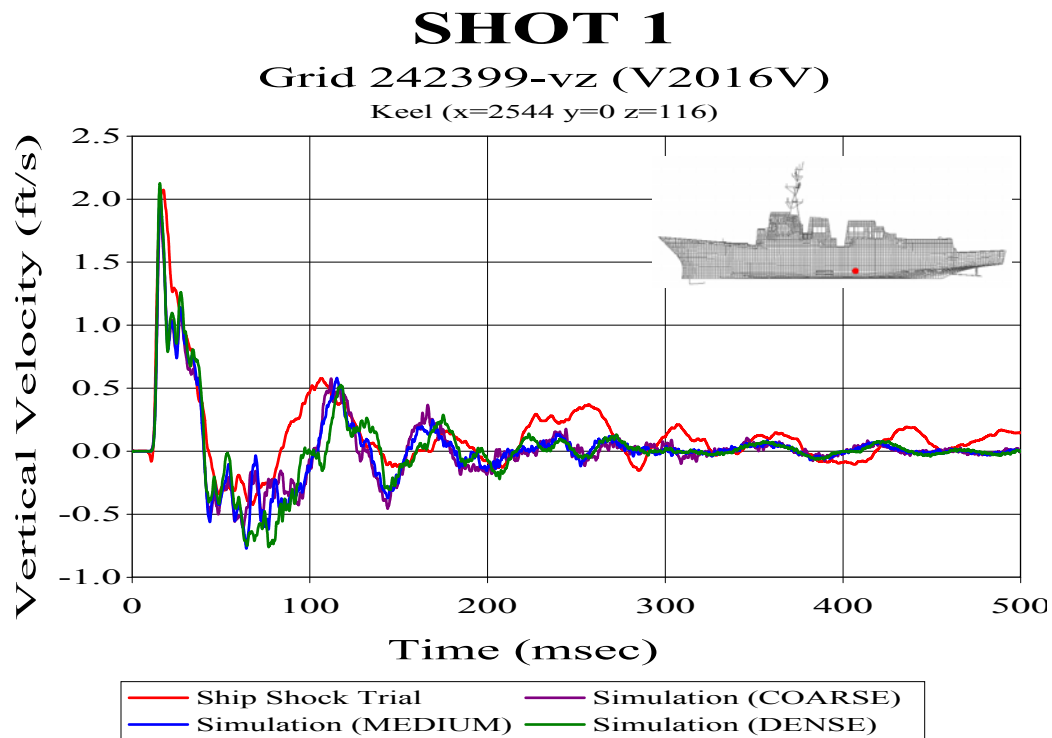


Figure 51. Keel Sensor V2016V

Moving to the furthest aft location compared, Figure 52 shows keel sensor V2020V. This shows poor correlation both in phase and in magnitude. The comparisons for all of the meshes were poor for this sensor. As discussed earlier, this can be attributed to the tangential propagation of the shock wave in this region.

Shown in Figure 53 is sensor A2240V, an accelerometer, was located high in the structure on the starboard mast leg. Excellent phase and magnitude correlation is shown in this comparison. This excellent correlation is evidence of proper structural damping in the model and a minimal amount of measured data error. As with Shot 3, most of the comparisons made with accelerometer data showed significantly lower predictions errors than comparisons made with velocity meter data.

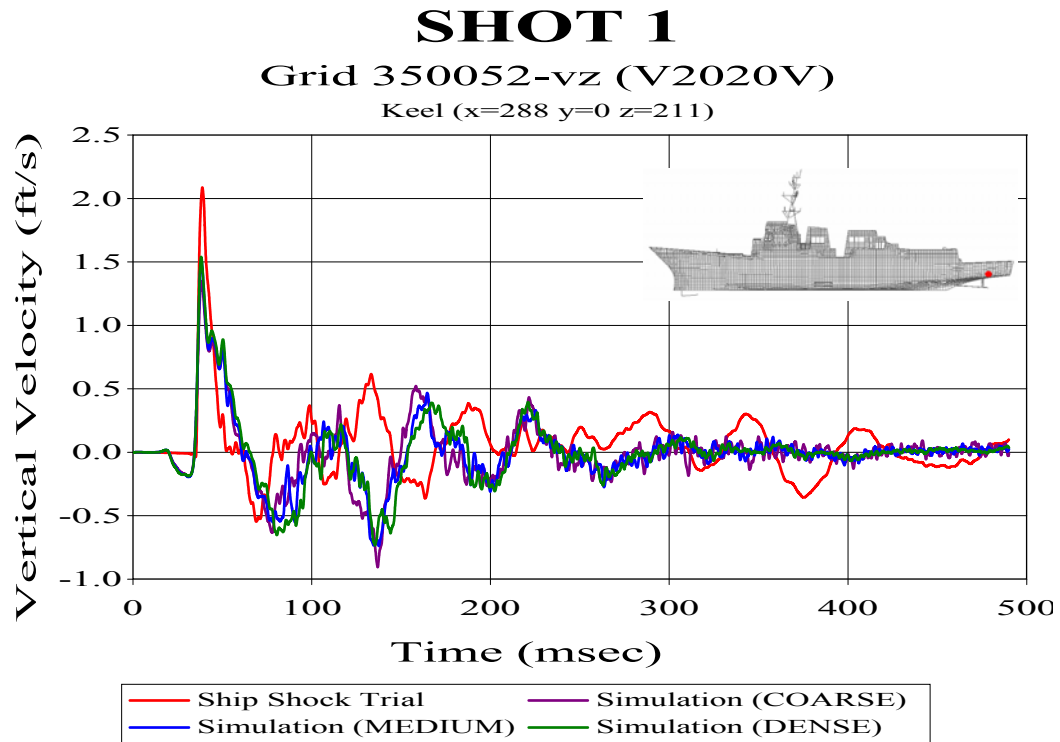


Figure 52. Keel Sensor V2020V.

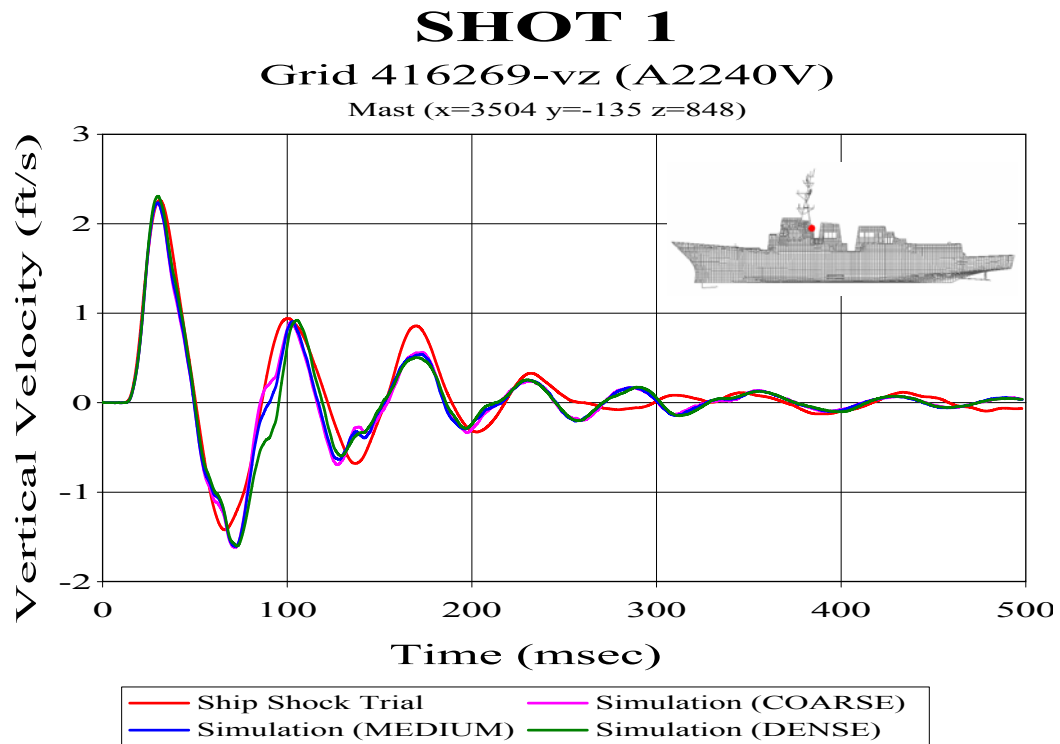


Figure 53. Mast Sensor A2240V.

D. SHOT 2

The final shot compared is Shot 2. This shot was the only shot detonated on the starboard side of DDG 81. In this shot, the charge was located off the beam, slightly forward of where the Shot 3 charge was detonated on the port side and with a larger stand-off distance. Figure 54 shows the relative aspect of the Shot 2 charge to the ship.

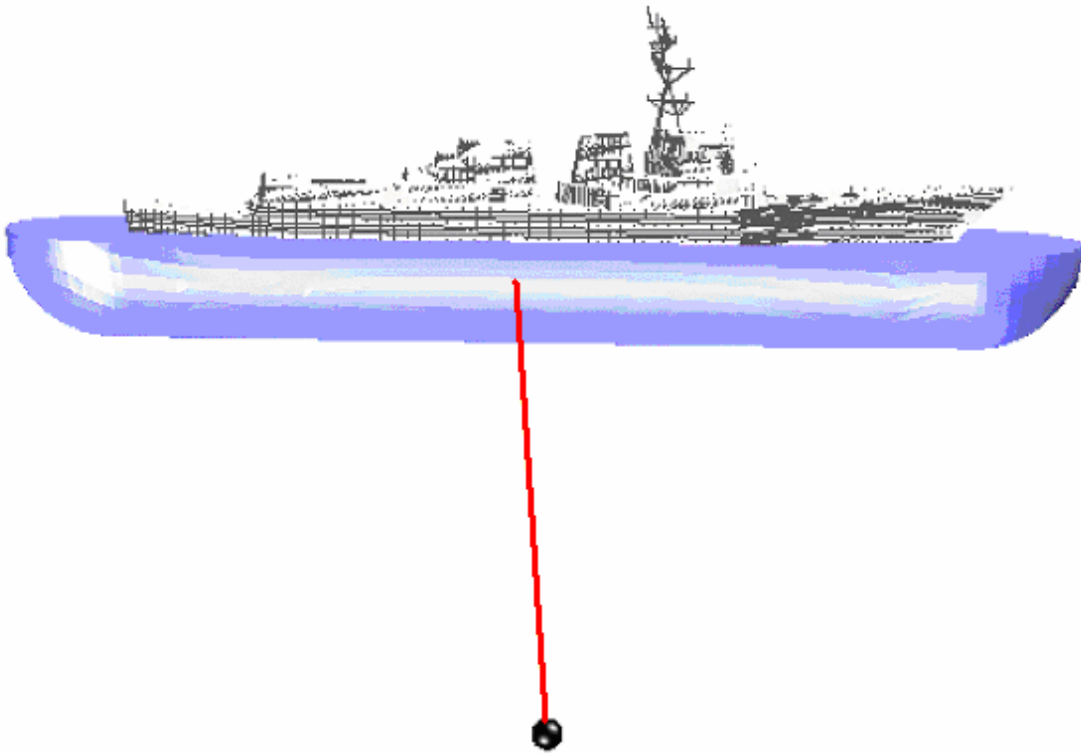


Figure 54. Shot 2 Geometry. Charge Off Starboard Midships

Three 3rd generation models of varying density were constructed for the Shot 2 simulation. A summary of the fluid model properties is shown in Table 17.

Table 17. Shot 2 Fluid Model Properties

Property	Coarse Mesh	Medium Mesh	Dense Mesh
Inner Mesh Elements	5	6	7
Inner Mesh Element Spacing (Ave.)	11.4 in	10.0 in	9.3 in
Transition Mesh Elements	5	6	7
Transition Mesh Element Spacing (Ave.)	13.4 in	11.6 in	10.1 in
Outer Mesh Elements	10	20	32
Outer Mesh Element Spacing (Ave.)	36 in	20 in	12 in
Fluid Nodes	150,879	213,329	287,197
DAA Elements	5048	5090	5132
Simulation Run Time	31.5 hrs	37.2 hrs	42.8 hrs

1. Error Comparison

A summary of the Russell's error factors found in the comparison of all three meshes is shown in Figures 55 through 57.

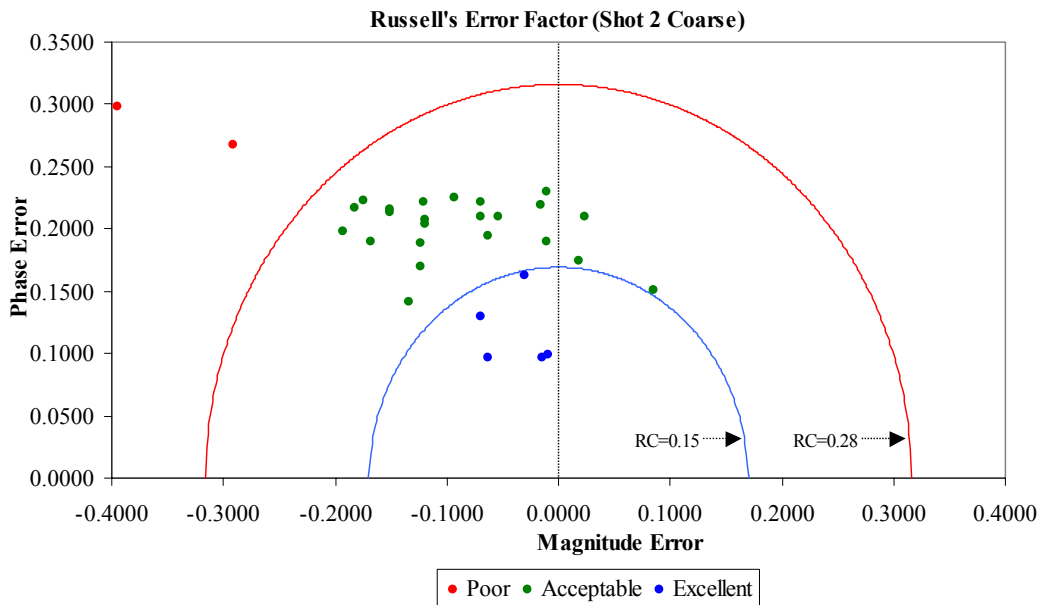


Figure 55. Russell's Error Factors for Coarse Mesh Fluid Model Comparison

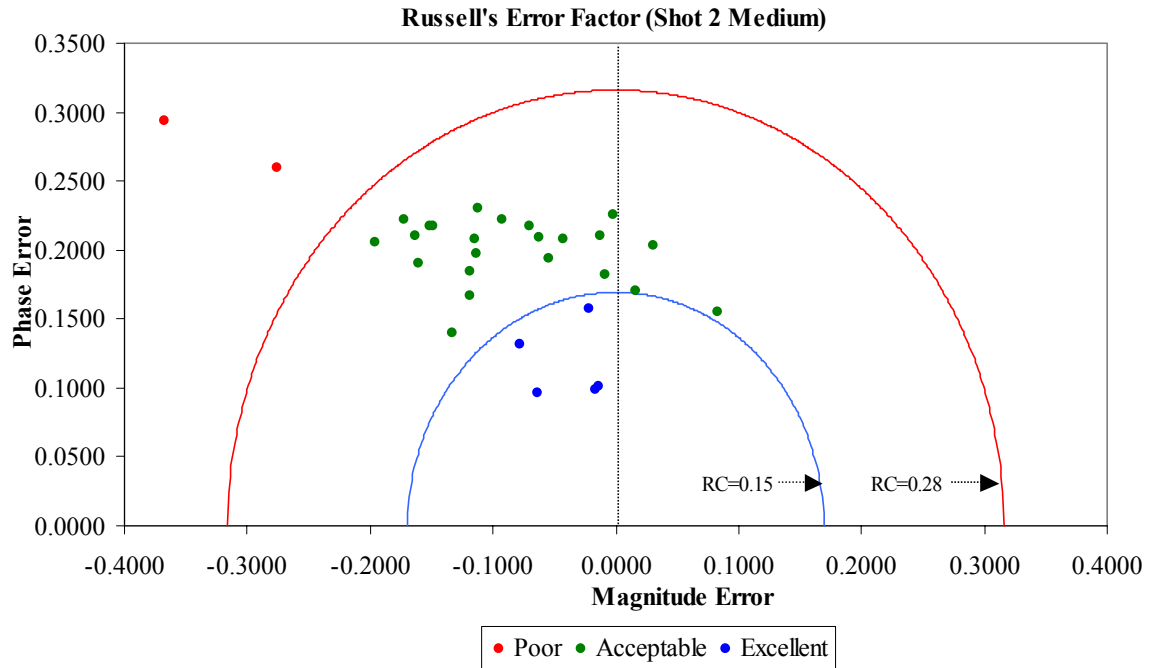


Figure 56. Russell's Error Factors for Medium Mesh Fluid Model Comparison

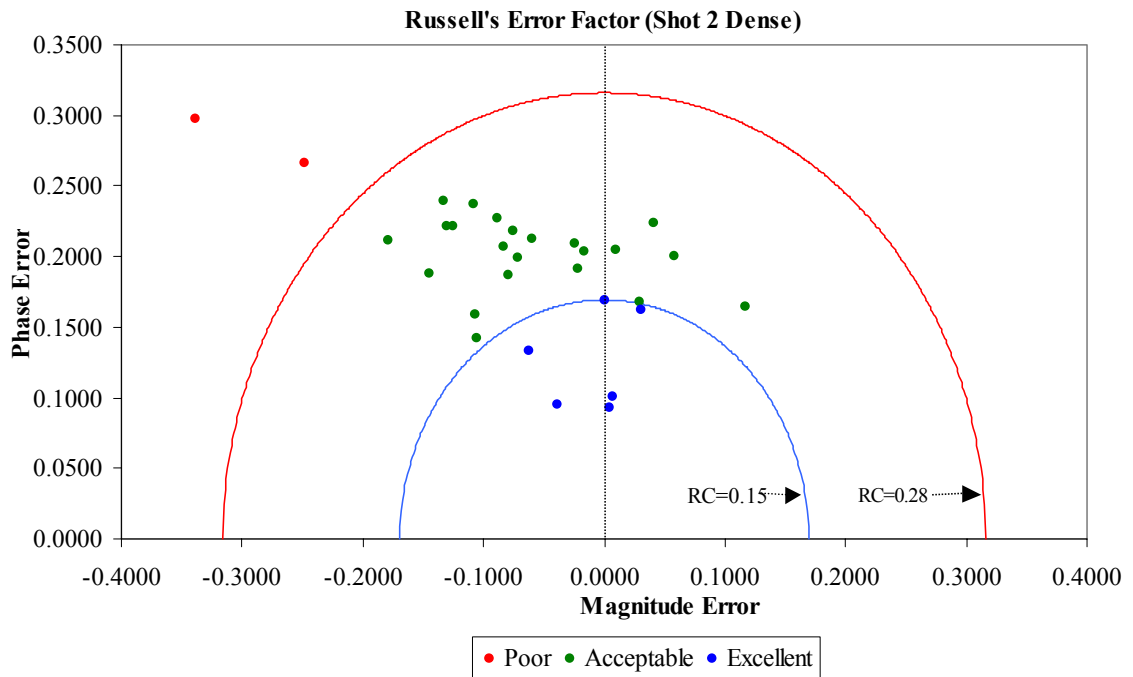


Figure 57. Russell's Error Factors for Dense Mesh Fluid Model Comparison

The trends in these comparisons are very similar to those observed in Shot 3. The dense mesh shows significant improvement in the overall error factors. This improvement is most significant in terms of the magnitude error. As in Shot 3, the general trend of the error factor plots is that the points move primarily to the right, indicative of a larger velocity magnitude response being predicted as the density of the fluid mesh is increased. The phase error remains fairly constant throughout.

Table 18 lists all of the sensors compared and their corresponding Russell's error factors. The averages for each error factor are shown at the bottom of their respective columns along with the variation. As shown in the table, the dense mesh has a significantly lower magnitude error than the other two meshes. As was the case with Shot 3, the most significant improvement is shown between the medium and dense meshes. This shot comparison represents the best overall comparison of the three shots compared. Every mesh compared for this shot had a mean comprehensive error significantly less than the other two shot comparisons.

Figure 58 shows the comprehensive error trends of each mesh comparison over the length of the ship. This trend plot shows that the most accurate predictions occur around the midship regions, while the least accurate predictions are at either end. The dense mesh shows a significantly better prediction at these ends and in the aft section of the ship. By comparison, the Shot 3 trend was very similar.

Table 18. Shot 2: Russell's Error Factor

Sensor	NODE	Bulkhead Keel	Location (in)			Shot 2: Coarse Mesh			Shot 2: Medium Mesh			Shot 2: Dense Mesh		
			x	y	z	RM	RP	RC	RM	RP	RC	RM	RP	RC
V2000V	120217	Keel	5328	0	82	-0.3953	0.2976	0.4385	-0.3671	0.2936	0.4165	-0.3385	0.2971	0.3991
V2002V	142489	Keel	4656	27	82	0.0236	0.2101	0.1874	0.0309	0.2032	0.1822	0.0579	0.2001	0.1846
V2009VI	210808	Bulkhead	4080	-174	177	-0.1204	0.2212	0.2232	-0.1120	0.2307	0.2272	-0.0882	0.2272	0.2160
V2008VI	210894	Bulkhead	4080	174	177	-0.1190	0.2037	0.2091	-0.1136	0.1968	0.2014	-0.0714	0.1994	0.1877
V2007V	210430	Keel	4080	0	82	-0.0701	0.2098	0.1961	-0.0623	0.2095	0.1937	-0.0245	0.2092	0.1866
V2108V	212196	Bulkhead	4080	312	390	-0.1227	0.1883	0.1992	-0.1186	0.1843	0.1943	-0.0788	0.1872	0.1800
A8516V	210993	Bulkhead	4080	238.5	202	-0.0303	0.1625	0.1465	-0.0217	0.1571	0.1405	0.0311	0.1623	0.1464
A2109V	414953	Bulkhead	4059	0	722.8	-0.0851	0.1507	0.1534	0.0830	0.1549	0.1557	0.1170	0.1647	0.1790
V2124V	222060	Bulkhead	3504	-375.4	390	-0.1929	0.1981	0.2451	-0.1956	0.2055	0.2514	-0.1793	0.2113	0.2456
V2012VI	221102	Bulkhead	3504	-216	177	-0.1512	0.2135	0.2319	-0.1507	0.2172	0.2343	-0.1299	0.2211	0.2273
V2011VI	221188	Bulkhead	3504	216	177	-0.0104	0.2293	0.2034	-0.0015	0.2259	0.2002	0.0412	0.2240	0.2018
V2010V	220589	Keel	3504	0	85.5	-0.1194	0.2077	0.2123	-0.1147	0.2082	0.2106	-0.0827	0.2070	0.1975
V2125V	222436	Bulkhead	3504	375.4	390	-0.0627	0.194	0.1807	-0.0549	0.1937	0.1785	-0.0214	0.1914	0.1707
V2013V	221601	Bulkhead	3504	0	280	-0.1344	0.1413	0.1728	-0.1326	0.1403	0.1710	-0.1049	0.1420	0.1565
A2240V	416269	Bulkhead	3504	-135	848	-0.0700	0.1292	0.1302	-0.0779	0.1311	0.1352	-0.0626	0.1335	0.1307
A2104V	222240	Bulkhead	3504	0	390	-0.0623	0.0965	0.1018	-0.0636	0.0963	0.1023	-0.0388	0.0953	0.0912
A2116V	414367	Bulkhead	3504	0	702	-0.0088	0.0986	0.0877	-0.0134	0.1011	0.0903	0.0070	0.1003	0.0891
A2237V	416419	Bulkhead	3504	135	848	-0.0148	0.0968	0.0868	-0.0159	0.0991	0.0889	0.0047	0.0931	0.0826
V2014V	230461	Keel	2952	0	85.5	-0.0696	0.2213	0.2056	-0.0701	0.2173	0.2024	-0.0590	0.2126	0.1956
A3565V	231696	Bulkhead	2952	-81	316.7	0.0184	0.1749	0.1558	0.0165	0.1699	0.1513	0.0290	0.1675	0.1506
V2016V	242399	Keel	2544	0	116	-0.0534	0.2102	0.1923	-0.0428	0.2082	0.1884	-0.0169	0.2038	0.1812
V2026V	312302	Keel	1992	0	55	-0.0931	0.2254	0.2162	-0.0922	0.2224	0.2134	-0.0751	0.2185	0.2047
A2310V	320746	Bulkhead	1536	0	177	-0.0155	0.2194	0.1949	-0.0121	0.2102	0.1866	0.0103	0.2047	0.1816
V2034V	330759	Keel	1152	-135	193.3	-0.1679	0.1899	0.2247	-0.1601	0.1898	0.2200	-0.1442	0.1874	0.2095
V2032V	330764	Keel	1152	0	196	-0.1232	0.1697	0.1859	-0.1183	0.1669	0.1813	-0.1067	0.1593	0.1699
V2035V	330769	Keel	1152	135	193.3	-0.0106	0.1894	0.1681	-0.0090	0.1823	0.1618	0.0009	0.1692	0.1500
V2019V	340167	Keel	672	0	196.5	-0.1747	0.2229	0.2510	-0.1727	0.2222	0.2494	-0.1327	0.2391	0.2423
V2018VI	340992	Bulkhead	672	0	364.8	-0.1509	0.2152	0.2329	-0.1492	0.2176	0.2338	-0.1076	0.2369	0.2306
V2020V	350052	Keel	288	0	211	-0.2916	0.2676	0.3507	-0.2760	0.2592	0.3355	-0.2477	0.2657	0.3219
A2413V	350220	Bulkhead	288	0	273.4	-0.1822	0.2169	0.2510	-0.1625	0.2104	0.2356	-0.1245	0.2219	0.2255
Sum(E(X))						-2.89030	5.77170	6.03520	-2.75070	5.72490	5.93370	-1.93630	5.75280	5.73580
Sum(E(X^2))						0.55106	1.17304	1.35421	0.50179	1.15183	1.29863	0.37537	1.16764	1.21171
Mean						-0.09634	0.19239	0.20117	-0.09169	0.19083	0.19779	-0.06454	0.19176	0.19119
Variation						0.00940	0.00216	0.00483	0.00861	0.00205	0.00431	0.00863	0.00222	0.00397

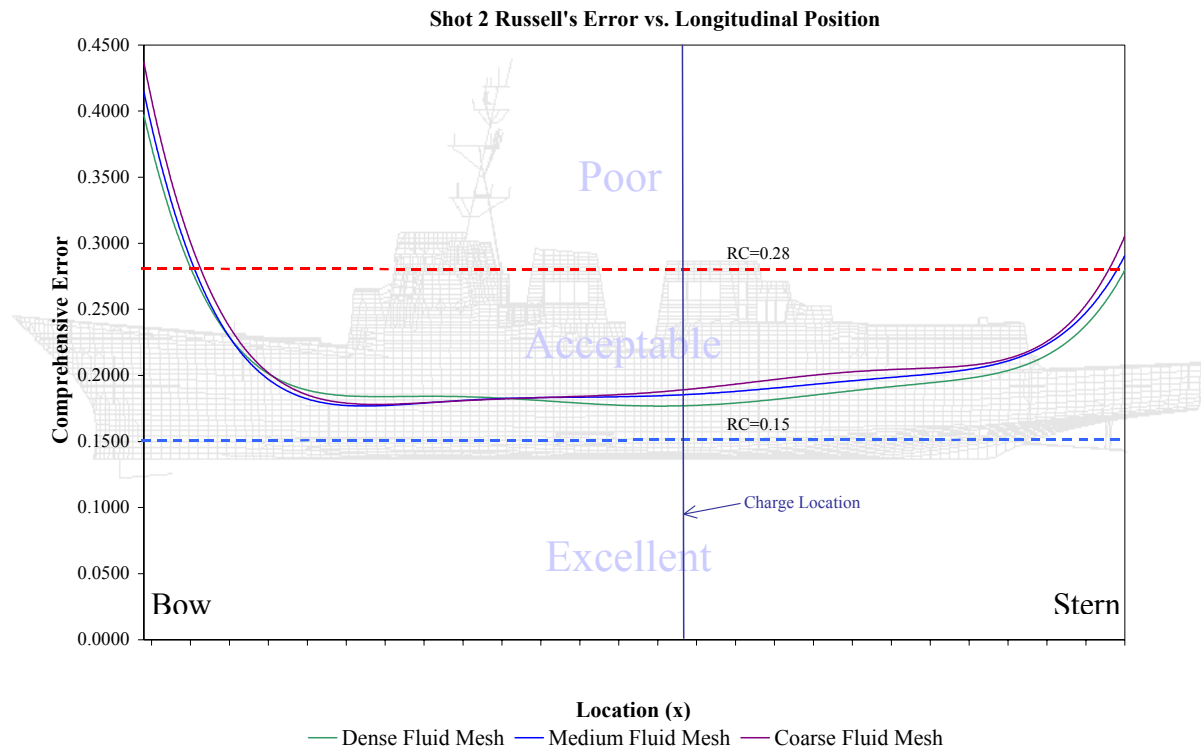


Figure 58. Russell's Comprehensive Error Trend as a Function of Longitudinal Position

2. Velocity Plots

It is useful to correlate the errors summarized above using actual velocity comparison plots. The same sensor velocity plots shown for Shot1 and Shot 3 are shown below in Figures 59 through 63. Several more velocity plots from Shot 2 are included in Appendix A.

Figure 59 shows keel sensor V2000V located above the sonar dome. This sensor has shown little correlation in the Shot 1 and Shot 3 comparisons, the Shot 2 comparison is no exception. Though the best overall correlation, the Shot 2 prediction at this sensor showed the worst correlation of all the sensors compared for all three shots.

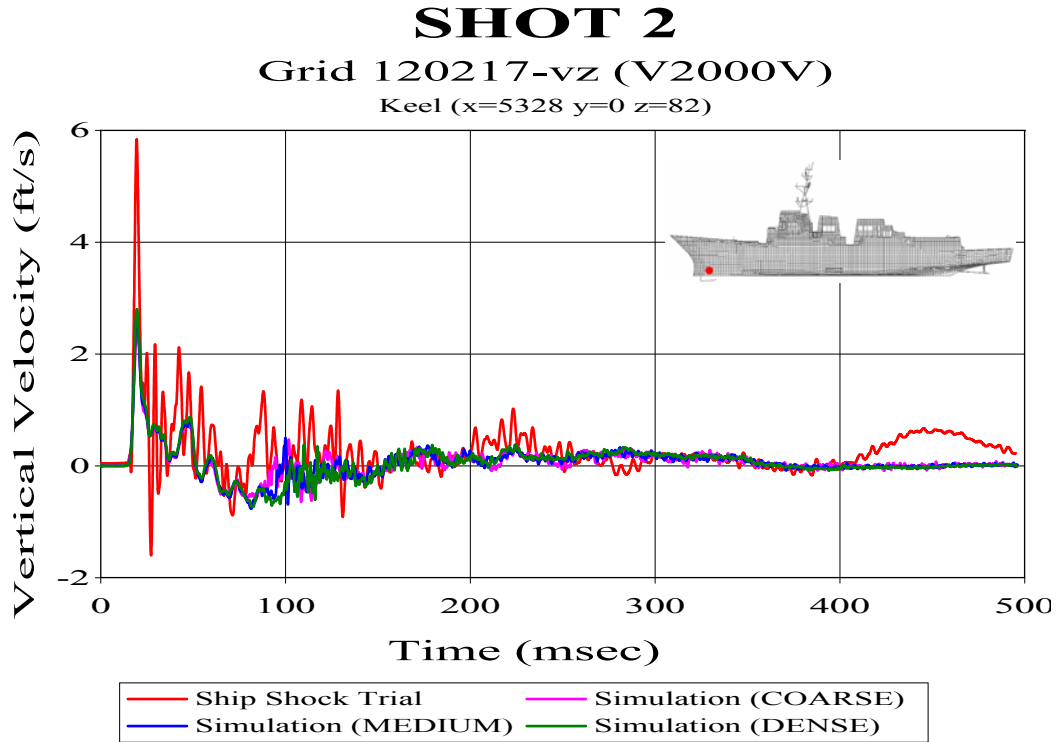


Figure 59. Keel Sensor V2000V

Figure 60 shows bulkhead sensor V2124V. This sensor is located higher in the structure, making the prediction more dependent on the structural model and structural damping. Though showing signs of being slightly over damped, this comparison shows fairly good phase correlation. There is drift apparent in the late time measure response data which explains one reason why this sensor comparison had one of the highest comprehensive error factors of the Shot 2 sensors compared.

Further aft and lower on the ship is keel sensor V2016V shown in Figure 61. The velocity comparison at this sensor shows exceptional peak response agreement, followed by a relatively good correlating late time response magnitude, but with a small phase shift in all three cases. Minor measured data drift is apparent in the late time response, contributing some to the error factor calculated for this sensor.

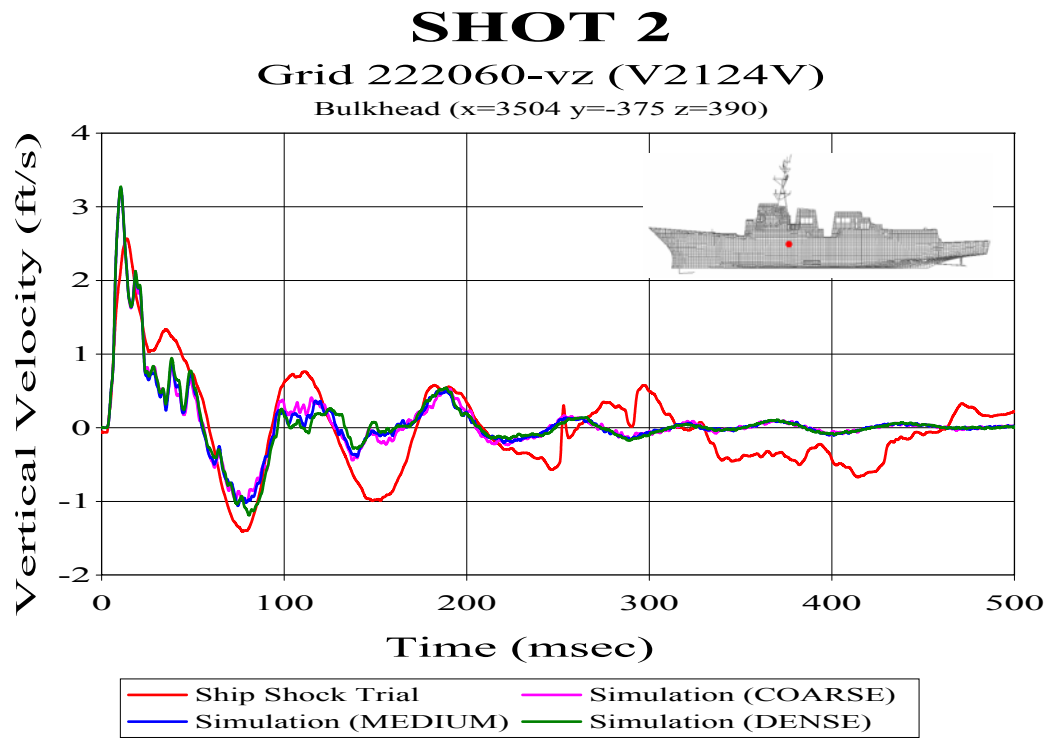


Figure 60. Bulkhead Sensor V2124V

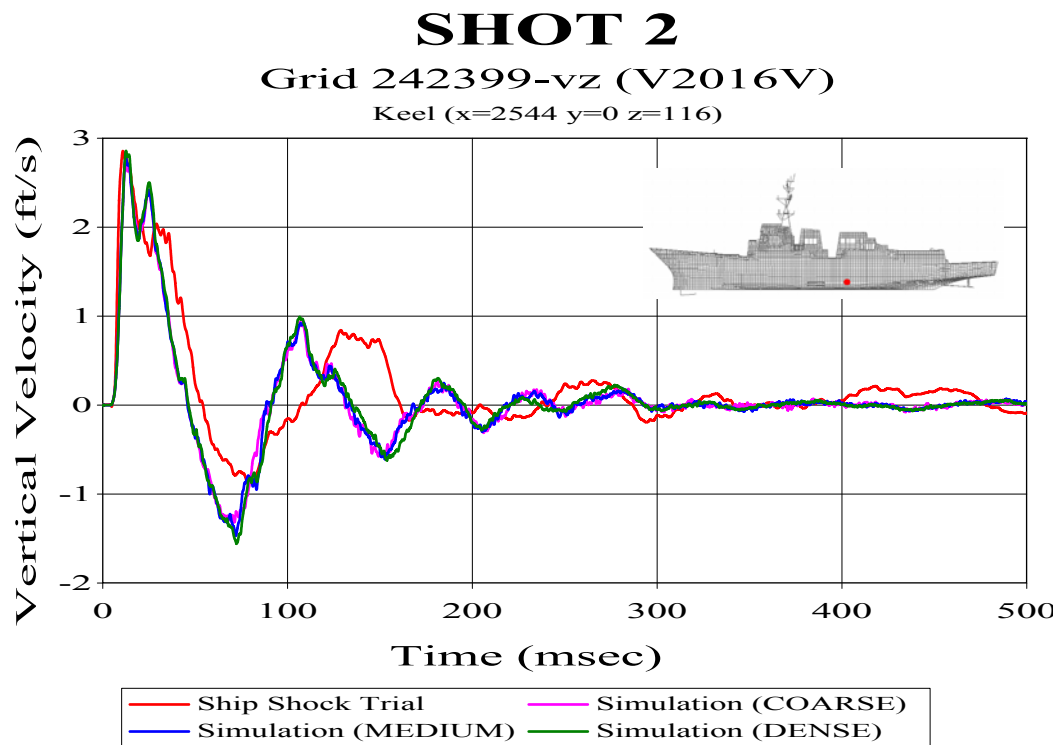


Figure 61. Keel Sensor V2016V

The furthest aft sensor compared is keel sensor V2020V shown in Figure 62. This comparison showed the second worst correlation of all of the Shot 2 sensors compared. In fact, for Shot 2 only two sensor predictions did not meet the acceptance criteria of 0.28 Russell's comprehensive error factor or lower. Sensor V2000V shown in Figure 59 and this sensor were those sensors. As shown, little correlation exists both in early and the late time response. The predicted initial peak magnitude is approximately half that which was measured for all three fluid meshes. The late time predicted response continues to underestimate the magnitude and there is significant phase error.

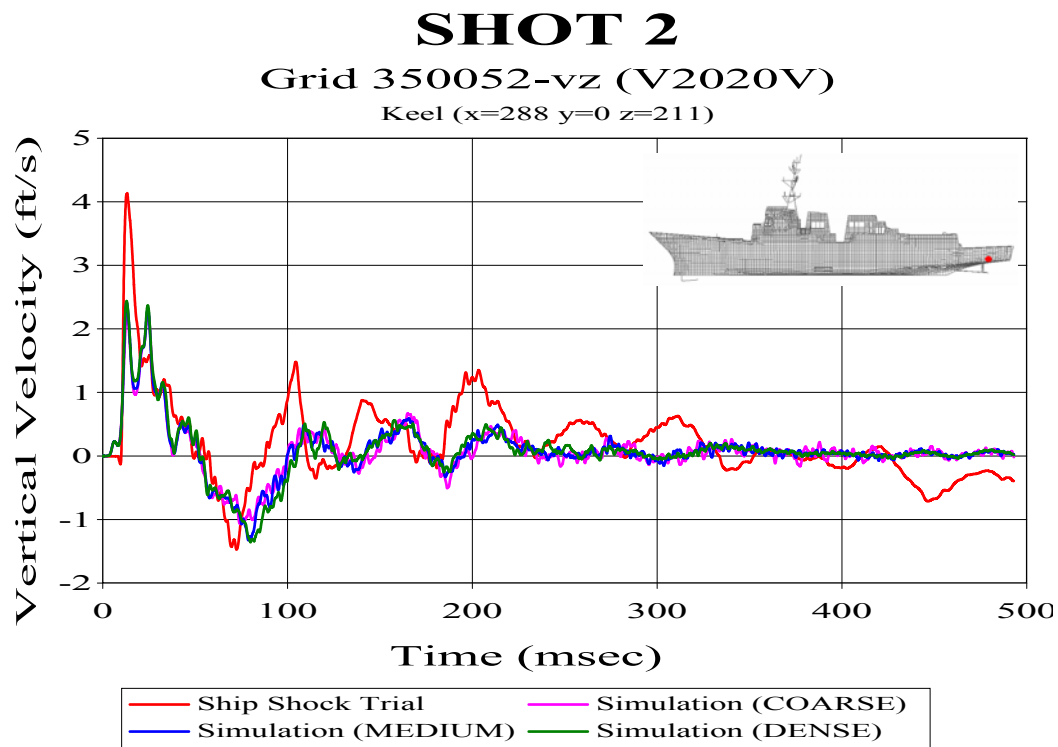


Figure 62. Keel Sensor V2020V

The last sensor comparison shown, mast sensor A2237V shown in Figure 63, had the best correlation of all of the comparisons for all three shots. The early time correlation between predicted and measured response was nearly perfect. Exceptional correlation was shown in the late time response correlation. Only a minor phase error exists and the model appears to be slightly over-damped. The comprehensive error factor for this sensor comparison was below 0.9 in all three cases, with the majority of the error

due to the phase error. As in the previous two shots compared, significantly better correlation was observed when using measured data from accelerometers than with velocity meter data.

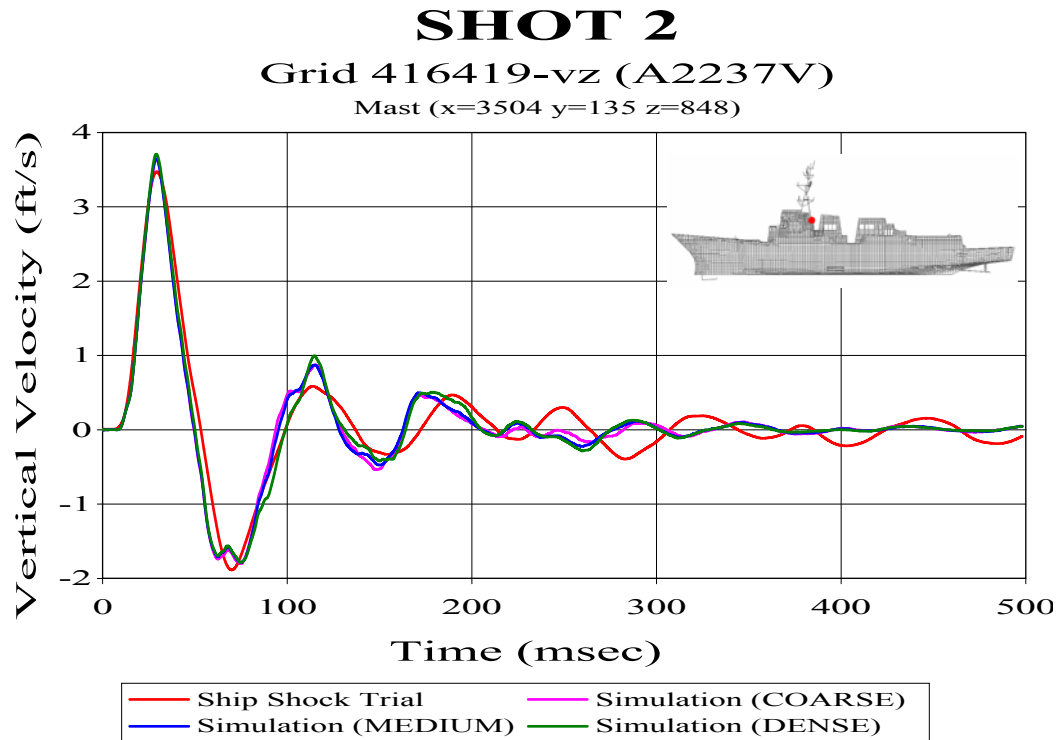


Figure 63. Mast Sensor A2237V

E. QUALITATIVE COMPARISON

In conducting the fluid mesh density comparisons, several trends emerged which were prevalent in all three shot comparisons. In all cases, the predicted response correlation was better when comparing sensors mounted higher up in the structure. Figure 64 shows the error trend in relation to the vertical position on the ship. This plot was developed by averaging all nine shot comparisons at each vertical region of the ship. This plot shows the significant improvement in correlation in the higher regions of the structure. This improvement can be contributed to a good fluid and structural model, accurate proportional structural damping coefficient, and less measured data drift. The decrease in correlation in the lower regions may be due to the fact that the response is generally more dramatic in this region amplifying any error between the predicted and measured response. An additional source of error may be due to the fact that the model,

though accounting for the liquid loading mass, does not model the fluid-structure interface in the water compensated fuel oil tanks which line the majority of the lower hull. To do this would require an extraordinary amount of effort due to the complex geometries inherent to the inner regions of these tanks. The fluid in these tanks most certainly has an effect on the response of the actual ship.

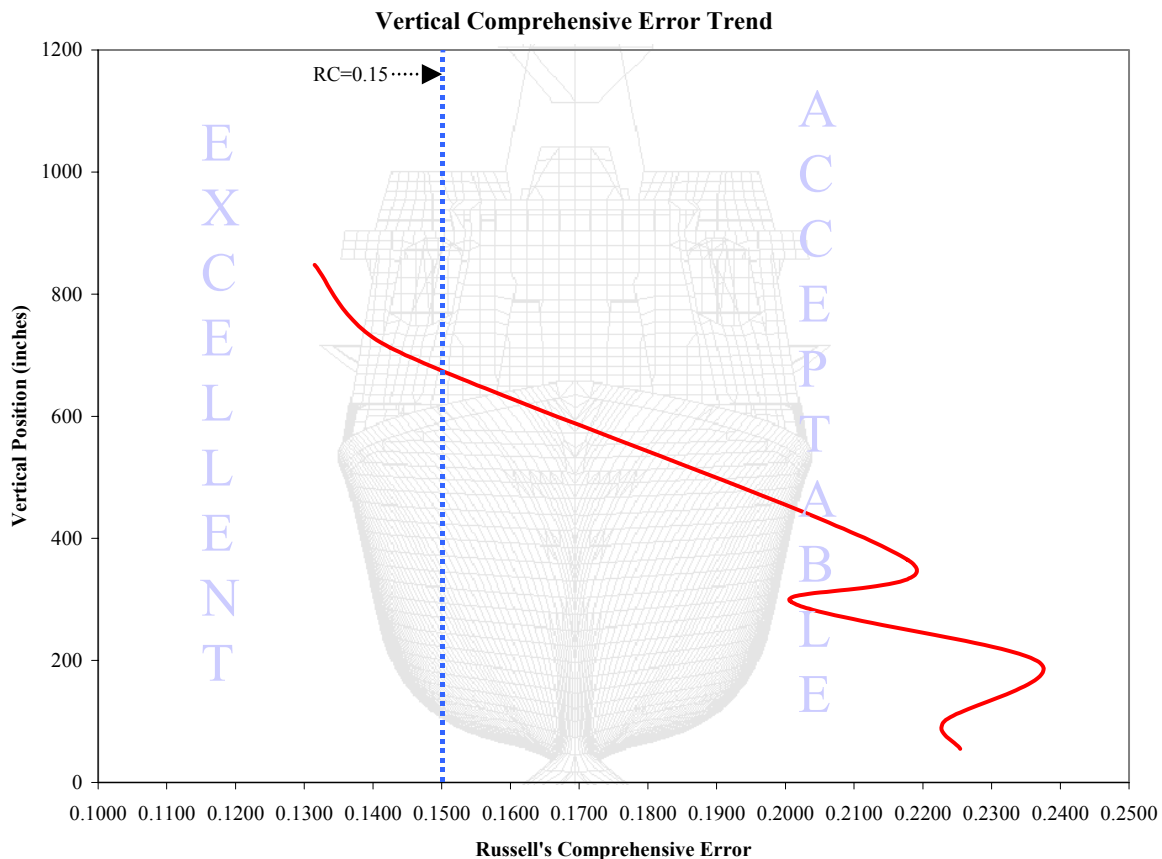


Figure 64. Average Russell's Comprehensive Error Factor Vertical Trend

One significant reason for this improved correlation in the higher regions of the ship could be due to the fact that many of the sensors used in the comparisons in these regions were accelerometers. Comparisons made using integrated accelerometer data showed significantly better correlation between the predicted and measured response than those comparisons made using velocity meter data. As shown in several of the plots, much of this error can be contributed to the drift in the velocity meter data. While some integrated accelerometer plots required minor drift correction, the majority of the plots

showed no apparent drift. In sharp contrast to this, all of the velocity meter plots showed substantial late time drift and required considerable manipulation of the data to make a valid comparison with the predicted velocity response. Table 19 shows the average comprehensive errors for each shot based on whether the measured data was from an accelerometer or a velocity meter. Each value is an average of all three meshes compared for each shot.

Table 19. Accelerometer vs. Velocity Meter Correlation Comparison

SENSOR	AVERAGE COMPREHENSIVE RUSSELL'S ERROR FACTOR			
	Shot 1	Shot 2	Shot 3	Overall
Accelerometer	0.1845	0.1434	0.1910	0.1730
Velocity Meter	0.2269	0.2196	0.2315	0.2260

As shown in Table 19, the difference in correlation between accelerometer data and velocity meter data is significant with an overall average comprehensive error factor difference of over 0.05. It can be argued that at least some of this improvement can be contributed to many of these accelerometers being mounted higher. While this is true, Tables 13, 16, and 18 show that in other regions of the ship where accelerometers were used there is significant improvement over the surrounding velocity meter correlations.

Overall, using the comparison of the fluid mesh displaying the best correlation for each shot, the average Russell's magnitude, phase, and comprehensive error factors were -0.0401 , 0.2051 , and 0.1995 respectively. Out of a total of 90 comparisons made for all three shots, 84 (93.3%) predictions were considered acceptable, 11 (12.2%) were considered excellent, and 6 (6.7%) were considered unacceptable. Shot 2 showed the best correlation ($RC_{\text{mean}} = 0.1912$) overall while Shot 3 showed the least ($RC_{\text{mean}} = 0.2114$).

F. EXTENDED DEPTH FLUID MODEL

The effect of the depth of the surrounding fluid on underwater shock simulation predictions was the focus of study in Reference [21]. This study used four different models of various sizes and compared the resulting simulation predictions with the

measured DDG 81 response for Shot 3. Two of these fluid models included one model having a depth approximately equal to the cavitation depth and the other model having a depth of twice this value. This study concluded that while the cavitation depth model yielded excellent predictions, the model having a depth twice the cavitation depth yielded poor predictions. Table 20 shows the resultant Russell's error factors doing a 120 msec comparison using this 2X-cavitation depth model. The results of the cavitation depth model were shown previously in Table 8.

Table 20. 2X Cavitation Fluid Mesh Russell's Error Comparison (120 msec) [from Ref. 21]

Sensor	RM	RP	RC
V2000V	-0.6022	0.3148	0.6022
V2002V	-0.3407	0.1664	0.3360
V2007V	-0.4032	0.2202	0.4071
V2008VI	-0.3683	0.2736	0.4066
V2009VI	-0.3466	0.1847	0.3481
V2010V	-0.3472	0.1959	0.3533
V2011VI	-0.3287	0.1901	0.3365
V2012VI	-0.3097	0.1485	0.3044
V2013V	-0.3048	0.1543	0.3027
V2014V	-0.2080	0.1621	0.2337
V2016V	-0.2350	0.1687	0.2564
V2018VI	-0.3806	0.2692	0.4132
V2019V	-0.3924	0.2887	0.4317
V2020V	-0.4265	0.2606	0.4430
V2026V	-0.2738	0.2147	0.3084
V2032V	-0.4255	0.1587	0.4024
V2034V	-0.3917	0.1392	0.3684
V2035V	0.4147	0.1442	0.3891
V2108V	-0.3856	0.1992	0.3846
V2124V	-0.3149	0.1734	0.3186
V2125V	-0.3355	0.2027	0.3474
Average	-0.3193	0.2014	0.3664

The two models compared in the study had the same number of hull normal elements. This resulted in the 2X-cavitation depth model having a hull normal spacing between elements in the outer mesh twice that of the cavitation depth model. As has

been shown in the previous comparisons, this large of variation in the mesh density would certainly have an effect on the resulting predictions.

To test whether or not increasing the mesh density of this 2X-cavitation depth model would improve the prediction correlation, a similar test was conducted using the 3rd generation model. This model was constructed to twice the actual cavitation depth but having a normal fluid element spacing equal to the dense cavitation depth model compared earlier. The resulting 120 msec error comparison for this model is shown below in Table 21. This comparison shows only the sensors compared in Reference [21].

Table 21. 2X Cavitation Depth Fluid Mesh Russell's Error Comparison (120 msec)

Sensor	RM	RP	RC
V2000V	-0.4389	0.2537	0.4492
V2002V	-0.1658	0.2096	0.2368
V2007V	-0.3123	0.2393	0.3487
V2008VI	-0.2991	0.2304	0.3346
V2009VI	-0.2467	0.1875	0.2746
V2010V	-0.3325	0.1950	0.3416
V2011VI	-0.3105	0.1649	0.3116
V2012VI	-0.2939	0.1500	0.2925
V2013V	-0.2929	0.1417	0.2884
V2014V	-0.2436	0.1790	0.2679
V2016V	-0.2643	0.1649	0.2760
V2018VI	-0.3270	0.1535	0.3201
V2019V	-0.3503	0.1795	0.3489
V2020V	-0.3600	0.1945	0.3626
V2026V	-0.2825	0.2074	0.3106
V2032V	-0.3472	0.1742	0.3443
V2034V	-0.2974	0.1637	0.3008
V2035V	-0.3268	0.1958	0.3376
V2108V	-0.2996	0.1749	0.3074
V2124V	-0.2938	0.1529	0.2935
V2125V	-0.3055	0.1674	0.3088
Average	-0.30431	0.18475	0.31698

It should be noted that because this model had a depth equal to twice the minimum cavitation depth, its depth was 17 feet less than the model used in the previous study. Additionally, as shown previously, the 3rd generation model displayed measurable improvement over the 1st generation model. However, the previous study used filtered

data which was shown to reduce the error factors significantly. Assuming that these variations essentially canceled each other out, the resulting error was significantly reduced using the denser fluid mesh.

The resulting error factors while significantly reduced, were still significantly higher than the comparable cavitation depth model. A side by side 500 msec error comparison of these two models is shown in Table 22.

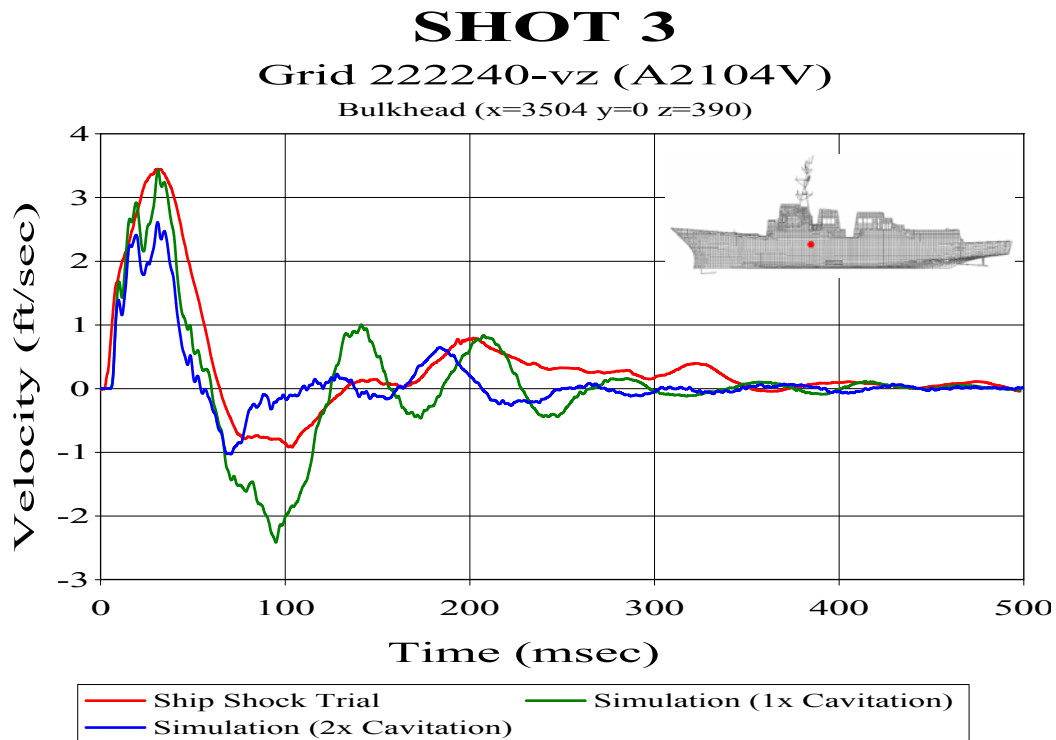
Table 22. Russell's Error Comparison: Cavitation Depth Model vs. 2X Cavitation Depth Model (500 msec)

Sensor	NODE	Bulkhead Keel	Location (in)			Dense Mesh: Cavitation Depth			Dense Mesh: 2x Cavitation		
			x	y	z	RM	RP	RC	RM	RP	RC
V2000V	120217	Keel	5328	0	82	-0.1795	0.2842	0.2979	-0.4112	0.3215	0.4626
V2002V	142489	Keel	4656	27	82	0.0762	0.2303	0.2150	-0.1692	0.2354	0.2569
V2007V	210430	Keel	4080	0	82	-0.1198	0.2883	0.2766	-0.3631	0.3075	0.4217
V2009VI	210808	Bulkhead	4080	-174	177	-0.0690	0.2144	0.1996	-0.3088	0.2332	0.3429
V2008VI	210894	Bulkhead	4080	174	177	0.0014	0.2561	0.2270	-0.3268	0.2764	0.3793
A8516V	210993	Bulkhead	4080	239	202	0.1217	0.2547	0.2502	-0.2536	0.3552	0.3868
A4701V	211371	Bulkhead	4080	0	280	0.0282	0.2149	0.1921	-0.3064	0.2283	0.3386
V2107V	211904	Bulkhead	4080	-312	390	-0.0295	0.2420	0.2161	-0.2907	0.3048	0.3733
V2108V	212196	Bulkhead	4080	312	390	-0.0216	0.2348	0.2089	-0.3463	0.2387	0.3728
V2010V	220589	Keel	3504	0	86	-0.1729	0.2549	0.2730	-0.3880	0.2768	0.4224
V2012VI	221102	Bulkhead	3504	-216	177	-0.0777	0.1935	0.1848	-0.3195	0.2137	0.3406
V2011VI	221188	Bulkhead	3504	216	177	-0.1468	0.2398	0.2468	-0.3784	0.2799	0.4171
V2013V	221601	Bulkhead	3504	0	280	-0.0342	0.1970	0.1772	-0.3202	0.2338	0.3514
V2124V	222060	Bulkhead	3504	-375	390	-0.0872	0.1882	0.1838	-0.3196	0.1945	0.3296
A2104V	222240	Bulkhead	3504	0	390	0.0207	0.1760	0.1571	-0.2873	0.1712	0.2964
V2125V	222436	Bulkhead	3504	375	390	-0.1264	0.2264	0.2298	-0.3494	0.2673	0.3898
V2014V	230461	Keel	2952	0	86	-0.0861	0.2501	0.2344	-0.2798	0.2355	0.3194
A3565V	231696	Bulkhead	2952	-81	317	0.0646	0.2003	0.1865	-0.1765	0.1842	0.2261
V2016V	242399	Keel	2544	0	116	-0.0879	0.2085	0.2005	-0.2804	0.1971	0.3037
V2026V	312302	Keel	1992	0	55	-0.0910	0.2312	0.2202	-0.2819	0.2225	0.3183
A2310V	320746	Bulkhead	1536	0	177	-0.1037	0.1635	0.1716	-0.3346	0.1806	0.3370
V2034V	330759	Keel	1152	-135	193	-0.0966	0.1537	0.1608	-0.3223	0.1813	0.3277
V2032V	330764	Keel	1152	0	196	-0.1534	0.2103	0.2307	-0.3700	0.2030	0.3740
V2035V	330769	Keel	1152	135	193	-0.1598	0.2233	0.2434	-0.3755	0.2394	0.3947
V2019V	340167	Keel	672	0	197	-0.1344	0.2266	0.2335	-0.3444	0.2366	0.3703
V2018VI	340992	Bulkhead	672	0	365	-0.1212	0.1830	0.1945	-0.3204	0.1938	0.3319
V2020V*	350052	Keel	288	0	211	-0.1499	0.2178	0.2343	-0.3804	0.2160	0.3877
A2413V	350220	Bulkhead	288	0	273	-0.1315	0.2150	0.2233	-0.3701	0.2153	0.3795
A2116V	414367	Bulkhead	3504	0	702	0.0353	0.1789	0.1616	-0.2645	0.1629	0.2753
A2109V	414953	Bulkhead	4059	0	723	0.1353	0.1846	0.2028	-0.1999	0.1936	0.2466
A2240V	416269	Bulkhead	3504	-135	848	0.0122	0.1747	0.1552	-0.2610	0.1525	0.2679
A2237V	416419	Bulkhead	3504	135	848	0.0613	0.1877	0.1750	-0.2626	0.1848	0.2846
Sum(E(X))						-1.82320	6.90470	6.76420	-9.96280	7.33730	11.02690
Sum(E(X^2))						0.34947	1.52398	1.47020	3.21065	1.75589	3.89648
Mean						-0.05698	0.21577	0.21138	-0.31134	0.22929	0.34459
Variation						0.00792	0.00110	0.00130	0.00351	0.00237	0.00312

*350msec comparison due to long time sensor data inaccuracy.

The cavitation depth fluid model produced significantly better predictions than the 2X-cavitation depth model. In fact, few of the 2X-cavitation depth model predictions even met the acceptable criteria. Though displaying significant amounts of error both in phase and in magnitude, the majority of the comprehensive error for the 2X-cavitation depth model is due to the magnitude error. This is in sharp contrast to the cavitation depth model where the majority of the comprehensive error is due to the phase error. The average phase error of the 2X-cavitation fluid model prediction is only slightly greater than the cavitation depth fluid model prediction. By comparison, the magnitude error of the 2X-cavitation model is nearly six times that of the cavitation depth model.

Of additional interest is the relatively small increase in the overall error of the 500 msec comparison compared with the 120 msec comparison. Here the majority of the increase in the comprehensive error is due to the increase in the phase error. This indicates that the majority of the magnitude error occurs in the early time response, where the peak response occurs. To help visualize this, Figures 65 and 66 show the velocity plot comparisons for sensors A2104V and V2034V respectively.



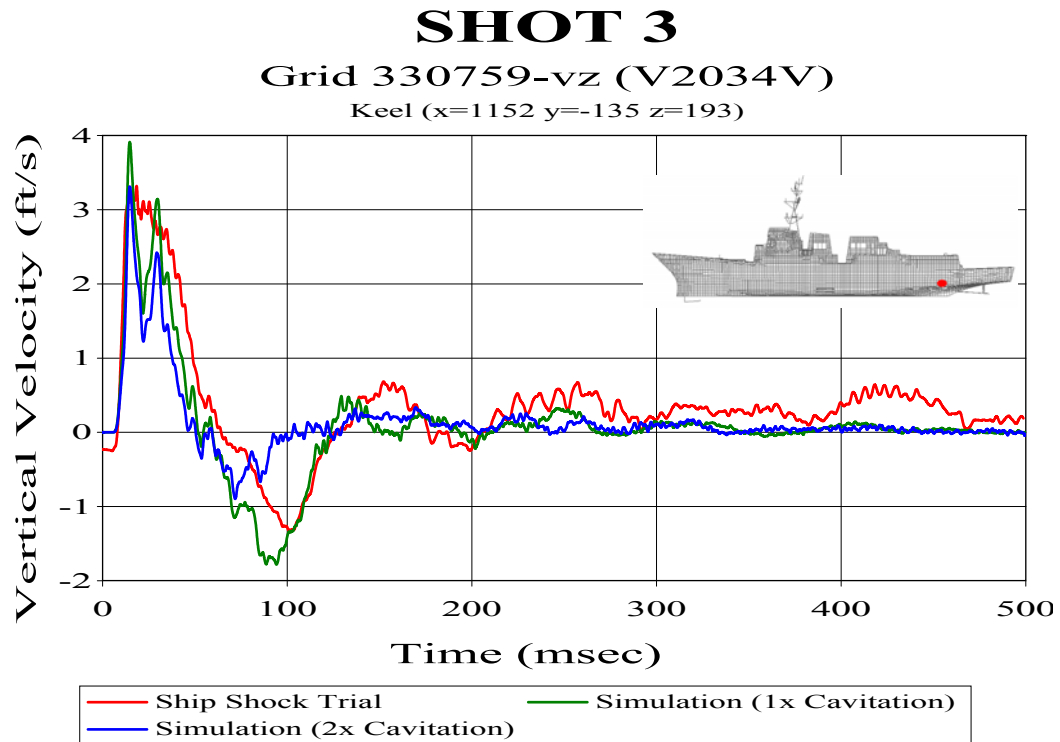


Figure 66. Keel Sensor V2034V

As is shown in these plots, the larger fluid mesh prediction significantly underestimates the initial kick and recovery of the structure. This portion of the response is due primarily to the incident pressure wave. This gives evidence of losses occurring in the incident pressure wave as the DAA boundary is moved further away from the hull. Dr. John DeRuntz, author of the USA code, suggests that these losses could be due to the extremely large fluid mesh causing dispersion of the shock wave front [Ref. 32].

THIS PAGE INTENTIONALLY LEFT BLANK

VII. CONCLUSIONS AND RECOMMENDATIONS

Creating a virtual underwater shock environment has proven to be a valid method of predicting the response of a surface ship to a variety of underwater explosions. This thesis has investigated simulation of three separate underwater explosions, all of which produced acceptable predictions overall. These underwater explosions originated from abeam the ship to off the bow, slightly forward of the ship. While the accuracy of these predictions falls off in regions of the ship furthest from the shot, the predictions in these regions still remain acceptable with only a few exceptions. The accuracy of the simulation predictions was shown to have little sensitivity to stand-off distance.

The depth of the fluid model had the largest impact on the accuracy of the predictions. A fluid model having a depth equal to the actual cavitation depth at the region closest to the charge resulted in the most accurate predictions. Small deviations of only a few feet significantly impacted the accuracy of the predictions.

Similarly, a fluid model having a depth equal to twice the cavitation depth yielded unacceptable predictions, significantly worse than the cavitation depth fluid model. This disparity appears to be primarily due to losses occurring in the incident pressure wave front.

The fluid model mesh density was shown to have a significant effect on the simulation predictions. For shocks originating from abeam the ship, a fluid mesh having a higher mesh density was shown to provide substantially better predictions. For the shot off the bow, closer to being an end-on shot than a beam shot, the coarser mesh was shown to produce the most accurate predictions. It is theorized that this disparity is due to the tangential propagation of the shock wave and the resultant fluid particle velocities. In this direction, the coarser mesh has more preferable fluid element aspect ratios than the higher density meshes.

Small variations in the quality of the fluid mesh were shown to have measurable but minor effects on the accuracy of the overall simulation predictions. Although this study did not investigate the effects of gross variations in the quality of the mesh, minor

improvements in the quality of the mesh were shown to result in overall improvement, but mixed results locally. Variables such as the size of the fluid mesh, the quality of the measured data, and environmental factors appear to outweigh any benefit gained by making small improvements in the quality of the mesh.

The correlation of the simulation predictions was found to be substantially better when being compared with accelerometer measured data than with velocity meter measured data. Substantial drift is apparent in nearly all of the velocity meter data. Data collected from accelerometer displayed significantly less drift even after being integrated. This suggests that a substantial amount of the calculated error may be due not to error in the simulation predictions, but in the measured data itself.

The study conducted in this paper has merely helped to prop open the door for further research using virtual underwater shock environments. By validation of underwater explosion simulations, the possibilities for the future use of virtual underwater shock environments are endless. Some recommendations for future study include:

1. In addition to producing significantly better predictions for beam shots, the dense fluid mesh simulations required considerably more time to process, especially as the size of the mesh was increased. This is counterproductive to simulating more of the overall structural response to underwater explosions. The model created in the course of this study is easily modified to model a wide range of underwater environments. It is recommended that this model be used to study the effects of reducing the size of the charge while maintaining the same shock factor. This would reduce the size of the fluid model required, allowing for a denser mesh to be used without having a large time requirement to process the simulation.

2. This study used models having a depth equal to the cavitation depth at the location on the keel closest to the charge. As the wave propagates outward the actual cavitation depth increases. This fluid model may be utilized to study the effects of contouring the depth of the fluid mesh to correspond with the actual cavitation depth throughout the length of the ship.

3. This study investigated blue water underwater explosions where bottom reflection is not a consideration. The evolution of the existing threats in recent years has placed an increased emphasis on littoral operations. In shallow water reflection of the shock wave off the ocean bottom and the bubble pulse cannot be ignored. Recent enhancements to the codes utilized in this study allow the capability to simulate time dependent bottom reflection and bubble pulse. It is recommended that the simulations be extended out in time to predict the structural response to these phenomena.

4. Recent studies, including the study conducted in this paper, have focused primarily on the velocity and acceleration response of the ship in order to validate the use of underwater shock simulation. The purpose for subjecting ship systems to an underwater shock is to ensure that the systems can survive the combat shock environment. It is suggested that underwater shock simulation be carried a step further by using simulation to conduct damage surveys of ship systems when tested at design level using more severe shock simulations.

THIS PAGE INTENTIONALLY LEFT BLANK

APPENDIX A. DDG 81 VERTICAL VELOCITY RESPONSE PLOTS

A. SHOT 1

The following velocity plots are from the Shot 1 fluid mesh density comparison. The Russell's error factors following each figure caption are from the coarse fluid model comparison. This fluid model mesh showed the best correlation overall for this shot.

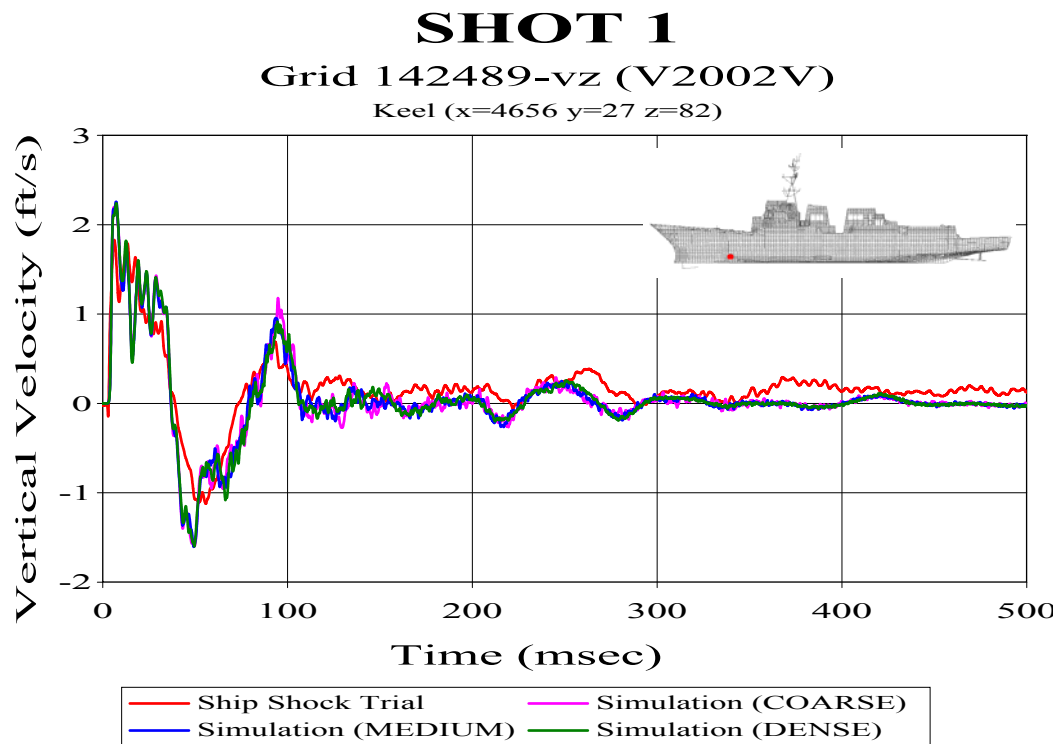


Figure 67. Keel Sensor V2002V: (RM=0.0772, RP=0.1755, RC=0.1699)

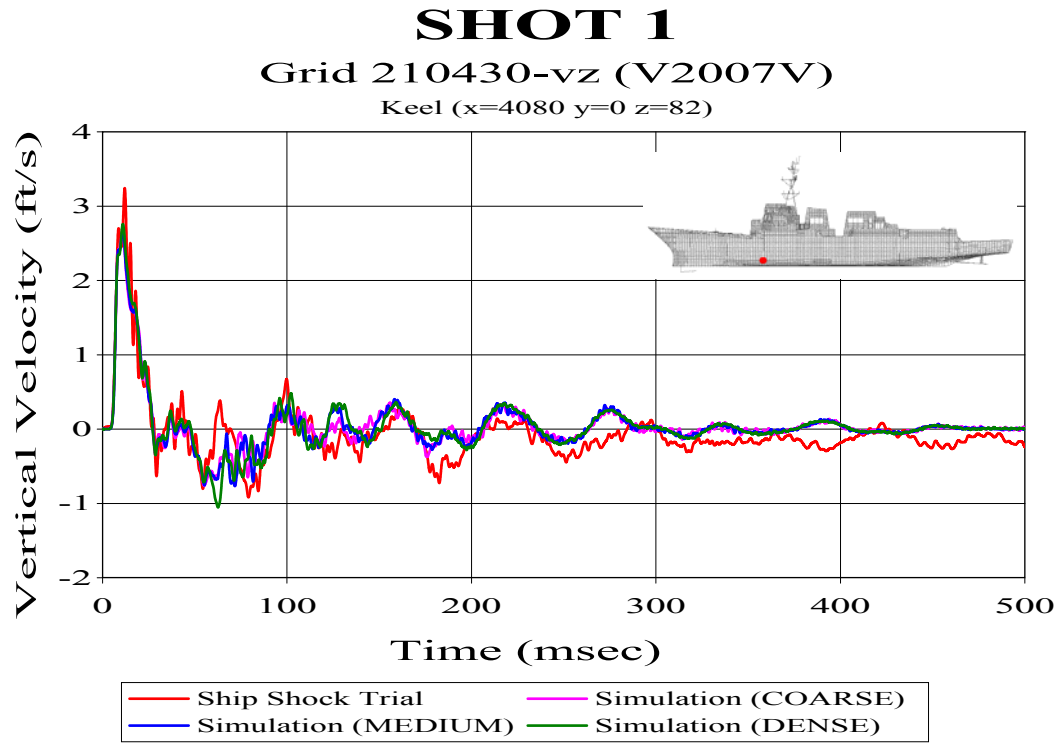


Figure 68. Keel Sensor V2007V: (RM=-0.1178, RP=0.1760, RC=0.1877)

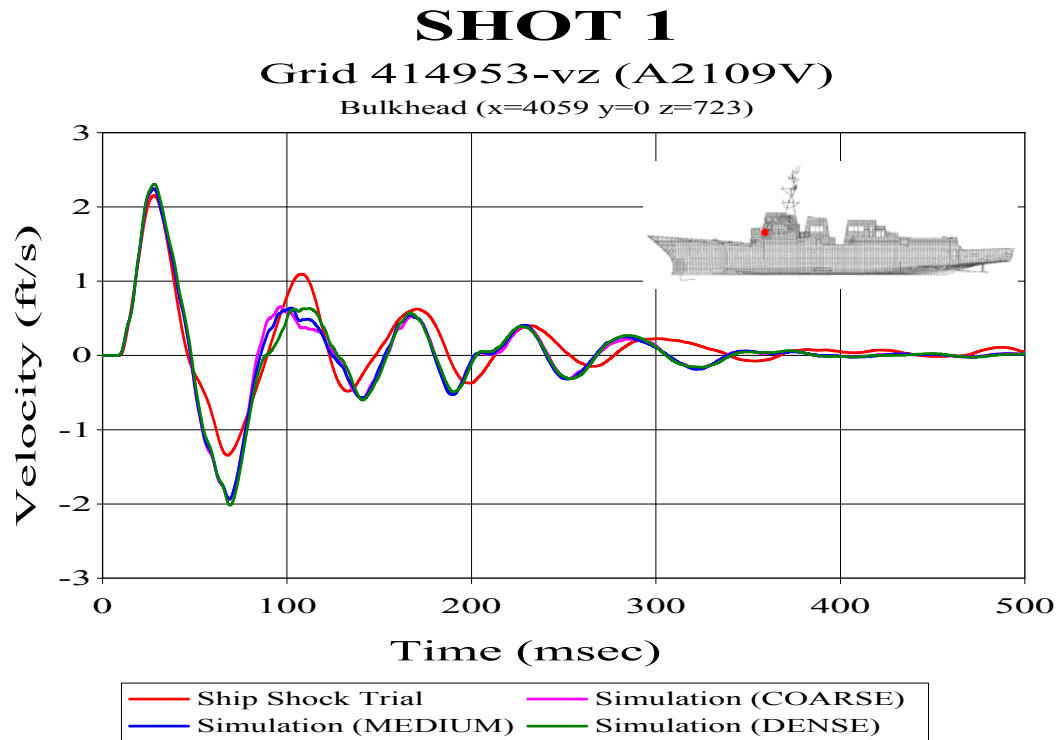


Figure 69. Bulkhead Sensor A2109V: (RM=-0.0679, RP=0.0848, RC=0.0962)

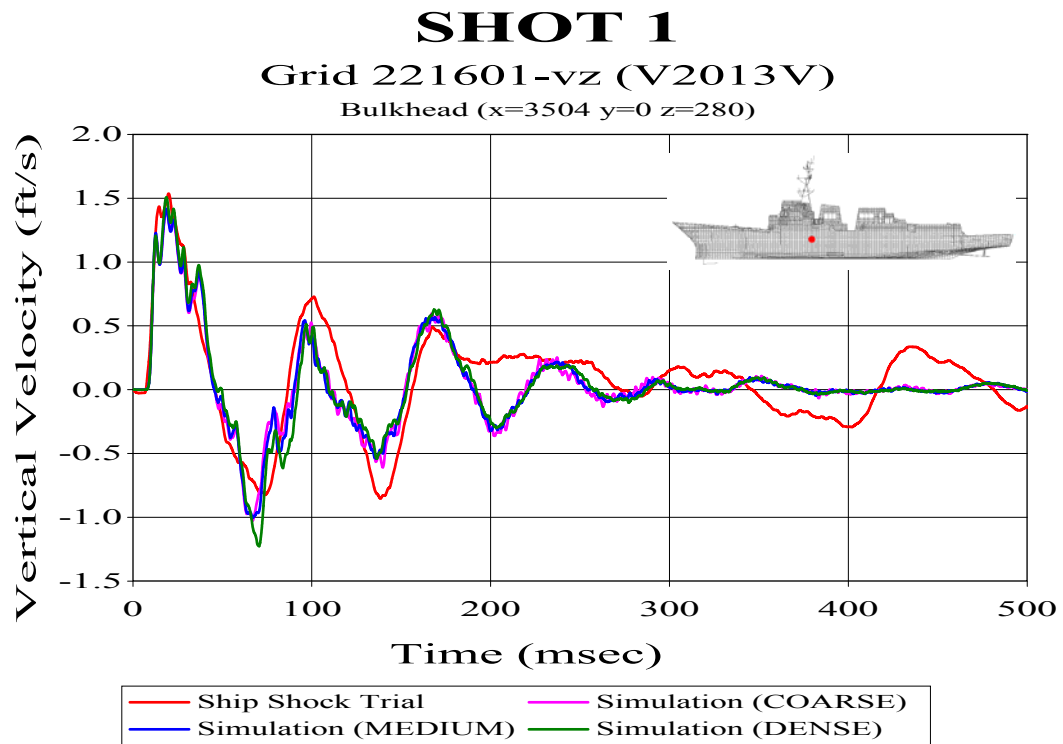


Figure 70. Bulkhead Sensor V2013V: (RM=-0.1366, RP=0.1819, RC=0.2016)

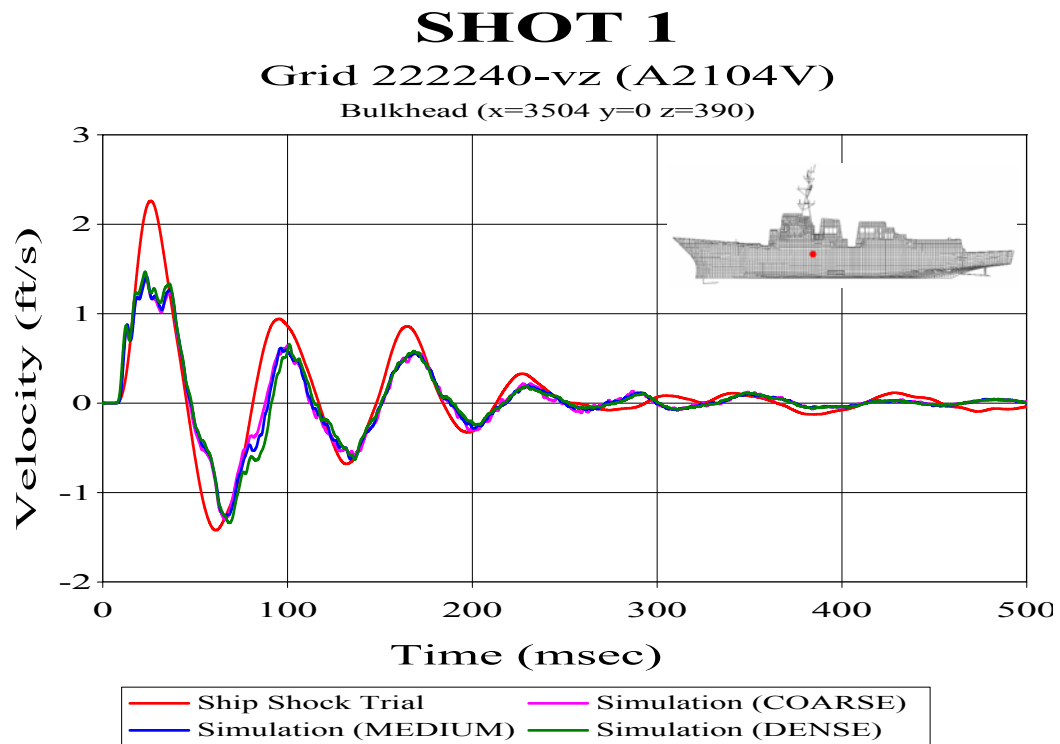


Figure 71. Bulkhead Sensor A2104V: (RM=-0.2235, RP=0.1184, RC=0.2241)

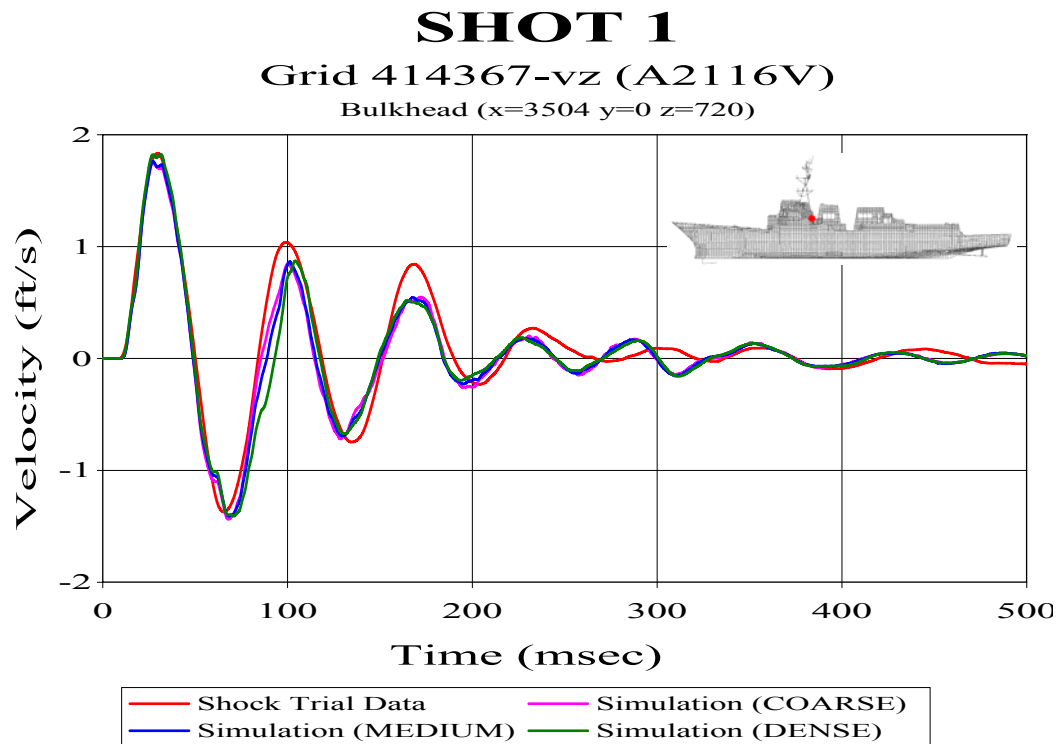


Figure 72. Bulkhead Sensor A2116V: (RM=-0.0679, RP=0.0848, RC=0.0962)

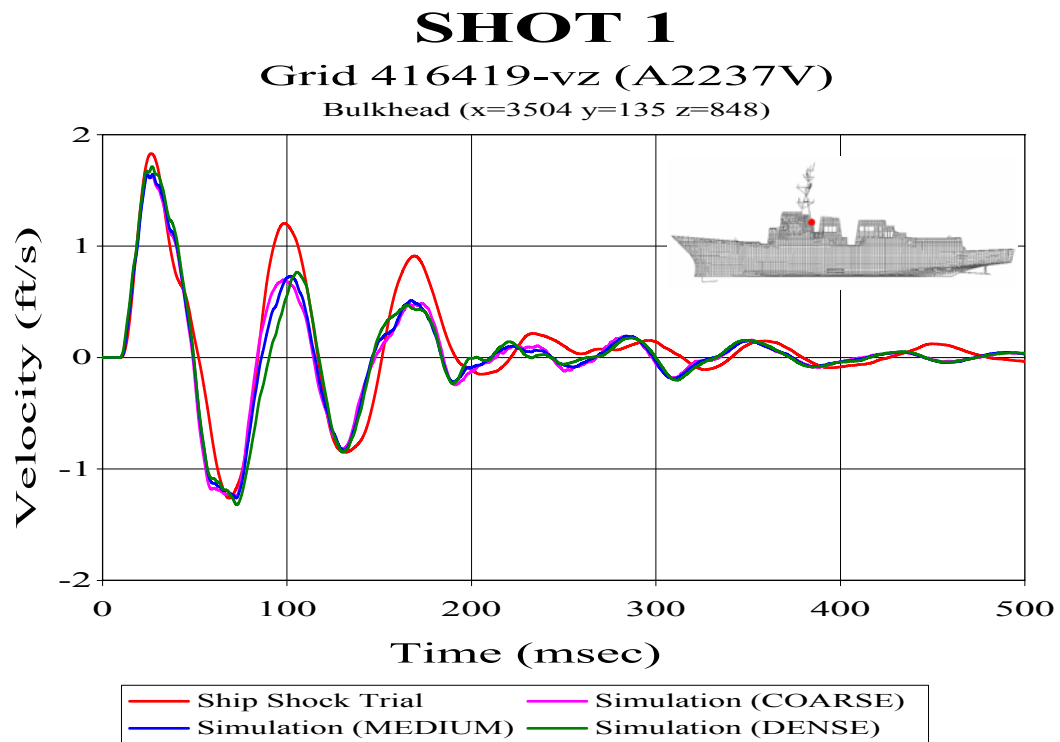


Figure 73. Bulkhead Sensor A2237V (RM=-0.0906, RP=0.1203, RC=0.1334)

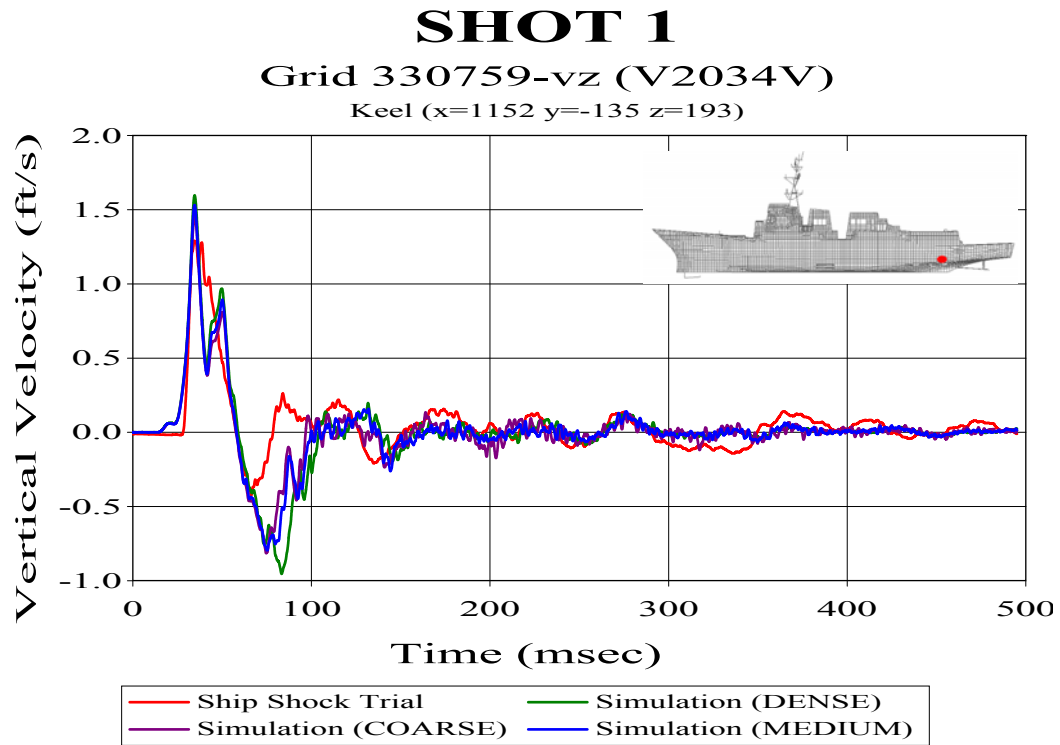


Figure 74. Keel Sensor V2034V: (RM=0.0296, RP=0.2233, RC=0.1996)

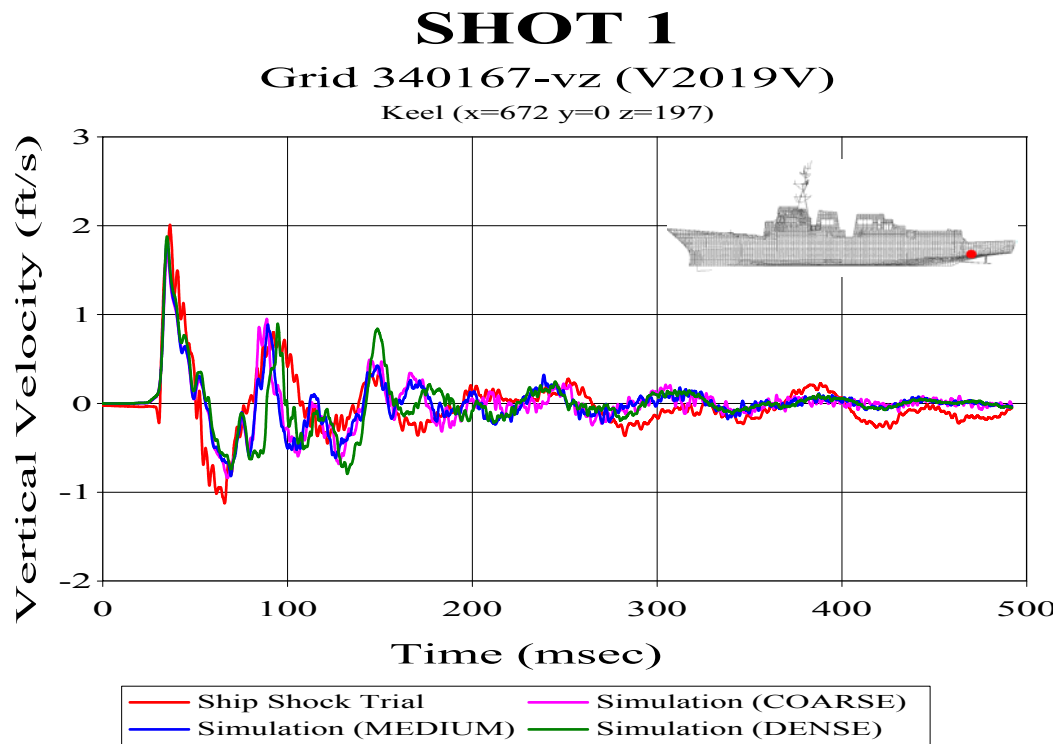


Figure 75. Keel Sensor V2019V: (RM=-0.1463, RP=0.2447, RC=0.2526)

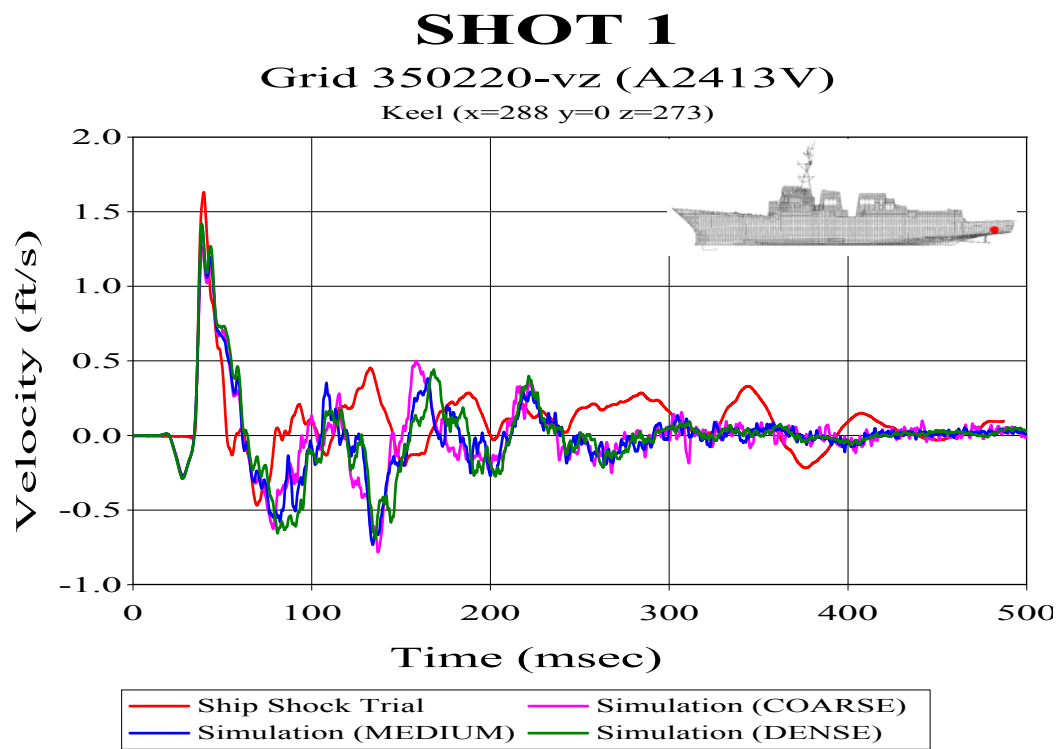


Figure 76. Keel Sensor A2413V: (RM=0.0171, RP=0.3649, RC=0.3238)

B. SHOT 2

The following velocity plots are from the Shot 2 fluid mesh density comparison. The Russell's error factors following each figure caption are from the dense fluid model comparison. This fluid model mesh showed the best correlation overall for this shot.

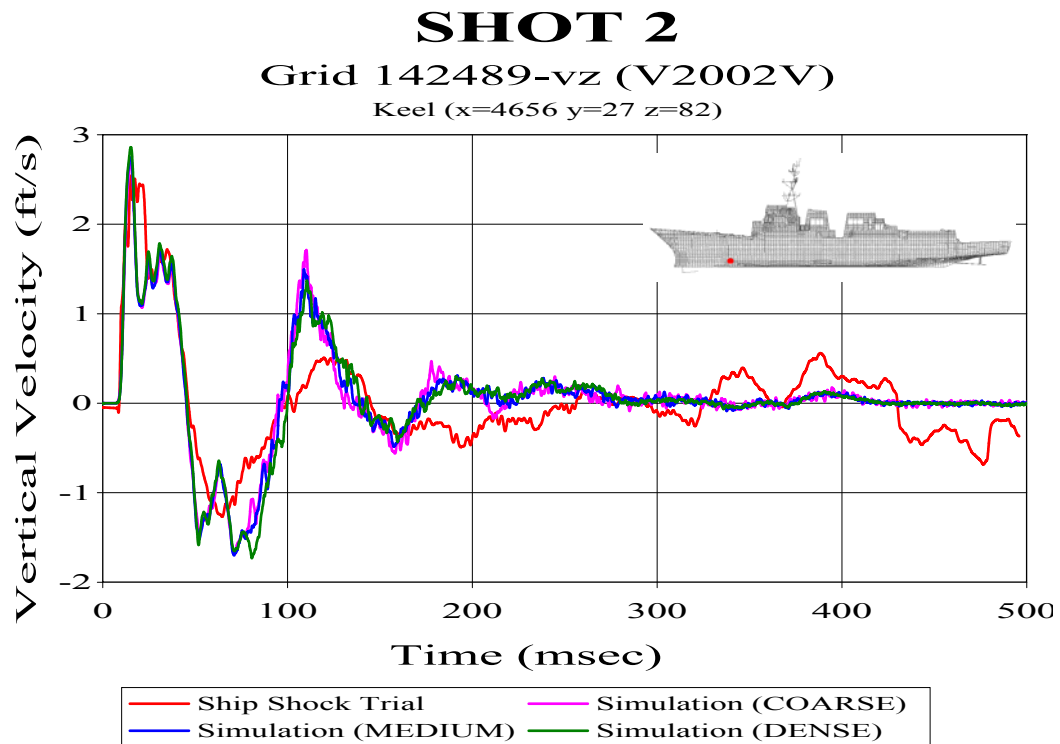


Figure 77. Keel Sensor V2002V: (RM=0.0579, RP=0.2001, RC=0.1846)

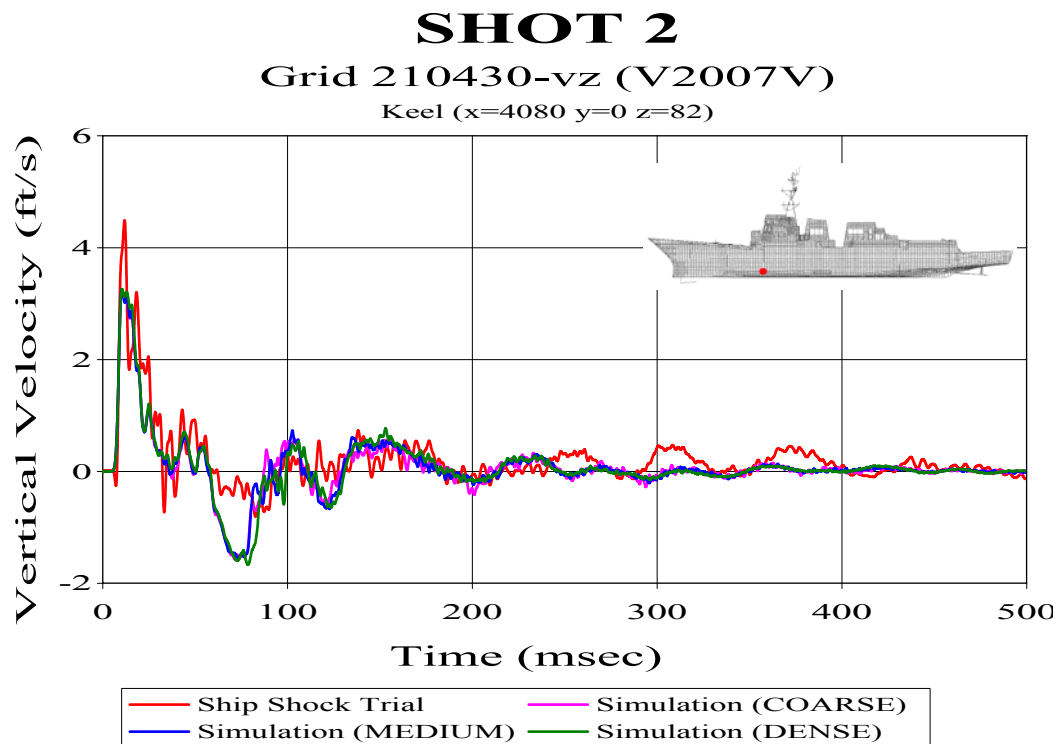


Figure 78. Keel Sensor V2007V: (RM=-0.0245, RP=0.2092, RC=0.1866)

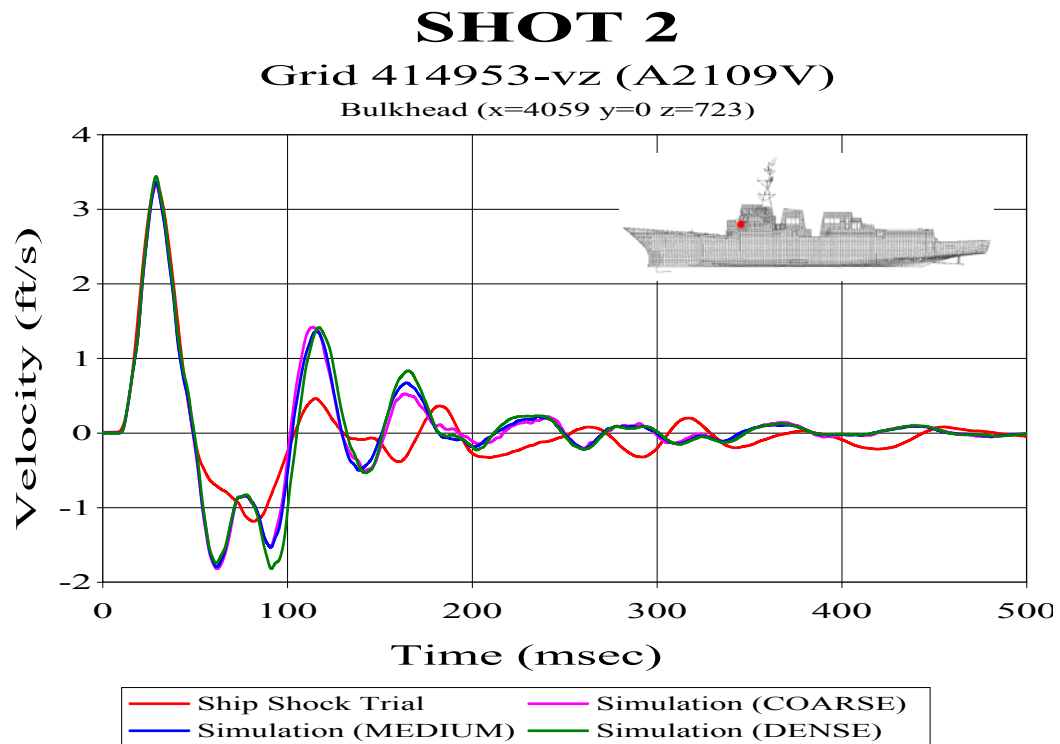


Figure 79. Bulkhead Sensor A2109V: (RM=0.1170, RP=0.1647, RC=0.1790)

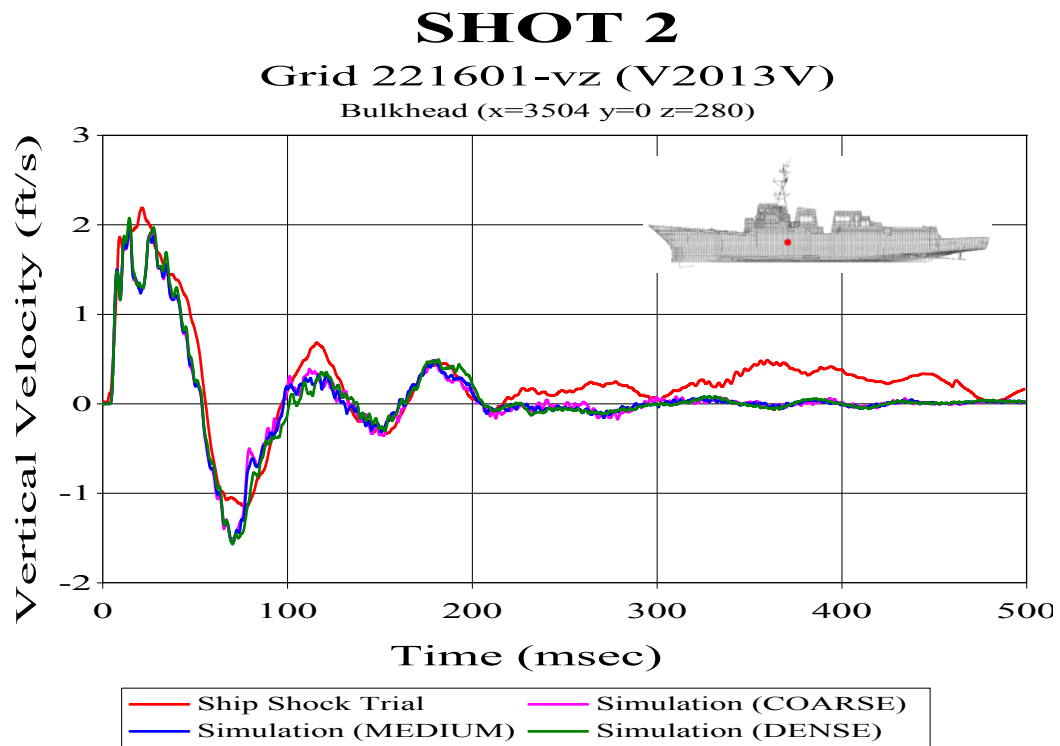


Figure 80. Bulkhead Sensor V2013V: (RM=-0.1049, RP=0.1420, RC=0.1565)

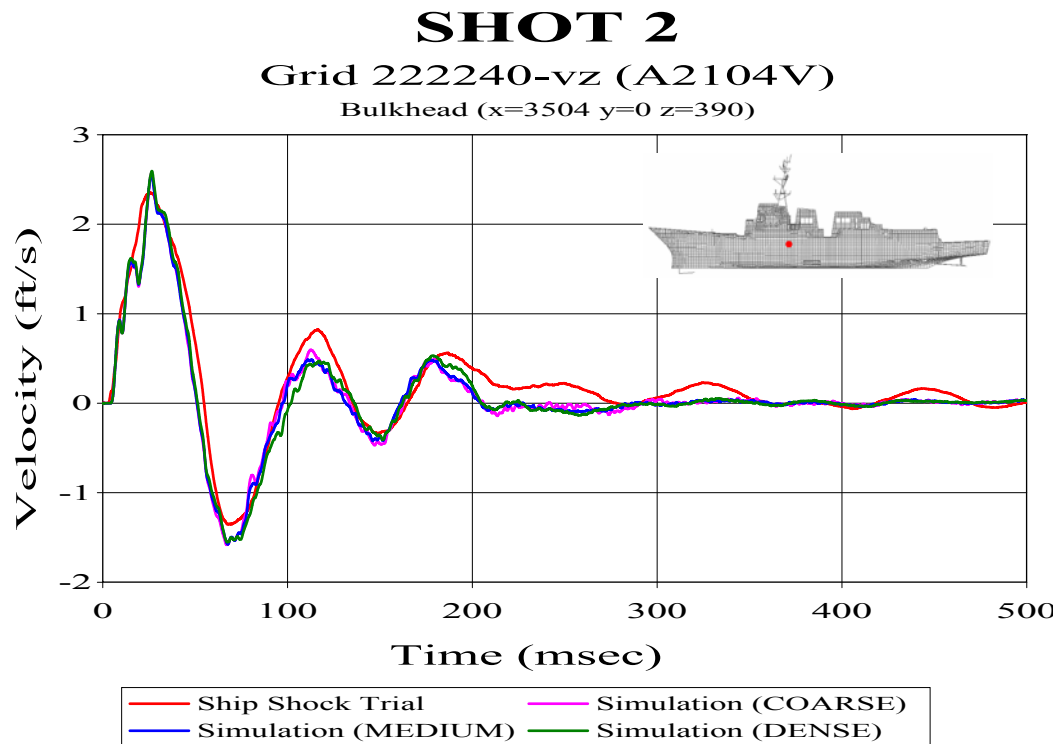


Figure 81. Bulkhead Sensor A2104V: (RM=-0.0388, RP=0.0953, RC=0.0912)

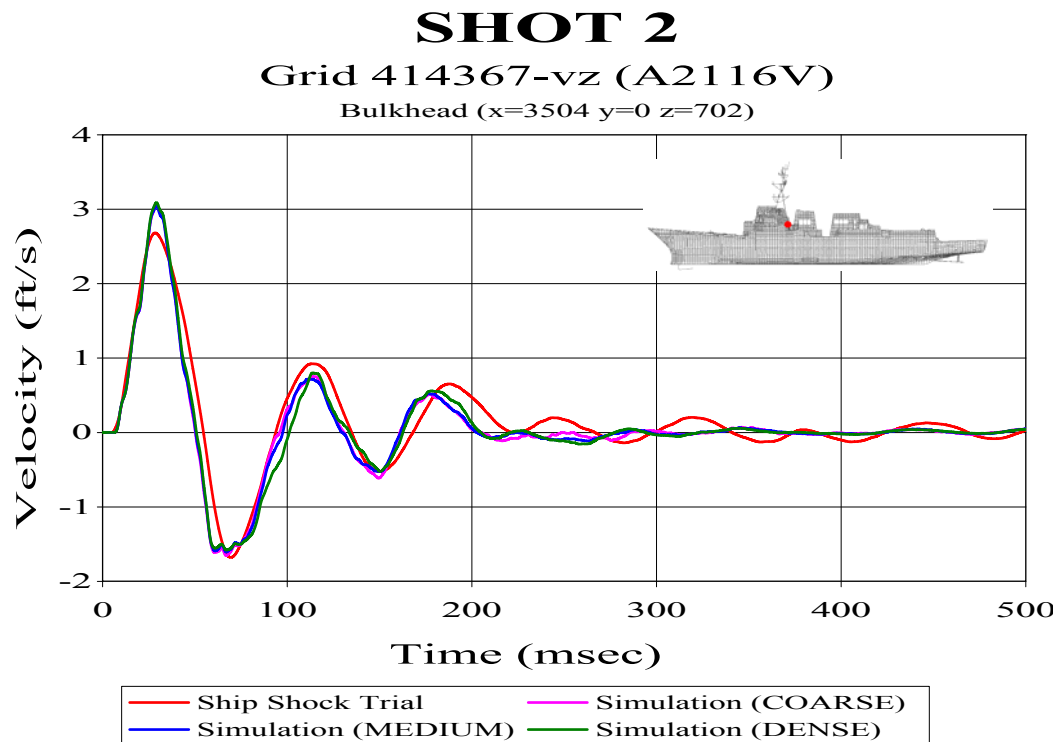


Figure 82. Bulkhead Sensor A2116V: (RM=0.0070, RP=0.1003, RC=0.0891)

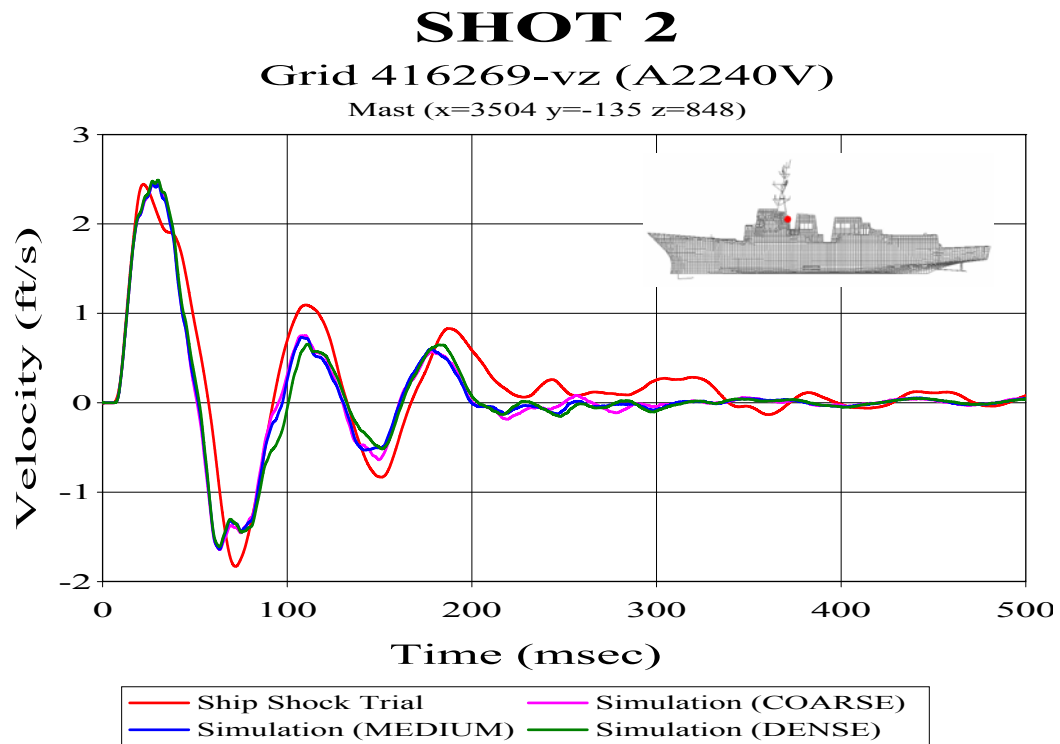


Figure 83. Mast Sensor A2240V: (RM=-0.0626, RP=0.1335, RC=0.1307)

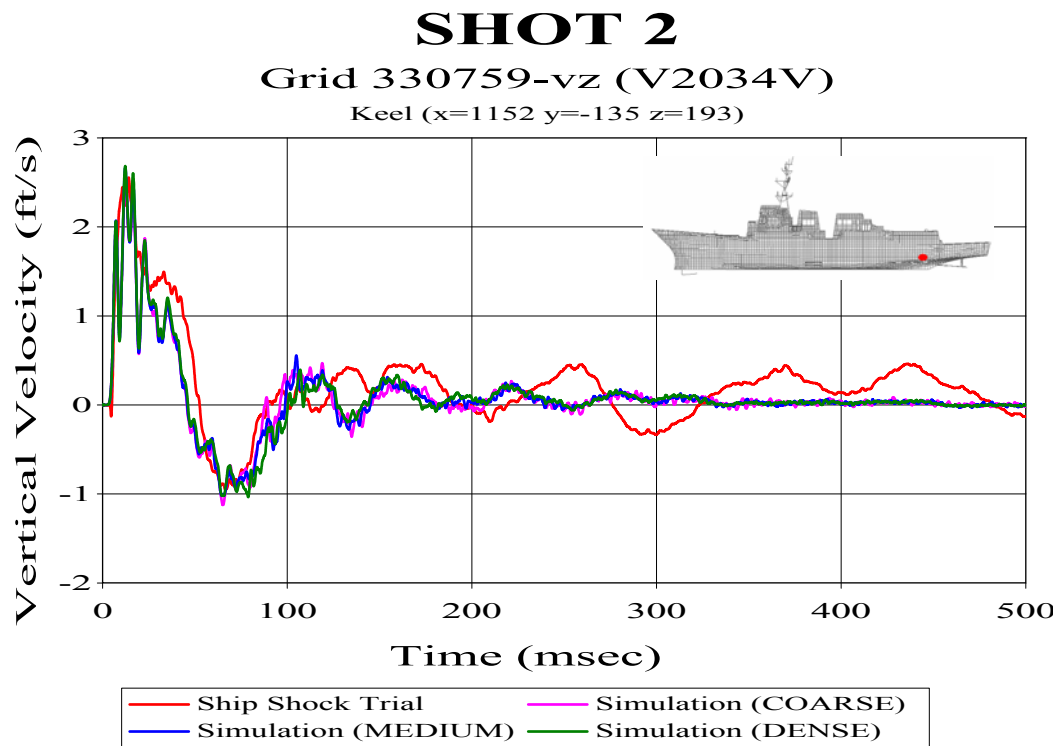


Figure 84. Keel Sensor V2034V: (RM=-0.1442, RP=0.1874, RC=0.2095)

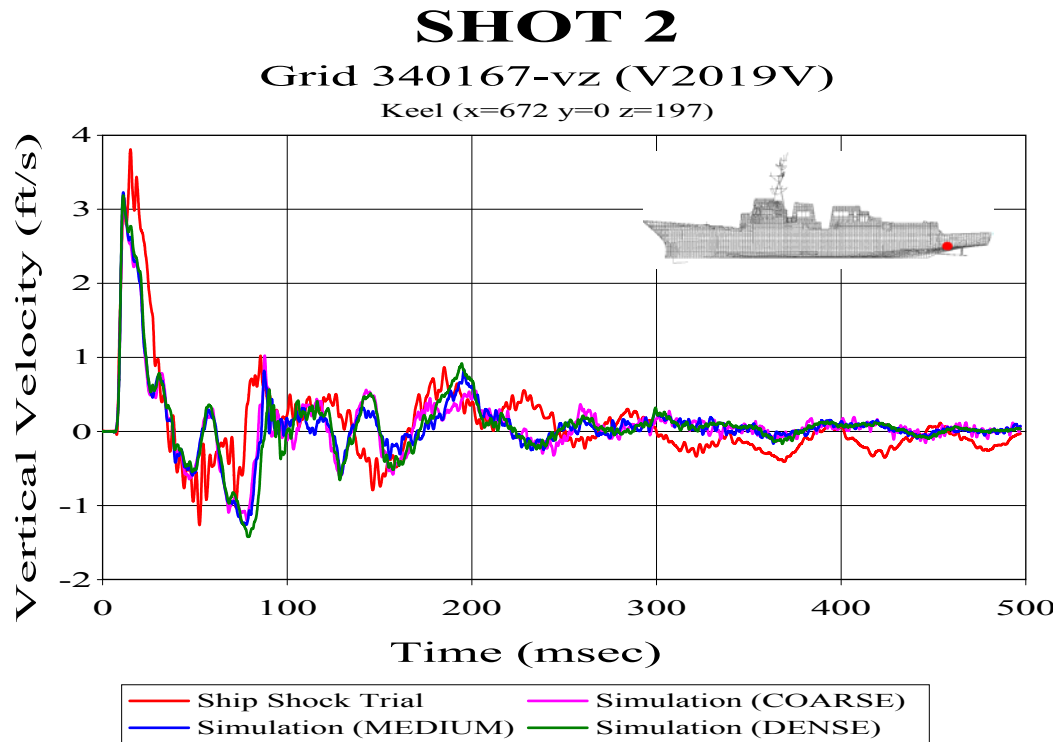


Figure 85. Keel Sensor V2019V: (RM=-0.1327, RP=0.2391, RC=0.2423)

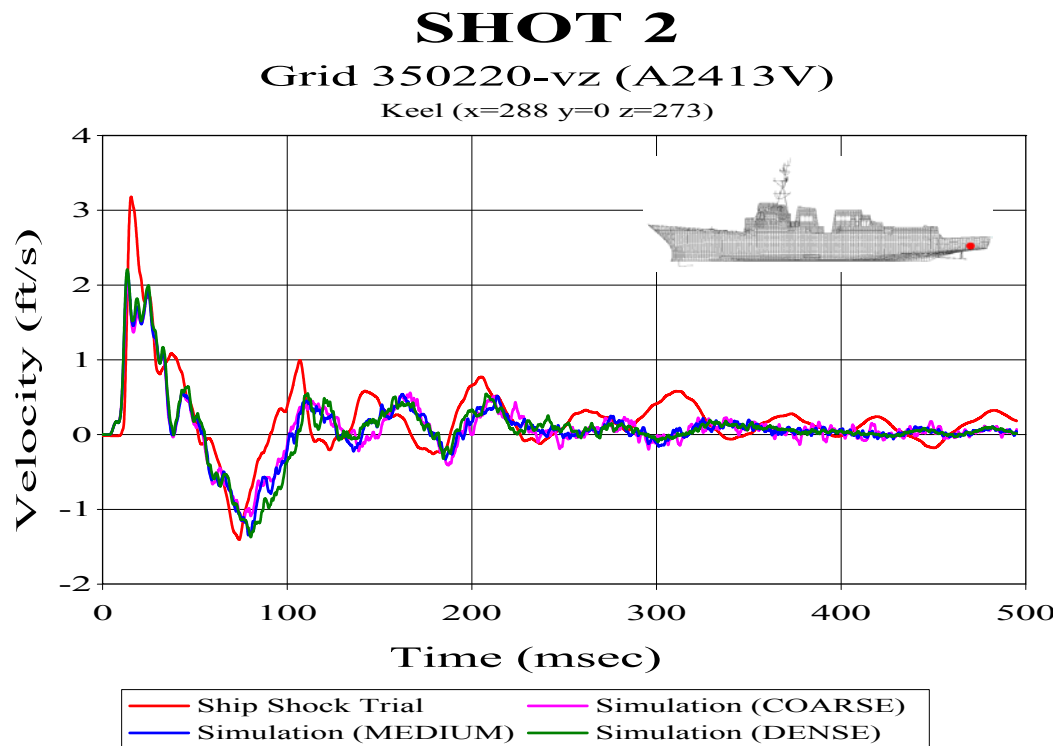


Figure 86. Keel Sensor A2413: (RM=-0.1245, RP=0.2219, RC=0.2255)

C. SHOT 3

The following velocity plots are from the Shot 3 fluid mesh density comparison. The Russell's error factors following each figure caption are from the dense fluid model comparison. This fluid model mesh showed the best correlation overall for this shot.

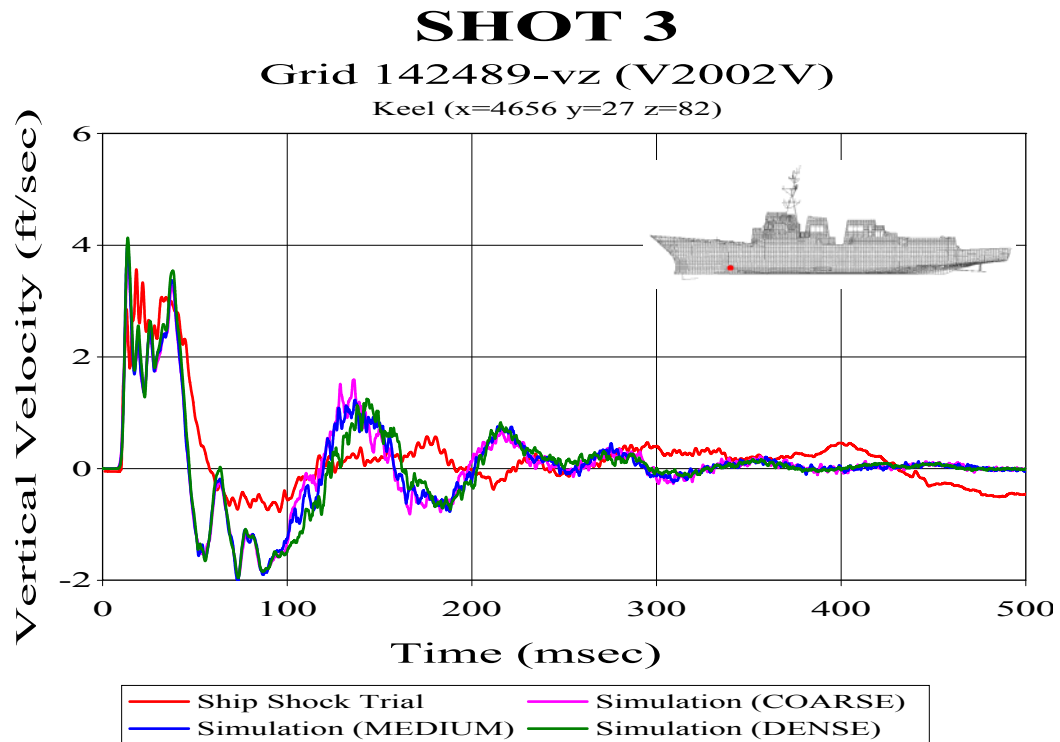


Figure 87. Keel Sensor V2002V: (RM=0.0762, RP=0.2303, RC=0.2150)

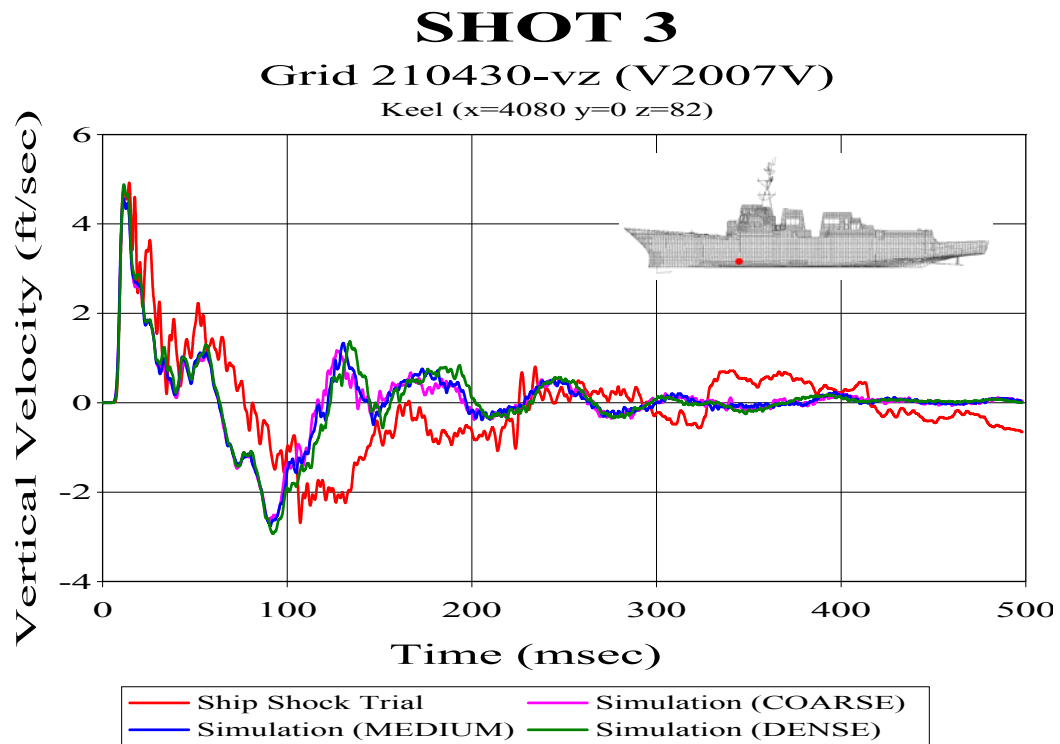


Figure 88. Keel Sensor V2007V: (RM=-0.1198, RP=0.2883, RC=0.2766)

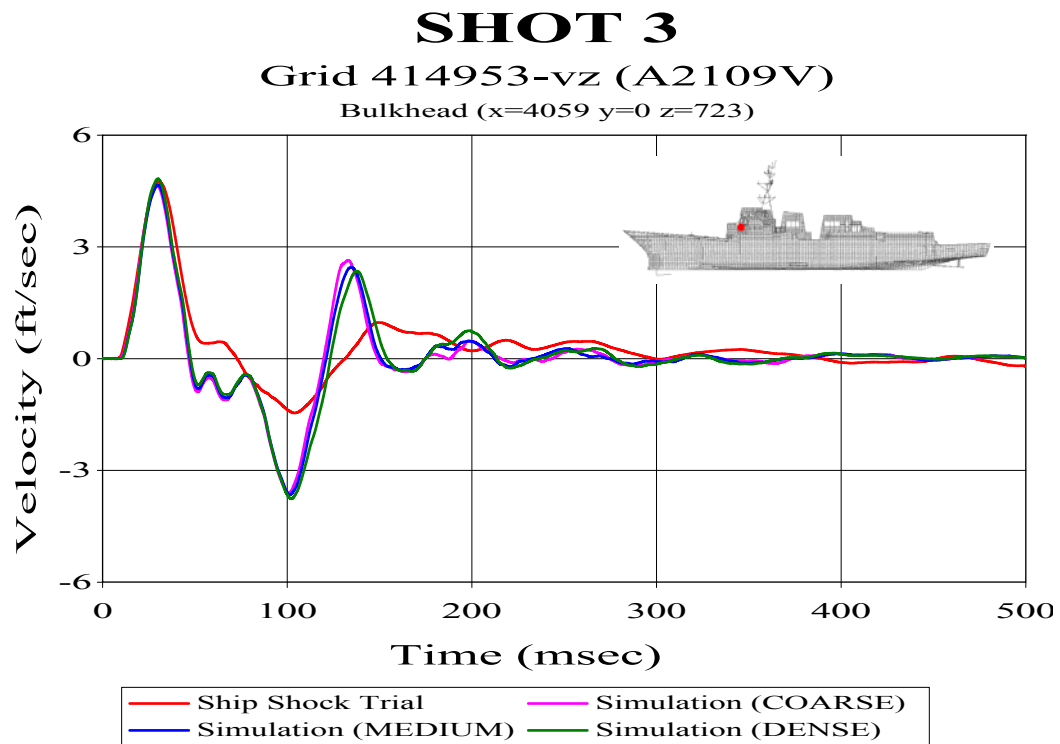


Figure 89. Bulkhead Sensor A2109V: (RM=0.1353, RP=0.1846, RC=0.2028)

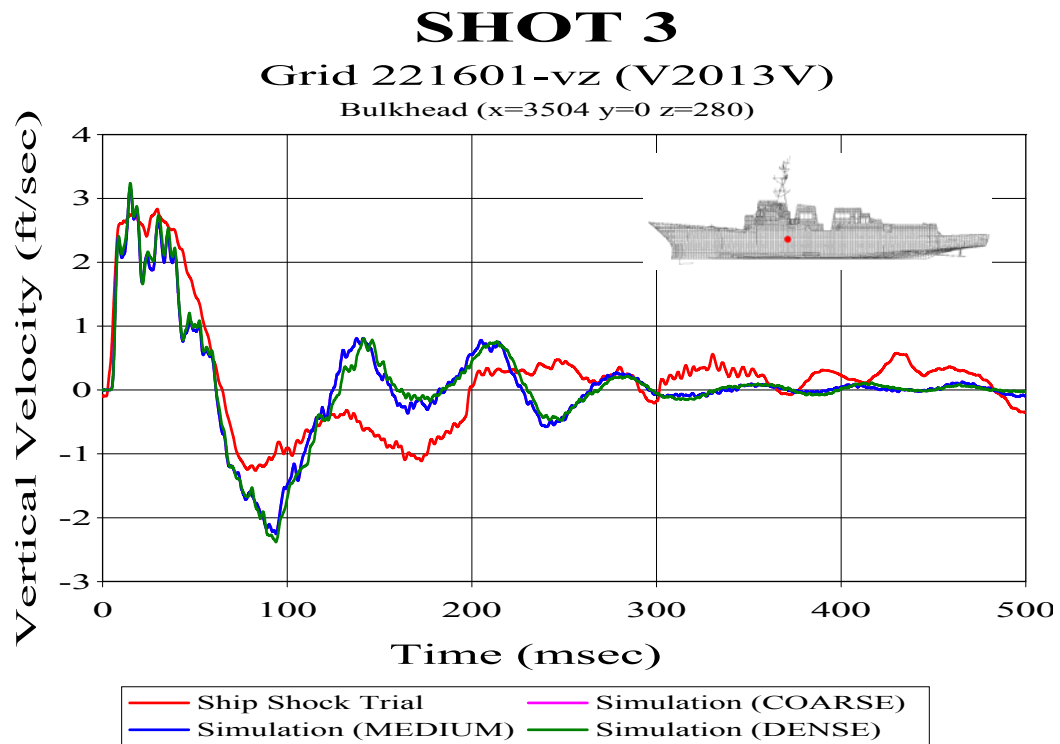


Figure 90. Bulkhead Sensor V2013V: (RM=-0.0342, RP=0.1970, RC=0.1772)

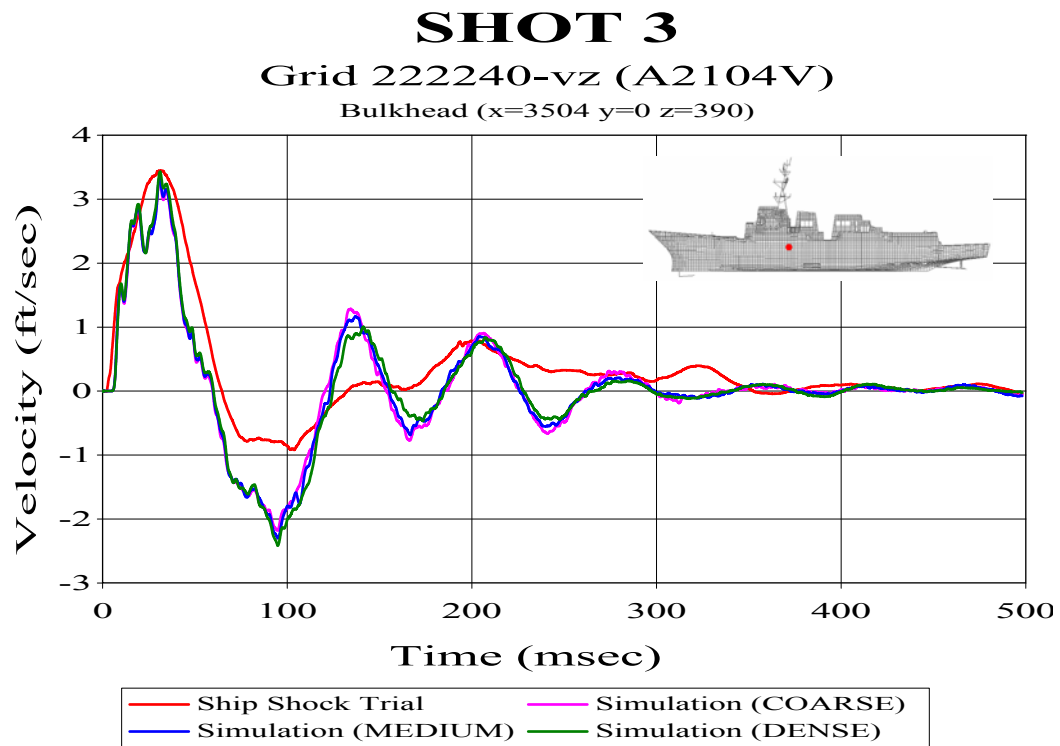


Figure 91. Bulkhead Sensor A2104V: (RM=0.0207, RP=0.1760, RC=0.1571)

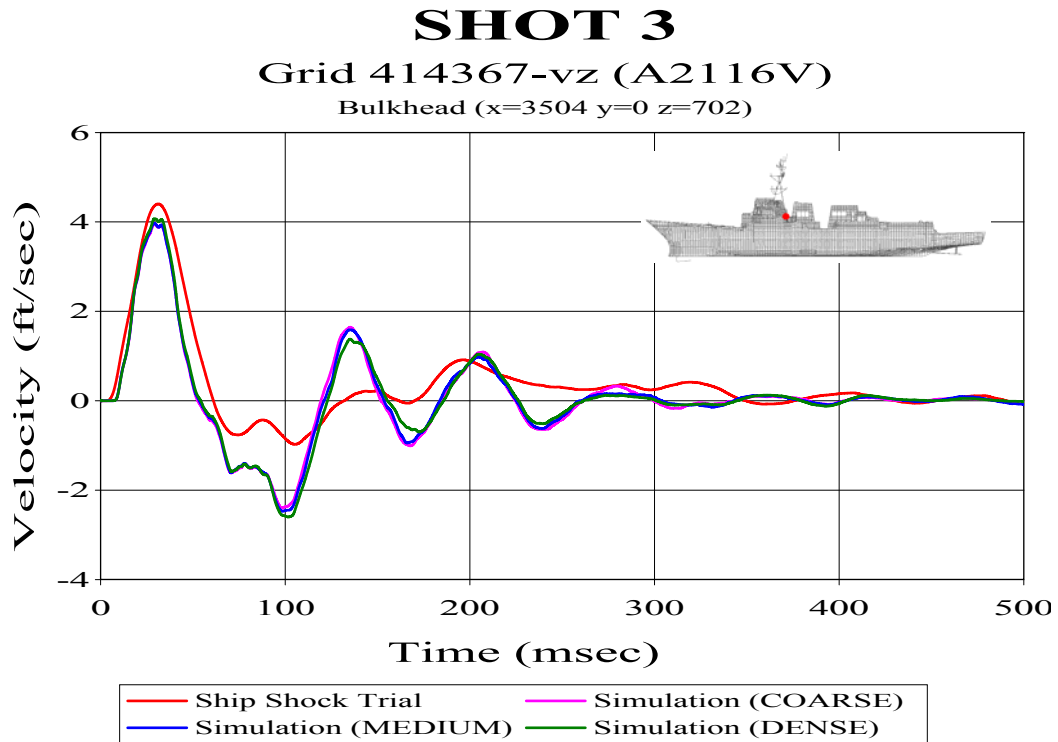


Figure 92. Bulkhead Sensor: (RM=0.0353, RP=0.1789, RC=0.1616)

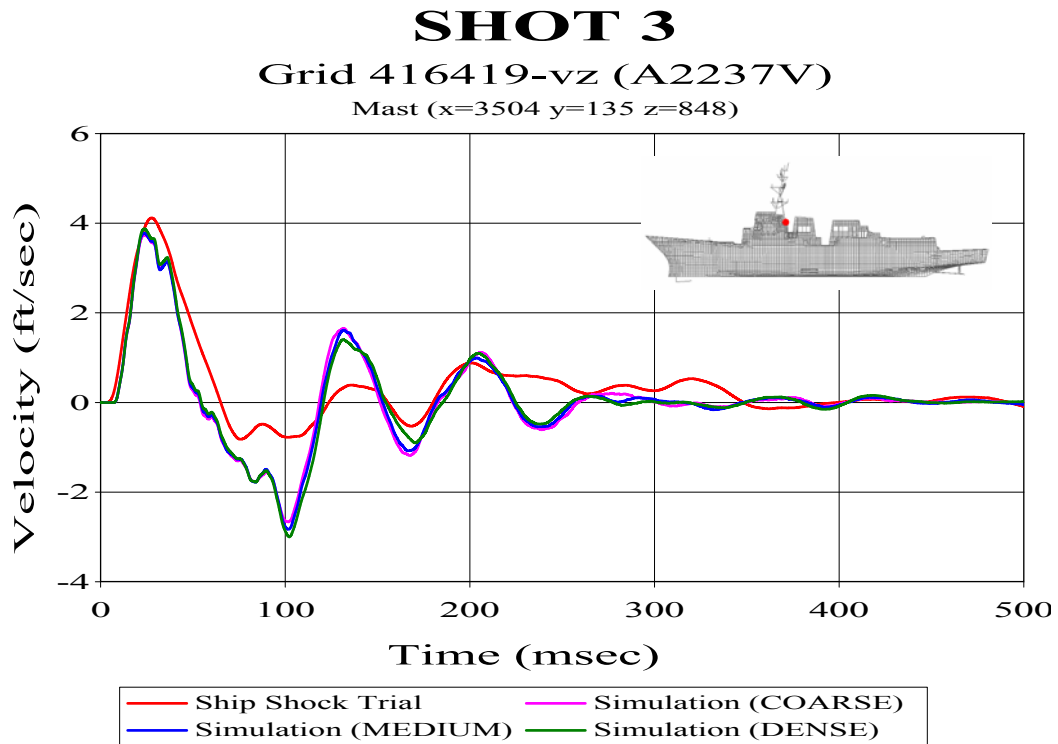


Figure 93. Mast Sensor A2237: (RM=0.0613, RP=0.1877, RC=0.1750)

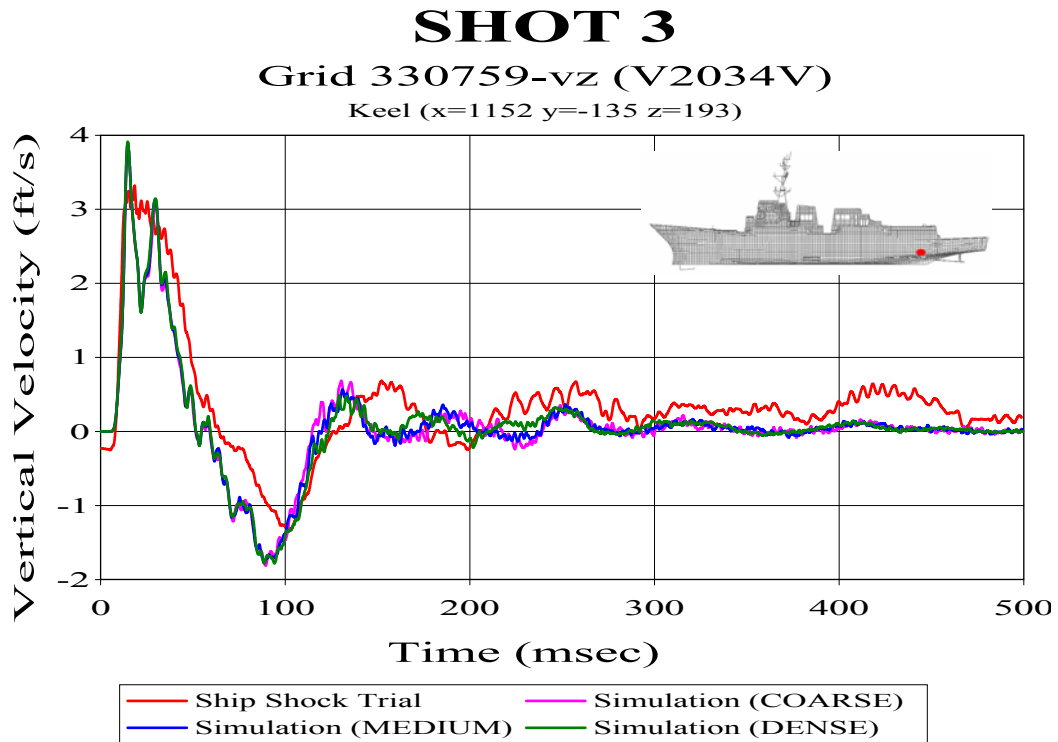


Figure 94. Keel Sensor V2034V: (RM=-0.0966, RP=0.1537, RC=0.1608)

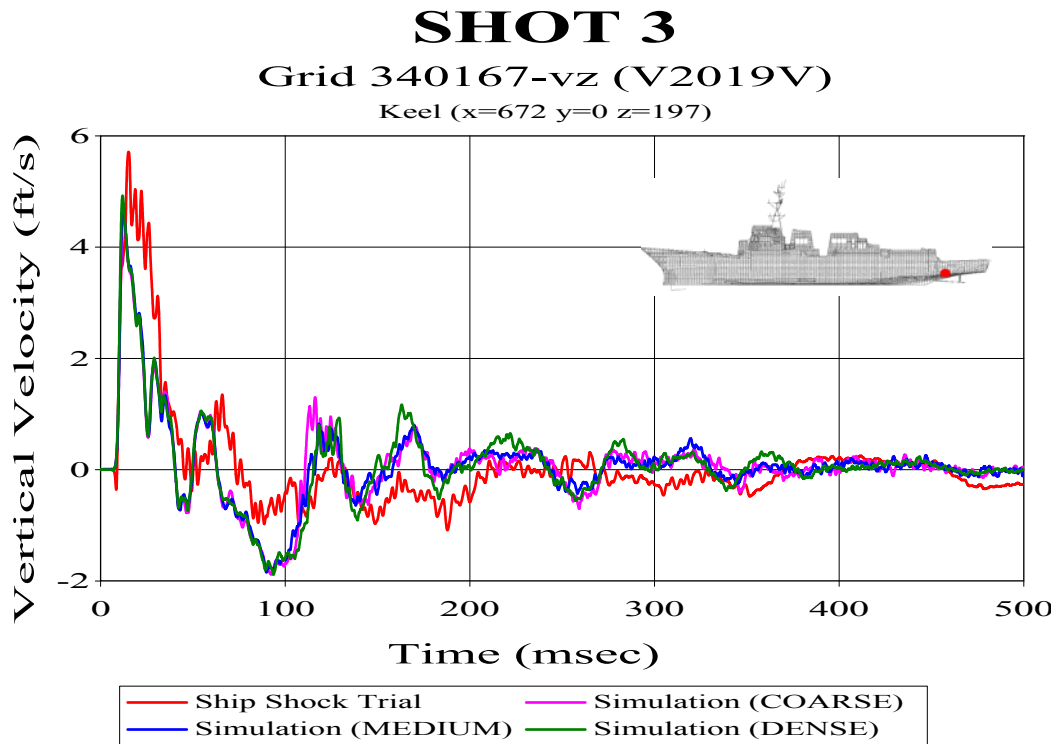


Figure 95. Keel Sensor V2019V: (RM=-0.1212, RP=0.1830, RC=0.1945)

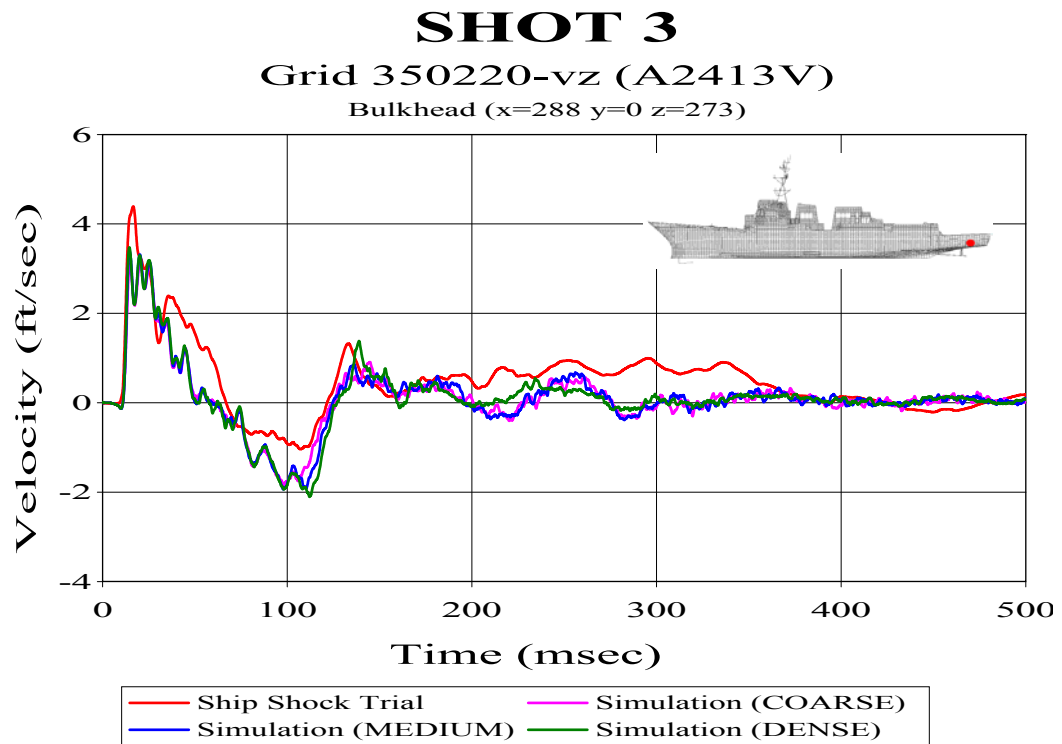


Figure 96. Bulkhead Sensor A2413V: (RM=-0.1315, RP=0.2150, RC=0.2233)

THIS PAGE INTENTIONALLY LEFT BLANK

APPENDIX B: FLUID MODELING IN TRUEGRID

This appendix describes the complete fluid modeling process from start to finish using TrueGrid. Most of the commands used in the modeling process, many of which are highlighted in bold in this appendix, have been explained in the following appendix, Appendix C. Further guidance is given in Reference [5]. The intent of these appendices is not to serve as a tutorial, but rather as a guide for the more experienced TrueGrid user to develop a similar high quality fluid model. It is suggested that first time users of TrueGrid begin by using one of several tutorials available for download online or attend the three day training course offered by XYZ Scientific Applications, Inc. More information on this and other TrueGrid services provided can be found at www.truegrid.com.

A. STRUCTURAL MODEL

To begin the fluid modeling process, the structural model must first be imported into TrueGrid. TrueGrid has the capability to import NASTRAN, NEUTRAL, LS-DYNA, and DYNA3D format models directly [Ref. 5]. This is accomplished using the **readmesh** command followed by the type of file, the filename, the **exclude** command, and then endpart. The **exclude** command is necessary to prevent the fluid nodes merged with the structural nodes to be redefined when the fluid mesh is output. Since the structural model is being defined separately in LS-DYNA, it is not desirable to have duplicate nodes. Similarly, since the structural properties are being defined separately, all materials and springs should be deleted from the model to avoid being output. This is done using the **delmats** and **delspds** commands respectively.

```
readmesh nastran ddg81shot3.nas exclude endpart
merge
delmats 1:346;
delspds 1:416;
delspds 1:100;
```

Rectangular voids were left where the two shafts exit the hull (stern tubes) on the DDG 81 model. Leaving these as voids would create an extremely challenging surface to merge the fluid model to. To fix this problem, two plates are constructed to cover the voids, leaving a smooth surface flush with the remainder of the hull. Two phases are involved in the TrueGrid modeling process, the part phase and the merge phase. The part phase is where each part is constructed separately while the merge phase is where these parts are merged together. While no parts are constructed in the merge phase, many precursors to building new parts, such as defining a face set, are done in this phase. Construction of the stern tube covers is quite simple and is done in the **block** part phase. The starboard stern tube cover is shown in the example below.

```
c PART 2: STARBOARD STERN TUBE COVER
block 1 8;-1;1 4;1.1520000e+03 1.4880000e+03 ;
      -135;9.9440002e+01 1.2893800e+02 ;
pb 2 1 2 2 1 2 xyz 1488.0 -202.125 95.4375
pb 2 1 1 2 1 1 xyz 1488.0 -135.0 60.875
pb 1 1 2 1 1 2 xyz 1152.0 -196.375 128.938
pb 1 1 1 1 1 1 xyz 1152.0 -135.0 99.440002
endpart
```

Following completion of these covers, the boundary nodes of the covers should be checked to ensure that they have merged properly with the original hull nodes. Improperly merged nodes are called “cracks”. It is advised that a small merging tolerance such as 0.25 inches or less be set using the **stp** command during the early stages of modeling. This merging tolerance is only applicable in the merge phase. No tolerance is recognized in the part phase. This results in cracks removed by an excessive merge tolerance reappearing in the part phase. As the fluid mesh is extended outward, cracks in the inner layers that were only 0.5 inch or less may grow in excess of several inches. If cracks are present, the part can be reconstructed, adding more partitions to attach each individual node to the hull. An alternative is to use the **pn** command and attach the unmerged nodes manually in the merge phase. Although this command is not to be abused, in this case it is perfectly acceptable.

B. INNER LINER

Construction of the fluid model begins first by wrapping the wetted hull structure with two individual fluid mesh layers. This allows the proper inner liner thickness to be ensured, creates transition regions at the corners of the hull, and transitions the structural mesh lines to the test waterline. This is the most complex portion of the fluid model, consisting of 37 individual parts merged together into the final two-layer inner liner.

The inner layer of the inner liner consists of 32 parts; the port and starboard lower hull parts, the sonar dome part, the lower and upper stern parts, the port and starboard upper hull parts, and several “seams” which connect these parts into one continuous fluid mesh layer. To begin, curves must be created using the **lp3** command along the keel seam, the sonar dome seams, the bow seam, and the stern seams. These curves must then be manually modified so as to produce curves approximately seven inches from the hull and 45° off from the original curves created. These curves will be utilized to attach the outer edges of the individual parts that will eventually form the inner layer of fluid mesh on the hull. Figure 97 shows an example of a portion of these curves.

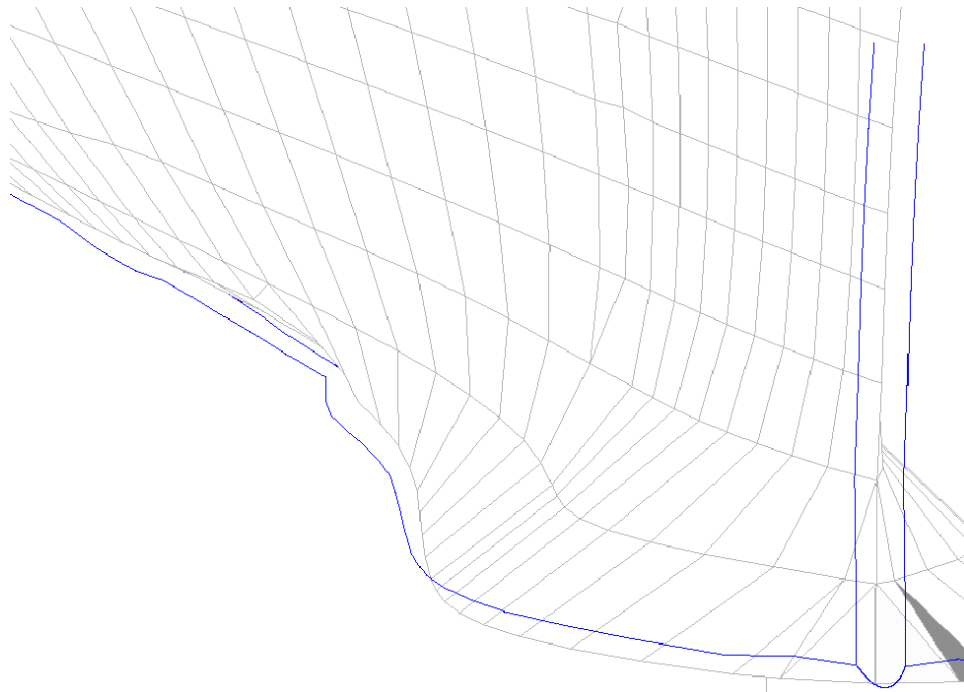


Figure 97. Example of Curves Used for Construction of Inner Fluid Mesh Layer

Prior to construction of the inner mesh layer, the face elements of the hull must first be selected using the manual **fset** method. This involves using the “pick;>sets;>faces” option in the environmental window of TrueGrid. The port and starboard face sets are separated at the keel and bow seam. Only the face elements up to three mesh lines from the mesh line closest to the test waterline on the ship are selected. The sonar dome structural face elements on the bottom of the structure and the lower stern face elements, up to one structural mesh line from the test waterline, make up separate face sets. Three face sets are defined to create each upper port and starboard fluid mesh layer. These face sets consist of the structural face elements not picked in the lower hull face sets up to the structural mesh line closest to the test waterline. This is to facilitate transitioning the structural mesh lines to the waterline at the top of the fluid mesh. Figure 98 provides some clarification as to exactly how these face sets should be defined. Each face set is differentiated by color.

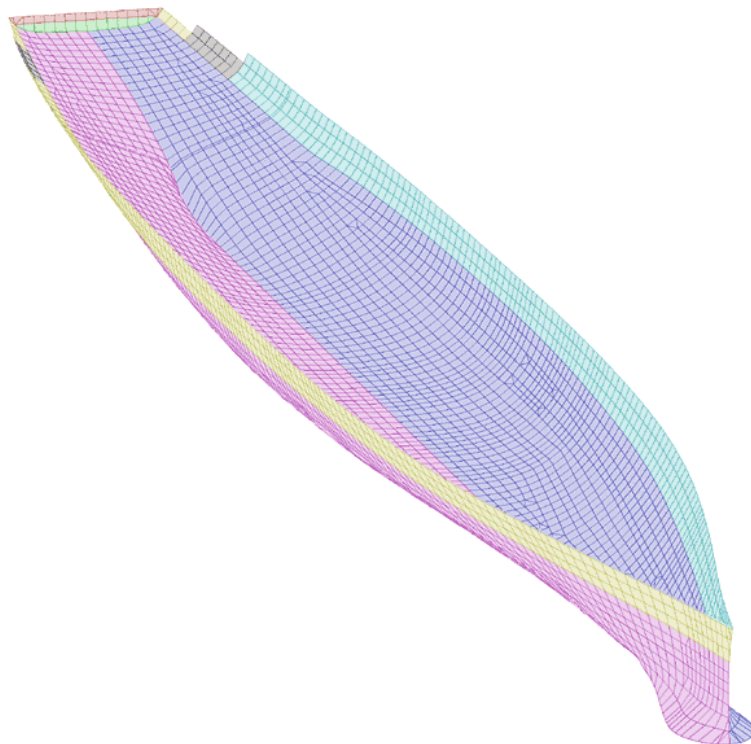


Figure 98. Face Sets Used to Generate Inner Fluid Mesh Layer [from Ref. 21].

The port and starboard lower hull mesh layers are constructed first using the corresponding face sets defined. This is accomplished by using the **blude** command to extrude the fluid mesh through the structural mesh and the **bb** and **normal** commands to ensure the mesh is orthogonal to the structure and no more than seven inches in thickness. The lower, bow, and stern outer edges of the mesh are attached to the corresponding curves generated earlier. This process is repeated for the sonar dome and the lower stern region.

To maintain orthogonality and fill in the gaps left at the seams between these parts, seam fluid mesh parts are constructed in the **block** part phase to form a wedge shaped fluid mesh in these transition regions. For the keel and sonar dome seams the wedge shaped parts are two elements thick along their length while the bow seam part is four elements thick. Pyramid shaped parts are necessary to properly transition the junction of the sonar dome and bow seams and terminate the keel seam at the stern. These are constructed in the **block** part phase as well. Figure 99 shows an exploded view of the extruded parts constructed so far as well as the seam parts.

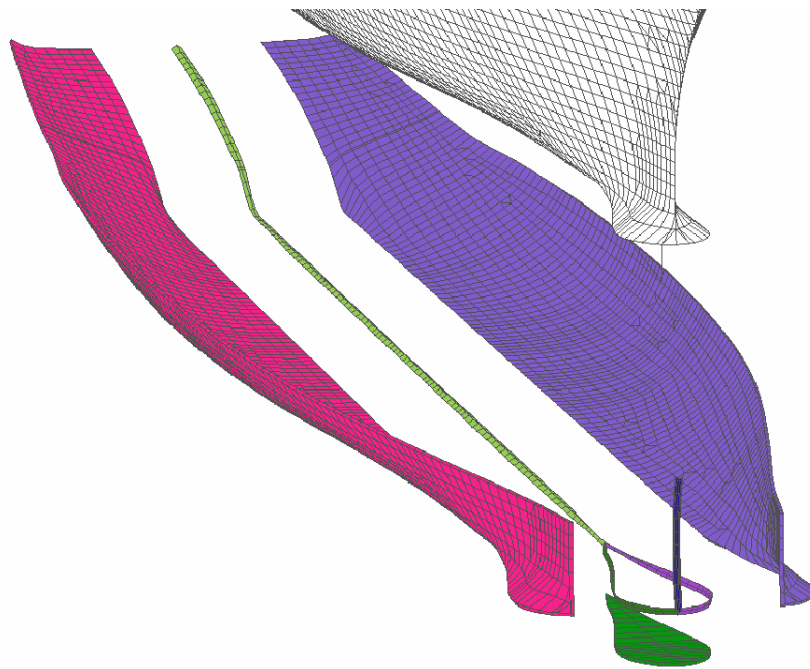


Figure 99. Inner Mesh: Lower Port and Starboard Hull, Sonar Dome, and Seams.

The next step is to extend the inner fluid mesh layer to the waterline. The lower port and starboard liner was only constructed up to three elements below the structural mesh line closest to the waterline because this structural mesh line does not remain at a constant height. It veers upward in the aft section of the ship, extending much higher than the test waterline. This requires that two “step-downs” must be taken along the structural mesh. To aid in this transition, triangular shell elements replaced the quadrilateral shell elements on the structural model on each side at two locations where they could transition from above the test waterline to below the test waterline. This only serves as an aid in making the transition to the test waterline. The transition is accomplished using eight separate parts for each side of the hull and one part for the stern. While this could be accomplished using fewer parts, using separate parts allows for more control over the final shape and orthogonality of the mesh.

These parts use a curve developed by first extruding a single seven inch thick normal mesh layer from the hull up to and beyond the test waterline. A surface is formed on the outer boundary of this part by creating a face set out of the boundary. A curve can then be created to extend the inner liner to the desired height at the outer boundary by using the **lp3** feature to pick points along this surface. It is then necessary to manually change the coordinates of the curve extending it to the desired height, while at the same time keeping it on the surface. At this point it is necessary to exit out of TrueGrid and save the file. The file can then be opened with any text editor, the part and surface used to generate this curve removed, keeping the curve generated with them. The file is then saved and reloaded. Since the wetted hull is symmetric, this curve can be transformed over to the opposite side by using the **rx** transformation command which reflects the curve about the xz-axis.

The upper portion of the inner liner is then constructed by attaching the outer top edge of the individual parts to this curve. The structural mesh line transitions from above to below the test waterline at three locations along each side of the hull. This requires constructing three tetrahedron elements on each side of the hull. While in most instances these would not be desirable, they are required to achieve a proper waterline and to allow for construction of the outer fluid mesh at the waterline. These elements can be deleted later after the file is output into LS-DYNA. Their location near the waterline make their

deletion transparent to the simulation results. The parts used to make the aft section of the inner mesh were made primarily in the **block** part phase, while the parts having more than two elements were constructed using the **blude** part phase. Figure 100 shows the aft section of the upper inner liner.

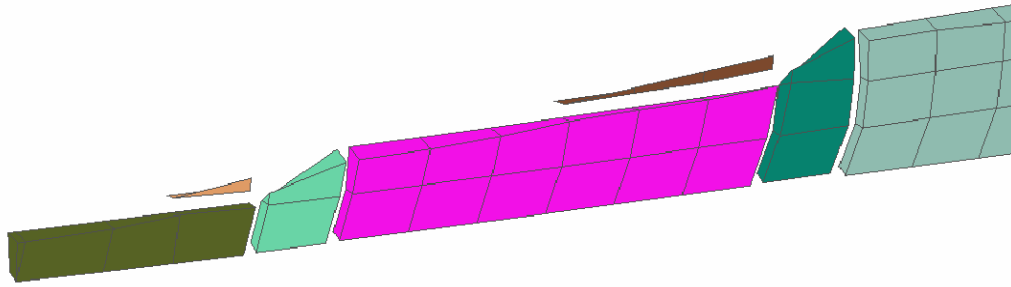


Figure 100. Transition to Test Waterline: Aft Section of Upper Inner Liner

The forward three quarters of the upper mesh consists of two parts. An initial part is first extruded from hull to form the majority of the fluid mesh in this region. A single element thick wedge shaped part is then extruded from the top of this fluid mesh. This transitions the structural mesh line, which is at a constant height of 254 inches for the majority of this region, to the test waterline of 258 inches. These parts are shown in Figure 101.

The inner mesh layer is completed by extruding a fluid mesh layer from the upper stern region, transitioning it down towards the test waterline. The stern seam is then transitioned using a wedge shaped stern part in the same manner in which the keel and bow seams were transitioned. Figure 102 shows the completed inner layer of the mesh.

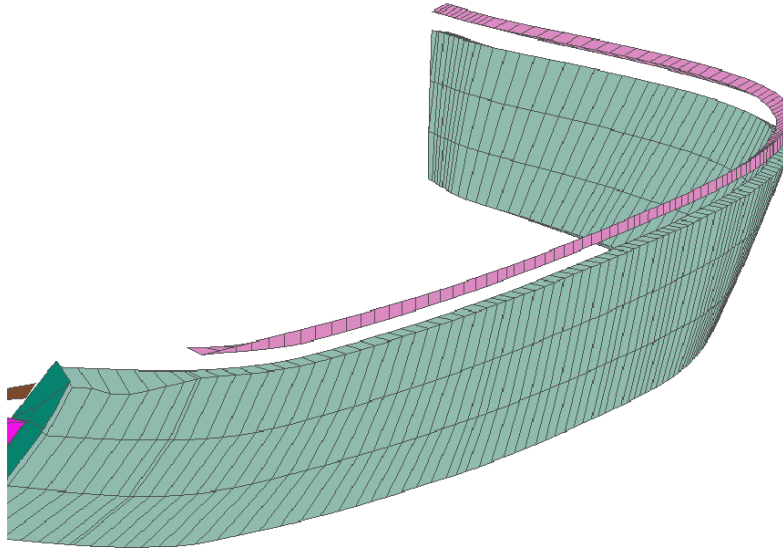


Figure 101. Transition to Test Waterline: Forward Section of Upper Inner Fluid Mesh

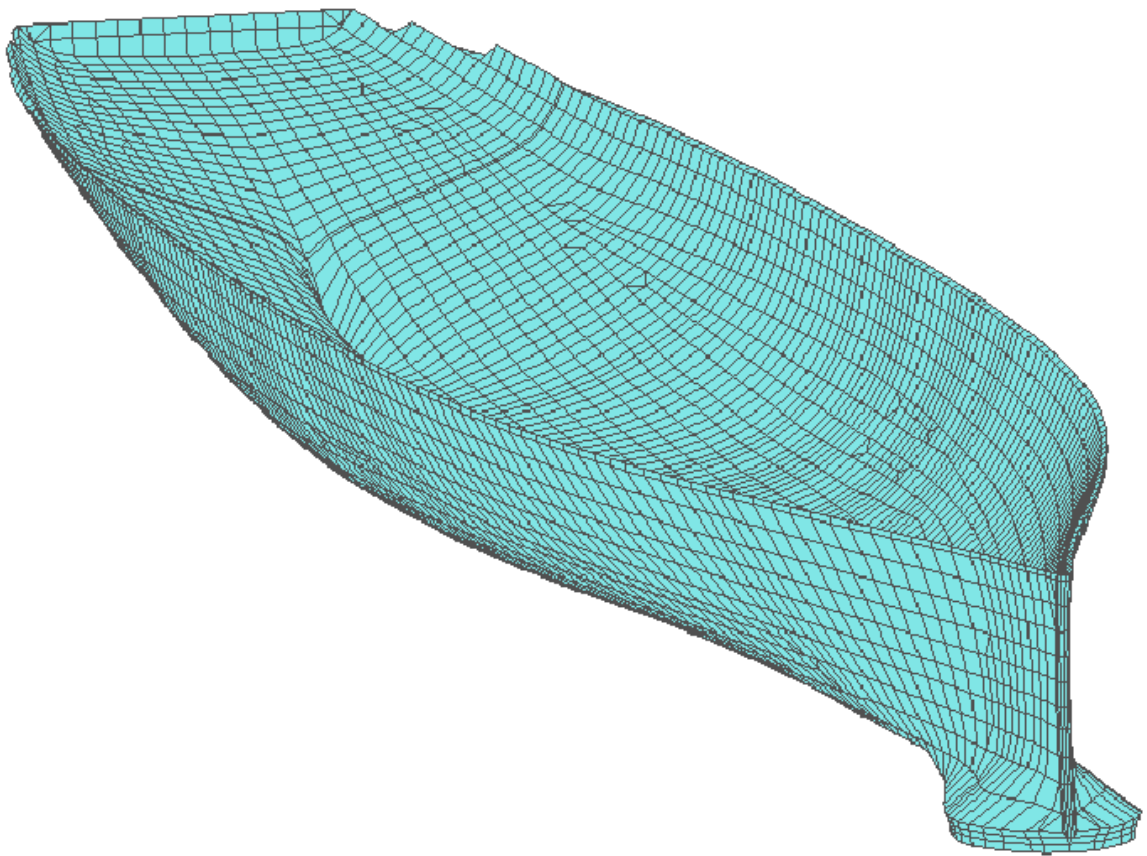


Figure 102. Completed Inner Mesh Layer of Inner Liner

Upon completion of the inner mesh layer, the fluid mesh has been transitioned to the test waterline everywhere except in the stern region. This is due to the large transition distance from the structural mesh line to the test waterline here. To avoid extremely non-orthogonal inner mesh elements, this transition is accomplished using two layers of fluid mesh.

The second layer of inner liner is eight inches in thickness and consists of five parts; a port and starboard mesh, a sonar dome mesh, a stern mesh, and a bow mesh. The sonar dome is first extruded from the inner mesh sonar dome constructed previously. The port and starboard meshes are then extruded from their respective inner meshes and their respective half of the inner mesh keel seam and the entire sonar dome seam on their respective side. In addition, the side of the inner mesh stern seam is encompassed in this extrusion. Curves must be generated at the desired waterline to which the upper outer edge of the port and starboard meshes can be attached. These parts merge together with each other and the sonar dome outer layer to form a continuous outer layer of the inner mesh. A single mesh layer is extruded from the stern, transitioning the upper boundary to the waterline. The final part is the bow constructed in the **block** part phase. This part extends the bow out eight inches and connects the port and starboard mesh layers at the bow. The completed outer layer of the inner liner is shown in Figure 103.

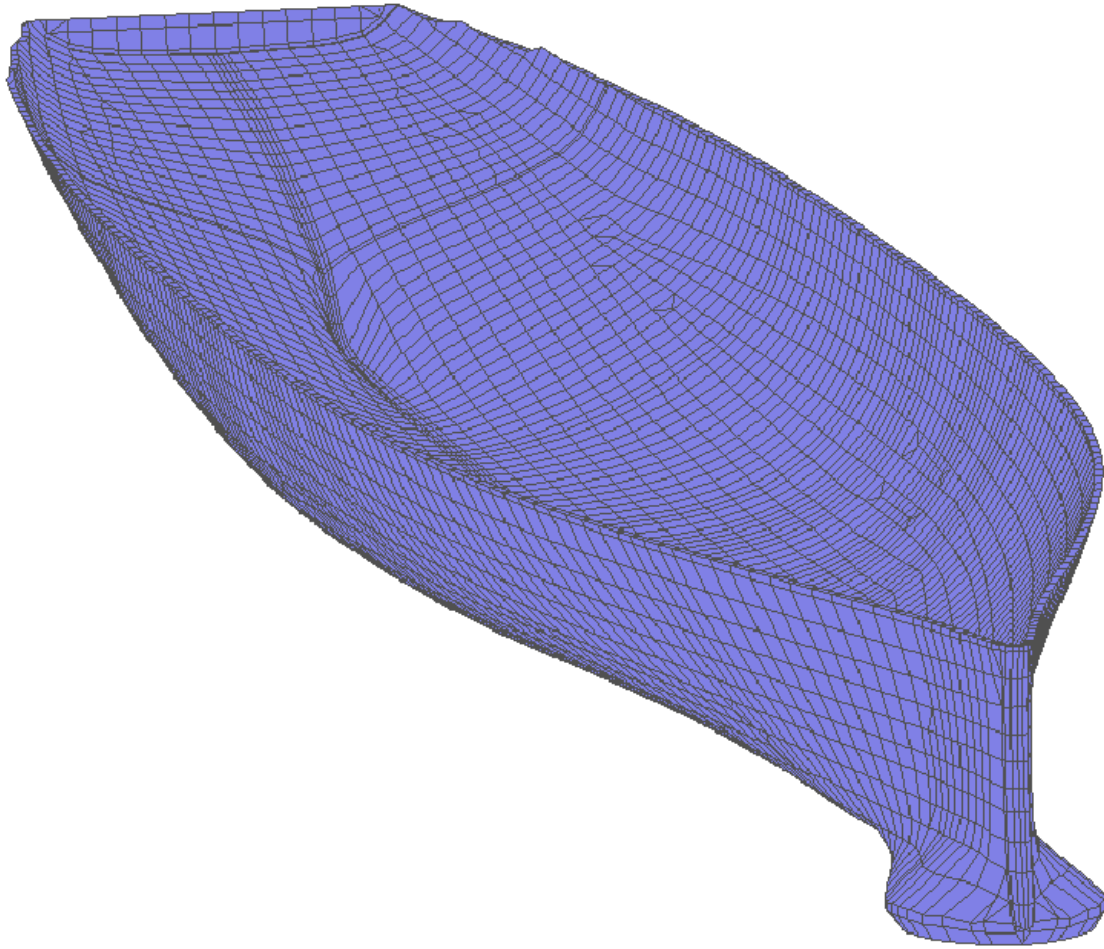


Figure 103. Completed Outer Mesh Layer of Inner Liner.

C. INNER MESH

After completion of the inner liner, the fluid mesh construction process moves to extending the fluid out to the desired depth. This process is accomplished using multiple fluid mesh layers. The first layer has been termed the “Inner Mesh”. The purpose of this mesh is to gradually “smooth” the contours of the ship. This greatly simplifies construction of the outer fluid mesh layers. This inner mesh extends out a nominal five feet from the outer boundary of the inner liner.

Before beginning, it is highly advised to use the **labels cracks** feature to identify any improperly merged nodes. If these cracks are allowed to remain, they will only multiply as the fluid model is expanded outward. These cracks should be removed either by reconstruction of the parts in which they appear or by using the **pn** command.

The mesh extrusion process used in the inner liner, though challenging for the beginner, was relatively simple. Due to the contours of the hull, constructing the inner mesh requires a much more complicated extrusion process. To accomplish this, a good conceptual understanding of how the extrusion process works is necessary. The mesh extrusion process involves first projecting the mesh being constructed to the predefined outer surface contour. The mesh is then projected to the inner surface through which the mesh is extruded. This method presents a problem in these areas as “shadow regions” exist. These shadow regions can be illustrated with a flashlight shining onto the model as shown in Figure 104.

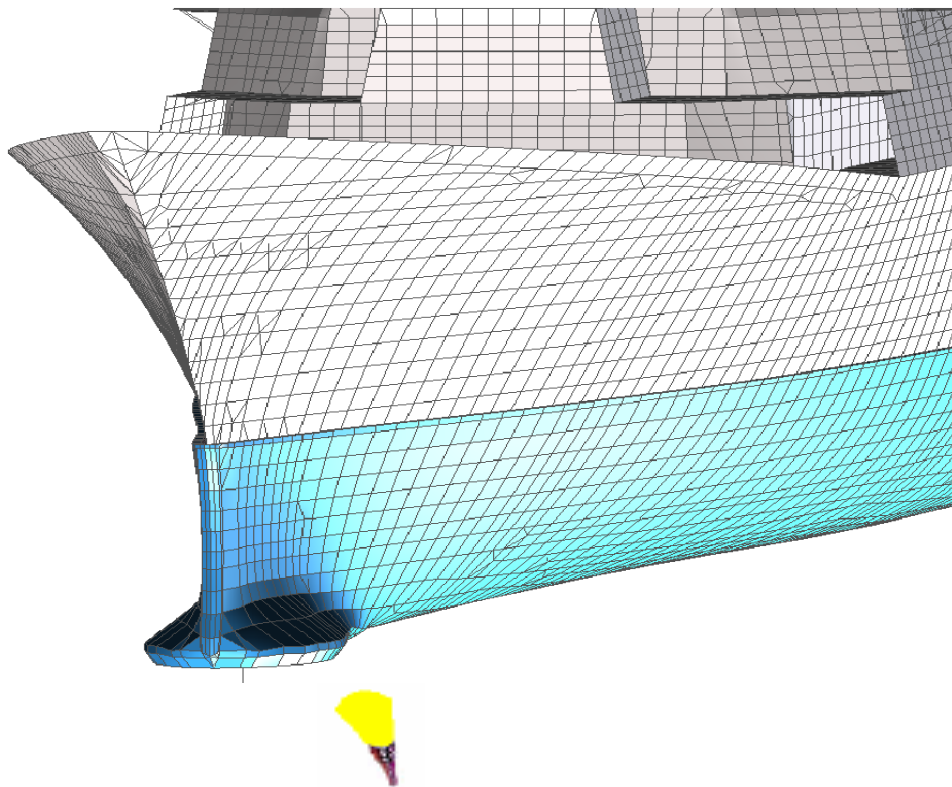


Figure 104. Fluid Model Projection Illustration Showing “Shadow Regions” Created by the Contours of the Ship Model

The flashlight can be thought of as a desired final outer boundary position of a fluid mesh line which begins on the previously defined surface. From this illustration,

one can see that by simply moving the flashlight to a different location these shadow regions would be eliminated. While this is true, the resulting mesh would be highly non-uniform with poor aspect ratios due to the large separations created in these transition areas. In these areas it is desirable to transition a mesh line which begins in the shadow region to the location of the flashlight as shown in Figure 104.

These shadow regions can be reduced or avoided entirely by projecting from all three sides of the hull. The best way to accomplish this is by using separate parts for each side in conjunction with curves and internal projections. These curves and internal projections can be thought of as essentially using fiber-optic cables to guide the projected mesh lines from the inner mesh to the desired location on the outer boundary. The end result is a high quality mesh with a minimal amount of non-uniformity.

The inner mesh was constructed using five separate parts; a port side mesh, a starboard side mesh, a sonar dome mesh, a keel mesh, and a small lower bow plug mesh. These parts are all created in the **blude** part phase. Before beginning this extrusion process, it is first necessary to define what the outer boundary of this mesh will be when completed. It is desirable to have a convex surface, but, at the same time, it is also desirable to not have any large variations in the inner mesh spacing normal to the hull. This requires an outer boundary which is not perfectly cylindrical. To form this surface a number of cubic spline curves are formed using the **csp3** command. These curves are constructed so that they follow the contours of the hull at a nominal distance of five feet from the inner liner. These curves essentially trace the outline of the desired outer boundary of this inner mesh. These curves are then combined to form surfaces using the **blend4** function in TrueGrid and the surfaces combined to form a single surface using the **sds** command. Figure 105 shows the curves and surfaces used to form the outer boundary of the inner mesh.

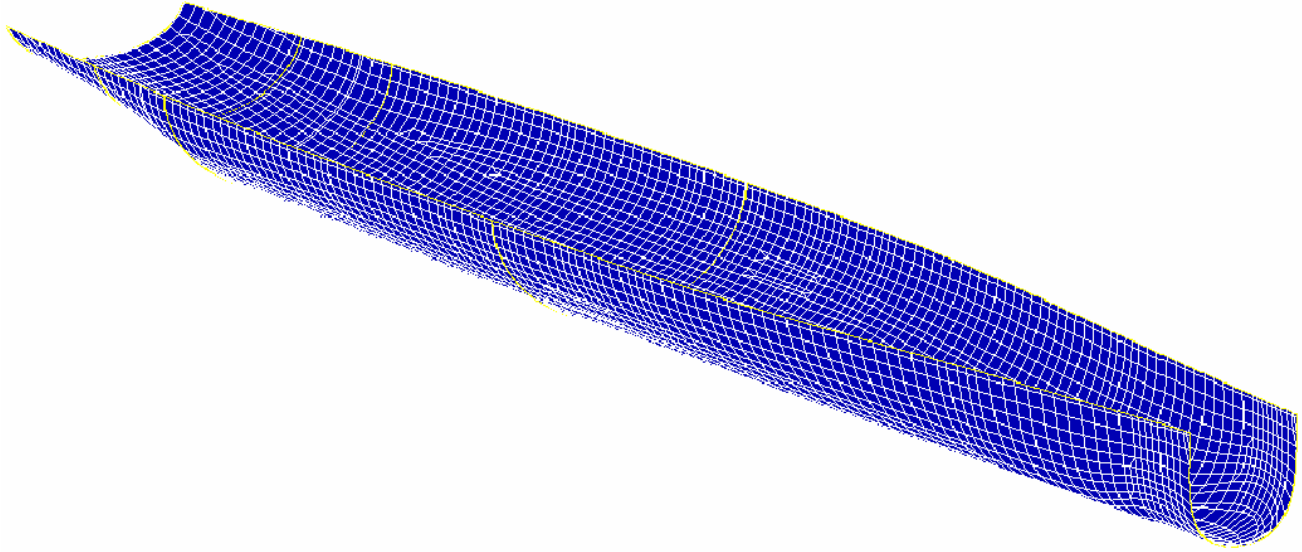


Figure 105. Curves and Surfaces Used to Form Outer Boundary of Inner Mesh

In addition to these curves and surfaces, several additional curves and surfaces are created to serve in order to control the mesh. Controlling the mesh in this manner is necessary to create a uniform mesh at the outer boundary.

The construction of the port and starboard inner mesh is very complex. The commands used to generate the starboard inner mesh are shown below:

```
blude 4 stbdfc2 1 2 3;1 %inner;1 2 3;-80 4897 5600;-450 -390;-75 176
258;
pb 1 2 1 1 2 1 xyz -69.286003 0.0 210.75
pb 1 2 2 1 2 2 xyz -77.0 -212.2 258.0
pb 1 1 1 1 1 1 xyz -80.0 -1.137e-07 130.0
pb 3 2 3 3 2 3 xyz 5595.0703 -15.323369 258.0
pb 3 2 1 3 2 1 xyz 5589.0005 -7.280057 -3.0631487
pbs 3 1 1 3 1 1 xyz 806.1
pb 2 2 1 2 2 1 xyz 4897.7222 -3.4121273 -13.485395
pb 2 2 3 2 2 3 xyz 4894.4614 -173.06313 257.99969
pbs 2 1 1 2 1 1 xyz 812.21
pbs 3 1 3 3 1 3 xyz 89.1
pbs 1 1 2 1 1 2 xyz 12.1
mseq i 200 50
mseq k 40 0
insprt 1 6 1 2
pb 3 2 2 3 2 2 xyz 5594.8252 -10.205372 6.3662529
pbs 3 1 2 3 1 2 xyz 9.1
```

insprt 1 2 1 2
 pbs 2 1 2 2 1 2 xyz 8.2
 pbs 2 1 1 2 1 1 xyz 812.1
 pb 2 2 1 2 2 1 xyz -56.667458 -6.0664253 210.01097
 pb 2 2 2 2 2 2 xyz -57.072742 -12.096737 210.11931
 pb 2 2 3 2 2 3 xyz -61.072933 -213.76886 257.99969
 pb 1 2 2 1 2 2 xyz -69.286003 0.0 210.75
 pbs 2 1 3 2 1 3 xyz 808.394.91
 pb 1 1 2 1 1 2 xyz -80.0 -1.137E-07 130.0
 pbs 4 2 3 4 2 3 xyz 1.1319.2
 pbs 3 2 3 3 2 3 xyz 1.9.1
 insprt 1 2 2 35
 insprt 1 2 3 2
 dei 1 3; 1 2; 3 4;
 pbs 4 1 3 4 1 3 xyz 115.1
 pbs 3 2 3 3 2 4 xyz 1.23.3
 pbs 4 2 4 4 2 4 xyz 1.78.2
 pbs 4 2 3 4 2 3 xyz 1.78.1
 pb 4 1 4 4 1 4 xyz 863.36 -382.3 [%dftaft+940*%trim/5672]
 pb 3 1 3 3 1 4 xyz 8.16E+02 -3.7938107E+02 [%dftaft+893*%trim/5672]
 pbs 3 2 1 3 2 1 xyz 1.120.2
 pbs 4 2 2 4 2 2 xyz 1.642.3
 pbs 4 2 1 4 2 1 xyz 1.1300.1
 pbs 3 2 2 3 2 2 xyz 1.50.2
 pbs 3 1 1 3 1 1 xyz 802.212.18
 pbs 4 1 1 4 1 1 xyz 802.212.13
 pbs 5 1 4 5 1 4 xyz 800.473.106
 pb 5 1 3 5 1 3 xyz 4.8934E+03 -2.47913E+02 [%dftaft+%trim*4970/5672-16]
 pbs 6 1 3 6 1 3 xyz 115.99
 pb 4 1 2 4 1 2 xyz 8.5765637E+02 -30 -3.3454285E+01
 pb 3 1 2 3 1 2 xyz 815 -30 -21.867
 mseq i 0 5 1 5 -10
 mseq k 1 0 0
 edge 3 2 4 4 2 4 1.2
 edge 4 2 4 5 2 4 1.2
 edge 5 2 4 6 2 4 1.2
 edge 1 2 3 2 2 3 1.2
 edge 2 2 3 3 2 3 1.2
 curs 3 1 4 6 1 4 801
 curs 1 1 3 3 1 3 801
 curs 4 1 3 6 1 3 115
 curs 4 2 3 6 2 3 112
 curs 1 1 1 1 1 2 12
 curs 1 1 2 1 1 3 12
 curs 2 1 2 5 1 2 8

curs 2 1 1 5 1 1 812
 edge 1 2 1 2 2 1 1.3
 edge 2 2 1 3 2 1 1.3
 edge 3 2 1 4 2 1 1.3
 edge 4 2 1 5 2 1 1.3
 edge 5 2 1 6 2 1 1.3
 curs 5 1 1 6 1 1 806
 curs 2 2 2 6 2 2 5
 curs 5 1 2 6 1 2 9
 curs 6 1 3 6 1 4 89
 curs 6 1 2 6 1 3 89
 edge 6 2 1 6 2 2 1.1
 edge 6 2 2 6 2 3 1.1
 edge 6 2 3 6 2 4 1.1
 edge 1 2 2 1 2 3 1.3
 curs 6 1 4 6 2 4 40
 curs 6 1 1 6 2 1 94
 curs 6 1 2 6 2 2 43
 curs 5 1 1 5 2 1 98
 curs 5 1 2 5 2 2 45
 curs 2 1 1 2 2 1 500
 insprt 1 2 2 9
 pbs 3 2 3 3 2 3 xyz 1.491.3
 pbs 3 2 2 3 2 2 xyz 1.196.2
 pbs 3 2 1 3 2 1 xyz 1.1989.1
 pbs 3 1 3 3 1 3 xyz 14.6
 pbs 3 1 1 3 1 1 xyz 14.127
 pbs 3 1 2 3 1 2 xyz 14.124
 curs 3 1 1 3 1 3 14
 insprt 1 2 3 5
 pbs 4 2 3 4 2 3 xyz 1.64.4
 pbs 4 2 2 4 2 2 xyz 1.734.3
 pbs 4 2 1 4 2 1 xyz 1.734.2
 pbs 4 1 1 4 1 1 xyz 17.95
 pbs 4 1 3 4 1 3 xyz 17.1
 pbs 4 1 2 4 1 2 xyz 17.98
 curs 4 1 1 4 1 3 17
 sfi 7 8;1 2;-1;sd 19
 sfi 7 8;1 2;-2;sd 15
 sfi 2 7;1 2;-1;sd 31
 sfi 2 7;1 2;-2;sd 35
 sfi 5 8;1 2;-4;sd 999
 sfi 1 5;1 2;-3;sd 999
 sfi 1 8;-1;1 4;sd 803
 sfi 1 8;-2;1 4;sd 1
 res 1 1 1 5 2 4 j 1

```

as 5 1 1 8 2 2 j 1 9
das 7 1 2 8 2 4 j [150/(%inner+2)] 10
tmei 1 5;1 2;2 3;50 0 1
tmei 5 8;1 2;1 4;50 0 1
relaxi 7 8;-2;1 4;50 0 1
relaxi 2 7;-2;2 3;50 0 1
relaxi 7 8;-1;1 4;50 0 1
relaxi 2 7;-1;2 3;50 0 1
bb 7 1 1 8 2 1 17;
bb 2 1 1 7 2 1 21;
endpart

```

The port mesh is constructed in a similar fashion. Key points to highlight in this example are the use of the **tme** and **relax** interpolation methods and the use of parameter functions. The mesh must be interpolated properly to generate a high quality mesh. This requires a fair amount of practice as some interpolation methods work better than others depending on the topology of the mesh and the way in which the boundaries are controlled. The parameter functions used are prefaced by the percent sign. These represent previously defined parameters created using the **para** command. Using these parameters and some simple FORTRAN expressions in the model is key to allowing automation of the mesh generation process. Using some creative modeling techniques, major modifications can be made to the fluid model by changing just a few of these parameter values.

The sonar dome and keel were constructed separately to allow for greater control of the mesh in these challenging areas. To avoid having several cracks between these individual parts, the **bb** command was used extensively. This command allows a face of a part to be defined as a master side in the part phase. Subsequent parts can define their coinciding face using the same boundary number, creating a slave side. When the parts are merged together, slave and master sides are glued together with their nodes properly merged throughout. Without using this feature, construction of the inner mesh in this manner would not be feasible. Figure 106 shows the parts used to generate this inner mesh after being merged together.

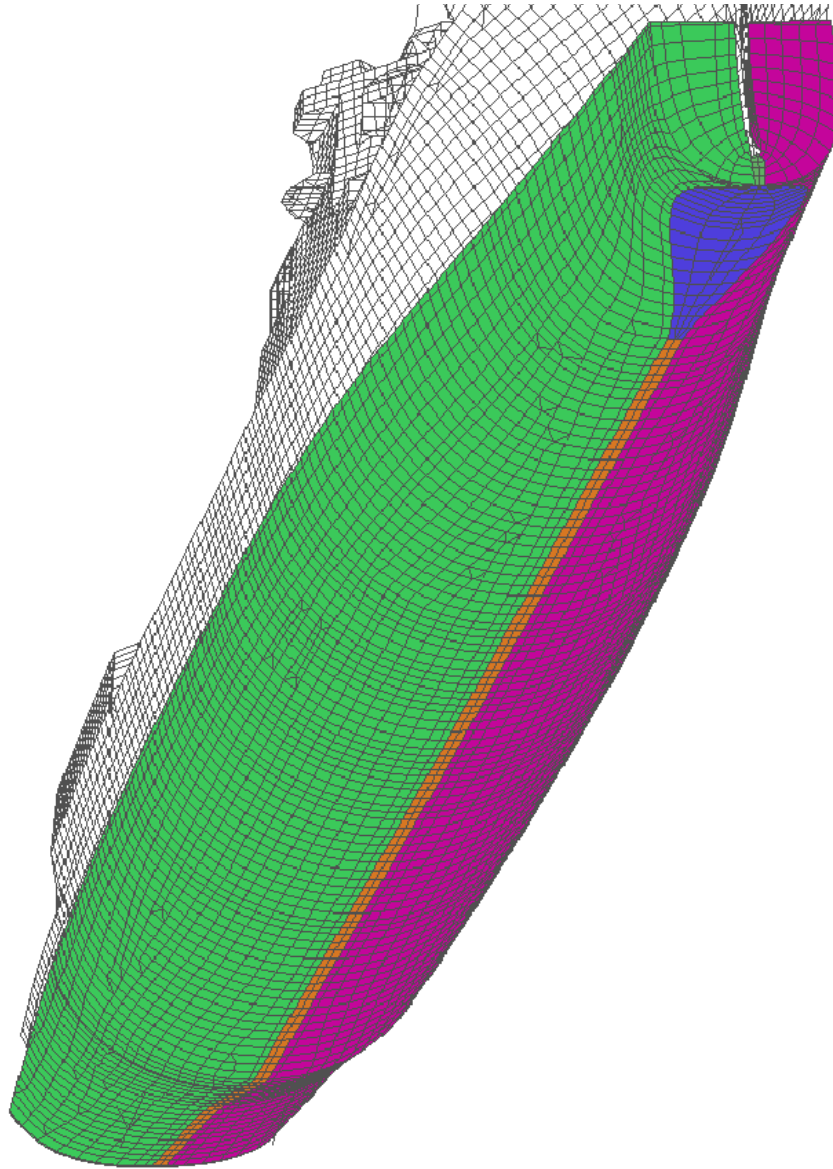


Figure 106. Completed Inner Mesh

D. TRANSITIONAL MESH

The inner mesh is encapsulated by another fluid mesh which extends the fluid mesh out another five feet, continuing the transition to a cylindrical outer boundary. This mesh consists of three parts; the mesh encapsulating the inner mesh and a bow and stern cone.

To extrude this mesh from the inner mesh, the face elements of the outer boundary of the inner mesh must be selected and saved as a surface. In the previous parts of the mesh it was necessary to perform this process manually using the lasso. A key

aspect in automating the mesh generation process is to have this process performed automatically. This is done by using the **fset surface** command in combination with the surface used to initially form the outer surface of the inner mesh. This command selects all of the faces in the model which have a user specified number of nodes within a user defined distance from the surface.

```
fset innrmesh = surface 803 2 3
```

By creating surfaces between curves on each end of the inner mesh, bow and stern face sets can be created in a similar fashion. It should be noted that the parts from which the face sets are to be defined must be displayed for this option to work.

The transitional mesh is much simpler to extrude then the inner mesh since the contours of the inner mesh are convex in nature. To form the outer surface of this mesh, curves are used to form a surface very similar to that which was done for the inner mesh. The difference in constructing this mesh is that the surface must have a bow and stern portion. To simplify construction of the outer mesh which will eventually encapsulate this transitional mesh, this surface is made to be spherical at each end. The curves and surfaces used to form this outer boundary are shown in Figure 107.

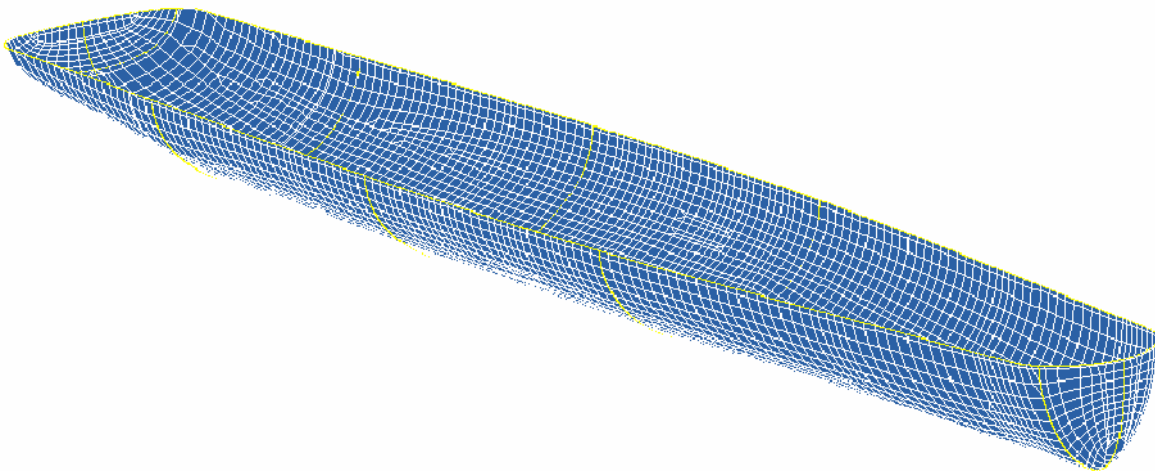


Figure 107. Curves and Surfaces Used to Form Outer Boundary of Transitional Mesh

One notable aspect of the transitional mesh is its ability to transition the inner mesh, which has a set waterline of 258 inches, to a different waterline which would result from different loading conditions of the ship. Though not used in the simulations in this paper, the ability to model different loading conditions is designed for future study. This is accomplished by first defining a large planar surface between two linear curves defined using parameters inside of functions that extrapolate the defined waterline out several thousand inches from the structure. A series of linear curves are generated at a height of 258 inches and equal to the transitional mesh in width at each location where an outer waterline node of the transitional mesh is attached. These curves are projected to the waterline surface using the **projcur** command. The outer waterline nodes of the transitional mesh are then connected to these floating curve points using the **pbs** command. The completed transitional mesh showing the three individual parts merged together is shown in Figure 108.

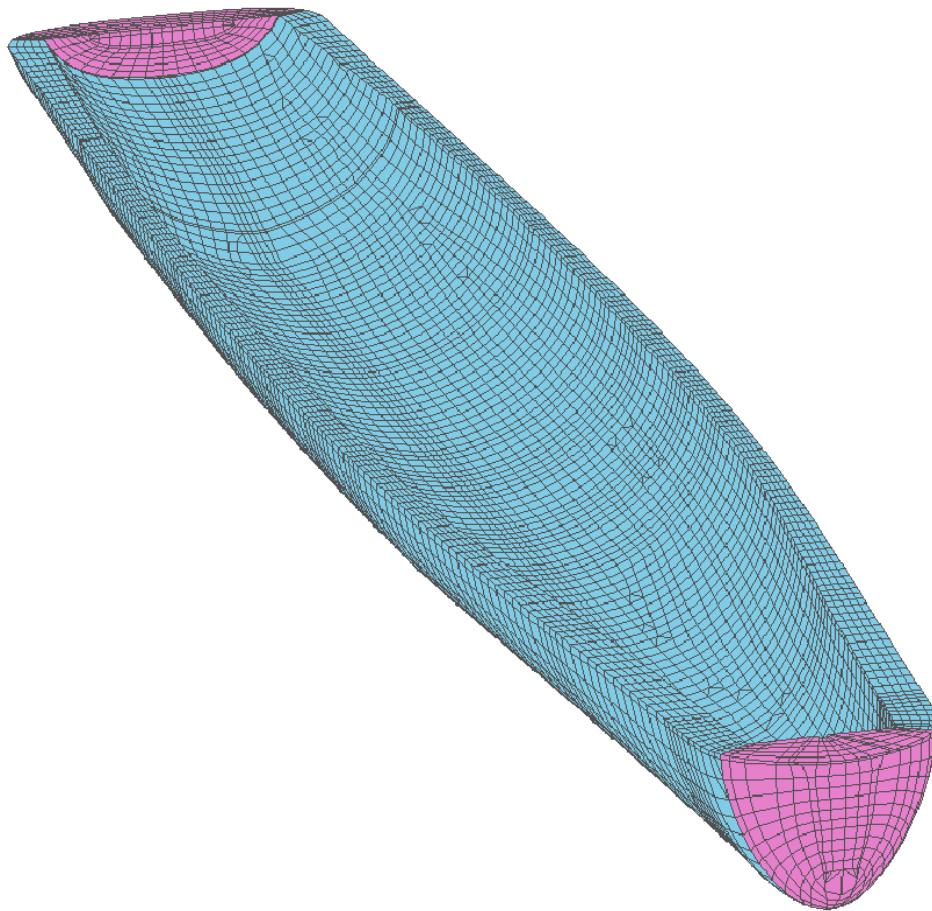


Figure 108. Completed Transitional Fluid Mesh

E. OUTER MESH

The outer mesh consists of a single mesh having a prolate spheroid shaped outer boundary contour. This portion of the fluid mesh is one of the easiest portions to extrude due to the convex contours of the transitional mesh. The most complex aspect of this mesh is in defining the surfaces and curves which form the outer boundary.

This outer mesh is designed to be easily expanded or reduced in size by using parameters. This requires that curves and surfaces be defined using these parameters. The outer boundary of the mesh is then attached to these floating surface and curve points rather than fixed coordinates. This allows the outer mesh to move with these curves and surfaces which are modified by only a few parameter inputs. Some care should be used when connecting to surfaces and curves as the numbering scheme of interpolated curves and surfaces changes as the size changes. Spheres and circular curves maintain their numbering scheme regardless of size making their use preferable if possible. The completed outermesh is shown in Figure 109.

```
blude 6 outermsh 1 202;1 52 103;1 %outerk;[-77-%daaft]
[5595+%daafwd];
[0-%daamid] 0 %daamid;[258-%daamid] -142;
pbs 1 3 2 1 3 2 xyz 43.275
pbs 1 2 2 1 2 2 xyz 42.176
pbs 1 1 2 1 1 2 xyz 43.1
pbs 1 1 1 1 1 1 xyz 141.240
pbs 1 3 1 1 3 1 xyz 141.1
pbs 1 2 1 1 2 1 xyz 136.121
pbs 2 1 2 2 1 2 xyz 44.1
pbs 2 2 2 2 2 2 xyz 42.1
pbs 2 3 2 2 3 2 xyz 44.353
pbs 2 3 1 2 3 1 xyz 127.240
pbs 2 2 1 2 2 1 xyz 128.1
pbs 2 1 1 2 1 1 xyz 127.1
curs 1 1 1 1 3 1 136
curs 2 1 1 2 3 1 126
curs 2 2 2 2 3 2 41
curs 1 1 2 1 2 2 42
curs 1 2 2 1 3 2 41
curs 1 3 2 2 3 2 41
curs 1 1 2 2 1 2 42
insprt 1 1 2 50
```

pbs 2 2 1 2 2 1 xyz 25.1.15
 pbs 2 3 1 2 3 1 xyz 25.21.55
 pbs 2 1 1 2 1 1 xyz 25.89.55
 pbs 2 1 2 2 1 2 xyz 44.1
 pbs 2 3 2 2 3 2 xyz 44.353
 pbs 2 2 2 2 2 2 xyz 44.177
 curs 2 1 2 2 3 2 44
 curs 2 1 1 2 3 1 127
 insprt 1 2 1 1
 pbs 2 1 2 2 1 2 xyz 43.1
 pbs 2 3 2 2 3 2 xyz 43.275
 pbs 2 2 2 2 2 2 xyz 43.138
 pbs 2 1 1 2 1 1 xyz 141.240
 pbs 2 3 1 2 3 1 xyz 141.1
 pbs 2 2 1 2 2 1 xyz 129.55.13
 curs 2 1 1 2 3 1 141
 curs 2 1 2 2 3 2 43
 insprt 1 2 2 9
 pb 3 3 2 3 3 2 xyz 143.01845 417.35803 258.0
 pb 3 1 2 3 1 2 xyz 143.01845 -417.35803 258.0
 pb 3 2 2 3 2 2 xyz 1.3415643E+02 -5.3800815E-01 -1.5499544E+01
 curs 3 1 1 3 3 1 241
 insprt 1 1 4 5
 pb 4 2 2 4 2 2 xyz 5461.3589 -0.7900944 -119.76952
 pb 4 3 2 4 3 2 xyz 5453.7617 281.53503 257.97253
 pb 4 1 2 4 1 2 xyz 5453.7622 -281.53503 257.97256
 curs 4 1 1 4 3 1 49
 curs 6 2 2 6 3 2 41
 curs 6 1 2 6 2 2 42
 mseq i 50 2 20 10 0
 curs 1 2 2 6 2 2 40
 curs 1 2 1 6 2 1 301
 curs 2 3 1 5 3 1 401
 curs 2 1 1 5 1 1 402
 res 1 1 1 6 3 2 k %ores
 sfi 1 6; 1 3; -2;sd 30
 sfi -1 0 -6; 1 3; 1 2;sd 999
 sfi 1 6; -1 0 -3; 1 2;sd 999
 Sfi 1 6;1 3;-1;SD 1
 tmei 1 6;1 3;1 2; 50 0 1
 relaxi 1 6;1 3;-2;20 .5 1
 relaxi 1 6;1 3;-1;20 1 1
 endpart
 merge

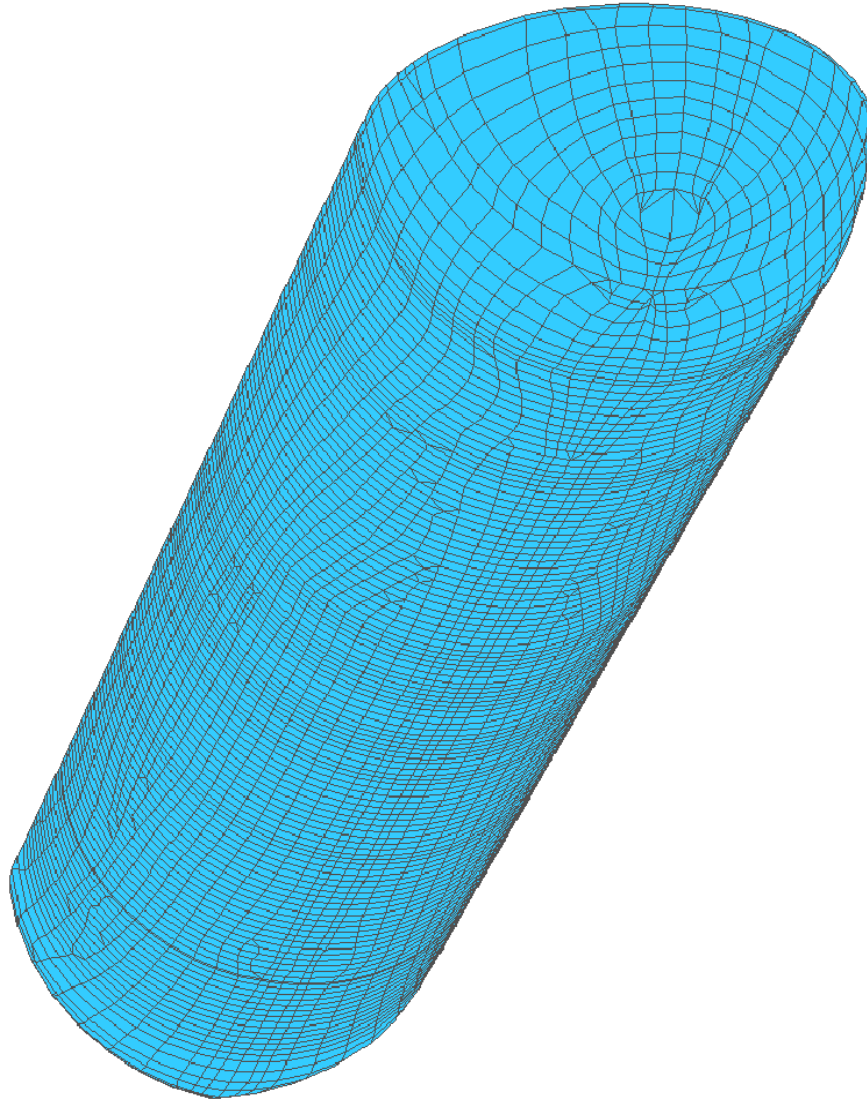


Figure 109. Completed Outer Mesh

F. DAA BOUNDARY

The **orpt** command should be used prior to defining the DAA boundary. This command ensures that the face sets are defined with their normal vectors pointing away from the point specified by the **orpt** command. Using a point located in the center of the fluid mesh ensures that this occurs at all locations on the boundary.

The DAA boundary is defined by defining a face set on the submerged outer boundary of the outer mesh using the surface generated to form the outer boundary of the mesh and the **fset** command. Once defined, all other face sets should be deleted using the

delset command. This avoids having these sets output into LS-DYNA. The fluid model is output into LS-DYNA by using the following command:

lsdyna keyword write

The completed coupled fluid structure model is shown in Figure 110.

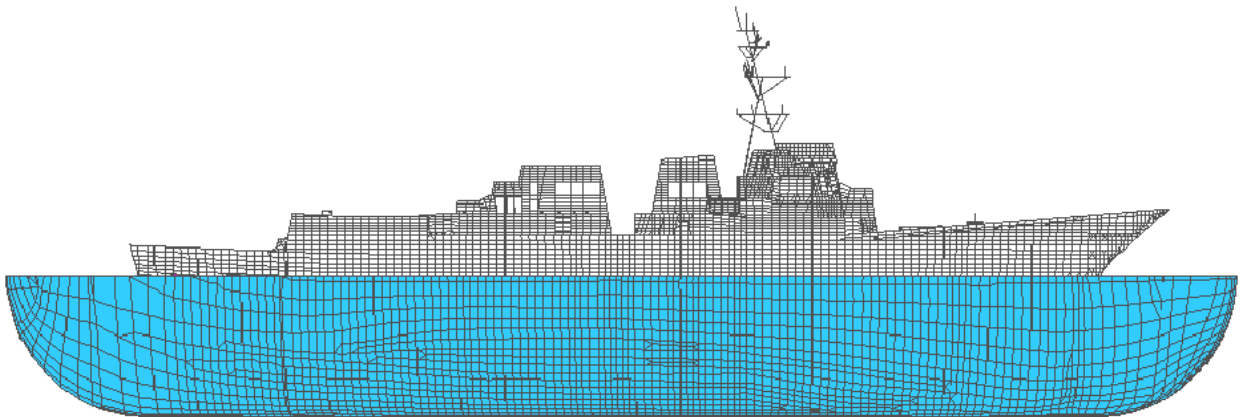


Figure 110. Coupled Fluid-Structural Model

THIS PAGE INTENTIONALLY LEFT BLANK

APPENDIX C: TRUEGRID MODELING COMMANDS

This appendix contains a brief description of many of the commands used in the fluid mesh modeling process in TrueGrid outlined in Appendix B. A complete description of all of the commands used in the fluid mesh modeling process plus many more that were not used can be found in Reference [5]. Commands have been grouped according to what phase of the modeling process they are used in.

IMPORT/EXPORT COMMANDS

1. READMESH: This command is utilized to import a NASTRAN, LS-DYNA, DYNA3D, or NEUTRAL mesh into TrueGrid. When used in conjunction with the EXCLUDE command the nodes of parts generated in TrueGrid which have merged with nodes on the imported mesh will not be redefined. Material properties of imported NASTRAN files must be redefined if being exported in another format.
2. DELMATS/DELSPPDS: These commands delete the material and spring properties of the imported model. TrueGrid does not support conversion of material and spring properties from NASTRAN to LS-DYNA. These properties must be deleted to allow the model to be exported in LS-DYNA format.
3. LSDYNA KEYWORD WRITE: This exports the model in LS-DYNA keyword format. The exported file is saved in the working directory as a trugrdo file.

PARAMETERS & PROGRAMMING

4. PARA: Parameters can be given a numerical value using this command,. To use this command a parameter is named and then followed by its numerical value. The parameters are used in the file by preceding the name of the parameter with a percent sign.

```

    PARA daafwd 900 daaft 954 daachg 900;
    curd 37 arc3 seqnc rt 5449 %daafwd 258 rt 5449 0 [258-%daafwd]
    rt 5449 [0-%daafwd] 258;

```

Parameters can allow automation of the mesh generation process when used in combination with formulas and basic FORTRAN-like code.

5. IF/ELSEIF/ELSE/ENDIF: TrueGrid allows basic control statements much like that of FORTRAN. This allows automation of the mesh generation process when used in conjunction with parameters.

```

    if (%outerk>20) then
    para ores 1;
    else
    para ores 0.96
    endif

```

CURVE COMMANDS

Note: All curve commands begin with the CURD command.

6. CPCD: This command allows the creation of a curve by performing a transformation to a previously defined curve. Since the wetted surface structure is symmetric about the xz-plane, many curves were reflected about this plane using the RZX command in conjunction with the CPCD command. Translation, reflection, and rotation transformations in all three dimensions are possible using this command.
7. PROJCUR: This command projects a curve onto a previously defined surface. This is a very useful command used alone or in conjunction with the other curve commands,.
8. CSP3: This command allows the creation of cubic spline curves. Extremely useful for defining the outer boundary curves as well as the mesh control curves in the sonar dome and skeg regions. This command allows the user to choose a natural end derivative, specify an end derivative, or match an existing curve's end derivative.

9. ARC3: This command allows the creation of a curve through a circular arc defined by three points. This is a useful command for defining spherical contours of the outer mesh.
10. LP3: The most basic curve command. This command defines a curve by a series of coordinates usually selected by picking a node or surface point with the computer mouse. This command allows modification of the coordinates which is particularly useful when manually creating the initial curves for the inner liner.
11. *PT: Following the above commands by PT allows the coordinates to be replaced with surface or curve points. This is particularly useful when automating the mesh generation process.

SURFACE COMMANDS

Note: All surface commands are preceded by the SD command.

12. PLAN/SP/CY: These commands form an infinite planar, spherical, and infinite cylindrical surface respectively.
13. BLEND3/4: This command is used to blend three or four curves together to form a surface. Very useful to form the contoured surfaces of the inner and transitional meshes as well as the surfaces required to form many of the face sets. Care should be used as the curves are combined in the order in which their nodes are defined. If a curve defined left to right is combined with a curve defined right to left the resulting surface will cross over itself.
14. RULE3D: This command combines a ruled surface between two three dimensional curves. The same rule as in the BLEND case applies concerning the order of the curve nodes.
15. SDS: Combines multiple surfaces into one surface.
16. FACESET: Creates a surface out of a previously defined face set.
17. R3DC: Creates a surface by rotating a 3D curve a specified angle about an arbitrary axis.

PART COMMANDS

18. BLOCK: This command is the most basic part generating process in TrueGrid. This command allows the user to generate parts in the part phase by defining nodal coordinates (cartesian) and through projections and curve/edge attachments.
19. BLUDE: This command extrudes a set of polygons through a defined face set by following the mesh lines formed by the block part. This command requires a thorough understanding of the block command from which it is based. The block part must completely cover the face from which it is being extruded. This command is essential in developing a properly coupled fluid-structure model.
20. PB/PBS: The PB command attaches the vertices of a block part to a set of coordinates. The PBS command attaches the vertices of a block part to surface or curve points. Careful use of the PBS command is necessary to automate the mesh generation process.
21. CURS: This command attaches an edge of the block part to a previously defined curve. The end nodes of the block part edge are attached to the curve first with the remaining nodes evenly distributed along the curve.
22. EDGE: Similar to the CURS command only this command attaches an edge of the block part to an edge of a surface.
23. SFI: This command projects the face of a block part to a previously defined surface. All surrounding vertex and edge attachments should be made prior to using this command.
24. DEI: This command deletes a region of the block part.
25. RES/AS/DAS: These commands are used to distribute the nodes along the boundary of the block part. The first or last spacing, both, or the relative spacing in a given direction can be specified.
26. BB: This command defines a boundary interface which can be used to attach two separate parts or to apply a transformation to a face set of the same block part.

- 27. NORMAL: Used in conjunction with the BB command, this command translates the slave boundary face of a block part out a specified distance normal to the master boundary face.
- 28. INSPRT: This command is used to insert a partition in the block part being created. This is done primarily in order to add additional boundary constraints to the block part
- 29. MSEQ: This command is used to add elements to or remove elements from the block part being created. Often it is easier to begin the construction process having only a few elements as a large amount of elements “clutters” the picture making attachments more difficult to see. This command can be used to add the desired number of elements to the block part just prior to attaching an edge to a curve or surface edge, adding a partition, and/or projecting to a surface.
- 30. TMEI/RELAXI: These are commands used to create a uniform mesh through interpolation methods. These commands should be issued as the last commands in the block part construction. Failure to use these or other interpolation methods will result in an improper extrusion and/or a low quality mesh.
- 31. ENDPART: This commands ends the part being worked on. No further part construction can occur after this command has been issued.
- 32. MERGE: This command ends the part phase and merges the individual parts together.

FACE SET COMMANDS

- 33. FSET “...” = LB6: This command allows a face set to be defined by manually selecting a group of face elements on a part while in the merge phase using the “pick” – “sets” – “faces” option. The faces are then selected using a lasso to circle the outer nodes of the desired faces.
- 34. FSET “...” = SURFACE: This command defines a face set by selecting all of the faces with a user defined number of nodes within a defined distance from

a surface. This command is necessary to automate mesh generation processes involving mesh extrusion.

- 35. FSET "...": This command defines a face set as another face set.
- 36. FSET "..." OR SET "...": This command adds the face set elements from one face set to another face set.
- 37. ORPT: This command allows the vector normals of the face set to be controlled. For USA, the vector normals should be pointing outward.
- 38. DELSET "...": This command deletes a face set. Prior to exporting the model into LS-DYNA, all of the face sets defined should be deleted with the exception of the face set defining the DAA boundary. This eliminates unnecessary data being exported into the output file.

MERGING COMMANDS

- 39. STP: This command is used to set the merging tolerance between nodes. Care should be used in using this command, particularly early in building the fluid model, as it is only active in the merge phase. Using a smaller tolerance in the early stages is advised to avoid large cracks appearing later on in the building process. Too large of a tolerance at any stage may result in nodes merging together undesirably.
- 40. PTOL: This command sets the merging tolerance for nodes within a specified part. Must be followed by the STP command to become active.
- 41. BPTOL: This command sets the merging tolerance for nodes between two parts. Must be followed by the STP command to become active.
- 42. PN: This command allows nodes to be repositioned in the merge phase. Useful to eliminate cracks in the mesh. Having to use this command excessively is often indicative of problems in the construction of the mesh.
- 43. LABELS CRACKS: This command is actually one of the diagnostics tools that TrueGrid has. It is used to show improperly merged nodes, cracks, in the mesh based on a user specified maximum allowable angle between nodes.

44. LABELS LOC3D: This command locates a solid element in the mesh. This is useful to find elements which have been identified by either TrueGrid or LS-DYNA as being illegal elements.
45. DELEM LB/LS: This command allows blocks or shells to be deleted in the mesh. The port and starboard stern tube covers were deleted using this command.

GRAPHICS COMMANDS

46. POSTSCRIPT: With this set to “on”, the current frame is output to the working directory as a postscript file each time the DRAW command is issued in the FILL mode. Using the right mouse button allows the user to specify resolution, enable/disable lighting, control color, etc.
47. SET PCOLOR: This command defines the color of a part by setting the levels of red, blue, and green.
48. PEXP: This command allows parts to be “exploded” a set distance from its actual position. This is useful in showing how individual parts are constructed in a model.

THIS PAGE INTENTIONALLY LEFT BLANK

APPENDIX D: USA/LS-DYNA INPUT DECKS

Examples of the USA and LS-DYNA input decks are shown in this appendix. These input decks consist of four files: the LS-DYNA “Keyword” file, and the USA FLUMAS, AUGMAT, and TIMINT files. References [6] and [7] should be consulted for explanation of each input shown. Confidential parameters pertaining to the actual shot geometry have been replaced by “XXXX” in each file.

A. LS-DYNA KEYWORD FILE

```
*KEYWORD
*TITLE
  SHOT3: COUPLED SHIP AND FLUID MODE, DAA1 BOUNDARY
*CONTROL_TERMINATION
0.51,0,0,0,0
*CONTROL_TIMESTEP
4.0E-6,0.9,0,0.0,0.0,1,0
*CONTROL_PARALLEL
1,0,1
*DEFINE_CURVE
1
0.,4.0E-6
0.51,4.0E-6
*DATABASE_HISTORY_NODE
*DATABASE_NODOUT
*DATABASE_BINARY_D3PLOT
*DATABASE_BINARY_D3THDT
*DATABASE_EXTENT_BINARY
*BOUNDARY_USA_SURFACE
1,1,0
*INITIAL_DETONATION
-1,XXXX,XXXX,XXXX,0.0
XXXX,XXXX,XXXX,XXXX,XXXX,2947
$ FLUID NODES
*NODE

"NOTE: FLUID MODEL NODE COORDINATE DEFINITIONS
OUTPUT FROM TRUEGRID ARE ENTERED HERE"

$SHIP NODES
```

"NOTE: STRUCTURAL MODEL NODE COORDINATE
DEFINITIONS ARE ENTERED HERE"

*MAT_ACOUSTIC
*PART
1
1,1,90
*SECTION_SOLID
1,8
*ELEMENT_SOLID

"NOTE: FLUID ELEMENTS ARE DEFINED HERE USING
TRUEGRID OUTPUT"

*SET_SEGMENT

"NOTE: DAA BOUNDARY FACESET DEFINED IN TRUEGRID
IS DEFINED HERE"

\$ SHIP
*PART
*SECTION_BEAM
*ELEMENT_BEAM
*PART
SPRING-ELEMENT
*SECTION_DISCRETE
*MAT_SPRING_ELASTIC
*ELEMENT_DISCRETE
*DEFINE_SD_ORIENTATION
*ELEMENT_MASS
*MAT_ELASTIC
*CONSTRAINED_NODAL_RIGID_BODY
*SET_NODE_LIST
*PART
*SECTION_SHELL
*ELEMENT_SHELL
*LOAD_SHELL_ELEMENT
*DEFINE_COORDINATE_SYSTEM
\$ RAYLEIGH DAMPING
*DAMPING_GLOBAL
*DAMPING_PART_STIFFNESS
\$ BEAM
\$SHELL
*END

B. USA INPUT FILES

1. FLUMAS

Note: The number of nodes (NSTRF) and number of DAA elements (NGENF) are fluid model specific.

DDG81 SHOT 3 COUPLED ANALYSIS - FLUMAS

```
flunam geonam strnam daanam $FLUNAMGEONAM GRDNAM DAANAM
F F F T $ PRTGMT PRTRRN PRTAMF CALCAM
T F F F $ EIGMAF TWODIM HAFMOD QUAMOD
F F T F $ PCHCDS NASTAM STOMAS STOINV
F F F T $ FRWTFL FRWTGE FRWTGR FRESUR
F T F F $ RENUMB STOGMT ROTGEO ROTQUA
F F F F $ PRTCOE STRMAS SPHERE ROTSYM
F F F F $ OCTMOD CAVFLU FRWTFV INTCAV
F F $ BOTREF MASREF
0 xxxxxx 0 xxxx $ NSTRC NSTRF NGEN NGENF
0 0 0 $ NBRA NCYL NCAV
0.9345E-4 60687.6 $ RHO CEE
2 $ NVEC
258. 0. 0. 1. $ DEPTH CXFS CYFS CZFS
14.7 386.4 $ PATM GRAVAC
0 $ NSRADI
0 $ NSORDR
```

2. AUGMAT

Note: The number of nodes (NSTR), number of degrees of freedom (NSFR), and last DAA element number (JSTOP) are fluid model specific.

DDG81 SHOT3-COUPLED ANALYSIS-AUGMAT

```
strnam flunam geonam prenam $ STRNAM FLUNAM GEONAM PRENAM
F F F F $ FRWTGE FRWTST FRWTFL LUMPFM
F F F T $ FLUSKY DAAFRM SYMCON DOFTAB
F F F F $ PRTGMT PRTRRN PRTSTF PRTAUG
F F F F $ MODTRN STRLCL INTWAT CFADYN
11 $ NTYPDA
xxxxxx xxxxxx 3 3 $ NSTR NSFR NFRE NFTR1
1 $ NSETLC
0 1 xxxx 1 $ NDICOS JSTART JSTOP JINC
```

3. TIMINT

Note: XC, YC, and ZC define the charge location. XS,YS, and ZS define the location of the closest point on the DAA boundary to the charge. SLANT is the distance from the charge to the closest point on the DAA boundary. XV, YV, and ZV is the coordinates of the fluid node one fluid element away from the closest structural node to the charge. All of these values have been omitted for confidentiality.

```

DDG81 SHOT3 COUPLED ANALYSIS-TIMINT
prenam posnam      $ PRENAM POSNAM
resnam             $ RESNAM WRTNAM
F T F F           $ REFSEC FLUMEM XXXXXX XXXXXX
F F F             $ INCTSR CENINT BUOYAN
1                 $ NTINT
0.0 4.0E-6        $ STRTIM DELTIM
T F F F           $ EXPWAV SPLINE VARLIN PACKET
F T F F           $ HYPERB EXPLOS DOUBDC VELINP
F F F F           $ BUBPUL SHKBUB XXXXXX XXXXXX
1                 $ NCHARG
0.                $ HYDPRE
XXXX XXXX XXXX    $ XC  YC  ZC
XXXX XXXX XXXX    $ XS  YS  ZS
201               $ JPHIST
1. 0.             $ PNORM DETIM
5.1E-5            $ DTHIST
1                 $ CHGTYP
XXXX XXXX XXXX    $ WEIGHT SLANT CHGDEP
99999 99999       $ NSAVR NRESET
0 0 0 0           $ LOCBEG LOCRES LOCWRT NSTART
F F F F           $ FORWRT STBDA2 ASCWRT XXXXXX
XXXX XXXX XXXX    $ XV  YV  ZV
F                 $ DISPLA

```

LIST OF REFERENCES

1. NAVSEA 0908-LP-000-3010A, Shock Design Criteria for Surface Ships, October 1994.
2. Military Specification, MIL-S-901D, Shock Tests, High Impact Shipboard Machinery, Equipment and Systems, Requirements for, March 1989.
3. OPNAV Instruction 9072.2, "Shock Hardening of Surface Ships", 12 January 1987
4. Mair, Hans U., Reese, Ronald, M., and Hartsough, Kurt, "Simulated Ship Shock Tests/Trials?", [www.dote.osd.mil/lfte/SSS.HTM]. April 2003.
5. XYZ Scientific Applications, Inc., *TrueGrid User Manual Version 2.4*, Livermore, CA 2002.
6. Livermore Software Technology Corporation, *LS-DYNA Keyword User's Manual*, Version 960, LSTC, Livermore, CA, March, 2001.
7. DeRuntz, Jr., J.A., *The Underwater Shock Analysis (USA) Manual*, Unique Software Applications, Colorado Springs, CO, May 1996.
8. Cole, R.H., *Underwater Explosions*, pp. 1-15, Princeton University Press, 1948.
9. Shin, Y.S., "Naval Ship Shock and Design Analysis", Course Notes for Underwater Shock Analysis, Naval Postgraduate School, Monterey, CA 1996.
10. Arons, A.B., et al, "Long Range Shock Propagation in Underwater Explosion Phenomena II", Underwater Explosion Compendium, Vol. 1, October 1949.
11. Geers, T.L., "Transient Response Analysis of Submerged Structures", ASME AMD – Vol. 14, 1975, ASME Winter Annual Meeting, Nov. 30 - Dec 5, 1975.
12. DeRuntz, Jr., J.A. "The Underwater Shock Analysis Code and Its Applications", 60th Shock and Vibration Symposium, Vol. I, pp. 89-107, November, 1989.
13. Geers, T.L., "Doubly Asymptotic Approximations for Transient Motions of Submerged Structures", The Journal of the Acoustical Society of America, Vol. 64, pp 1500-1508, 1978.
14. Gibbs and Cox, Inc., "DDG-81 Flight IIA Shock Simulation", Presentation at the Naval Postgraduate School, August 2002.
15. Shin, Y.S. and Park, S.Y., "Ship Shock Trial Simulation of USS John Paul Jones (DDG 53) Using LS-DYNA/USA: Three Dimensional Analysis", 70th Shock and Vibration Symposium Proceedings, Vol. I, November 1999.
16. Malone, P.E., "Surface Ship Shock Modeling and Simulation: Extended Investigation", Master's Thesis, Naval Postgraduate School, Monterey, CA, 2000.
17. MacNeal-Schwendler Corporation, "MSC/NASTRAN Quick Reference Guide," Version 69, Los Angeles, CA, 1996.
18. Smith, J.W., *Vibration of Structures: Applications in Civil Engineering Design*, 338p., Chapman and Hall, London, 1988.
19. Shin, Y.S., "Damping Modeling Strategy for Naval Ship System", Report NPS-ME-03-003, Naval Postgraduate School, May, 2003.
20. TEAM Engineering Ltd, "FEMAP: Real FEA Made Easy", [http://www.femap.co.uk]. May 2003.
21. Hart, D.T., "Ship Shock Trial Simulation of USS Winston S. Churchill (DDG-81): Surrounding Fluid Effect", Master's Thesis, Naval Postgraduate School, Monterey, CA, 2003

22. DeRuntz, Jr, J.A. "Application of the USA Code to Underwater Shock Problems", 72nd Shock and Vibration Symposium, November, 2001.
23. Wood, S.L., "Cavitation Effects on a Ship Like Box Structure Subjected to an Underwater Explosion", Master's Thesis, Naval Postgraduate School, Monterey, CA, 1998.
24. Deruntz, Jr.,J.A. and Shin, Y.S., "USA/LS-DYNA3D Software Training Course", Naval Postgraduate School, Monterey, CA, June 1996.
25. Ceetron ASA, "Glvie Pro Installation Guide & Tutorial: Glview Pro 6.3", Trondheim, Norway, 2001.
26. Thomas, P.D. and Middlecoff, J.F., "Direct Control of the Grid Point Distribution in Meshes Generated by Elliptic Equations", AIAA Journal, Vol. 18, June, 1980.
27. Bouche, R.R., *Calibration of Shock and Vibration Measuring Transducers*, pp. 22-115, Naval Research Laboratory, 1979.
28. Russel, D.D., "Error Measures for Comparing Transient Data: Part I: Development of a Comprehensive Error Measure", 68th Shock and Vibration Symposium Proceedings, Vol. I, November 1997.
- 29 Russell, D.D., "DDG53 Shock Trial Simulation Acceptance Criteria", 69th Shock and Vibration Symposium, October 1998.
- 30 Russel, D.D., "Error Measures for Comparing Transient Data: Part II: Error Measure Case Study", 68th Shock and Vibration Symposium Proceedings, Vol. I, November 1997.
- 31 Telephone conversation between Dr. John DeRuntz, Unique Software Applications, and Author, 19 May 2003.
- 32 Telephone conversation between Dr. John DeRuntz, Unique Software Applications, and Author, 20 February 2003.

INITIAL DISTRIBUTION LIST

1. Defense Technical Information Center
Ft. Belvoir, VA
2. Dudley Knox Library
Naval Postgraduate School
Monterey, CA
3. Mechanical Engineering Department Chairman, Code ME
Naval Postgraduate School
Monterey, CA
4. Naval/Mechanical Engineering Curriculum Code 34
Naval Postgraduate School
Monterey, CA
5. Professor Young S. Shin, Code ME/Sg
Department of Mechanical Engineering
Naval Postgraduate School
Monterey, CA
6. Michael J. Harrington
Gibbs and Cox, Inc.
Arlington, VA
7. Michael C. Winnette
Carderock Division
Naval Surface Warfare Center
West Bethesda, MD
8. Gus Constant
Naval Sea Systems Command
Arlington, VA
9. CAPT David H. Lewis
Program Manager (PMS 400D)
Aegis Shipbuilding
Washington, DC
10. CDR Jeff Riedel
DDG-51 Class Post Delivery Manager (PMS 400PSA)
Naval Sea Systems Command
Washington, DC

11. Fred A. Costanzo
Carderock Division
Naval Surface Warfare Center
West Bethesda, MD
12. Steven E. Rutgerson
Carderock Division
Naval Surface Warfare Center
West Bethesda, MD